TECHNISCHE UNIVERSITÄT MÜNCHEN

Professur für Mechanik auf Höchstleistungsrechnern

Multiphysics Modeling and Quantification of Early Atherosclerosis

Moritz P. Thon

Vollständiger Abdruck der von der Fakultät für Maschinenwesen der Technischen Universität München zur Erlangung des akademischen Grades eines

Doktor-Ingenieurs (Dr.-Ing.)

genehmigten Dissertation.

Vorsitzender:	Prof. Dr. rer. nat. Sonja Berensmeier
Prüfer der Dissertation:	
	1. Prof. Dr.-Ing. Michael W. Gee
	2. Prof. Dr. rer. nat. Rolf Krause

Die Dissertation wurde am 20.02.2018 bei der Technischen Universität München eingereicht und durch die Fakultät für Maschinenwesen am 22.10.2018 angenommen.

Abstract

Atherosclerosis is an inflammatory disease of the artery wall which induces severe cardiovascular sequelae like stroke or myocardial infarction. It is a major contributor to worldwide morbidity and mortality and is therefore addressed by scientific communities of all kinds. Nevertheless, many aspects, causalities and consequences of this burgeoning disease are not yet fully understood.

In this thesis, an *in silico* approach to a better understanding of atherosclerosis is chosen. Particular focus lies on the onset and early stages of atherosclerosis, as they are key to the prevention and medical treatment of atherosclerotic plaques. To investigate the inflammatory, immunological and mechanobiological processes and their causal dependencies, several mathematical models are developed, computationally treated and their implications are analyzed.

The first main objective of this thesis is to provide a mathematical and computational multiphysics framework for atherosclerosis which incorporates major aspects of the disease: cardiovascular mechanics, transport of low-density lipoproteins, inflammatory and immunological processes as well as growth and remodeling of the artery wall. Particular interest lies in investigating the interlacement of the different time scales and the parameterization of patient-specific anatomies and pathophysiologies. A methodology for the wall shear stress-dependent endothelial permeability with respect to lipoproteins is established which serves as an indicator for potential atherosclerotic-prone sites. The analysis of the multiphysics model corroborates that neglecting the short time scale of cardiovascular mechanics by time-averaging flows or neglecting the deformation of the artery wall is misleading in the context of atherosclerosis.

As existing models of the long time scale inflammatory and immunological processes are dominated by qualitative models, the second major goal of this thesis is to derive predictive mathematical models of crucial atherosclerotic processes based on available experimental data from the literature. Here, focus lies on key and measurable inflammatory and immunological processes of early atherosclerosis. The modeling and quantification of key processes and their interplay in a parameterized combined model lead to a deeper understanding of the formation of early atherosclerotic plaques. A sensitivity and stability analysis suggests that further experimental work quantifying the different fates of macrophages and the balance between intracellular cholesterols may add valuable insights toward predicting long-term plaque outcomes *in vivo*. Moreover, the results show that a persistent high supply of low-density lipoproteins and macrophages in combination with a lack of high-density lipoproteins *in vivo* render early atherosclerotic plaques progression-prone.

A decisive step toward the prevention and medical treatment of atherosclerosis is to understand under which biological and mechanobiological conditions early plaques are progressive or stagnating. Thus, the third main objective of this thesis is to develop a predictive and spatially resolved model of key contributors of early atherosclerosis. The established model allows to classify the stability of early plaques based on measurable or computable inputs, such as blood cholesterol concentrations and wall shear stresses a plaque is exposed to *in vivo*. The results indicate that the advective flux of lipoproteins through the endothelium is decisive, while the influence of the advective transport within the artery wall is negligible. Moreover, the model suggests that regions within the human cardiovascular system with an approximate wall shear

stress exposure below $1.3\ \mathrm{Pa}$ as well as their surroundings must be considered as potential regions of progression-prone atherosclerotic plaques.

By successive modeling and parameterization of crucial processes of atherosclerosis based on experimental data, several predictive mathematical models are established in this thesis. The analysis of these models deepen the understanding of key biological mechanisms and suggest future experimental investigations for biologists to take up.

Zusammenfassung

Atherosklerose ist eine Entzündungskrankheit der Arterienwand, die schwerwiegende kardiovaskuläre Folgeerkrankungen wie Schlaganfälle oder Herzinfarkte verursacht. Als weltweiter Hauptverursacher für Morbidität und Mortalität wird sie von wissenschaftlichen Disziplinen aller Art untersucht. Dennoch sind viele Aspekte, Zusammenhänge und Folgen dieser weitverbreiteten Krankheit bis heute nicht vollständig erforscht.

In dieser Arbeit wird ein *in silico* Ansatz verfolgt, um ein besseres Verständnis von Atherosklerose zu erlangen. Besonderer Fokus liegt dabei auf deren Ausbruch und frühen Stadien, da diese der Schlüssel zur Prävention und medizinischen Behandlung von atherosklerotischen Plaques sind. Um die Entzündungs-, Immun- und biomechanischen Prozesse und deren Kausalzusammenhänge zu untersuchen, werden verschiedene mathematische Modelle entwickelt, numerisch behandelt und deren Implikationen betrachtet.

Das erste Hauptziel dieser Arbeit ist die Entwicklung eines mathematischen und numerischen Multiphysik-Modells, welches maßgebliche Aspekte der Krankheit vereinigt: kardiovaskuläre Gefäßdynamik, Transport von Lipoproteinen niedriger Dichte, Entzündungs- und Immunprozesse sowie Wachstum und Umbau der Arterienwand. In diesem Zusammenhang liegt ein besonderes Interesse in der Untersuchung der Verflechtung verschiedener Zeitskalen und der Parametrisierung patientenspezifischer Anatomien und Pathopysiologien. Eine Methodik für die wandschubspannungsabhängige Durchlässigkeit des Endotheliums gegenüber Lipoproteinen wird etabliert, welche als Indikator für mögliche Regionen von atherosklerotischer Plaqueentwicklung dient. Die Analyse des Multiphysik-Modells untermauert die These, dass die Vernachlässigung der kurzen Zeitskala der kardiovaskulären Gefäßdynamik durch die Mittelung von Flüssen oder der Vernachlässigung der Deformation der Arterienwand im Zusammenhang von Atherosklerose irreführend ist.

Da bestehende Modelle für die Entzündungs- und Immunprozesse der langen Zeitskala von qualitativen Modellen dominiert werden, ist der zweite Hauptzweck dieser Arbeit die Entwicklung von prädiktiven mathematischen Modellen von entscheidenden atherosklerotischen Prozessen an Hand von auf verfügbaren experimentellen Daten aus der Literatur. Der Schwerpunkt liegt dabei auf messbaren Entzündungs- und Immunprozessen der frühen Atherosklerose. Die Modellierung und Quantifizierung von Schlüsselprozessen und deren Zusammenspiel innerhalb eines parametrisierten kombinierten Modells führt zu einem tieferen Verständnis der Entstehung von frühen atherosklerotischen Plaques. Eine Sensitivitäts- und Stabilitätsanalyse legt nahe, dass weitere experimentelle Arbeit zur Quantifizierung der verschiedenen Schicksale von Makrophagen sowie zum Gleichgewicht zwischen intrazellulären Cholesterolen wertvolle Erkenntnisse liefern kann, um die Vorhersage des Langzeitverhaltens von Plaques *in vivo* zu verbessern. Darüber hinaus zeigen die Ergebnisse, dass ein ständiger hoher Zufluss von Lipoproteinen niederer Dichte und Makrophagen in Kombination mit einem Mangel von Lipoproteinen hoher Dichte frühe atherosklerotische Plaques anfällig macht, sich zu späteren Stadien weiterzuentwickeln.

Ein entscheidender Schritt zur Prävention und medizinischen Behandlung von Atherosklerose ist, zu verstehen unter welchen biologischen und mechano-biologischen Bedingungen sich frühe Plaques weiterentwickeln oder stagnieren. Der dritte Hauptbeitrag dieser Arbeit ist daher

die Entwicklung eines prädiktiven und räumlich aufgelösten Modells der Hauptakteure früher Atherosklerose. Das eingeführte Modell ermöglicht es, die Stabilität früher Plaques auf Basis von messbaren oder berechenbaren Größen, wie den Cholesterolkonzentrationen im Blut oder den Wandschubspannungen, denen ein Plaque *in vivo* ausgesetzt ist, zu bestimmen. Die Ergebnisse deutet darauf hin der advektive Fluss von Lipoproteinen durch das Endothelium maßgeblich ist, während der Effekt des advektiven Transports innerhalb der Arterienwand vernachlässigt werden kann. Darüber hinaus legt das Modell nahe, dass Regionen innerhalb des kardiovaskulären Gefäßsystems mit einer Wandschubspannungsbelastung unterhalb von etwa $1.3\ \mathrm{Pa}$ sowie deren Umgebung als mögliche Regionen für sich weiterentwickelnde atherosklerotische Plaques angesehen werden müssen.

Durch die sukzessive Modellierung und Parametrisierung entscheidender Prozesse von Atherosklerose basierend auf experimentellen Daten, werden in dieser Arbeit mehrere prädiktive mathematische Modelle entwickelt. Die Analysen dieser Modelle vertiefen das Verständnis von biologischen Schlüsselmechanismen und legen zukünftige experimentelle Untersuchungen nahe, welche von Biologen aufgegriffen werden können.

Contents

List of Figures

List of Tables

List of Models

Nomenclature

This section contains the important abbreviations, notations and symbols that are used on several occasions in this thesis.

Abbreviations

ALE	Arbitrary-*Lagrange*an-*Euler*ian
CSF	Conductivity scaling factor
Fluid-scatra	Scalar transport with fluid flow
FSI	Fluid-structure interaction
FSSTI	Fluid-structure-scalar transport interaction
HDL	High-density lipoproteins
LDL	Low-density lipoproteins
MCC	Metabolic control coefficient
MCP	Monocyte chemoattractant protein
ODE	Ordinary differential equation
OSI	Oscillatory shear index
PFSTI	Porous medium fluid-scalar transport interaction
Poro-fluid	Porous medium fluid
Poro-scatra	Scalar transport with porous medium fluid flow
PSF	Permeability scaling factor
SI units	International System of Units
SMC	Smooth muscle cell
S2I	Fluid scalar transport-structure scalar transport interaction
Structure-scatra	Scalar transport within a structure
VCAM	Vascular cell adhesion molecule
WSS	Wall shear stresses

Nomenclature of problems and models

(Mathematical) problem	Collection of one or multiple equations that describe an “abstract” system
Subproblem	Smaller problem that describes only a subset of an “abstract” system

Multiphysics problem	Problem that combines subproblems that describe different physics
(Mathematical) model	Collection of one or multiple equations that describe a "concrete" system
Submodel	Smaller model that describes only a subset of a "concrete" system
Multiphysics model	Model that combines submodels that describe different physics
Multiscale model	Model that involves multiple time or space scales

Main notations and symbols

q, Q	Scalar quantity (non-bold)
$\boldsymbol{q}, \boldsymbol{Q}$	Vector, matrix or higher order tensor (bold)
t	Time
T	Specific instant of time
Ω	Domain
Γ	Boundary
$\boldsymbol{X}$	Material point or coordinate
$\boldsymbol{x}$	Spatial point or coordinate
$\boldsymbol{\chi}$	Reference point or coordinate
$\boldsymbol{d}$	Displacement
$\boldsymbol{u}$	Velocity
p	Pressure
c_i	i-th (abstract) concentration
$\boldsymbol{c}$	Vector of (abstract) concentrations
ϱ	Density
J	Jacobian
$\boldsymbol{F}$	Deformation gradient
$\boldsymbol{C}$	Right *Cauchy-Green* deformation tensor
$\boldsymbol{\sigma}$	*Cauchy* stress tensor
$\boldsymbol{S}$	Second *Piola-Kirchhoff* stress tensor
$\boldsymbol{b}$	Volume force
$\boldsymbol{t}$	Surfaces force
Ψ	Strain-energy density function

Superscripts

$(\bullet)^{\mathcal{F}}$	Quantity $(\bullet)$ related to fluid field
$(\bullet)^{\mathcal{S}}$	Quantity $(\bullet)$ related to structure field

$(\bullet)^{\mathcal{G}}$	Quantity $(\bullet)$ related to ALE field
$(\bullet)^{\mathcal{FS}}$	Quantity $(\bullet)$ related to fluid-scatra field
$(\bullet)^{\mathcal{SS}}$	Quantity $(\bullet)$ related to structure-scatra field
$(\bullet)^{\mathcal{PF}}$	Quantity $(\bullet)$ related to poro-fluid field
$(\bullet)^{\mathcal{PS}}$	Quantity $(\bullet)$ related to poro-scatra field

Operators and symbols

$\cup$	Union of sets
$\uplus$	Disjunct union of sets
$\cap$	Intersection of sets
$(\bullet)^T$	Transpose of $(\bullet)$
$(\bullet)^{-1}$	Inverse of $(\bullet)$
$(\bullet)^{-T}$	Transpose of inverse of $(\bullet)$
$\det$	Determinant
tr	Trace
$\otimes$	Dyadic product
$(\bullet)_+$	Positive branch of $(\bullet)$
$\|(\bullet)\|$	2-norm of $(\bullet)$
$\|(\bullet)\|_\infty$	Supremum norm of $(\bullet)$
$\|(\bullet)\|_{\mathcal{L}^2}$	$\mathcal{L}^2$-norm of $(\bullet)$
$\frac{\mathrm{d}}{\mathrm{d}t}(\bullet)$	Material time derivative of $(\bullet)$
$\frac{\partial}{\partial t}(\bullet)\big\|_{\chi}$	ALE time derivative of $(\bullet)$
$\frac{\partial}{\partial t}(\bullet)$	Partial time derivative of $(\bullet)$
$\nabla(\bullet)$	Spatial gradient of $(\bullet)$
$\nabla_0(\bullet)$	Material gradient of $(\bullet)$
$\nabla \cdot (\bullet)$	Spatial divergence of $(\bullet)$
$\nabla_0 \cdot (\bullet)$	Material divergence of $(\bullet)$
$\overline{(\bullet)}$	Spatial average of $(\bullet)$
$<(\bullet)>$	Temporal average of $(\bullet)$
$\widehat{(\bullet)}$	Steady-state value of $(\bullet)$
$\mathcal{O}(\bullet)$	Order of magnitude of $(\bullet)$
$\mathbf{1}$	Identity function
$\mathcal{H}$	Heavyside step function
$\mathbb{R}$	Set of real numbers
$\mathbb{R}_{\geq 0}$	Set of non-negative real numbers

Coordinates, Domains and Boundaries

$\boldsymbol{X}$	Material point or coordinate
$\boldsymbol{x}$	Spatial point or coordinate
$\boldsymbol{\chi}$	Reference point or coordinate
φ	Deformation map from material to spatial configuration
Φ	Deformation map from reference to spatial configuration
Θ	Deformation map from material to reference configuration
Ω_0	Material domain
$\Omega_t, \Omega(t)$	Spatial domain
$\boldsymbol{n}, \boldsymbol{N}$	Spatial and material outward pointing surface normal
Γ_{D}	*Dirichlet* boundary
Γ_{N}	*Neumann* boundary
Γ_{I}	Interaction boundary
Γ_{In}	Inlet boundary
$\Gamma_{\mathrm{Out},i}$	i-th outlet boundary
Γ_{End}	Endothelium boundary
Γ_{Adv}	Media-adventitia boundary
Γ_{Wall}	Outer wall boundary
R	Radius
T	Thickness of artery wall
H	Thickness of plaque
L	Length of segment

Fluid specific

$p^{\mathcal{F}}$	Pressure of fluid
$\boldsymbol{u}^{\mathcal{F}}$	Velocity of fluid
$\varrho^{\mathcal{F}}$	Spatial mass density of fluid
$\boldsymbol{\sigma}^{\mathcal{F}}$	*Cauchy* stress tensor of fluid
$\boldsymbol{\varepsilon}^{\mathcal{F}}$	Strain rate tensor of fluid
$\boldsymbol{b}^{\mathcal{F}}, \boldsymbol{t}^{\mathcal{F}}$	Spatial volume and surfaces forces of fluid
$\boldsymbol{\tau}^{\mathcal{F}}$	Wall shear stress of fluid
$\mu^{\mathcal{F}}$	Dynamic viscosity of fluid
$\dot{\gamma}^{\mathcal{F}}$	Shear-rate of fluid
$\mu_0^{\mathcal{F}}, \mu_\infty^{\mathcal{F}}$	Dynamic viscosity for zero and high shear rates
$\kappa^{\mathcal{F}}, b^{\mathcal{F}}, a^{\mathcal{F}}$	Parameters of *Carreau-Yasuda* model
$Q_{\mathrm{In}}^{\mathcal{F}}, <Q_{\mathrm{In}}^{\mathcal{F}}>$	Volume influx and time-averaged volume influx rate of fluid
T_{Cycl}	Length of cardiac cycle
$C_i^{\mathcal{F}}, R_{\mathrm{C},i}^{\mathcal{F}}, R_{\mathrm{P},i}^{\mathcal{F}}$	Parameters of i-th Windkessel submodel
$p_{\mathrm{dia}}^{\mathcal{F}}, p_{\mathrm{sys}}^{\mathcal{F}}$	Diastolic and systolic pressure of fluid

Structure specific

$\boldsymbol{d}^{\mathcal{S}}$	Displacement of structure
$\boldsymbol{u}^{\mathcal{S}}$	Velocity of structure
$\varrho^{\mathcal{S}}, \varrho_0^{\mathcal{S}}$	Spatial and material mass density of structure
$\boldsymbol{\sigma}^{\mathcal{S}}, \boldsymbol{S}^{\mathcal{S}}$	*Cauchy* and second *Piola-Kirchhoff* stress tensor of structure
$\boldsymbol{b}_0^{\mathcal{F}}$	Material volume forces of structure
$J^{\mathcal{S}}$	Jacobian of structure
$\boldsymbol{F}^{\mathcal{S}}$	Deformation gradient of structure
$\boldsymbol{F}_{\mathrm{Gr}}^{\mathcal{S}}, \boldsymbol{F}_{\mathrm{El}}^{\mathcal{S}},$	Growth and elastic parts of deformation gradient of structure
$\Delta \boldsymbol{F}_{\mathrm{Gr}}^{\mathcal{S}}$	Incremental growth deformation gradient
$\boldsymbol{C}^{\mathcal{S}}, \boldsymbol{C}_{\mathrm{El}}^{\mathcal{S}}$	Right and elastic right *Cauchy-Green* deformation tensor of structure
$\Psi^{\mathcal{S}}$	Strain-energy density function of structure
$\overline{I}_{(\bullet)}, \overline{II}_{(\bullet)}$	First and second modified invariant of $(\bullet)$
$\Psi_{\mathrm{Ao}}^{\mathcal{S}}, \Psi_{\mathrm{FC}}^{\mathcal{S}}$	Strain-energy density function of aortic and foam cell material
$c_{0,\mathrm{Ao}}^{\mathcal{S}}, c_{0,\mathrm{FC}}^{\mathcal{S}}$	Ground stiffness of aortic and foam cell material
$\delta_i^{\mathcal{S}}, \varpi_i^{\mathcal{S}}$	Orientation angle and stretch of i-th fiber of aortic material
$c_{1,i}^{\mathcal{S}}, c_{2,i}^{\mathcal{S}}$	Parameters of i-th fiber of aortic material
$\tau_{\mathrm{FC}}^{\mathcal{S}}$	Relaxation time of foam cell material
$k_{\mathrm{Wall}}^{\mathcal{S}}, k_{\mathrm{Out}}^{\mathcal{S}}$	Spring stiffness of surrounding and succeeding tissue
$c_{\mathrm{Wall}}^{\mathcal{S}}, c_{\mathrm{Out}}^{\mathcal{S}}$	Dashpot viscosity of surrounding and succeeding tissue
$\alpha_i^{\mathcal{S}}$	Growth parameter of species i
ϑ	Growth factor
λ	Remodeling factor

Scalar transport specific

n_c	Amount of species
c_i	i-th abstract concentration
$\boldsymbol{c}$	Vector of abstract concentrations
D_i	Diffusion coefficient of species i
$\varkappa_i$	Reaction term of species i
$J_{\mathrm{Sol},i}$	Solute flux of species i through membrane
P_i	Diffusive permeability of species i
$\sigma_{\mathrm{F},i}$	Filtration reflection coefficient of species i
ω_i	Weighting factor for average concentration of species i

Porous medium specific

ϕ	Porosity of porous medium
$\Omega_{\mathrm{Mic}}^{\mathcal{PF}}$	Microscopic fluid phase of porous medium
$\Omega_{\mathrm{Mic}}^{\mathcal{PS}'}$	Microscopic structure phase of porous medium
$\boldsymbol{u}_{\mathrm{Mic}}^{\mathcal{PF}}$	Microscopic velocity of porous medium fluid
$\boldsymbol{u}^{\mathcal{PF}}$	Fluid intrinsic volume-averaged velocity of porous medium fluid
$p^{\mathcal{PF}}$	Pressure of porous medium fluid
$K^{\mathcal{PF}}$	*Darcy* permeability of porous medium fluid
$\mu^{\mathcal{PF}}$	Dynamic viscosity of porous medium fluid
$\boldsymbol{b}^{\mathcal{PF}}$	Spatial volume forces of porous medium
$c_{\mathrm{Mic},i}^{\mathcal{PS}}$	i-th microscopic concentration in porous medium fluid
$c_i^{\mathcal{PS}}$	i-th fluid intrinsic volume-averaged concentration in porous medium fluid
$D_{\mathrm{Eff},i}^{\mathcal{PS}}$	Effective diffusion coefficient of species i
$K_i^{\mathcal{PS}}$	Hindrance coefficient of species i
J_{Vol}	Volume flux through membrane
$\sigma_{\mathrm{D},i}$	Osmotic reflection coefficient of species i
L_p	Hydraulic conductivity

Discretization specific

$(\bullet)^n$	Temporal discrete quantity $(\bullet)$ at time step n
$(\bullet)_{\mathrm{h}}$	Spatial discrete quantity $(\bullet)$
$(\bullet)_{\mathrm{j}}$	Quantity $(\bullet)$ at *Newton* step j
$\mathcal{S}_{(\bullet)}$	Solution space for $(\bullet)$
$\mathcal{T}_{(\bullet)}$	Trial space for $(\bullet)$
$\mathcal{L}^2(\bullet)$	Function space of square-integrable functions on domain $(\bullet)$
$\mathcal{H}^1(\bullet)$	Sobolev space of functions with square-integrable weak derivative on domain $(\bullet)$
$r^{(\bullet)}$	Weak residual of problem $(\bullet)$
$\boldsymbol{r}_{\mathrm{h}}^{(\bullet),n}$	Discrete residual of problem $(\bullet)$
Δt	Time step size
h	Characteristic element length

Atherosclerosis specific species

ℓ	Concentration of native LDL
$\tilde{\ell}$	Concentration of modified LDL

a	Concentration of ingested LDL
m	Density of macrophages
e	Density of endothelial cells
h	Concentration of native HDL
$\tilde{h}$	Concentration of modified HDL
ς	Concentration of copper sulfate
f	Concentration of intracellular free cholesterol
b	Concentration of intracellular cholesterol ester
r	Concentration of excreted cholesterol

Atherosclerosis specific parameters

p	Abstract parameter
d_ℓ, γ_ℓ, ℓ_{Thres}	Parameters of simplistic atherosclerosis model
s, s_{P}	(Diffusive) permeability scaling factor
ζ_τ, γ_τ	Parameters of permeability scaling factor
$q_{\ell,m}, q_{\ell,e}$	Rate of modification of native LDL by macrophages and endothelial cells
$q_{h,m}, q_{h,e}$	Rate of modification of native HDL by macrophages and endothelial cells
$\mu_\ell, \xi_\ell, n_\ell$	Parameters for ingestion of native LDL by macrophages
$\mu_{\tilde{\ell}}, \xi_{\tilde{\ell}}, n_{\tilde{\ell}}$	Parameters for ingestion of modified LDL by macrophages
$N_{\tilde{\ell}}, N_{\tilde{h}}$	Lipid peroxide per modified LDL and modified HDL
$q_{\ell,\varsigma}, q_{h,\varsigma}$	Rate of lipid peroxidation in native LDL and HDL by copper sulfate
k_h, n_h	Parameters for inhibition of modification by native HDL
N_f	Number of ingested intracellular free cholesterol per ingested LDL
$f_{\mathrm{Min}}, f_{\mathrm{Max}}$	Minimum and maximum intracellular free cholesterol for esterification
k_f, k_b	Rate of esterification and hydrolysis of intracellular free cholesterol
c_f	Rate of efflux of intracellular free cholesterol
μ_f, ξ_f, n_f	Parameters for efflux of intracellular free cholesterol to native HDL
f_{In}	Intracellular free cholesterol of recruited macrophages
μ_m, ξ_m, n_m	Parameters for apoptosis of macrophages by intracellular free cholesterol
f_0	Initial intracellular free cholesterol per macrophages
$r_\ell, r_{\tilde{\ell}}, r_h, r_m$	Rate of native LDL, modified LDL, native HDL and macrophage recruitment into intima
P_m	Rate of recruitment of macrophages
δ_m, k_m	Parameters of saturation of macrophage recruitment by modifies LDL
$\delta_\tau, \xi_\tau, \nu_\tau$	Parameters of saturation of macrophage recruitment by WSS
η_ℓ, η_h	(Constant) concentration of native LDL and HDL in blood
η_p	(Constant) blood pressure in lumen
s_{L}	(Hydraulic) conductivity scaling factor
γ_p, μ_p, ξ_p	Parameters of conductivity scaling factor

1 Introduction

Atherosclerosis is a chronic inflammatory disease of the artery wall [75, 173, 233]. Inducing severe cardiovascular sequelae like stroke or myocardial infarction, atherosclerosis is a major contributor to worldwide morbidity, loss of productive life years and mortality [202]. According to the *World Health Organization*, an approximate fraction of 31% of all deaths worldwide in 2015 were attributable to cardiovascular diseases [290] and they are projected to remain the leading cause of death until at least 2030 [289]. Thus, it is of major interest for all societies to reduce social and economic burdens arising from atherosclerosis.

A deep understanding of factors involved in the onset and progression of atherosclerosis is crucial to allow the prevention and medical treatment of this burgeoning disease. Although substantial progress was made over the past decades, the transition from *in vitro* experimental and *in vivo* animal findings to human atherosclerosis and clinical applications remains a major challenge [174]. Many inflammatory, immunological and biomechanical aspects as well as their causalities and consequences for atherosclerosis are not fully understood. Hence, atherosclerosis is addressed by scientific communities of all kinds – from biologists and physicians to mathematicians, physicists and engineers.

In this thesis, an *in silico* approach to better understand atherosclerosis is chosen which consists of three steps – mathematical modeling, numerical simulation and analysis of model results. For mathematical modeling suitable *key species* (i.e., predominant contributors, such as cells or particles) must be identified and their interactions and implications precisely defined. Validated mathematical models reduce atherosclerosis to its key processes and functions, providing a condensed view which is interesting not only for theoretical but also for experimental scientists. An appropriate numerical treatment and software implementation of mathematical models allow computationally investigating implications and hypotheses in a fast and resource-efficient manner.

This first chapter is structured as follows: To begin with, an overview of medical fundamentals of atherosclerosis is given in Section 1.1. In Section 1.2, existing modeling approaches, their challenges and applications are reviewed. Finally, the objectives and outline of this thesis are presented in Sections 1.3 and 1.4.

1.1 Atherosclerosis: the disease

In this section, the medical fundamentals of atherosclerosis required throughout this thesis are presented. Focus lies on key species and processes of the onset and early stages of the disease and

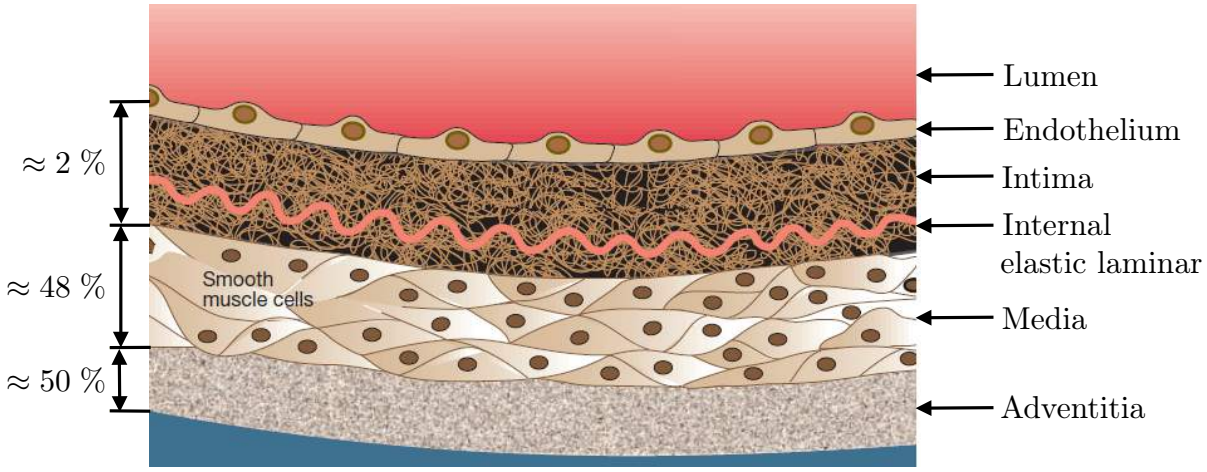

Figure 1.1 Schematic overview of the structure of walls of large arteries and their relative layer thicknesses. Modified figure taken (with permission) from *Lusis* [184]. Relative layer thicknesses are estimated for large arteries based on values given in [84, 120, 124, 221, 294].

their causal relations, which serve as a basis to put up mathematical models of various aspects of atherosclerosis in the subsequent chapters. It is important to note, however, that this section gives only a snapshot of the current view of atherosclerosis which is partly subject to ongoing research and rapid changes. Previous reviews on key species and processes of atherosclerosis can be found in the publications by *Faxon et al.* [75], *Libby* [173], *Lusis* [184] or *Ross* [233] or in the theses by *Ougrinovskaia* [212] or *Peiffer* [217].

Atherosclerosis is a non-communicable, inflammatory vascular disease occurring in the inner artery wall of large arteries, such as the aorta. Artery walls consist of three morphologically distinct sections – *intima*, *media* and *adventitia* [123, 184, 222]. The interior region of arteries, where blood flows, is called *lumen*. The luminal surface is delimited by a monolayer of endothelial cells called *endothelium* leading to a distinct interface between lumen and intima. In contrast, the transition from intima to media is rather smooth, but their delimiter is frequently defined by the *internal elastic lamina*. The three innermost layers – endothelium, intima, internal elastic lamina – are thin and soft compared to the media and adventitia [123, 125, 221, 294]. As a consequence, the mechanical properties of artery walls are dominated by media and adventitia. In the context of atherosclerosis, however, the intima is of major importance. A schematic overview of the structure of walls of large arteries and their relative layer thicknesses is given in Figure 1.1.

Atherosclerosis causes a pathological alteration of intima and media, and is characterized by the development of ineffective inflammatory lesions within the artery wall called *atherosclerotic plaques* or *atheroma*. Atherosclerotic plaques result from a complex and not yet fully understood cascade of immunological processes as response to an inflammation of the artery wall, which leads to the accumulation of lipid-rich cells and debris in the intima. The growth of plaques is associated with a thickening and hardening of artery walls. The artery lumen can be narrowed due to the protruding of the plaque, or become blocked by a blood clot resulting from a plaque rupture and a release of thrombotic plaque constituents into the bloodstream. Both phenomena can lead to a lack of nourishment of the subsequent organs, tissues and muscles and thus to severe

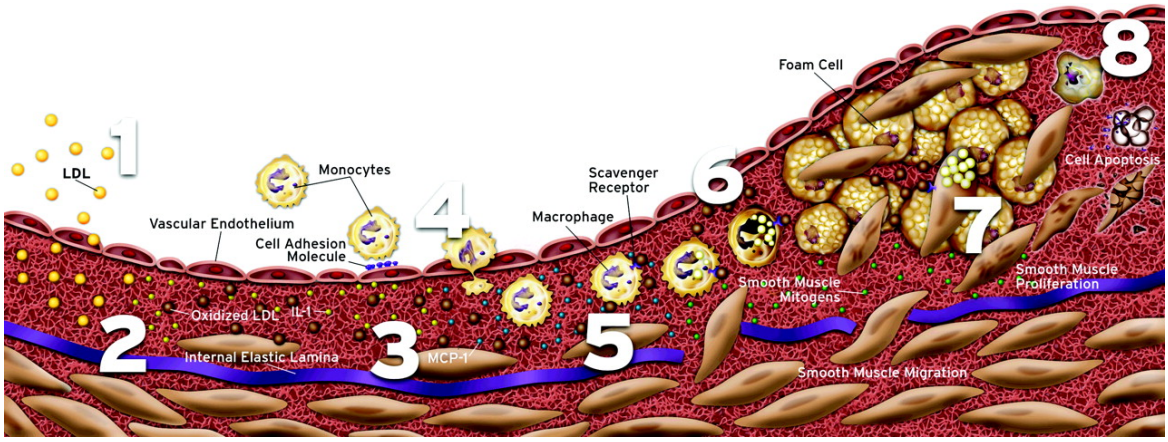

Figure 1.2 The eight stages of development of atherosclerotic plaques. Figure taken (with permission) from *Faxon et al.* [75].

sequelae, such as stroke or myocardial infarction. According to *Faxon et al.* [75], the formation of atherosclerotic plaques can be subdivided into the following eight stages:

1. Penetration of *low-density lipoproteins* (LDL) from the lumen into the intima, cf. Section 1.1.2.

2. Oxidative modification of LDL by endothelial cells, macrophages and *smooth muscle cells* (SMCs), cf. Section 1.1.2.

3. Initiation of the inflammatory processes by modified LDL which leads to the release of *monocyte chemoattractant proteins* (MCPs), *vascular cell adhesion molecules* (VCAMs) and other monocyte attracting factors, cf. Section 1.1.3.

4. Migration of monocytes from the bloodstream into the intima and their differentiation into macrophages, cf. Section 1.1.3.

5. Ingestion of modified LDL by macrophages which become *foam cells*, cf. Section 1.1.4.

6. Accumulation of foam cells in the intima which further stimulates the inflammation and leads to a thickening of the artery wall, cf. Section 1.1.4.

7. Migration and proliferation of SMCs from the media into the plaque leading to an increased thickening of the artery wall, cf. Section 1.1.5.

8. Sealing of the plaque's *necrotic core* by the *fibrous cap*, cf. Section 1.1.5.

An illustration of the eight stages is given in Figure 1.2. Details on the individual stages and further key processes are reviewed in the following sections. Here, a particular focus lies on inflammatory, immunological and biomechanical aspects that initiate atherosclerosis and drive its early stages.

1.1.1 Endothelial dysfunction and localization

It is well-accepted that a significant first step for the onset of atherosclerotic plaques is a dysfunction of the endothelium increasing the penetration of LDL from the bloodstream into the vessel wall. The role of the endothelium is crucial since it acts as a transport barrier between lumen and intima. Over the past decades, more and more evidence was found that hemodynamical factors, such as low *wall shear stresses* (WSS), resulting from flow recirculations and oscillatory flows, locally disturb the endothelium [22, 216]. Thus, plaques tends to form at inner sites of curved segments and at outer sites of bifurcations [5, 37, 190]. In humans, predominant sites for plaques are the coronary arteries and the carotids [99, 167]. As the endothelial cells react to the flow conditions they are exposed to [190], the endothelium can essentially be seen as a "shear stress sensor" [222], regulating the flux of lipoproteins and cells into the artery wall. Still, the interplay of hemodynamic forces, endothelial permeability and atherosclerosis progression is not yet understood in full detail [216, 227, 280].

1.1.2 Lipoprotein transport and modification

Lipoproteins are compositions of lipids and proteins and are retained in blood in different sizes and concentrations. Their function is to transport hydrophobe lipids, such as *cholesterol* in the hydrous blood environment. There are five distinct groups of lipoproteins according to their compositions (amount of lipids and proteins) and densities: *chylominkrone*, *very low-density lipoproteins*, *low-density lipoproteins*, *intermediate-density lipoproteins* and *high-density lipoproteins* (HDL). Of particular interest in the context of atherosclerosis are LDL and HDL. Due to their parts in atherosclerosis, LDL and HDL are commonly referred to as "bad" and "good" cholesterol, respectively.

In general, there are three pathways for the transport of blood solutes through the endothelium: by *vesicular transcytosis* (through cells), by *normal junctions* (through gaps in-between individual cells) and by *leaky junctions* (through leaks associated with dying or replicating cells) [210, 267]. For LDL particles the vesicular pathway is not eligible and their main pathway through the endothelium is by leaky junctions [30].

According to *Olgac et al.* [210] and references therein, the WSS sensor-like behavior of endothelial cells with respect to LDL transport can be explained as follows: Endothelial cells elongate in the flow direction [190] and have a lower rate of *mitosis* (cell division) when exposed to high steady WSS. Thus, the amount of leaky junctions and the associated amount of LDL seeping into the vessel wall through their main pathway is decreased by high WSS. In contrast, the transport of HDL through the endothelium is scarcely investigated. Due to their related structure and smaller size [151, 225], however, analog transport mechanisms with faster transport rates can be expected for HDL [251].

LDL and HDL retained in the artery wall are prone to oxidative modifications by endothelial cells, macrophages and smooth muscle cells [116, 165, 200, 204, 252]. In this thesis, when a differentiation between unmodified LDL (as retained in blood) and oxidatively modified LDL is required, they are referred to as *native* LDL and *modified* LDL, respectively. Analog terms are

used for HDL too. The modification of LDL and HDL is induced by oxidants, such as *radical oxygen species* or *free radicals* which are excreted from cells. Native HDL, however, provides an atheroprotective behavior as it offers a protection against the oxidative modification of native LDL [187, 188, 244]. Details on the oxidative modification of native LDL and native HDL can be found in the extensive review by *Stocker* and *Keaney* [252].

1.1.3 Endothelial activation and monocyte recruitment

The oxidative modification of native LDL renders it pro-inflammatory [252, 286, 287], which initiates an immune response in the artery wall. Modified LDL activates endothelial cells causing the production of VCAM-1 and other cell adhesion molecules [49, 93]. Thus, modified LDL increases the adhesiveness of the endothelium with respect to monocytes [16, 134, 141, 169, 169].

Monocytes in the bloodstream roll and adhere on the endothelium surface due to VCAM-1 [2, 171], which enables their migration into the artery wall. Monocytes, however, can also be detached by the mechanical force of the fluid, i.e., the wall shear stresses acting on the endothelium. Due to the increased VCAM-1 production by activated endothelial cells, modified LDL enhances the binding of monocytes against WSS induced detachment [2, 141]. In contrast, the production of VCAM-1 by endothelial cells is decreased under high wall shear stress conditions [42] which weakens the monocyte adhesion in addition to their increased detachment.

Although substantial progress was made over the past decades, important aspects of the influence of local flow conditions on the endothelium remain unclear [168]. For example, monocytes show an increased attachment in response to oscillatory flows [127], even though monocytes are also dragged away under steady flow conditions. Further, it is controversial whether endothelial cells in different vessels and species are primed to a uniform range of WSS, or to location- and species-dependent ranges [40, 238].

Modified LDL also causes the production of MCP-1 by endothelial cells and SMCs in the artery wall which creates a *chemotactic* gradient of MCP-1 [110]. Therefore, firmly attached monocytes actively migrate through the endothelium into the intima [171]. Other monocyte-attracting molecules, such as MCP-2, MCP-3, MCP-4, MCP-5, *Interleukin-8* or *Interferon-*γ take part in the monocyte migration process too. However, it is widely accepted that MCP-1 is the most prominent contributor. Genetically modified mice with an absence of MCP-1 or its receptor on monocytes have shown significant lesion retardations [18, 105]. Once within the intima, monocytes can also transmigrate into the media [189, 239] depending on chemotactic gradients.

1.1.4 Fate of macrophages and cholesterol cycle

Ubiquitous macrophages (Greek: “big eaters”) are decisive for the disease pathogenesis and resolution. They promote inflammation resolution by removing pro-inflammatory materials from plaques but at the same time also drive the inflammation in response to LDL [110, 198].

Macrophages exhibit a wide variety of phenotypes [201]. Nevertheless, solely the inflammatory phenotype of macrophages within plaques is of particular interest in atherosclerosis.

Endothelial cells, SMCs and plaque-resident macrophages secrete *Macrophage Colony Stimulating Factor* (MCSF) causing the differentiation of monocytes to scavenger-receptor expressing macrophages [110, 191, 224, 260]. MCSF is crucial for the survival of macrophages in lesions [260] and the onset of atherosclerosis. Mice lacking MCSF show a retarded lesion development with markedly reduced macrophage accumulation in plaques [173, 260].

The Nobel Prize winning work of *Brown* and *Goldstein* [23] revealed the cholesterol cycle in macrophages. Cholesterol in cells is stored in the cell membrane in two distinct states – *free* and *esterified* cholesterol. Intracellular free and esterified cholesterol are in a dynamic equilibrium due to *hydrolysis* and *esterification*, which together are referred to as *cholesterol cycle* [25]. Most cells endocytose LDL (transport LDL into the cell) only when being low on cholesterol to maintain a stable intracellular cholesterol content [23]. Cholesterol is essential to keep the integrity of cell membranes but is cytotoxic in excess. Thus, LDL uptake and efflux are tightly regulated by cells to be within essential and cytotoxic limits.

Using their *scavenger receptors*, however, macrophages in lesions actively scavenge and ingest modified LDL, removing it from the plaque [156] and reducing its inflammatory implications. As a consequence, macrophages gain lipids in excess and store its cholesterol content as intracellular free and esterified cholesterol. Hence, the intracellular cholesterol balance is disrupted in plaque macrophages, causing cholesterol cytotoxicity. Macrophages with an excess of intracellular lipids are known as *foam cells*.

Increased intracellular cholesterol concentrations in macrophages enhance their pro-inflammatory response [299] and their rate of *apoptosis* (controlled cell death) [63, 296]. Above the cytotoxic cholesterol limit, *necrosis* (uncontrolled cell death) is inevitable [77, 175, 259]. To prevent cholesterol cytotoxicity, macrophages offload their intracellular free cholesterol content to native HDL, a process called *reverse cholesterol transport* [24, 25]. In contrast to native HDL, modified HDL no longer takes part in the reverse cholesterol transport [204].

Besides modified LDL, macrophages also scavenge and ingest other noxious extracellular substances, such as necrotic debris or other apoptotic macrophages. By efferocytosis (clearance of defective cells, Latin: “to bury”) the cholesterol content in apoptotic macrophage is recycled and retained in the macrophage population [91]. As a consequence, dead and dying macrophages worsen the whole population’s state leading to a vicious cycle of cell death and efferocytosis. With poor access to native HDL, the intracellular cholesterol content in plaque macrophages increases [218] above the cytotoxic cholesterol limit, causing necrosis and thus the accumulation of necrotic debris and extracellular lipids in plaques [103, 198].

Besides apoptosis and necrosis, the fate of macrophages is also driven by emigration from and proliferation within plaques. However, only apoptosis is important in early stages of atherosclerosis [220]. Emigration [170, 180, 220], proliferation [228] and necrosis [258] are crucial in advanced stages. Thus, the particular interest on the fate of macrophages in this thesis lies on apoptosis.

Apoptosis, proliferation and necrosis all contribute to a maladaptive inflammatory response, whereas emigration and reverse cholesterol transport reduce the inflammatory response. As emigration is yet poorly studied and hard to influence *in vivo*, reverse cholesterol transport and thus HDL has received considerable attention in therapy design offering a possibility to break the vicious cycle of cell death and efferocytosis. Its pathway for cholesterol removal from plaques [24] and its antioxidant effects that reduce LDL modification *in vitro* [187], together with its easy application by injections, make it an interesting target as a drug. Nevertheless, there is controversy over the efficacy of increasing HDL concentration in the blood serum as a therapy for late-stage plaques, but infusions of HDL mimetics show some promise [26, 39].

1.1.5 Advanced stages and sequelae

If the inflammatory response is sustained by the persistent influx and modification of LDL and poor access to native HDL, the plaque renders from progression-resistant to progression-prone [249]. In such plaques, further processes are triggered that aim to contain the inflammatory lesion.

Advanced plaques are populated by a variety of cells, such as *T-cells* ($\approx 10\,\%$), macrophages ($\approx 40\,\%$), SMCs ($\approx 50\,\%$) and small populations of other cells [110]. T-cells are immune cells that enter the intima similar to monocytes: They adhere on the endothelium surface due to adhesion molecules, such as VCAM-1 and actively migrate through the endothelium due to chemoattractants, such as Interferon-γ [173]. In the artery wall, T-cells bind modified LDL by their *antigen receptors*. This, together with macrophage-produced *cytokines* (mediating signal molecules), activates T-cells to produce additional pro-inflammatory and anti-inflammatory cytokines [110, 173].

In contrast to early stages, in late stages of atherosclerosis, macrophage proliferation and emigration from the plaque are enhanced to minimize the populations intracellular cholesterol content [170, 180, 220, 228, 258]. By emigration, macrophages (and also T-cells) can traffic between bloodstream, lesioned artery wall, *vasa vasorum* (microvasculatures that penetrate the artery wall, Latin: “vessel of the vessel”) and regional *lymph nodes*. Moreover, efferocytosis of apoptotic T-cells by macrophages results in the secretion of *vascular endothelial growth factor*, which promotes endothelial cell proliferation [102, 258]. Thus, lipid influx is promoted by macrophage efferocytosis due to an increased amount of leaky junctions in the endothelium.

SMCs are assumed to play an important role, even though their part in atherogenesis is not yet fully understood [68]. For a review of SMCs and their part in atherosclerosis the publication by *Doran et al.* [68] is recommended. Activated by growth factors and cytokines produced by macrophages and T-cells, SMCs undergo a phenotypic change from their usual contractile state (medial SMCs) to a synthetic state (intimal SMCs). The phenotypic change of SMCs leads to an agile and secretory cell which migrates into the intima [75]. One of the most prominent functions of intimal SMCs is to secrete extracellular matrix consisting of *collagen*, *elastin* and *fibronectin* [68, 184]. However, Interferon-γ, produced by T-cells, inhibits the production of extracellular matrix by SMCs. Further, macrophages produce various *proteases* (protein dissecting enzymes), that degrade extracellular matrix. SMCs use the collagen and fibronectin gradients

(secreted by other SMCs) to *haptotactically* move into the plaque and toward the endothelium. This process is further enhanced by their chemotaxation along the gradient of *platelet-derived growth factor* secreted by macrophages [206].

The role of SMCs is complex as they can be both pro-inflammatory and anti-inflammatory. SMCs modify LDL to a form that is recognized by macrophages and thus retain the inflammation [116]. Similar to macrophages, SMCs also ingest modified LDL and can therefore become foam cell-like cells [68]. However, SMCs can also perform endothelial cell-like functions, such as the production of VCAM-1, which is taken over by SMCs in advanced stages [110], retaining the migration of monocytes and T-cells even in the absence of intact endothelial cells.

Synthetic SMCs in the intima secrete significantly more collagen than contractile SMCs. Over time, the secreted extracellular matrix (especially collagen) by SMCs give rise to a thick *fibrous cap* sealing the plaque and separating its constituents from the bloodstream. Additionally, synthetic SMCs are more proliferative than their contractile counterparts, which is assumed to be a major factor in the growth of advanced plaques [206]. Together, necrotic cells (macrophages, T-cells *and* SMCs) and other lipid-laden extracellular debris form the *necrotic core* within plaques [206]. The successive migration, necrosis and defective clearance of more and more cells in the plaque lead to a growing necrotic core which induces a swelling of the inner artery wall. Experimental results indicate that the thickening of the artery wall can initially be compensated by an enlargement of the artery [101, 113, 136, 168] called *Glagov remodeling* [84]. Still, the plaque may grow large enough to cause a drastic narrowing of the lumen and the formation of a severe stenosis [173].

It is known, however, that serious clinical symptoms can occur also without a preexisting severe stenosis [109, 172]. Nowadays, the occurrence of severe sequelae of atherosclerosis is commonly associated with plaque ruptures. Atherosclerosis involves a hardening and loss of elasticity of the artery wall [271]. The increased artery stiffness may be induced by degenerative changes of the extracellular matrix (e.g., by SMCs) [214] or by calcifications of the intimal and medial layers [33, 186]. However, the influence of the latter is controversial as uncalcified late-stage plaques also exist [186, 271]. Yet, the pathway which leads to the hardening and remodeling of the artery wall is under frequent investigation.

Due to increased artery stiffness, loss of elasticity and continuous mechanical loading by the blood, advanced plaques are prone to a rupture or superficial erosion of their fibrous cap [172]. When *thrombogenic* material within plaques, such as macrophage-produced *tissue factor* comes into contact with blood, a coagulation cascade that results in the production of thrombin is unleashed [56]. This causes blood platelets and other blood constituents to form a blood clot known as *thrombus* at the site of injury. The thrombus can trigger an occlusion event at the site of the injury or downstream that may result in serious clinical symptoms, such as myocardial infarction, stroke or other *ischaemia*. However, not all disruptions of atherosclerotic plaques must result in severe symptoms [172] and thus atherosclerotic sequelae can be clinically silent too.

1.1.6 Clinical relevance and classification

In general, atherosclerosis itself is asymptomatic (clinically silent). Some of its sequelae, such as stenoses can induce slowly advancing noticeable symptomatic consequences (e.g., *angina*

pectoris) and thus may be medically treated in time. However, most of the secondary diseases which result from a plaque rupture and an associated thrombosis usually occur instantaneously and may lead to life-threatening clinical symptoms which can only be treated *a posteriori* to the symptomatic event.

In a clinical context, an important indicator for early atherogenesis is an increased intima-media thickness [33, 107, 219]. The intima-media thickness of vulnerable superficial arteries, such as the carotid can be assessed in patients by high-resolution ultrasonography [107, 219]. However, in general the non-invasive detection of vulnerable atherosclerotic plaques remains a challenge and is often a by-product of other clinical diagnostics. Thus, the focus in atherosclerosis lies more on its prevention by actively reducing the modifiable risk factors [88, 253]. Modifiable risk factors include elevated blood pressure, *dyslipidemia* (abnormal blood lipid profile, usually high LDL profile), obesity, smoking and *diabetes mellitus* [108]. Important non-modifiable risk factors for atherosclerosis-induced clinical events are sex, age and genetic predisposition. The prevention or cure of atherosclerosis is at its beginning [229] and thus cardiovascular diseases are projected to remain the leading cause of death until at least 2030 according to the *World Health Organization* [289, 290].

During the course of a human lifetime, the interplay between lipids and immune cells drives characteristic changes in plaque constituents [199]. These changes are used by clinicians to quantify and describe the individual stages of the disease based on its pathology. The classification by the *American Heart Association* proposed by *Stary et al.* [249] considers nine different types of the atherosclerotic process divided into six different stages denoted as I-VI. The designated types can be used by clinicians to assess atherosclerotic plaques – often even based on the appearance to the unaided eye. An overview of the nomenclature, main histology, main growth mechanism, earliest onset and clinical correlation of the different stages of atherosclerosis in humans is given in Table 1.1.

The inflammatory, immunological and biomechanical processes described in the previous sections are roughly linked to the classification by the *American Heart Association* as follows: *Early* plaques that contain lipid-rich macrophages and T-cells are known as types I and IIb. Lesions that contain a cap of SMCs over a lipid-rich core present themselves as *intermediate* types IIa, III and IV. By the time a thick fibrous cap has formed, lesions usually possess a necrotic core and give rise to characteristics of type Va. The *advanced* and final stages, when the cap becomes fibrous, calcified and is potentially rupture-prone are designated to type Vb, Vc or VI.

1.1.7 Plaque stability

In this thesis, particular interest lies on the quantification of early plaques and the assessment of their long-term development and stability. Therefore, the differentiation of progression-prone and progression-resistant fatty streaks (i.e., type IIa and IIb) in the classification by the *American Heart Association* is of particular interest. Progression-resistant fatty streaks correspond to early plaques that remain in their current state (i.e., are stable) or are even regressive to some extent. On the other hand, progression-prone plaques keep growing and become potentially vulnerable. However, advanced plaques can also stabilize, and even eroded or ruptured plaques can heal. A

Table 1.1 Classification of atherosclerotic lesions in humans by the *American Heart Association* based on their pathology. Types of lesions including their nomenclature, main histology, main growth mechanism and clinical relevance in humans. Modified table as given in [249].

Type	Nomenclature	Main Histology	Main growth mechanism	Earliest onset (human)	Clinical correlation
I	Initial lesion	Isolated macrophage foam cells	Growth mainly by lipid accumulation	From first decade	Clinically silent
IIa	Progression-prone fatty streak (or fatty dot)	Mainly intracellular lipid accumulation			
IIb	Progression-resistant fatty streak (or fatty dot)				
III	Intermediate lesion	II & small extracellular lipid pools		From third decade	
IV	Atheroma (or atheromatous plaque)	II & core of extracellular lipids			Clinically silent or overt
Va	Fibroatheroma (or fibrolipid plaque)	One or multiple lipid cores & fibrotic layers	Accelerated smooth muscle and collagen increase	From fourth decade	
Vb	Calcific lesion (or calcified plaque)	Mainly calcific fibrolipid lesions			
Vc	Fibrotic lesion (or fibrous plaque)	Mainly fibrotic layers			
VI	Complicated lesion (or complicated plaque)	Surface defect, hematoma-hemorrhage, thrombus	Thrombosis, hematoma		

schematic overview of the life history and possible terminations of atherosclerotic plaques is given in Figure 1.3.

In general, the presence of large numbers of macrophages, a large necrotic core and a thin fibrous cap are the hallmarks of dangerous and asymptomatic plaques [274]. Nevertheless, the question of why some initial plaques evolve toward advanced plaques whereas others do not, is yet unanswered. Therefore, an important aim of this thesis is to model and quantify processes that determine the stability of early plaques and if they are progression-prone or progression-resistant.

1.1.8 Atherosclerosis in mouse models

Currently, mice are the most frequently employed animal to study atherosclerosis [99]. Clear advantages of mouse models are their unproblematic acquisition, easy keeping and short time means leading to relatively cheap and quick studies. More important, however, is the possibility of

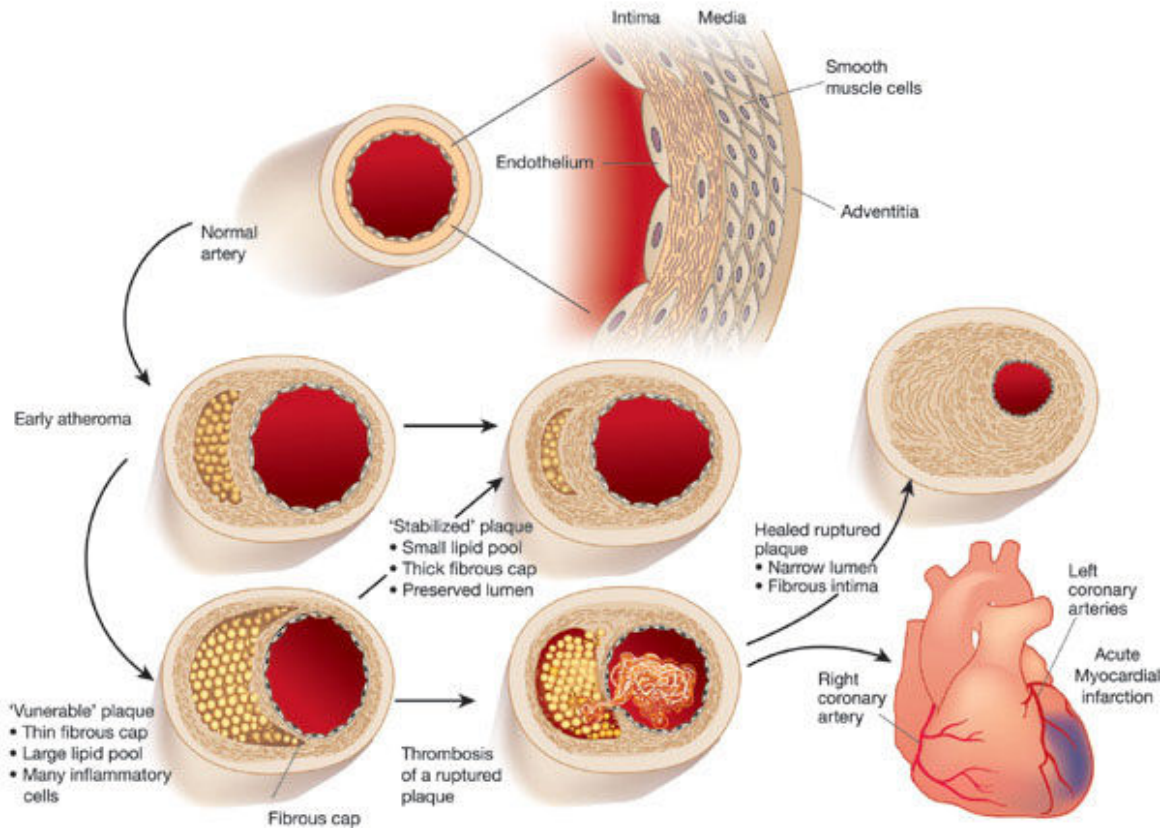

Figure 1.3 Life history and possible terminations of atherosclerotic plaques. Figure taken (with permission) from *Libby* [173].

genetic manipulations of mice which enables the knockout of genes to "modify" specific processes and to study their part in atherosclerosis *in vivo*. The great importance of genetic manipulations can be seen in the example of macrophages-specific and SMC-specific manipulations. It is common practice to genetically modify mice to bear macrophages-specific knockouts (see [283] for a tabular overview) and thus much is known concerning the behavior of macrophages *in vivo*. In contrast, SMC-specific gene manipulations are yet rather novel such that SMC-related processes *in vivo* and details on their participation in atherosclerosis are just recently surfacing [68].

Besides all benefits, mouse models also come along with a severe drawback: Wild-type mice are naturally resistant to atherosclerosis [167, 283]. An important reason for their protection is that mice have low plasma cholesterol levels where sanatory HDL is predominant (in humans deleterious LDL is predominant) [167]. However, other factors, such as their failure to develop a thick fibrous cap [232], their lack of vasa vasorum [167] or their differently primed endothelial cells [40] might be of great influence too.

Therefore, atherosclerotic plaques in mice are induced by high-fat diets drastically altering blood cholesterol profiles and thus enforcing the development of plaques [272]. However, concerns have been raised that this non-physiological diet also alters the atherogenesis such that it differs from that in humans [167, 241]. And even if the atherosclerotic process in mice is enforced,

they are – depending on their genetic manipulation – usually restricted to develop solely early and intermediate plaques of type I-IV which are not prone to rupture [283]. An exception are *apolipoprotein E deficient* mice, where also type V and VI lesions have been reported in the innominate artery [98, 167]. Other predominant sites for atherosclerotic plaques in mice on high-fat diets are the aortic sinus and aortic arch [99, 167, 185, 232].

Another drawback of mouse models is that due to their small size the imaging and the localization of plaques *in vivo* is challenging [167]. However, advances have been made using high-resolution *magnetic resonance imaging* [284] or gold particle-enhanced *computer tomography* [61]. Despite the mentioned drawbacks, mouse models are an indispensable part of the scientific research on atherosclerosis, and they may bear the key for the prevention or cure of this burgeoning disease.

1.2 Existing modeling approaches and challenges

Mathematical and computational models play an important role in increasing the understanding of atherosclerosis. Therefore, a broad spectrum of models of various aspects of atherosclerosis was established over the past decades. In this section, mathematical and computational models and challenges that are of particular interest in this thesis are reviewed. A comprehensive tabular overview of existing models of atherosclerosis and their specific applications can be found in the publication by *Parton et al.* [215]. In the publication by *Holzapfel et al.* [125] a review of mechanical models of plaques and plaque rupture is given.

A great challenge for computational models are the different time scales involved in the atherosclerotic process. On the one hand, most of the atherosclerosis-specific processes, such as the penetration of lipids and monocytes through the endothelium, the development and accumulation of foam cells or the migration of SMCs into the intima are – depending on the species – on the time scale of hours to weeks, months or years. On the other hand, the cardiovascular mechanics and thus WSS-related aspects of atherosclerosis, such as the endothelial permeability with respect to lipids and monocytes are governed by the time scale of the cardiac cycle being in the order of magnitude of a second. Therefore, existing modeling approaches can be divided into short and long time scale models. For the scope of this thesis, the long time scale models can again roughly be subdivided into three groups which focus on the LDL transport, the inflammatory and immunological processes and the growth of the artery wall. A schematic illustration of selected mathematical and computational models including their approximate time scales and topics is given in Figure 1.4

1.2.1 LDL transport

Following *Zunino et al.* [221, 305], LDL transport models can be classified into three groups according to their complexity: The *wall-free* model estimates the LDL concentration in the lumen and takes the artery wall solely into account in terms of suitable boundary conditions. The *fluid-wall* model considers the LDL concentrations in the lumen *and* intima and their exchange of LDL. Finally, the *multilayer* model additionally considers the LDL concentrations in the

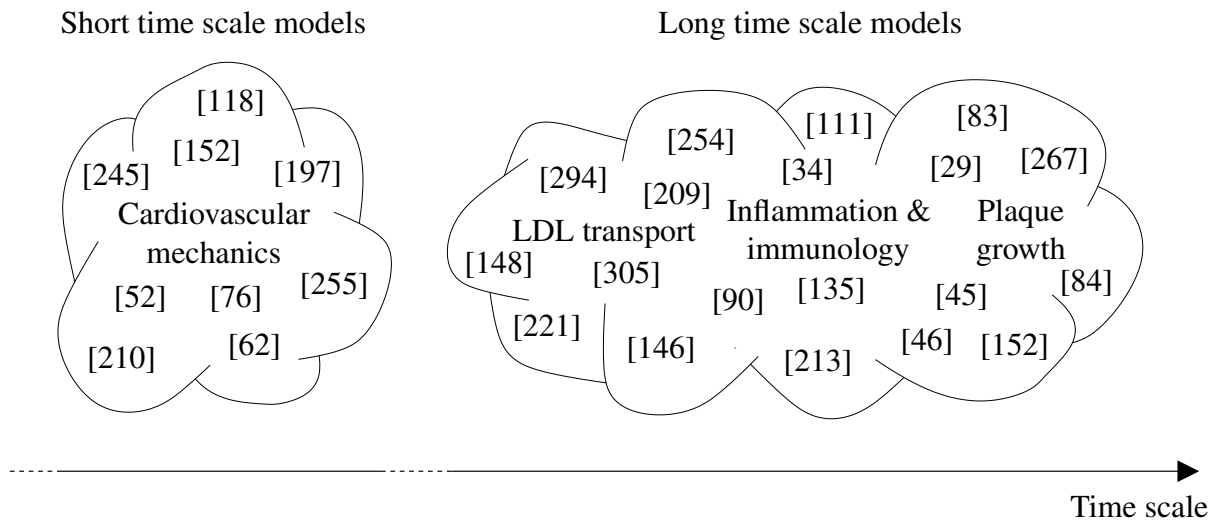

Figure 1.4 Illustration of selected existing mathematical and computational models including their approximate time scales and topics.

media and the LDL exchange in-between all three layers – lumen, intima *and* media. However, experimental results [19, 54, 195, 268] and computational studies [146, 221, 294] indicate that the concentration of LDL in the media is almost vanishing and thus negligible. Hence, the fluid-wall model is commonly employed when investigating LDL transport in the context of atherosclerosis [29, 152, 209, 210, 254, 255, 264, 267].

Independent of the specific wall model, the transport barriers conditions between the individual layers (i.e., endothelium and internal elastic lamina) are commonly modeled as semi-permeable membranes described by the equations of *Kedem* and *Katchalsky* [148]. The crucial role of the biomechanics in the transport of LDL through the endothelium is usually incorporated by adapting parameters of the *Kedem-Katchalsky* equations by WSS-dependent laws. A sophisticated approach proposed by *Olgac et al.* [209] is the *three-pore model* where the three LDL transport pathways (vesicular, normal junctions and leaky junctions) are considered and the amount of leaky junctions is estimated based on the local WSS. Other approaches consider a WSS-dependent *hydraulic conductivity* [254] or utilize heuristic laws that adapt the *diffusive permeability* [29] which drastically reduces the complexity but can still mimic a physiological correct behavior.

There is divisiveness, however, on the importance of driving mechanisms for the LDL transport into the intima. According to the *Kedem-Katchalsky* equations, the flux through the endothelium and internal elastic lamina can be split into a concentration gradient-driven diffusive flux and an advective flux. The advective flux is due to the *transmural flow* of blood plasma driven by the pressure gradient across the endothelium. Yet, there is no experimental data that allows to rate the importance of the advective flux. The analog holds for the LDL transport *within* the artery wall which might be driven by advection *and* diffusion, or solely by diffusion. Many models consider the transmural flow across the endothelium and within the artery wall by *porous media* approaches [210, 221, 267, 294], whereas others model the penetration or transport as a purely diffusive process [29, 126, 268]. Still, the importance of the porous media flow on the LDL transport and on atherosclerosis is controversial and requires further investigations. Besides

the transport of LDL, the penetration and transport of HDL and monocytes are key aspects of atherosclerosis that have received only scarce attention [45, 90, 251]. Especially the latter is problematic, as the pathway for the active migration and movement of monocytes (and other cells) is independent of the pathways of the lipoprotein transports.

1.2.2 Inflammation and immunology

A broad spectrum of models of the inflammatory and immunological processes of all stages of atherosclerosis exists [7, 29, 34, 45, 46, 48, 72, 83, 90, 111, 135, 213, 304]. However, due to the incomplete knowledge of many aspects and causalities from a biological point of view, there is barely any continuity in-between different models. Some models consider only a few key species [29, 34], whereas others identify up to 16 important species [90]. Some identify chemotaxis to be crucial [34, 35, 90, 111], whereas others restrict themselves to pure ordinary differential equation (ODE) models [46, 48, 213]. The complete picture of inflammatory and immunological models is even more fuzzy when considering *how* specific processes are incorporated into different models. A comprehensive tabular overview of existing models can be found in the review by *Parton et al.* [215]. A quantitative validation of the models by experimental results is barely achieved and it is difficult to distinguish the validity of the different models. Thus, enhanced by poor access to quantitative experimental data, the development of data-driven mathematical models with predictive capabilities remains a major challenge.

1.2.3 Plaque growth

In addition to the inflammatory and immunological processes, some models consider the growth of atherosclerotic plaques in terms of heuristic growth laws [29, 45, 83, 90, 267]. Even though mechanically motivated growth models are successfully employed for other biomechanical problems, such as tumor or tissue growth [3, 55, 119, 132, 149, 155], only scarce work has been done in the context of atherosclerosis [84].

The mechanical properties of the individual plaque constituents are well quantified and are essential to assess the risk of plaque damages and ruptures due to mechanical loading [9, 125, 261]. The mechanical models, however, commonly solely analyze snapshots of the continuous remodeling process of artery walls. The dynamic change of mechanical properties of atherosclerotic artery walls associated with their growth is not yet considered.

Only few models take a holistic approach of the atherosclerotic process and consider all the aforementioned processes. For models of the long time scale of atherosclerosis, one can highlight the works by *Calvez et al.* [29] and *Cilla et al.* [45] which both consider the transmural flow in the artery wall, a simple but convenient inflammatory and immunological model and an induced heuristic growth. As most porous media based models, however, they consider solely an artificial and simple geometrical setup, which at best produces qualitative results.

1.2.4 Cardiovascular mechanics

Short time scale models generally focus on a physiologically correct description of the cardiovascular mechanics and therefore do not have to be specific to atherosclerosis. They commonly include two aspects missing in most of the long time scale models: pulsatile blood flow and compliance of the vessel wall. In contrast to the inflammatory and immunological processes, models of the macroscopic cardiovascular mechanics are well quantifiable [52, 62, 76, 197], but also often come along with high computational costs.

It is frequently stated that pulsatile blood flow should not be neglected [152, 178, 255]. Still, many models – especially porous media models – commonly assume stationary blood *and* transmural flows [29, 76, 82, 142, 177, 178, 267, 276]. Besides the (instantaneous) WSS, a pulsatile model allows to estimate other hemodynamical factors, such as *time-averaged WSS*, *oscillatory shear index* (OSI) or *relative residence time* [118, 245]. Such hemodynamical factors indicate recirculating or oscillatory blood flows which disturb the endothelium and are frequently employed to alter the endothelial permeability in mathematical and computational models. The definition of the "correct" hemodynamical factor in the context of the endothelial permeability is addressed by many computational studies. Still, the findings are ambiguous. For example, low time-averaged WSS are frequently found to correlate with atherosclerotic plaque locations [154, 216], even though the contrary is reported too [121]. This ambivalence holds also for OSI, relative residence time and other hemodynamical factors which suggests that important biomechanical functions of the endothelium are still unknown.

The influence of the compliance of the artery is usually investigated using fluid-structure interaction (FSI) models allowing for a physiologically realistic deformation of the artery wall [52, 81, 152, 197, 295]. However, the influence of the artery compliance on the atherosclerotic process has not been considered much [59]. For a model of the short time scale of atherosclerosis, one can highlight the work by *Koshiba et al.* [152], where a non-stationary FSI simulation, a model of the species transport and penetration as well as a linked model of the transmural flow is considered. The back coupling from the long time scale, i.e., the plaque formation and induced narrowing of the lumen, crucial to atherogenesis are not included therein.

1.2.5 Multiscale and multiphysics

A suitable multiscale in time strategy is necessary to bring together the aforementioned small and long time scale phenomena. General multiscale frameworks exist [81], but an all-embracing framework for atherosclerosis is not yet established. As a first step *Koshiba et al.* [152] and *Sun et al.* [255] investigated the influence of pulsatile flow patterns to the LDL penetration, but not *vice versa*. In contrast, *Tomaso et al.* [267] and *Calvez et al.* [29] modeled the long time scale growth process and studied the induced changes to the hemodynamics. However, both assumed stationary flows and phenomenological growth laws. Still, [267] shows that the back-coupling from the long time scale due to growth is of major importance: *Tomaso et al.* explained that fatty streak formation observable in early stages of the disease might in fact be a result of the adjusted LDL penetration due to the thickened artery wall altering blood flow.

The chosen time scale separation into short and long time scale is accompanied by a separation of two other important aspects – the space scale and the describing physics. The short time scale of atherosclerosis is driven by the cardiac cycle. Thus, the flow of blood and its solutes and the deformation of the artery wall are of particular interest. To capture those processes properly, it is required to take into account a considerable part of the lumen and its adjacent entire artery wall. Accordingly, immanent with the short time scale is a space scale corresponding to the "organ level" being – depending on the species – in the order of magnitude of dozens of micrometers to millimeters. The driving physics of the short time and large space scale are the *Navier-Stokes* equations (blood), the balance of linear momentum (artery wall) and the advection-diffusion equation (blood solutes) which will be derived and described in detail in the following Section 2. In contrast, the long time scale is driven by the penetration of lipids, inflammatory and immunological processes, growth, remodeling and the transmural flow which mainly take place in the intima and media. Thus, immanent with the long time scale is a space corresponding to the intima-media thickness being approximately half of the entire artery wall thickness, cf. Figure 1.1. To accurately capture the processes within the intima, an even smaller space scale of around $2\,\%$ of the artery wall must be resolved. The driving physics of the long time and small space scale are the advection-diffusion-reaction equation (inflammation and immunology), *Darcy*'s law (transmural flow), and the specific growth and remodeling formulation (foam cell accumulation).

1.3 Objectives

The great need for a deeper understanding of inflammatory, immunological and biomechanical processes and their interplay in atherosclerosis are the motivation of this work. The objective is to develop predictive mathematical and computational approaches that resolve urgent issues described in the previous sections. In particular, the focus of this thesis lies on the following challenges:

- **Development of a mathematical and computational multiphysics approach for atherosclerosis**

  Atherosclerosis is a multiscale disease which can be characterized as the interplay between (the short time and large space scale) cardiovascular mechanics and (the long time and small space scale) inflammatory and immunological processes. The computational treatment of the disease is a great challenge and currently a model of the short time scale, which is capable to dynamically adjust to changes in the long time scale and *vice versa*, is not established. To computationally resolve the problem of the different time and space scales, a multiphysics approach can be utilized which follows the separation of the different scales.

  A main contribution of this thesis is to develop a novel mathematical and computational multiphysics approach for atherosclerosis which incorporates inflammatory, immunological and biomechanical processes of all time scales of the disease. Here, the interlacement of the different time scales and the influence of patient-specific anatomies and pathophysiologies is of particular interest.

- **Quantification of early atherosclerotic plaque formation**

  Many studies exist that quantify the cardiovascular mechanics and allow a predictive computation of cardiovascular quantities of interest in atherosclerosis, such as WSS. In contrast, the field of modeling atherosclerosis is dominated by qualitative models which are usually not validated against experimental results. Even though a growing number of studies model inflammatory and immunological processes of atherosclerosis, one of the major problems remains that the models' parameters are commonly unknown and can often only be estimated vaguely. Yet, there has been scarce work done resolving this issue by quantifying crucial processes that cause the onset and progression of atherosclerotic plaques.

  A major goal of this thesis is to establish predictive data-driven mathematical models of crucial processes of the formation of atherosclerotic plaques that improve this issue by experiment-based derivations and parameterizations. Here, focus lies on key and measurable processes of early atherosclerosis, such as endothelial permeability with respect to lipoproteins, oxidative modification and ingestion of lipoproteins, intracellular cholesterol cycle, reverse cholesterol transport and macrophage recruitment, apoptosis and clearance.

- **Assessment of stability of early plaques**

  A decisive step for the prevention and medical treatment of atherosclerosis is to understand under which conditions plaques continue to grow, stagnate or become regressive. Still, the driving biological and mechanobiological mechanisms that determine the stability of plaques are yet rather unknown. A key to assess the long-term outcome of plaques lies in their early stages where it is decided if a plaque is progression-prone or progression-resistant, i.e., of type IIa or IIb in the classification by the *American Heart Association*, cf. Table 1.1.

  A main objective of this thesis is to develop a spatially resolved model of key species in order to assess the local stability of early atherosclerotic plaques. Here, focus lies on the identification and classification of progression-prone and progression-resistant atherosclerotic regions based on measurable or computable inputs, such as blood cholesterol concentrations and wall shear stresses a plaque is exposed to *in vivo*.

1.4 Outline

The remainder of this work is structured as follows: In the following Chapter 2, basic continuum mechanical principles are used to derive mathematical formulations of several abstract single-field and multiphysics problems. The relevant single-field problems such as fluid, solid, scalar transport and porous media flow problems are derived in Section 2.1. Subsequently, single-field problems are merged to multiphysics problems by appropriate coupling conditions in Section 2.2. The

abstract multiphysics *problems* serve as a basis to develop mathematical *models*[1] of different aspects of atherosclerosis in this thesis.

Chapter 3 gives details on the numerical treatment of the mathematical single-field and multiphysics problems that are required to computationally solve them efficiently under complex premises, such as patient-specific geometries and setups. After the weak formulations of the single-field problems are presented and discretized in time and space in Section 3.1, the treatment of the multiphysics problems is detailed in Section 3.2.

In Chapter 4, a multiphysics model of the cardiovascular mechanics and transport of species is developed which incorporates major biomechanical processes of all time scales of atherosclerosis and their interactions. After the multiphysics model is established in Section 4.1, details on the numerical procedure are given in Section 4.2. A computational case study of the multiphysics model on a murine-specific geometry is performed and the interlacement of the different time scales is investigated in Section 4.3. The computational results of the multiphysics model are discussed, critically reflected and summarized in Sections 4.4, 4.5 and 4.6, respectively.

Chapter 5 focuses on the modeling and quantification of the formation of early atherosclerotic plaques. Therefore, several ODE submodels that describe key inflammatory and immunological processes in early atherosclerosis are developed, parameterized by least-square fitting to existing *in vitro* experimental results and subsequently merged into a combined ODE model in Section 5.1. Details on the analysis of the combined model are given in Section 5.2. The computational results of the ODE models are presented, discussed and summarized in Sections 5.3, 5.4 and 5.5, respectively.

In Chapter 6, a spatially resolved model of key species of early atherosclerosis is developed and the local stability of early plaques is assessed. To this end, further ODE submodels of the recruitment of species are developed, parameterized and embedded into a spatially resolved generalization of the combined model in Section 6.1. Section 6.2 gives details on the parameterization of the models and the methods to classify the stability of model plaques. The computational results of the model of key species are presented, discussed and summarized in Sections 6.3, 6.4 and 6.5, respectively.

Finally, an overall summary of this thesis and an outlook on possible future work is given in Chapter 7.

[1] Throughout this thesis, a mathematical *problem* is understood as a set of equations that describe an "abstract" system, whereas a mathematical *model* describes a "concrete" system, cf. page xv.

2 Mathematical formulations

This chapter gives a brief introduction to the mathematical formulations that are necessary to develop a mathematical and computational multiphysics model of atherosclerosis. First, the governing equations of all relevant single-field problems required in this thesis are derived from basic continuum mechanical principles in Section 2.1. In the subsequent Section 2.2, the single-field problems are merged by appropriate coupling conditions which leads to several multiphysics problems. The numerical treatment of the single-field and multiphysics problems is described in the subsequent Chapter 3.

More extensive reviews on the presented aspects can be found in the literature and will be referenced at the beginning of the individual sections. However, for a broad overview of many fundamental aspects that are essential in this thesis the exhaustive textbooks by *Donea* and *Huerta* [67] and *Formaggia et al.* [85] are recommended.

2.1 Single-field problems

This section first introduces different observers and their relations (Sections 2.1.1 and 2.1.2). Subsequently, brief derivations of the mathematical single-field formulations of fluid mechanics (Section 2.1.3), solid mechanics (Section 2.1.4), scalar transport (Section 2.1.5) and porous medium transport (Section 2.1.6) problems are given.

2.1.1 *Lagrange*an, *Euler*ian and ALE observer

To derive the governing equations of the single-field problems, a basic understanding of observers and their relation is required. In this section, a short introduction on different observers and the fundamental ALE equation is given. A more detailed review can be found in the textbooks by *Donea* and *Huerta* [67] or *Formaggia et al.* [85] or the theses by *Vuong* [275] or *Wall* [278].

It is common practice to describe the deformation of solids by a *Lagrangean* observer, where the motion of a set of specific *material points* $\boldsymbol{X}$ is followed. The position of a material point at initial time $t = 0$ is its *material coordinate*, denoted also by $\boldsymbol{X} \in \mathbb{R}^3$ (as there is a unique one-to-one relation by the initial time). The set of all material coordinates, i.e., the initial position of all considered material points, is the *material domain* $\Omega_0 \subset \mathbb{R}^3$. The *spatial coordinate* $\boldsymbol{x} \in \mathbb{R}^3$

is the position of a material point $\boldsymbol{X} \in \Omega_0$ at time $t \geq 0$ and let be described by the unique *deformation map* (diffeomorphism)

$$\varphi : \begin{cases} \mathbb{R}_{\geq 0} \times \Omega_0 & \to \mathbb{R}_{\geq 0} \times \Omega_t(t), \\ (t, \boldsymbol{X}) & \mapsto \varphi(t, \boldsymbol{X}) = (t, \boldsymbol{x}(t, \boldsymbol{X})). \end{cases} \tag{2.1}$$

Hence, the *spatial domain* $\Omega_t(t) := \{\boldsymbol{x}(t, \boldsymbol{X}) \in \mathbb{R}^3 | \boldsymbol{X} \in \Omega_0\}$ contains the spatial coordinates of all material points in the material domain Ω_0 that are transported by φ. The *displacement* $\boldsymbol{d}(t, \boldsymbol{X})$ of a material point $\boldsymbol{X}$ is given by $\boldsymbol{d}(t, \boldsymbol{X}) = \boldsymbol{x}(t, \boldsymbol{X}) - \boldsymbol{X}$ and its *material velocity* by $\boldsymbol{u}(t, \boldsymbol{X}) = \frac{\mathrm{d}}{\mathrm{d}t}\boldsymbol{x}(t, \boldsymbol{X}) = \frac{\mathrm{d}}{\mathrm{d}t}\boldsymbol{d}(t, \boldsymbol{X})$. Here, $\frac{\mathrm{d}}{\mathrm{d}t}$ denotes the *material time derivative*, i.e., the partial time derivative $\frac{\partial}{\partial t}$ where material coordinates $\boldsymbol{X}$ are fixed coordinates.

In contrast to solids, fluids are usually described by an *Eulerian* observer, where the state of material points $\boldsymbol{X}$ is investigated that happen to be at the position of a *spatial point* $\boldsymbol{x}$ in the fixed spatial domain $\Omega_t \subset \mathbb{R}^3$. The respective material point $\boldsymbol{X}$ to a given fixed spatial coordinate $\boldsymbol{x} \in \Omega_t$ at time $t \geq 0$ is uniquely defined by the inverse of the mapping given by (2.1), i.e., $(t, \boldsymbol{x}) \mapsto \varphi^{-1}(t, \boldsymbol{x}) = (t, \boldsymbol{X}(t, \boldsymbol{x}))$.

However, in some applications, such as fluid-structure interaction problems, spatial domains $\Omega_t(t)$ deform over time t. In these cases, an *Arbitrary-Lagrangean-Eulerian* (ALE) observer can be employed which can be conveniently thought of as the deforming underlying grid of the spatial fluid domain. An ALE observer allows to handle the deformation of the spatial domain $\Omega_t(t)$ like a *Lagrange*an observer, but at the same time still decouples the spatial domain from the material points which happen to be within it like an *Euler*ian observer. For this purpose, a third domain is needed, denoted as the *reference domain* or *ALE domain* $\Omega^{\mathcal{G}}(t)$. The reference domain contains the corresponding *reference coordinates* $\boldsymbol{\chi} \in \Omega^{\mathcal{G}}(t)$ which identify the position of the grid of the spatial domain at time t. The deformation maps (diffeomorphisms) from and to the reference domain are given by

$$\Phi : \begin{cases} \mathbb{R}_{\geq 0} \times \Omega^{\mathcal{G}}(t) & \to \mathbb{R}_{\geq 0} \times \Omega_t(t) \\ (t, \boldsymbol{\chi}) & \mapsto \Phi(t, \boldsymbol{\chi}) = (t, \boldsymbol{x}(t, \boldsymbol{\chi})) \end{cases} \tag{2.2}$$

and

$$\Theta : \begin{cases} \mathbb{R}_{\geq 0} \times \Omega_0 & \to \mathbb{R}_{\geq 0} \times \Omega^{\mathcal{G}}(t), \\ (t, \boldsymbol{X}) & \mapsto \Theta(t, \boldsymbol{X}) = (t, \boldsymbol{\chi}(t, \boldsymbol{X})), \end{cases} \tag{2.3}$$

such that

$$\boldsymbol{x}(t, \boldsymbol{X}) = \boldsymbol{x}(t, \boldsymbol{\chi}(t, \boldsymbol{X})), \text{ i.e., } \varphi = \Phi \circ \Theta. \tag{2.4}$$

For a schematic overview of the different domains and mappings, see Figure 2.1. Defining the *ALE velocity* by $\boldsymbol{u}^{\mathcal{G}}(t, \boldsymbol{\chi}) = \frac{\partial}{\partial t}\boldsymbol{x}(t, \boldsymbol{\chi})\big|_{\boldsymbol{\chi}}$, where $\big|_{\boldsymbol{\chi}}$ means "with holding $\boldsymbol{\chi}$ fixed", it follows:

$$\begin{aligned} \boldsymbol{u}(t, \boldsymbol{X}) &= \frac{\mathrm{d}}{\mathrm{d}t}\boldsymbol{x}(t, \boldsymbol{X}) \overset{(2.4)}{=} \frac{\partial}{\partial t}\boldsymbol{x}(t, \boldsymbol{\chi}(t, \boldsymbol{X})) \\ &= \frac{\partial}{\partial t}\boldsymbol{x}(t, \boldsymbol{\chi})\big|_{\boldsymbol{\chi}=\boldsymbol{\chi}(t,\boldsymbol{X})} + \frac{\partial}{\partial \boldsymbol{\chi}}\boldsymbol{x}(t, \boldsymbol{\chi})\big|_{\boldsymbol{\chi}=\boldsymbol{\chi}(t,\boldsymbol{X})} \frac{\partial}{\partial t}\boldsymbol{\chi}(t, \boldsymbol{X}) \\ &= \boldsymbol{u}^{\mathcal{G}}(t, \boldsymbol{X}) + \frac{\partial}{\partial \boldsymbol{\chi}}\boldsymbol{x}(t, \boldsymbol{\chi})\big|_{\boldsymbol{\chi}=\boldsymbol{\chi}(t,\boldsymbol{X})} \frac{\partial}{\partial t}\boldsymbol{\chi}(t, \boldsymbol{X}). \end{aligned} \tag{2.5}$$

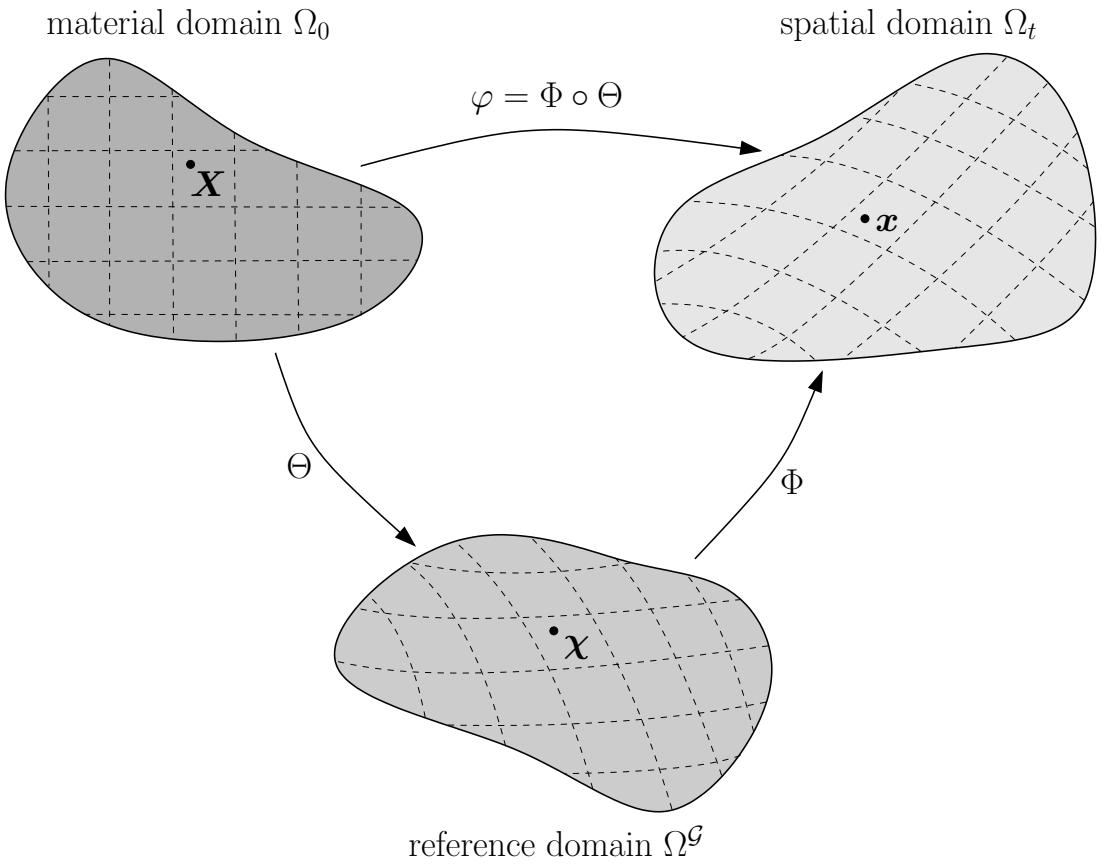

Figure 2.1 Schematic overview of material, reference and spatial domains ($\Omega_0, \Omega^{\mathcal{G}}$ and Ω_t) and coordinates ($\boldsymbol{X}, \boldsymbol{\chi}$ and $\boldsymbol{x}$) and their mappings (φ, Θ and Φ).

Let $q(t, \boldsymbol{x})$ be an arbitrary scalar-valued spatial quantity. By the mappings φ, Θ and Φ and their inverses, q can be expressed in terms of any of the three coordinates:

$$\begin{aligned} q^*(t, \boldsymbol{\chi}) &:= q \circ \Phi(t, \boldsymbol{\chi}) = q(t, \boldsymbol{x}(t, \boldsymbol{\chi})) \\ q^{**}(t, \boldsymbol{X}) &:= q \circ \varphi(t, \boldsymbol{X}) = q(t, \boldsymbol{x}(t, \boldsymbol{X})). \end{aligned} \tag{2.6}$$

It follows that the material time derivative of the spatial quantity $q(t, \boldsymbol{x})$ can be expressed as

$$\begin{aligned} \frac{\mathrm{d}}{\mathrm{d}t} q(t, \boldsymbol{x}) &\overset{(2.6)}{=} \frac{\partial}{\partial t} q^*(t, \boldsymbol{\chi}(t, \boldsymbol{x})) = \frac{\partial}{\partial t} q^*(t, \boldsymbol{\chi})\big|_{\boldsymbol{\chi}=\boldsymbol{\chi}(t,\boldsymbol{x})} + \frac{\partial}{\partial \boldsymbol{\chi}} q^*(t, \boldsymbol{\chi}(t, \boldsymbol{x})) \frac{\partial}{\partial t} \boldsymbol{\chi}(t, \boldsymbol{x}) \\ &= \frac{\partial}{\partial t} q^*(t, \boldsymbol{\chi})\big|_{\boldsymbol{\chi}=\boldsymbol{\chi}(t,\boldsymbol{x})} + \frac{\partial}{\partial \boldsymbol{x}} q(t, \boldsymbol{x}) \cdot \frac{\partial}{\partial \boldsymbol{\chi}} \boldsymbol{x}(t, \boldsymbol{\chi})\big|_{\boldsymbol{\chi}=\boldsymbol{\chi}(t,\boldsymbol{x})} \frac{\partial}{\partial t} \boldsymbol{\chi}(t, \boldsymbol{x}) \\ &\overset{(2.5)}{=} \frac{\partial}{\partial t} q^*(t, \boldsymbol{\chi})\big|_{\boldsymbol{\chi}=\boldsymbol{\chi}(t,\boldsymbol{x})} + \underbrace{\frac{\partial}{\partial \boldsymbol{x}} q(t, \boldsymbol{x})}_{=:\nabla q(t,\boldsymbol{x})} \cdot \left(\boldsymbol{u}(t, \boldsymbol{x}) - \boldsymbol{u}^{\mathcal{G}}(t, \boldsymbol{x})\right), \end{aligned} \tag{2.7}$$

which is called the *fundamental ALE equation*. The derivative $\frac{\partial}{\partial t} q^*(t, \boldsymbol{\chi})\big|_{\boldsymbol{\chi}}$ is called the *ALE time derivative* of q. The term $\left(\boldsymbol{u} - \boldsymbol{u}^{\mathcal{G}}\right)$ is named *convective velocity*.

Remark. *With the choice $\Theta(t, \boldsymbol{X}) = (t, \boldsymbol{X})$, i.e., $\boldsymbol{X} = \boldsymbol{\chi}(t, \boldsymbol{X})$, the* Lagrange*an description is obtained from the ALE description. In this case, the ALE time derivative $\frac{\partial}{\partial t}(\bullet)\big|_{\boldsymbol{\chi}}$ is equivalent to the material time derivative $\frac{\mathrm{d}}{\mathrm{d}t}(\bullet)$ and it yields $\boldsymbol{u}^{\mathcal{G}} = \boldsymbol{u}$. In contrast, by choosing $\Phi(t, \boldsymbol{x}) = (t, \boldsymbol{x})$, i.e., $\boldsymbol{\chi} = \boldsymbol{x}(t, \boldsymbol{\chi})$, the* Euler*ian description is obtained from the ALE description. Here, the ALE time derivative $\frac{\partial}{\partial t}(\bullet)\big|_{\boldsymbol{\chi}}$ is equivalent to the partial time derivative $\frac{\partial}{\partial t}(\bullet)$ (with fixed x) and it follows $\boldsymbol{u}^{\mathcal{G}} = \boldsymbol{0}$.*

2.1.2 ALE transport equation

In this section, the fundamental ALE equation is used to derive the continuum mechanical equivalent for an arbitrary spatial conserved quantity with an arbitrary observer. It is an abstraction of content presented in *Donea* and *Huerta* [67]. For more details the reader is referred to the textbooks by *Donea* and *Huerta* [67], *Eck et al.* [69] or *Formaggia et al.* [85].

Let $q(t, \boldsymbol{x})$ now be the scalar-valued spatial density of an arbitrary physical *conserved* quantity on an arbitrary spatial domain $\Omega(t)$ with boundary $\Gamma(t) = \partial\Omega(t)$. If $q_\Omega(t, \boldsymbol{x})$ and $\boldsymbol{q}_\Gamma(t, \boldsymbol{x})$ denote the quantity's volume sources and boundary influxes, respectively, then its balance equation in the domain $\Omega(t)$ at time $t \geq 0$ is

$$\frac{\mathrm{d}}{\mathrm{d}t} \int\limits_{\Omega(t)} q(t, \boldsymbol{x}) \, \mathrm{d}v = \int\limits_{\Omega(t)} q_\Omega(t, \boldsymbol{x}) \, \mathrm{d}v - \int\limits_{\Gamma(t)} \boldsymbol{q}_\Gamma(t, \boldsymbol{x}) \cdot \boldsymbol{n}(t, \boldsymbol{x}) \, \mathrm{d}s, \tag{2.8}$$

where $\boldsymbol{n}$ denotes the *outward pointing unit surface normal* on the spatial boundary $\Gamma(t)$. Applying the Reynold*'s transport theorem* and *Gauß's theorem* to the left- and right-hand side of Equation (2.8), respectively, yields

$$\int\limits_{\Omega(t)} \left(\frac{\mathrm{d}}{\mathrm{d}t} q(t, \boldsymbol{x}) + q(t, \boldsymbol{x}) \, \nabla \cdot \boldsymbol{u}(t, \boldsymbol{x}) + q_\Omega(t, \boldsymbol{x}) - \boldsymbol{\nabla} \cdot \boldsymbol{q}_\Gamma(t, \boldsymbol{x}) \right) \mathrm{d}v = 0, \tag{2.9}$$

where $\boldsymbol{u}$ is again the material velocity with which material points are transported. Equation (2.9) holds also for any subset of $\Omega(t)$ and hence its integrand vanishes locally such that

$$\frac{\mathrm{d}}{\mathrm{d}t} q(t, \boldsymbol{x}) + q(t, \boldsymbol{x}) \, \nabla \cdot \boldsymbol{u}(t, \boldsymbol{x}) - q_\Omega(t, \boldsymbol{x}) + \boldsymbol{\nabla} \cdot \boldsymbol{q}_\Gamma(t, \boldsymbol{x}) = 0, \ \forall t \geq 0, \ \forall \boldsymbol{x} \in \Omega(t). \tag{2.10}$$

Using the fundamental ALE Equation (2.7) leads to

$$\begin{aligned} \frac{\partial}{\partial t} q^*(t, \boldsymbol{\chi})\big|_{\boldsymbol{\chi}=\boldsymbol{\chi}(t,\boldsymbol{x})} + \big(\boldsymbol{u}(t, \boldsymbol{x}) - \boldsymbol{u}^{\mathcal{G}}(t, \boldsymbol{x})\big) \cdot \nabla q(t, \boldsymbol{x}) + q(t, \boldsymbol{x}) \, \nabla \cdot \boldsymbol{u}(t, \boldsymbol{x}) \\ + \boldsymbol{\nabla} \cdot \boldsymbol{q}_\Gamma(t, \boldsymbol{x}) = q_\Omega(t, \boldsymbol{x}), \quad \forall t \geq 0, \ \forall \boldsymbol{x} \in \Omega(t), \end{aligned} \tag{2.11}$$

which is called the *ALE transport equation*.

Throughout the remainder of this thesis the asterisks as well as the time and space dependencies are omitted to ease notation, except in cases where it is crucial. Further, one global common *Cartesian coordinate system* is assumed for all coordinates and domains.

Remark. *Besides a sufficient smoothness and the particular description by Equation* (2.8)*, no further assumptions on the spatial density* q *and the ALE observer were made in order to derive the ALE transport equation. Hence, the ALE transport equation can be seen as the fundamental conservation law from which all spatial conservation laws required in this thesis can be derived.*

2.1.3 Fluid mechanics

The derivation of the governing equations that are required to describe viscous incompressible fluids is briefly presented in this section. A more detailed review on conservation laws and the derivation of the *Navier-Stokes* equations can be found in the textbooks by *Donea* and *Huerta* [67], *Eck et al.* [69] or *Formaggia et al.* [85]. Extensive reviews on non-*Newton*ian fluids are the textbooks by *Astarita* and *Marrucci* [8] or *Chhabra* and *Richardson* [41], whereas an overview of rheological models for blood is given in the textbook by *Formaggia et al.* [85].

Material points that make up a fluid can undergo large deformations like vortices, which could lead to infeasible mesh distortions when describing the fluid in terms of a *Lagrange*an observer. In contrast, fluids described by an *Euler*ian observer can only have fixed spatial domains. However, this restriction is infeasible in the context of multiphysics problems where the spatial domain of the fluid $\Omega^{\mathcal{F}}(t)$ is deformed over time t. Hence, an ALE observer is exploited where the ALE observer is chosen such that it captures the full deformation of the spatial fluid domain, i.e., $\Omega^{\mathcal{G}}(t) = \Omega^{\mathcal{F}}(t)$.

The physical principles that drive the mechanics of fluids are the conservation of mass and the balance of linear momentum which can both be derived from the ALE transport Equation (2.11) as follows. All quantities and parameters that are related to the fluid problem are indicated by the superscript $\mathcal{F}$.

2.1.3.1 Conservation of mass

The assumption that the global mass of the fluid in the spatial domain $\Omega^{\mathcal{F}}(t)$ is conserved over time t, i.e., no mass is generated or lost, reads

$$\frac{\mathrm{d}}{\mathrm{d}t} \int\limits_{\Omega^{\mathcal{F}}(t)} \varrho^{\mathcal{F}}(t, \boldsymbol{x}) \, \mathrm{d}v = 0, \tag{2.12}$$

where $\varrho^{\mathcal{F}}(t, \boldsymbol{x})$ is the *spatial mass density* of the fluid. Hence, by setting $q(t, \boldsymbol{x}) = \varrho^{\mathcal{F}}(t, \boldsymbol{x})$, $q_\Omega(t, \boldsymbol{x}) = 0$ and $\boldsymbol{q}_\Gamma(t, \boldsymbol{x}) = \boldsymbol{0}$ in Equation (2.11), it follows the continuum mechanical equivalent for the conservation of mass in an ALE frame

$$\frac{\partial}{\partial t} \varrho^{\mathcal{F}} \big|_{\boldsymbol{\chi}} + \left(\boldsymbol{u}^{\mathcal{F}} - \boldsymbol{u}^{\mathcal{G}} \right) \cdot \nabla \varrho^{\mathcal{F}} + \varrho^{\mathcal{F}} \, \nabla \cdot \boldsymbol{u}^{\mathcal{F}} = 0, \tag{2.13}$$

which is called the *continuity equation* (in an ALE frame). Here, $\boldsymbol{u}^{\mathcal{F}}$ is the material velocity of the fluid. If the fluid is incompressible, i.e., has a constant material mass density $\varrho^{\mathcal{F}}(t, \boldsymbol{X}) = const$, it follows

$$\nabla \cdot \boldsymbol{u}^{\mathcal{F}} = 0 \quad \forall t \geq 0,\ \forall \boldsymbol{x} \in \Omega^{\mathcal{F}}(t), \tag{2.14}$$

which is known as the *incompressibility equation*.

2.1.3.2 Balance of linear momentum

The balance of linear momentum is in fact well-known as *Newton*'s second law. It states that the change of the global balance of linear momentum in the domain $\Omega^{\mathcal{F}}(t)$ is equal to the *volume forces* $\boldsymbol{b}^{\mathcal{F}}$ and *surface forces* $\boldsymbol{t}^{\mathcal{F}}$ acting on it:

$$\frac{\mathrm{d}}{\mathrm{d}t} \int\limits_{\Omega^{\mathcal{F}}(t)} \varrho^{\mathcal{F}}(t, \boldsymbol{x}) \boldsymbol{u}^{\mathcal{F}}(t, \boldsymbol{x}) \, \mathrm{d}v = \int\limits_{\Omega^{\mathcal{F}}(t)} \boldsymbol{b}^{\mathcal{F}}(t, \boldsymbol{x}) \, \mathrm{d}v + \int\limits_{\Gamma^{\mathcal{F}}(t)} \boldsymbol{t}^{\mathcal{F}}(t, \boldsymbol{x}) \, \mathrm{d}s. \tag{2.15}$$

Expressing the surface forces $\boldsymbol{t}^{\mathcal{F}}$ by the *Cauchy stress tensor* $\boldsymbol{\sigma}^{\mathcal{F}}$ yields

$$\boldsymbol{t}^{\mathcal{F}}(t, \boldsymbol{x}) = \boldsymbol{\sigma}^{\mathcal{F}}(t, \boldsymbol{x}) \boldsymbol{n}^{\mathcal{F}}(t, \boldsymbol{x}). \tag{2.16}$$

where $\boldsymbol{n}^{\mathcal{F}}$ denotes again the outward pointing unit surface normal on the spatial boundary $\Gamma^{\mathcal{F}}(t)$. Hence, by setting $\boldsymbol{q}(t, \boldsymbol{x}) = \varrho^{\mathcal{F}}(t, \boldsymbol{x}) \boldsymbol{u}^{\mathcal{F}}(t, \boldsymbol{x})$, $\boldsymbol{q}_{\Omega}(t, \boldsymbol{x}) = \boldsymbol{b}^{\mathcal{F}}(t, \boldsymbol{x})$ and $\boldsymbol{q}_{\Gamma}(t, \boldsymbol{x}) = -\boldsymbol{\sigma}^{\mathcal{F}}(t, \boldsymbol{x})$ and componentwise use of Equation (2.11) it follows

$$\frac{\partial}{\partial t}(\varrho^{\mathcal{F}} \boldsymbol{u}^{\mathcal{F}})\big|_{\boldsymbol{\chi}} + \left(\left(\boldsymbol{u}^{\mathcal{F}} - \boldsymbol{u}^{\mathcal{G}}\right) \cdot \boldsymbol{\nabla}\right)(\varrho^{\mathcal{F}} \boldsymbol{u}^{\mathcal{F}}) + (\varrho^{\mathcal{F}} \boldsymbol{u}^{\mathcal{F}}) \nabla \cdot \boldsymbol{u}^{\mathcal{F}} - \boldsymbol{\nabla} \cdot \boldsymbol{\sigma}^{\mathcal{F}} = \boldsymbol{b}^{\mathcal{F}}. \tag{2.17}$$

By using Equation (2.13), the common continuum mechanical equivalent for the conservation of linear momentum in an ALE frame is achieved:

$$\varrho^{\mathcal{F}} \frac{\partial}{\partial t} \boldsymbol{u}^{\mathcal{F}}\big|_{\boldsymbol{\chi}} + \varrho^{\mathcal{F}} \left(\left(\boldsymbol{u}^{\mathcal{F}} - \boldsymbol{u}^{\mathcal{G}}\right) \cdot \boldsymbol{\nabla}\right) \boldsymbol{u}^{\mathcal{F}} - \boldsymbol{\nabla} \cdot \boldsymbol{\sigma}^{\mathcal{F}} = \boldsymbol{b}^{\mathcal{F}} \quad \forall t \geq 0,\ \forall \boldsymbol{x} \in \Omega^{\mathcal{F}}(t). \tag{2.18}$$

Remark. *Equation* (2.18) *is valid also for fluids with a non-constant density.*

Remark. *Using Equation* (2.18) *one can show that the conservation of angular momentum is equivalent to the symmetry of the* Cauchy *stress tensor, i.e.,* $\boldsymbol{\sigma}^{\mathcal{F}} = \left(\boldsymbol{\sigma}^{\mathcal{F}}\right)^T$ *[69].*

Remark. *The continuum mechanical equivalents for the conservation of internal and total energy in ALE frames are also a consequence of the ALE transport Equation* (2.11)*. However, the conservation of energy is not of particular interest in this thesis and the reader is referred to the textbook by* Donea *and* Huerta *[67].*

2.1.3.3 Governing equations

The governing equations for *viscous incompressible* fluids are derived from the continuum mechanical equivalents for the conservation of mass and the balance of linear momentum with an appropriate *Cauchy* stress tensor $\boldsymbol{\sigma}^{\mathcal{F}}$. The *Cauchy* stress tensor $\boldsymbol{\sigma}^{\mathcal{F}}$ for viscous incompressible *Newtonian* fluids reads

$$\boldsymbol{\sigma}^{\mathcal{F}}(p^{\mathcal{F}}, \boldsymbol{u}^{\mathcal{F}}) = -p^{\mathcal{F}}\mathbf{1} + 2\mu^{\mathcal{F}}\boldsymbol{\varepsilon}^{\mathcal{F}}\left(\boldsymbol{u}^{\mathcal{F}}\right), \tag{2.19}$$

where $p^{\mathcal{F}}$ is the *pressure* of the fluid and

$$\boldsymbol{\varepsilon}^{\mathcal{F}}\left(\boldsymbol{u}^{\mathcal{F}}\right) = \frac{1}{2}\left(\boldsymbol{\nabla}\boldsymbol{u}^{\mathcal{F}} + \left(\boldsymbol{\nabla}\boldsymbol{u}^{\mathcal{F}}\right)^{T}\right) \tag{2.20}$$

is the *strain rate tensor* of the fluid. For *Newton*ian fluids, the *dynamic viscosity* $\mu^{\mathcal{F}}$ is a constant. Together, equations (2.13), (2.18) and (2.19) yield the *incompressible Navier-Stokes equations* in an ALE frame on the spatial domain $\Omega^{\mathcal{F}}(t)$:

$$\varrho^{\mathcal{F}}\frac{\partial}{\partial t}\boldsymbol{u}^{\mathcal{F}}\big|_{\boldsymbol{\chi}} + \varrho^{\mathcal{F}}\left(\left(\boldsymbol{u}^{\mathcal{F}} - \boldsymbol{u}^{\mathcal{G}}\right)\cdot\boldsymbol{\nabla}\right)\boldsymbol{u}^{\mathcal{F}} + \nabla p^{\mathcal{F}} - 2\mu^{\mathcal{F}}\boldsymbol{\nabla}\cdot\boldsymbol{\varepsilon}^{\mathcal{F}}\left(\boldsymbol{u}^{\mathcal{F}}\right) = \boldsymbol{b}^{\mathcal{F}}, \tag{2.21}$$

$$\boldsymbol{\nabla}\cdot\boldsymbol{u}^{\mathcal{F}} = 0, \tag{2.22}$$

where the fluid velocity $\boldsymbol{u}^{\mathcal{F}}$ and the fluid pressure $p^{\mathcal{F}}$ are the primary unknowns.

Important classes of *non-Newtonian* fluids are *shear-thinning* and *shear-thickening* fluids which are described by rheological models with *non-constant* dynamic viscosities

$$\mu^{\mathcal{F}} = \mu^{\mathcal{F}}(\dot{\gamma}^{\mathcal{F}}(\boldsymbol{u}^{\mathcal{F}})) \tag{2.23}$$

depending on the *shear-rate* $\dot{\gamma}^{\mathcal{F}}$ of the fluid. The shear-rate $\dot{\gamma}^{\mathcal{F}}$ is given by:

$$\dot{\gamma}^{\mathcal{F}}(\boldsymbol{u}^{\mathcal{F}}) = \sqrt{2\ \mathrm{tr}\left(\boldsymbol{\varepsilon}^{\mathcal{F}}(\boldsymbol{u}^{\mathcal{F}})^2\right)}. \tag{2.24}$$

On the disjunct boundaries $\Gamma_{\mathrm{D}}^{\mathcal{F}}(t) \subset \Gamma^{\mathcal{F}}(t)$ and $\Gamma_{\mathrm{N}}^{\mathcal{F}}(t) \subset \Gamma^{\mathcal{F}}(t)$, *Dirichlet* and *Neumann boundary conditions* are applied, respectively. In the case of the *Navier-Stokes* equations, *Dirichlet* boundary conditions prescribe given velocities $\boldsymbol{u}_{\mathrm{D}}^{\mathcal{F}}(t, \boldsymbol{x})$ on the spatial boundary $\Gamma_{\mathrm{D}}^{\mathcal{F}}(t)$

$$\boldsymbol{u}^{\mathcal{F}}(t, \boldsymbol{x}) = \boldsymbol{u}_{\mathrm{D}}^{\mathcal{F}}(t, \boldsymbol{x}), \tag{2.25}$$

whereas *Neumann* boundary conditions load the fluid with *external spatial surface tractions* $\boldsymbol{t}_{\mathrm{N}}^{\mathcal{F}}(t, \boldsymbol{x})$ on the spatial boundary $\Gamma_{\mathrm{N}}^{\mathcal{F}}(t)$:

$$\boldsymbol{\sigma}^{\mathcal{F}}(t, \boldsymbol{x})\boldsymbol{n}_{\mathrm{N}}^{\mathcal{F}}(t, \boldsymbol{x}) = \boldsymbol{t}_{\mathrm{N}}^{\mathcal{F}}(t, \boldsymbol{x}). \tag{2.26}$$

2.1.4 Solid mechanics

In this section, the derivation of the governing equations that are required to describe growing hyperelastic solids is briefly presented. A more detailed review on solid mechanics can be found in the textbooks by *Holzapfel* [122], *Ragab* and *Bayoumi* [223] or *Wriggers* [291]. For more details on the theory of growth the reader is referred to the publications by *Himpel et al.* [119], *Klisch et al.* [149], *Rodriguez et al.* [231] or others [3, 73, 94, 104, 155, 242].

In contrast to fluids, solids are usually described by a *Lagrange*an observer as the position and state of particular material points (that define the solid) are of interest. The physical principles that drive the mechanics of solids are the conservation of mass and the balance of linear momentum. All quantities and parameters that are related to the structure problem are indicated by the superscript $\mathcal{S}$.

2.1.4.1 Conservation of mass

Analog to the conservation of mass of a fluid (Section 2.1.3.1), the global conservation of mass of a solid in the spatial domain $\Omega^{\mathcal{S}}(t)$ reads

$$0 = \frac{\mathrm{d}}{\mathrm{d}t} \int\limits_{\Omega^{\mathcal{S}}(t)} \varrho^{\mathcal{S}}(t, \boldsymbol{x}) \, \mathrm{d}v = \frac{\mathrm{d}}{\mathrm{d}t} \int\limits_{\Omega_0^{\mathcal{S}}} J^{\mathcal{S}}(t, \boldsymbol{X}) \varrho^{\mathcal{S}}(t, \boldsymbol{X}) \, \mathrm{d}V, \tag{2.27}$$

where $\varrho^{\mathcal{S}}$ is the spatial mass density of the structure. In the last step, the integral was *pulled-back* to the material domain $\Omega_0^{\mathcal{S}}$ which introduced the *Jacobian* $J^{\mathcal{S}} = \det(\boldsymbol{F}^{\mathcal{S}})$ of the structure, where

$$F^{\mathcal{S}}(t, \boldsymbol{X}) = \frac{\partial}{\partial \boldsymbol{X}} \boldsymbol{x}(t, \boldsymbol{X}) = \boldsymbol{1} + \underbrace{\frac{\partial}{\partial \boldsymbol{X}} \boldsymbol{d}^{\mathcal{S}}(t, \boldsymbol{X})}_{=: \boldsymbol{\nabla}_0 \, \boldsymbol{d}^{\mathcal{S}}(t, \boldsymbol{X})} \tag{2.28}$$

is the *deformation gradient* of the structure. Equation (2.27) directly yields the continuum mechanical equivalent for the conservation of mass on the material domain $\Omega_0^{\mathcal{S}}$

$$0 = \frac{\mathrm{d}}{\mathrm{d}t} (J^{\mathcal{S}} \varrho^{\mathcal{S}}) = \frac{\mathrm{d}}{\mathrm{d}t} \varrho_0^{\mathcal{S}}, \tag{2.29}$$

where $\varrho_0^{\mathcal{S}} = J^{\mathcal{S}} \varrho^{\mathcal{S}}$ is the *material mass density* of the structure. By integration over time it follows that the material mass density is constant over time:

$$\varrho_0^{\mathcal{S}}(t, \boldsymbol{X}) = \varrho_0^{\mathcal{S}}(0, \boldsymbol{X}) \quad \forall t \geq 0, \; \forall \boldsymbol{X} \in \Omega_0^{\mathcal{S}}. \tag{2.30}$$

2.1.4.2 Balance of linear momentum

The global balance of linear momentum of the structure on the spatial domain $\Omega^{\mathcal{S}}(t)$ reads analog to Equation (2.15). By pulling-back the integrals to the material domain $\Omega_0^{\mathcal{S}}$, the continuum mechanical equivalent for the balance of linear momentum on the material domain $\Omega_0^{\mathcal{S}}$ is achieved:

$$\varrho_0^{\mathcal{S}} \frac{\mathrm{d}^2}{\mathrm{d}t^2} \boldsymbol{d}^{\mathcal{S}} - \boldsymbol{\nabla}_0 \cdot \left(\boldsymbol{F}^{\mathcal{S}} \boldsymbol{S}^{\mathcal{S}} \right) = \boldsymbol{b}_0^{\mathcal{S}}, \tag{2.31}$$

where $\boldsymbol{S}^{\mathcal{S}}$ is the *second Piola-Kirchhoff stress tensor* of the structure. The second *Piola-Kirchhoff* stress tensor is given by the *Piola Transformation* of the *Cauchy* stress tensor $\boldsymbol{\sigma}^{\mathcal{S}}$ (cf. Equation (2.16)) which reads

$$\boldsymbol{S}^{\mathcal{S}} = J^{\mathcal{S}} (\boldsymbol{F}^{\mathcal{S}})^{-1} \boldsymbol{\sigma}^{\mathcal{S}} (\boldsymbol{F}^{\mathcal{S}})^{-T}. \tag{2.32}$$

In this thesis, *hyperelastic* solids with *strain-energy density function* $\Psi^{\mathcal{S}}$ are assumed such that the second *Piola-Kirchhoff* stress tensor is given as

$$\boldsymbol{S}^{\mathcal{S}} = 2 \frac{\partial}{\partial \boldsymbol{C}^{\mathcal{S}}} \Psi^{\mathcal{S}} \left(\boldsymbol{C}^{\mathcal{S}} \right), \tag{2.33}$$

where $\boldsymbol{C}^{\mathcal{S}} = \left(\boldsymbol{F}^{\mathcal{S}} \right)^T \boldsymbol{F}^{\mathcal{S}}$ is the *right Cauchy-Green deformation tensor* of the structure.

2.1.4.3 Growth

In this thesis, solids can grow due to an increase of their global mass. To incorporate growth, a common approach is to assume that the deformation gradient $\boldsymbol{F}^{\mathcal{S}}$ of the structure can be multiplicatively decomposed into

$$\boldsymbol{F}^{\mathcal{S}} = \boldsymbol{F}_{\mathrm{El}}^{\mathcal{S}} \, \boldsymbol{F}_{\mathrm{Gr}}^{\mathcal{S}}. \tag{2.34}$$

Here, $\boldsymbol{F}_{\mathrm{Gr}}^{\mathcal{S}}$ is the *growth deformation gradient* which describes the growth of the material domain $\Omega_0^{\mathcal{S}}$ to a discontinuous but stress-free *growth domain* denoted as $\Omega_{\mathrm{Gr}}^{\mathcal{S}}(t)$ [231, 242]. The respective coordinates are denoted by $\boldsymbol{\chi}_{\mathrm{Gr}}$. The second part $\boldsymbol{F}_{\mathrm{El}}^{\mathcal{S}}$ denotes the *elastic deformation gradient* which maps the growth domain $\Omega_{\mathrm{Gr}}^{\mathcal{S}}(t)$ to the spatial domain $\Omega_t^{\mathcal{S}}(t)$ where the domain is continuous again. An illustration of this assumption is given in Figure 2.2.

Further, it is common to assume that the growth is *density preserving* in the growth domain $\Omega_{\mathrm{Gr}}^{\mathcal{S}}(t)$ [119] reading analog to Equation (2.29):

$$\frac{\mathrm{d}}{\mathrm{d}t} \varrho_{\mathrm{Gr}}^{\mathcal{S}}(t, \boldsymbol{\chi}_{\mathrm{Gr}}) = 0, \quad \forall t \geq 0, \; \forall \boldsymbol{\chi}_{\mathrm{Gr}} \in \Omega_{\mathrm{Gr}}^{\mathcal{S}}(t), \tag{2.35}$$

where $\varrho_{\mathrm{Gr}}^{\mathcal{S}}$ is the mass density in the growth domain. The pull-back into the material domain $\Omega_0^{\mathcal{S}}$ yields a generalization of Equation (2.30) reading [94, 119, 231]

$$\varrho_0^{\mathcal{S}}(t, \boldsymbol{X}) = J_{\mathrm{Gr}}^{\mathcal{S}}(t, \boldsymbol{X}) \varrho_0^{\mathcal{S}}(0, \boldsymbol{X}), \quad \forall t \geq 0, \; \forall \boldsymbol{X} \in \Omega_0^{\mathcal{S}} \tag{2.36}$$

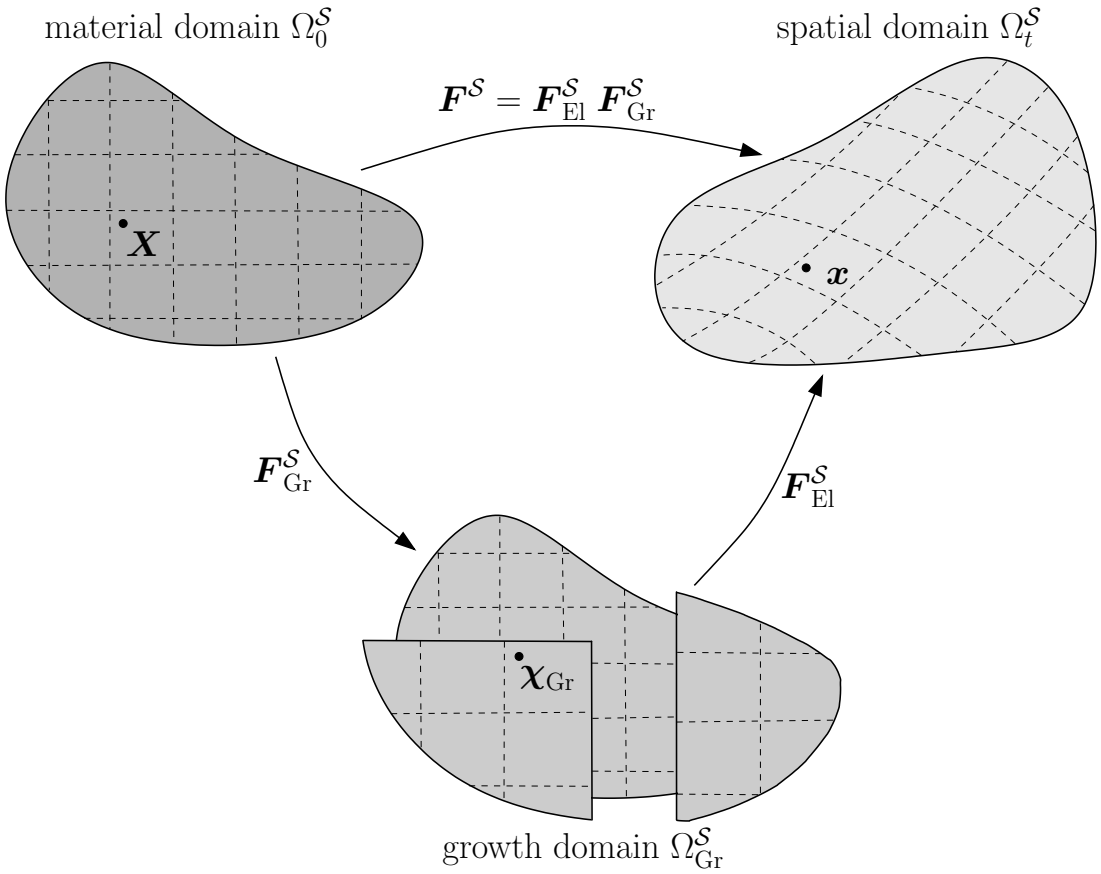

Figure 2.2 Schematic overview of material, growth and spatial domains ($\Omega_0^{\mathcal{S}}, \Omega_{\mathrm{Gr}}^{\mathcal{S}}$ and $\Omega_t^{\mathcal{S}}$), coordinates ($\boldsymbol{X}, \boldsymbol{\chi}_{\mathrm{Gr}}$ and $\boldsymbol{x}$) and their deformation gradients ($\boldsymbol{F}^{\mathcal{S}}, \boldsymbol{F}^{\mathcal{S}}_{\mathrm{Gr}}$ and $\boldsymbol{F}^{\mathcal{S}}_{\mathrm{El}}$).

where $J^{\mathcal{S}}_{\mathrm{Gr}} = \det\left(\boldsymbol{F}^{\mathcal{S}}_{\mathrm{Gr}}\right)$ is the Jacobian of the growth deformation gradient $\boldsymbol{F}^{\mathcal{S}}_{\mathrm{Gr}}$. To respect the stress-freeness of the growth configuration, the second *Piola-Kirchhoff* stress tensor $\boldsymbol{S}^{\mathcal{S}}$ is computed by a pull-back of the elastic stresses $\boldsymbol{S}^{\mathcal{S}}_{\mathrm{El}}$:

$$\boldsymbol{S}^{\mathcal{S}} = (\boldsymbol{F}^{\mathcal{S}}_{\mathrm{Gr}})^{-1}\boldsymbol{S}^{\mathcal{S}}_{\mathrm{El}}(\boldsymbol{F}^{\mathcal{S}}_{\mathrm{Gr}})^{-T}. \tag{2.37}$$

By again taking the assumption of a hyperelastic solid with strain-energy density function $\Psi^{\mathcal{S}}$ the elastic stresses are given by

$$\boldsymbol{S}^{\mathcal{S}}_{\mathrm{El}} = 2\frac{\partial}{\partial \boldsymbol{C}^{\mathcal{S}}_{\mathrm{El}}}\Psi^{\mathcal{S}}\left(\boldsymbol{C}^{\mathcal{S}}_{\mathrm{El}}\right), \tag{2.38}$$

where $\boldsymbol{C}^{\mathcal{S}}_{\mathrm{El}} = \left(\boldsymbol{F}^{\mathcal{S}}_{\mathrm{El}}\right)^{T}\boldsymbol{F}^{\mathcal{S}}_{\mathrm{El}} = (\boldsymbol{F}^{\mathcal{S}}_{\mathrm{Gr}})^{-T}\boldsymbol{C}^{\mathcal{S}}(\boldsymbol{F}^{\mathcal{S}}_{\mathrm{Gr}})^{-1}$ is the *elastic right Cauchy-Green deformation tensor*.

Remark. *So far, no assumptions on the specific form of the growth deformation gradient $\boldsymbol{F}^{\mathcal{S}}_{\mathrm{Gr}}$ were made and it remains to be modeled. By choosing $\boldsymbol{F}^{\mathcal{S}}_{\mathrm{Gr}} = \mathbf{1}$ the standard formulation for hyperelastic structures is recovered.*

2.1.4.4 Governing equations

The mathematical description of *hyperelastic solids undergoing growth* is derived from the continuum mechanical equivalents for the conservation of mass and the balance of linear momentum. Together, Equations (2.31), (2.36), (2.37) and (2.38) yield the governing equations of the structure problem on the material domain $\Omega_0^{\mathcal{S}}$:

$$\varrho_0^{\mathcal{S}} \frac{\mathrm{d}^2}{\mathrm{d}t^2} \boldsymbol{d}^{\mathcal{S}} - \boldsymbol{\nabla}_0 \cdot \left(\boldsymbol{F}^{\mathcal{S}} \boldsymbol{S}^{\mathcal{S}} \right) = \boldsymbol{b}_0^{\mathcal{S}} \tag{2.39}$$

with

$$\boldsymbol{S}^{\mathcal{S}} = \left(\boldsymbol{F}_{\mathrm{Gr}}^{\mathcal{S}}\right)^{-1} \left(2 \frac{\partial}{\partial \boldsymbol{C}_{\mathrm{El}}^{\mathcal{S}}} \Psi^{\mathcal{S}} \left(\boldsymbol{C}_{\mathrm{El}}^{\mathcal{S}} \right) \right) \left(\boldsymbol{F}_{\mathrm{Gr}}^{\mathcal{S}}\right)^{-T}. \tag{2.40}$$

where the *structure displacement field* $\boldsymbol{d}^{\mathcal{S}}$ is the primary unknown. In the case of the structure problem, *Dirichlet* boundary conditions prescribe given displacements $\boldsymbol{d}_{\mathrm{D}}^{\mathcal{S}}(t, \boldsymbol{X})$ on the material boundary $\Gamma_{\mathrm{D}}^{\mathcal{S}}$:

$$\boldsymbol{d}^{\mathcal{S}} = \boldsymbol{d}_{\mathrm{D}}^{\mathcal{S}}. \tag{2.41}$$

Neumann boundary conditions load the structure with external *material* surface tractions $\boldsymbol{T}_{\mathrm{N}}^{\mathcal{S}}(t, \boldsymbol{X})$ on the material boundary $\Gamma_{\mathrm{N}}^{\mathcal{S}}$:

$$\boldsymbol{F}^{\mathcal{S}} \boldsymbol{S}^{\mathcal{S}} \boldsymbol{N}_{\mathrm{N}}^{\mathcal{S}} = \boldsymbol{T}_{\mathrm{N}}^{\mathcal{S}}, \tag{2.42}$$

where $\boldsymbol{N}_{\mathrm{N}}^{\mathcal{S}}$ is the outward pointing surface normal on the material boundary $\Gamma_{\mathrm{N}}^{\mathcal{S}}$.

2.1.5 Scalar transport

The derivation of the governing equations that are required to describe the advective, diffusive and reactive transport of scalar-valued quantities (*scalar transport*) is briefly presented in this section. A more detailed review on this topic can be found in the textbooks by *Donea* and *Huerta* [67] or *Eck et al.* [69].

As the fluid problem, the scalar transport problem is described in terms of an ALE observer. The ALE observer is chosen such that it captures the full deformation of the spatial scalar transport domain $\Omega^{\mathcal{SC}}(t)$. The physical principle that drives the scalar transport is the balance of mass. All quantities and parameters that are related to general scalar transport problems are indicated by the superscript $\mathcal{SC}$. For an easy distinction between the special cases of scalar transport with a fluid or structure, their quantities and parameters are indicated by the superscripts $\mathcal{FS}$ or $\mathcal{SS}$, respectively. The special case of scalar transport in porous media, indicated by the superscript $\mathcal{PS}$, is presented in Section 2.1.6 together with the porous media flow problem.

2.1.5.1 Balance of mass

In this thesis, the transport of scalars is viewed in the sense of the transport of concentrations even though the derived equations are valid also for other scalar-valued quantities. Let $c_i^{\mathcal{SC}}$ ($i = 1, \dots, n_c$) denote the scalar-valued concentrations of n_c reactive contributors. Then, the global balance of mass of concentration $c_i^{\mathcal{SC}}(t, \boldsymbol{x})$ in the spatial domain $\Omega^{\mathcal{SC}}(t)$ reads

$$\frac{\mathrm{d}}{\mathrm{d}t} \int\limits_{\Omega^{\mathcal{SC}}(t)} M_i c_i^{\mathcal{SC}}(t, \boldsymbol{x}) \, \mathrm{d}v = \int\limits_{\Omega^{\mathcal{SC}}(t)} M_i \varkappa_i^{\mathcal{SC}}(\boldsymbol{c}^{\mathcal{SC}}(t, \boldsymbol{x})) \, \mathrm{d}v - \int\limits_{\Gamma^{\mathcal{SC}}(t)} M_i \boldsymbol{q}_i^{\mathcal{SC}}(t, \boldsymbol{x}) \cdot \boldsymbol{n}(t, \boldsymbol{x}) \, \mathrm{d}s, \tag{2.43}$$

where M_i denotes the mass per unit of concentration $c_i^{\mathcal{SC}}$. The *reaction term* $\varkappa_i^{\mathcal{SC}}(\boldsymbol{c}^{\mathcal{SC}})$ of scalar i depends on the vector of *all* concentrations $\boldsymbol{c}^{\mathcal{SC}} = [c_1^{\mathcal{SC}}, \dots, c_{n_c}^{\mathcal{SC}}]^T$. The *diffusive influx* is denoted by $\boldsymbol{q}_i^{\mathcal{SC}}$ and is further described by *Fick's law* [80]:

$$\boldsymbol{q}_i^{\mathcal{SC}}(t, \boldsymbol{x}) = -D_i^{\mathcal{SC}} \nabla c_i^{\mathcal{SC}}(t, \boldsymbol{x}), \tag{2.44}$$

where the constant $D_i^{\mathcal{SC}}$ is the *diffusion coefficient*. Hence, by setting $q(t, \boldsymbol{x}) = c_i^{\mathcal{SC}}(t, \boldsymbol{x})$, $q_\Omega(t, \boldsymbol{x}) = \varkappa_i^{\mathcal{SC}}(\boldsymbol{c}^{\mathcal{SC}}(t, \boldsymbol{x}))$ and $\boldsymbol{q}_\Gamma(t, \boldsymbol{x}) = D_i^{\mathcal{SC}} \nabla c_i^{\mathcal{SC}}(t, \boldsymbol{x})$ in Equation (2.11), it follows the *advection-diffusion-reaction equation* in an ALE frame

$$\begin{aligned} \frac{\partial}{\partial t} c_i^{\mathcal{SC}}\big|_{\boldsymbol{\chi}} + \left(\boldsymbol{u} - \boldsymbol{u}^{\mathcal{SCG}}\right) \cdot \nabla c_i^{\mathcal{SC}} + c_i^{\mathcal{SC}} \, \nabla \cdot \boldsymbol{u} - \boldsymbol{\nabla} \cdot (D_i^{\mathcal{SC}} \nabla c_i^{\mathcal{SC}}) = \varkappa_i^{\mathcal{SC}}(\boldsymbol{c}^{\mathcal{SC}}), \\ \forall t \geq 0, \ \forall \boldsymbol{x} \in \Omega^{\mathcal{SC}}(t), \ \forall i = 1, \dots, n_c, \end{aligned} \tag{2.45}$$

where $\boldsymbol{u}$ is the material velocity the concentration $c_i^{\mathcal{SC}}(t, \boldsymbol{x})$ is transported with. The velocity of the ALE observer is denoted as $\boldsymbol{u}^{\mathcal{SCG}}$ to avoid confusion with the ALE observer of the fluid problem.

2.1.5.2 Governing equations

The governing equations of two special scalar transport problems are derived which describe the scalar transport with a fluid flow (*fluid-scatra*) and the scalar transport within a deforming structure (*structure-scatra*).

Scalar transport with fluid flow

The transport of concentrations $c_i^{\mathcal{FS}}(t, \boldsymbol{x})$ in the spatial fluid-scatra domain $\Omega^{\mathcal{FS}}(t) \subseteq \Omega^{\mathcal{F}}(t)$ is driven by diffusion and advection with the fluid velocity $\boldsymbol{u}^{\mathcal{F}}$. Using the same ALE observer as the fluid problem (with ALE velocity $\boldsymbol{u}^{\mathcal{G}}$), the incompressibility Equation (2.22) and dropping the reactive term, the advection-diffusion-reaction Equation (2.45) yields the *advection-diffusion equation* in an ALE frame describing the fluid-scatra problem on the spatial domain $\Omega^{\mathcal{FS}}(t)$:

$$\frac{\partial}{\partial t} c_i^{\mathcal{FS}}\big|_{\boldsymbol{\chi}} + \left(\boldsymbol{u}^{\mathcal{F}} - \boldsymbol{u}^{\mathcal{G}}\right) \cdot \nabla c_i^{\mathcal{FS}} - \boldsymbol{\nabla} \cdot (D_i^{\mathcal{FS}} \nabla c_i^{\mathcal{FS}}) = 0, \quad \forall i = 1, \dots, n_c, \tag{2.46}$$

where the fluid-scatra concentrations $c_i^{\mathcal{FS}}(t, \boldsymbol{x})$ are the primary unknowns. *Dirichlet* and *Neumann* boundary conditions of the fluid-scatra problem prescribe given concentrations $c_{i,\mathrm{D}}^{\mathcal{FS}}(t, \boldsymbol{x})$ on the spatial boundary $\Gamma_{\mathrm{D}}^{\mathcal{FS}}(t)$

$$c_i^{\mathcal{FS}} = c_{i,\mathrm{D}}^{\mathcal{FS}} \tag{2.47}$$

and given *diffusive influxes* $q_{\mathrm{N}}^{\mathcal{FS}}(t, \boldsymbol{x})$ through the spatial boundary $\Gamma_{\mathrm{N}}^{\mathcal{FS}}(t)$

$$-D_i^{\mathcal{FS}} \nabla c_i^{\mathcal{FS}} \cdot \boldsymbol{n}_{\mathrm{N}}^{\mathcal{FS}} = q_{\mathrm{N}}^{\mathcal{FS}}, \tag{2.48}$$

respectively.

Remark. *At first glance, a more intuitive definition of the* Neumann *boundary condition would be an* advective and diffusive *flux condition:* $\left(c_i^{\mathcal{FS}} \left(\boldsymbol{u}^{\mathcal{F}} - \boldsymbol{u}^{\mathcal{G}}\right) - D_i^{\mathcal{FS}} \nabla c_i^{\mathcal{FS}}\right) \cdot \boldsymbol{n}_{\mathrm{N}}^{\mathcal{FS}} = q_{\mathrm{N}}^{\mathcal{FS}}$*. However, by this definition, a zero-*Neumann *condition would prevent* any *flux through the* Neumann *boundary and special boundary conditions would be required at fluid outflux boundaries, where the scalar quantity is supposed to leave the domain together with the fluid. Further, both definitions are equivalent at regions, where a* no-slip *boundary condition is prescribed on the fluid, i.e., where* $\boldsymbol{u}^{\mathcal{F}} = \boldsymbol{u}^{\mathcal{G}}$.

Scalar transport within deforming structure

The transport of concentrations $c_i^{\mathcal{FS}}(t, \boldsymbol{x})$ in the spatial structure-scatra domain $\Omega^{\mathcal{SS}}(t) \subseteq \Omega^{\mathcal{S}}(t)$ is driven by diffusion, reaction and advection due to the deformation of the structure (with velocity $\boldsymbol{u}^{\mathcal{S}}$). As the structure-scatra domain $\Omega^{\mathcal{SS}}(t)$ deforms with the structure domain $\Omega_t^{\mathcal{S}}(t)$, the natural choice for the ALE observer of the structure-scatra problem is given by the structure problem (with ALE velocity $\boldsymbol{u}^{\mathcal{S}}$). Hence, the advection-diffusion-reaction Equation (2.45) yields the *diffusion-reaction equation* in an ALE frame describing the structure-scatra problem on the spatial domain $\Omega^{\mathcal{SS}}(t)$:

$$\frac{\partial}{\partial t} c_i^{\mathcal{SS}}\big|_{\boldsymbol{\chi}} + c_i^{\mathcal{SS}} \boldsymbol{\nabla} \cdot \boldsymbol{u}^{\mathcal{S}} - \boldsymbol{\nabla} \cdot \left(D_i^{\mathcal{SS}} \nabla c_i^{\mathcal{SS}}\right) = \varkappa_i^{\mathcal{SS}}(\boldsymbol{c}^{\mathcal{SS}}), \quad \forall i = 1, \ldots, n_c, \tag{2.49}$$

where the structure-scatra concentrations $c_i^{\mathcal{SS}}(t, \boldsymbol{x})$ are the primary unknowns. *Dirichlet* boundary conditions prescribe given concentrations $c_{i,\mathrm{D}}^{\mathcal{SS}}(t, \boldsymbol{x})$ on the spatial boundary $\Gamma_{\mathrm{D}}^{\mathcal{SS}}(t)$

$$c_i^{\mathcal{SS}} = c_{i,\mathrm{D}}^{\mathcal{SS}}, \tag{2.50}$$

whereas *Neumann* boundary conditions prescribe given *diffusive influxes* $q_{\mathrm{N}}^{\mathcal{SS}}(t, \boldsymbol{x})$ through the spatial boundary $\Gamma_{\mathrm{N}}^{\mathcal{SS}}(t)$

$$-D_i^{\mathcal{SS}} \nabla c_i^{\mathcal{SS}} \cdot \boldsymbol{n}_{\mathrm{N}}^{\mathcal{SS}} = q_{\mathrm{N}}^{\mathcal{SS}}. \tag{2.51}$$

2.1.6 Porous medium fluid and scalar transport

The governing equations that describe the fluid flow and scalar transport within a porous medium are briefly presented in this section. For an introduction to porous media problems and a derivation of their governing equations, see the textbooks by *Bear* and *Bachmat* [14], *Coussy* [51] or *Formaggia et al.* [85] or the thesis by *Vuong* [275].

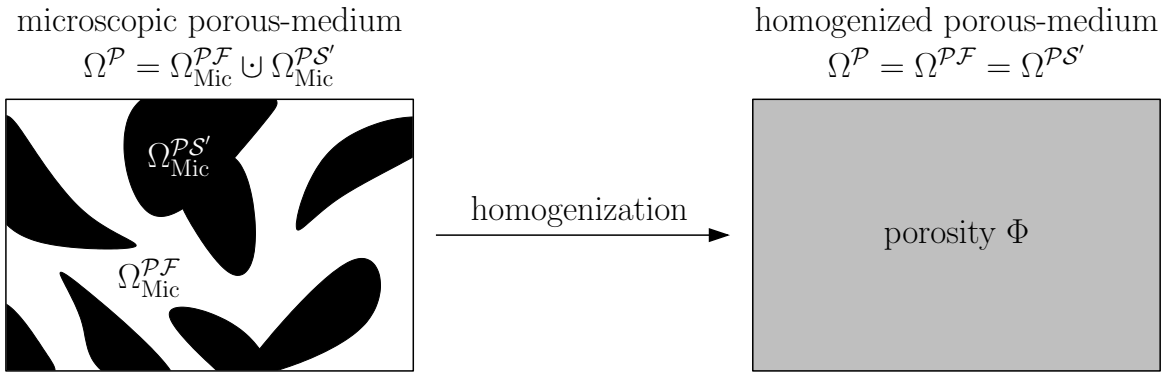

Figure 2.3 Schematic overview of homogenization of porous media. The microscopic porous media fluid phase $\Omega^{\mathcal{PF}}_{\text{Mic}}$ and microscopic porous media solid phase $\Omega^{\mathcal{PS}'}_{\text{Mic}}$ within the porous media domain $\Omega^{\mathcal{P}} = \Omega^{\mathcal{PF}}_{\text{Mic}} \cup \Omega^{\mathcal{PS}'}_{\text{Mic}}$ are homogenized to the (homogenized) porous media fluid domain $\Omega^{\mathcal{PF}}$ and (homogenized) porous media structure domain $\Omega^{\mathcal{PS}'}$.

2.1.6.1 Fundamentals

A *saturated porous medium* is a body that consists of a solid phase with pores that are filled with a fluid. In this thesis, only porous media are considered where the fluid and solid phases are fine-grained such that a sharp distinction between the phases is only possible on the microscopic scale. However, the microscopic scale is not resolvable from a computational perspective. Therefore, the microscopic structure of porous media consisting of the fluid phase $\Omega^{\mathcal{PF}}_{\text{Mic}}$ and solid phase $\Omega^{\mathcal{PS}'}_{\text{Mic}}$ in the porous media domain $\Omega^{\mathcal{P}} = \Omega^{\mathcal{PF}}_{\text{Mic}} \cup \Omega^{\mathcal{PS}'}_{\text{Mic}}$ is homogenized to the macroscopic porous media fluid domain $\Omega^{\mathcal{PF}} = \Omega^{\mathcal{P}}$ and porous media structure domain $\Omega^{\mathcal{PS}'} = \Omega^{\mathcal{P}}$. The local microscopic fraction of the fluid phase is represented by the *porosity* ϕ which considers only the interconnected parts of the fluid phase which are accessible to the microscopic porous media fluid. After the homogenization, a differentiation between the two phases is no longer possible, nor is it required. An illustration of the homogenization of porous media is given in Figure 2.3.

In this thesis, the deformation of the homogenized porous medium structure is not of particular interest. Thus, the governing equations describing a porous medium structure are not stated but can be found in the referenced literature. For completeness, however, the influence of a potential porous medium structure to the porous medium fluid will be considered at first and be neglected later on. Further, only the case of a temporal *and* spatial constant porosity ϕ is considered. Additional to the mechanics of porous media, the scalar transport of concentrations with the porous media fluid is considered, similar to Section 2.1.5.

Both, the porous media fluid and scalar transport are described in terms of an ALE observer. As the spatial porous media fluid and scalar transport domains $\Omega^{\mathcal{PF}}(t)$ and $\Omega^{\mathcal{PS}}(t)$ deform as the spatial porous medium structure domain $\Omega^{\mathcal{PS}'}(t)$, the natural choice for their ALE observers is given by the porous medium structure problem (with ALE velocity $\boldsymbol{u}^{\mathcal{PS}'}$). All quantities and

parameters that are related to the porous media fluid, structure and scalar transport are indicated by the superscripts $\mathcal{PF}$, $\mathcal{PS}'$ and $\mathcal{PS}$, respectively.

2.1.6.2 Governing equations

In the following, the governing equations that describe a porous medium fluid (*poro-fluid*) and the scalar transport with a porous medium fluid flow (*poro-scatra*) are stated.

Porous medium fluid

The velocity $\boldsymbol{u}^{\mathcal{PF}}$ of the poro-fluid is assumed to be quasi-stationary and driven purely by the poro-fluid pressure $p^{\mathcal{PF}}$. Hence, it can be described by the *stationary Darcy's law* on the spatial domain $\Omega^{\mathcal{PF}}$(t):

$$\phi \left(\boldsymbol{u}^{\mathcal{PF}} - \boldsymbol{u}^{\mathcal{PS}'} \right) = \frac{K^{\mathcal{PF}}}{\mu^{\mathcal{PF}}} \left(-\nabla p^{\mathcal{PF}} + \boldsymbol{b}^{\mathcal{PF}} \right), \tag{2.52}$$

where $K^{\mathcal{PF}}$ and $\mu^{\mathcal{PF}}$ are the *Darcy permeability* and the *dynamic viscosity* of the poro-fluid, respectively. Here, $\boldsymbol{u}^{\mathcal{PF}}$ is the *fluid intrinsic volume-averaged* velocity which corresponds to the microscopic poro-fluid velocity $\boldsymbol{u}^{\mathcal{PF}}_{\mathrm{Mic}}$ (in $\Omega^{\mathcal{PF}}_{\mathrm{Mic}}$) locally averaged over the fluid phase $\Omega^{\mathcal{PF}}_{\mathrm{Mic}}$. Analog, $\boldsymbol{u}^{\mathcal{PS}'}$ is the *structure intrinsic volume-averaged* velocity which corresponds to the microscopic velocity $\boldsymbol{u}^{\mathcal{PS}'}_{\mathrm{Mic}}$ (in $\Omega^{\mathcal{PS}'}_{\mathrm{Mic}}$) of the porous medium structure locally averaged over the structure phase $\Omega^{\mathcal{PS}'}_{\mathrm{Mic}}$.

Additionally, the conservation of mass of the poro-fluid is required. The continuum mechanical equivalent of the conservation of mass reads similar to the case of a pure fluid (cf. Equation (2.13)):

$$\frac{\partial}{\partial t}\phi\big|_{\boldsymbol{x}} + \left(\boldsymbol{u}^{\mathcal{PF}} - \boldsymbol{u}^{\mathcal{PS}'} \right) \cdot \nabla \phi + \phi \, \nabla \cdot \boldsymbol{u}^{\mathcal{PF}} = 0, \tag{2.53}$$

Considering a constant material porosity $\phi(t, \boldsymbol{X}) = const$, the continuum mechanical equivalent of the conservation of mass of the porous medium fluid reads analog to the incompressibility equation of a pure fluid (cf. Equation (2.22)):

$$\boldsymbol{\nabla} \cdot \boldsymbol{u}^{\mathcal{PF}} = 0. \tag{2.54}$$

Assuming a fixed porous medium structure, i.e., $\boldsymbol{u}^{\mathcal{PS}'} = \boldsymbol{0}$, taking the divergence of Equation (2.52) and using Equation (2.54) yields a *Poisson*-like equation for the poro-fluid problem on the fixed spatial domain $\Omega^{\mathcal{PF}}$:

$$-\boldsymbol{\nabla} \cdot \left(\frac{K^{\mathcal{PF}}}{\phi \mu^{\mathcal{PF}}} \nabla p^{\mathcal{PF}} \right) = -\frac{K^{\mathcal{PF}}}{\phi \mu^{\mathcal{PF}}} \boldsymbol{\nabla} \cdot \boldsymbol{b}^{\mathcal{PF}}, \tag{2.55}$$

where the porous medium fluid pressure $p^{\mathcal{PF}}$ is the primary unknown. *Dirichlet* boundary conditions prescribe given pressures $p^{\mathcal{PF}}_{\mathrm{D}}(t, \boldsymbol{x})$ on the spatial boundary $\Gamma^{\mathcal{PF}}_{\mathrm{D}}$

$$p^{\mathcal{PF}} = p^{\mathcal{PF}}_{\mathrm{D}}, \tag{2.56}$$

whereas *Neumann* boundary conditions prescribe given *volume influxes* $q_{\mathrm{N}}^{\mathcal{PF}}(t, \boldsymbol{x})$ through the spatial boundary $\Gamma_{\mathrm{N}}^{\mathcal{PF}}$

$$-\frac{K^{\mathcal{PF}}}{\phi \mu^{\mathcal{PF}}} \nabla p^{\mathcal{PF}} \cdot \boldsymbol{n}_{\mathrm{N}}^{\mathcal{PF}} = q_{\mathrm{N}}^{\mathcal{PF}}. \tag{2.57}$$

Remark. *More sophisticated porous media flow models, such as the* generalized Darcy's law *or the* Darcy-Brinkmann equation *exist, see for example the textbook by* Bear *and* Bachmat *[14]. However, for the purpose of this thesis, the* stationary Darcy*'s law is sufficient to describe the porous media flow within artery walls.*

Scalar transport with porous medium fluid

On the microscopic scale, the microscopic concentrations $c_{\mathrm{Mic},i}^{\mathcal{PS}}$ $(i = 1, \ldots, n_c)$ are transported only with the poro-fluid located in the fluid phase $\Omega_{\mathrm{Mic}}^{\mathcal{PF}}$ of the porous medium. Hence, the balance of mass for the microscopic concentrations $c_{\mathrm{Mic},i}^{\mathcal{PS}}$ reads analog to Equation (2.43), but with an integration over the fluid phase $\Omega_{\mathrm{Mic}}^{\mathcal{PF}}$. The governing equations for the *fluid intrinsic volume-averaged* concentrations $c_i^{\mathcal{PS}}$ (i.e., the concentrations $c_{\mathrm{Mic},i}^{\mathcal{PS}}$ locally averaged over the fluid phase $\Omega_{\mathrm{Mic}}^{\mathcal{PF}}$) on the deformable spatial domain $\Omega^{\mathcal{PS}}(t)$ read

$$\phi \frac{\partial}{\partial t} c_i^{\mathcal{PS}}\big|_{\boldsymbol{\chi}} + \phi \, K_i^{\mathcal{PS}} \left(\boldsymbol{u}^{\mathcal{PF}} - \boldsymbol{u}^{\mathcal{PS}'} \right) \cdot \nabla c_i^{\mathcal{PS}} - \boldsymbol{\nabla} \cdot (\phi D_{\mathrm{Eff},i}^{\mathcal{PS}} \nabla c_i^{\mathcal{PS}}) = \phi \, \varkappa_i^{\mathcal{PS}}\big(\boldsymbol{c}^{\mathcal{PS}}\big), \tag{2.58}$$

where $D_{\mathrm{Eff},i}^{\mathcal{PS}}$ is the *effective diffusion coefficient* as observable on the macroscopic scale. The reduction of the advective transport by the collision of the transported quantity with the solid phase of the porous medium is taken into account by the introduction of the *hindrance coefficient* $0 \leq K_i^{\mathcal{PS}} \leq 1$.

Using Equation (2.54) and taking the assumptions of a fixed porous medium structure with constant material porosity ϕ leads to a similar result as Equation (2.45) called the *porous medium-advection-diffusion-reaction equation* describing the poro-scatra problem on the fixed spatial domain $\Omega^{\mathcal{PS}}$:

$$\frac{\partial}{\partial t} c_i^{\mathcal{PS}} + \boldsymbol{\nabla} \cdot \left(K_i^{\mathcal{PS}} c_i^{\mathcal{PS}} \boldsymbol{u}^{\mathcal{PF}} \right) - \boldsymbol{\nabla} \cdot \left(D_{\mathrm{Eff},i}^{\mathcal{PS}} \nabla c_i^{\mathcal{PS}} \right) = \varkappa_i^{\mathcal{PS}}\big(\boldsymbol{c}^{\mathcal{PS}}\big), \quad \forall i = 1, \ldots, n_c. \tag{2.59}$$

The primary unknowns of the poro-scatra problem are the volume-averaged concentrations $c_i^{\mathcal{PS}}$. *Dirichlet* boundary conditions prescribe given concentrations $c_{i,\mathrm{D}}^{\mathcal{PS}}(t, \boldsymbol{x})$ on the spatial boundary $\Gamma_{\mathrm{D}}^{\mathcal{PS}}$

$$c_i^{\mathcal{PS}} = c_{i,\mathrm{D}}^{\mathcal{PS}}, \tag{2.60}$$

whereas *Neumann* boundary conditions prescribe given *advective and diffusive fluxes* $q_{\mathrm{N}}^{\mathcal{PS}}(t, \boldsymbol{x})$ through the spatial boundary $\Gamma_{\mathrm{N}}^{\mathcal{PS}}$

$$\left(K_i^{\mathcal{PS}} c_i^{\mathcal{PS}} \boldsymbol{u}^{\mathcal{PF}} - D_{\mathrm{Eff},i}^{\mathcal{PS}} \nabla c_i^{\mathcal{PS}} \right) \cdot \boldsymbol{n}_{\mathrm{N}}^{\mathcal{PS}} = q_{\mathrm{N}}^{\mathcal{PS}}. \tag{2.61}$$

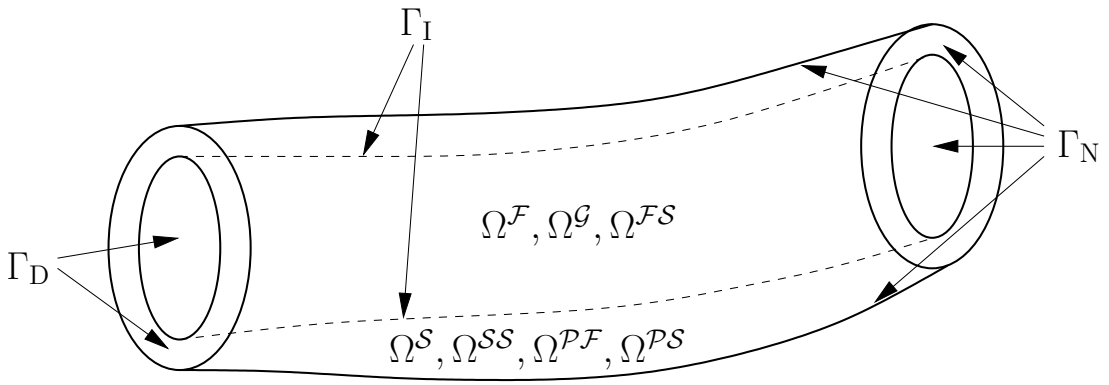

Figure 2.4 Schematic overview of domains (fluid $\Omega^{\mathcal{F}}$, ALE $\Omega^{\mathcal{G}}$, fluid-scatra $\Omega^{\mathcal{FS}}$, structure $\Omega^{\mathcal{S}}$, structure-scatra $\Omega^{\mathcal{SS}}$, poro-fluid $\Omega^{\mathcal{PF}}$ and poro-scatra $\Omega^{\mathcal{PS}}$) and boundaries (*Dirichlet* Γ_{D}, *Neumann* Γ_{N} and interaction Γ_{I}) of surface coupled and volume coupled multiphysics problems.

2.2 Multiphysics problems

The modeling of early atherosclerosis in this thesis involves the coupling of multiple physics introduced in the previous Section 2.1. In this section, the relevant multiphysics problems and their couplings are briefly presented.

In general, there are two different classes of coupled problems - *surface coupled* and *volume coupled* problems. Surface coupled problems involve two or more subproblems which share a joint boundary denoted as the *interaction boundary* Γ_{I}. For surface coupled problems, the coupling between the subproblems is solely in terms of *coupling conditions* on the interaction boundary Γ_{I}. Additional to the coupling condition on Γ_{I}, each subproblem still may have respective boundary conditions prescribed on its *Dirichlet* and *Neumann* boundaries Γ_{D} and Γ_{N}, respectively. Together, the *Dirichlet* boundary Γ_{D}, *Neumann* boundary Γ_{N} and interaction boundary Γ_{I} form a disjunct partition of the respective domain boundary Γ, i.e., $\Gamma = \Gamma_{\mathrm{D}} \cup \Gamma_{\mathrm{N}} \cup \Gamma_{\mathrm{I}}$.

In contrast, volume coupled problems involve two or more subproblems which share a joint domain. Volume coupled subproblems interact by couplings on the joint domain. Examples for surface and volume coupled multiphysics problems in this thesis are fluid-structure interaction, multi-field scalar transport, fluid-structure-scalar transport interaction or porous medium fluid-scalar transport interaction problems which are introduced in the following section. A schematic overview of the arrangement of relevant domains and boundaries of surface and volume coupled multiphysics problems in this thesis is given in Figure 2.4.

2.2.1 Fluid-structure interaction

Fluid-structure interaction (FSI) problems are common examples for multiphysics problems. For a schematic overview of the arrangement of the domains and boundaries of the involved fluid, structure and ALE subproblems, see Figure 2.4.

Detailed reviews on fluid-structure interaction problems can be found in the textbooks by *Bazilevs et al.* [13] or *Formaggia et al.* [85] or in the theses by *Küttler* [158], *Mayr* [192] or *Wall* [278].

2.2.1.1 ALE subproblem

The numerical treatment of the physical *two-field* FSI problem, requires to solve a computational *three-field* problem as the fluid problem introduced in Section 2.1.3 is formulated in an ALE fashion to respect the deformation of the fluid domain $\Omega^{\mathcal{F}}(t)$ over time t. It is convenient to think of the introduced (fluid) ALE subproblem on the material ALE domain $\Omega_0^{\mathcal{G}}$ as the underlying grid of the discretized fluid problem. Hence, the motion of the ALE observer has to be chosen such that it captures the deformation of the fluid domain $\Omega^{\mathcal{F}}(t)$, i.e., such that $\Omega^{\mathcal{G}}(t) = \Omega^{\mathcal{F}}(t)$.

In this thesis, the motion of the ALE observer is described as a quasi-elastostatic hyperelastic pseudo-structure on the domain $\Omega_0^{\mathcal{G}}$ with a neo-Hookean strain-energy density function $\Psi^{\mathcal{G}}$ [122] as constitutive law. It is governed by the stationary version of the structure problem as described in Section 2.1.4. The governing equations of the ALE subproblem on the material domain $\Omega_0^{\mathcal{G}}$ read

$$-\boldsymbol{\nabla}_0 \cdot \left(\boldsymbol{F}^{\mathcal{G}} \boldsymbol{S}^{\mathcal{G}}\right) = \boldsymbol{0}, \tag{2.62}$$

where $\boldsymbol{F}^{\mathcal{G}} = \boldsymbol{1} + \boldsymbol{\nabla}_0 \boldsymbol{d}^{\mathcal{G}}$, $\boldsymbol{C}^{\mathcal{G}} = \left(\boldsymbol{F}^{\mathcal{G}}\right)^T \boldsymbol{F}^{\mathcal{G}}$ and $\boldsymbol{S}^{\mathcal{G}} = 2\frac{\partial}{\partial \boldsymbol{C}^{\mathcal{G}}} \Psi^{\mathcal{G}}\left(\boldsymbol{C}^{\mathcal{G}}\right)$ are the deformation gradient, the right *Cauchy-Green* tensor and the second *Piola-Kirchhoff* stress tensor of the ALE subproblem, respectively. The *ALE displacement field* $\boldsymbol{d}^{\mathcal{G}}$ is the primary unknown of the ALE subproblem. The *Dirichlet* and *Neumann* boundaries of the ALE subproblem coincide with the *Dirichlet* and *Neumann* boundaries of the fluid subproblem, i.e., $\Gamma_{\mathrm{D}}^{\mathcal{G}} = \Gamma_{\mathrm{D}}^{\mathcal{F}}$ and $\Gamma_{\mathrm{N}}^{\mathcal{G}} = \Gamma_{\mathrm{N}}^{\mathcal{F}}$. Zero-displacements and zero-tractions are prescribed on the *Dirichlet* boundary $\Gamma_{\mathrm{D}}^{\mathcal{G}}$ and *Neumann* boundary $\Gamma_{\mathrm{N}}^{\mathcal{G}}$, respectively.

The fluid subproblem is volume coupled to the ALE subproblem by the ALE velocity field $\boldsymbol{u}^{\mathcal{G}}$ in the *Navier-Stokes* Equations (2.21). Further, all three subproblems - the fluid, structure and ALE subproblem - are surface coupled by the FSI coupling conditions.

Remark. *The task of the ALE observer model is to enable a smooth and mesh quality preserving computational approach for the extension of the ALE displacements from its domain boundaries $\Gamma^{\mathcal{G}}$ to its full domain $\Omega_0^{\mathcal{G}}$. The proposed approach of a pseudo-structure is just one possible choice to do so and other approaches, such as by springs, laplacian or bilaplacian approaches exist, cf. [192] or [295] and references therein. An advantage of the chosen pseudo-structure approach is that the implementation required to solve the structure problem can be reused. Further, the pseudo-structure approach offers a large flexibility by the particular choice for an appropriate constitutive law and its parameters which gives the opportunity to preserve the mesh quality at regions where the mesh is especially vulnerable, e.g., at thin fluid boundary layers.*

2.2.1.2 Coupling conditions

The fluid, structure and ALE subproblems are surface coupled by the *FSI coupling conditions* prescribed on the interaction boundary $\Gamma_{\mathrm{I}} = \Omega^{\mathcal{F}} \cap \Omega^{\mathcal{S}} \cap \Omega^{\mathcal{G}}$. The FSI coupling conditions enforce the kinematic continuity of the three fields by a *Dirichlet*-like conditions on the fluid interaction boundary $\Gamma_{\mathrm{I}}^{\mathcal{F}}$

$$\boldsymbol{u}^{\mathcal{F}} = \boldsymbol{u}^{\mathcal{G}} \tag{2.63}$$

and a *Dirichlet*-like conditions on the ALE interaction boundary $\Gamma_{\mathrm{I}}^{\mathcal{G}}$

$$\boldsymbol{d}^{\mathcal{G}} = \boldsymbol{d}^{\mathcal{S}}. \tag{2.64}$$

Taking the derivative of Equation (2.64) with respect to time leads to the (in the continuous regime) equivalent conditions for the kinematic continuity between the fluid, structure and ALE subproblems:

$$\boldsymbol{u}^{\mathcal{F}} = \boldsymbol{u}^{\mathcal{G}} = \boldsymbol{u}^{\mathcal{S}}. \tag{2.65}$$

The third FSI coupling condition is in fact well-known as *Newton*'s third law – *actio=-reactio*. It ensures the equilibrium of forces by a *Neumann*-like condition on the structure interaction boundary $\Gamma_{\mathrm{I}}^{\mathcal{S}}$

$$\boldsymbol{\sigma}^{\mathcal{S}} \boldsymbol{n}_{\mathrm{I}}^{\mathcal{S}} = -\boldsymbol{\sigma}^{\mathcal{F}} \boldsymbol{n}_{\mathrm{I}}^{\mathcal{S}}. \tag{2.66}$$

In subsequent discussions, the ALE subproblem is dropped, as it is required only to computationally treat the deforming fluid subproblem and does not possess a physical relevance on its own. Hence, in the following FSI problems will be seen as surface coupled problems of ALE-fluids and structures coupled solely by the FSI coupling conditions (2.65) and (2.66).

Remark. *The FSI coupling conditions were presented as a* Dirichlet-*To*-Neumann *scheme [158, 159], which has been chosen for simplicity. However, other impositions of the FSI coupling conditions are possible [160], which can be derived by using the in the continuous regime equivalent formulations in Equation* (2.65)*. However, the different formulations gained by using Equation* (2.65) *might differ, depending on the chosen temporal discretization [193].*

2.2.2 Fluid-structure-scalar transport interaction

The multiphysics model for atherosclerosis in this thesis is a *fluid-structure-scalar transport interaction* (FSSTI) problem bringing together the previously introduced FSI problem and a multi-field scalar transport problem that is subsequently denoted as *(fluid-scatra)-(structure-scatra) interaction* (S2I) problem. The interaction of the two scalar problems is governed by the *Kedem-Katchalsky* equations. For a schematic overview of the arrangement of the domains and boundaries of the involved subproblems, see Figure 2.4.

Further information on FSSTI problems can be found in the publications by *Coroneo et al.* [50], *Thon et al.* [266] or *Yoshihara et al.* [297]. A derivation and details on the *Kedem-Katchalsky* equations are given in the textbooks by *Formaggia et al.* [85] or *Katchalsky* and *Curran* [147] or the publication by *Kedem* and *Katchalsky* [148].

2.2.2.1 *Kedem-Katchalsky* equations

The equations of *Kedem* and *Katchalsky* were developed in 1958 to describe the transport of non-electrolyte solutions through semi-permeable membranes [148]. The *Kedem-Katchalsky equations* describe the volume flux J_{Vol} and solute flux $J_{\mathrm{Sol},i}$ through semi-permeable membranes in dependency of the hydraulic pressure gradient Δp, the osmotic pressure gradient $\Delta\pi$ and the solute concentration gradient Δc_i across the membrane. In their *practical form*, the *Kedem-Katchalsky* equations read

$$\begin{aligned} J_{\mathrm{Vol}} &= L_p \left(\Delta p - \sigma_{\mathrm{D},i}\Delta\pi\right), \\ J_{\mathrm{Sol},i} &= P_i\Delta c_i + (1-\sigma_{\mathrm{F},i})\overline{c_i}J_{\mathrm{Vol}}, \end{aligned} \tag{2.67}$$

where the constants L_p and P_i are the *hydraulic conductivity* and the *diffusive permeability* of solute i. The *osmotic reflection coefficient* $0 \leq \sigma_{\mathrm{D},i} \leq 1$ and *filtration reflection coefficient* $0 \leq \sigma_{\mathrm{F},i} \leq 1$ are employed to account for the effects of the osmotic pressure and the selective rejection of solutes by the membrane. The *average concentration* of the solute i within the membrane is denoted by $\overline{c_i}$.

The osmotic pressure gradient $\Delta\pi$ can be estimated by *Van't Hoff's law*: $\Delta\pi = RT\Delta c_i$, where R and T are the *gas constant* and *absolute temperature*. In many applications, concentrations and temperatures are rather low such that the osmotic pressure gradient $\Delta\pi$ is minor by orders compared to hydraulic pressure gradient Δp. Hence, the osmotic volume flux is frequently dropped decoupling the volume flux J_{Vol} from the solute flux $J_{\mathrm{Sol},i}$.

In the most general context of this thesis, the membranes correspond to the interaction boundary Γ_{I} that connects the fluid-scatra and poro-scatra problems. Therefore, the hydraulic pressure gradient Δp and the solute concentration gradient Δc across Γ_{I} are given by

$$\begin{aligned} \Delta p &= p^{\mathcal{F}} - p^{\mathcal{PF}}, \\ \Delta c_i &= c_i^{\mathcal{FS}} - c_i^{\mathcal{PS}}. \end{aligned} \tag{2.68}$$

The average concentration $\overline{c}$ within the membrane is estimated by the *weighted arithmetic average* given by

$$\overline{c_i} = \omega_i c_i^{\mathcal{FS}} + (1-\omega_i)c_i^{\mathcal{PS}}, \tag{2.69}$$

where $0 \leq \omega_i \leq 1$ is the *weighting factor* of the two concentrations $c_i^{\mathcal{FS}}$ and $c_i^{\mathcal{PS}}$ at the two sides of the membrane Γ_{I}. Together, Equation (2.67), (2.68) and (2.69) yield the *Kedem-Katchalsky* equations used in this thesis to describe the membrane transport between the fluid-scatra and poro-scatra problems:

$$\begin{aligned} J_{\mathrm{Vol}} &= \underbrace{L_p \left(p^{\mathcal{F}} - p^{\mathcal{PF}}\right)}_{\text{volume flux}} \\ J_{\mathrm{Sol},i} &= \underbrace{P_i \left(c_i^{\mathcal{FS}} - c_i^{\mathcal{PS}}\right)}_{\text{diffusive solute flux}} + \underbrace{(1-\sigma_{\mathrm{F},i})(\omega_i c_i^{\mathcal{FS}} + (1-\omega_i)c_i^{\mathcal{PS}})J_{\mathrm{Vol}}}_{\text{advective solute flux}}. \end{aligned} \tag{2.70}$$

The solute flux J_{Sol} can be seen as a superposition of a diffusive and advective solute flux. In the special case of a non-porous solid, the volume flux vanishes, i.e., $J_{\mathrm{Vol}} = 0$, and hence does also

the advective solute flux. Thus, the membrane transport between fluid-scatra and *structure*-scatra problems is given by the diffusive solute flux of the *Kedem-Katchalsky* equations:

$$J_{\mathrm{Sol},i} = P_i \left(c_i^{\mathcal{FS}} - c_i^{\mathcal{SS}} \right) . \tag{2.71}$$

Remark. *Other averages, such as the* arithmetic average *or the* logarithmic average *[148] can be used to estimate the average concentration $\overline{c}$ from the concentrations of both sides of the membrane. The logarithmic average, however, is valid only for extreme thin membranes, cf. [85]. Thus, the weighted arithmetic average is used as it contains the arithmetic average as special case.*

2.2.2.2 Multi-field scalar transport

The S2I problem is a surface coupled problem that brings together the advective and diffusive scalar transport with a fluid and the diffusive and reactive scalar transport in the structure as described in Section 2.1.5. The (fluid-scatra)-(structure-scatra) interaction boundary $\Gamma_{\mathrm{I}} = \Omega^{\mathcal{FS}} \cap \Omega^{\mathcal{SS}}$ of the S2I problem is treated as a transport barrier which leads to a significant discontinuity between the concentrations on the fluid-scatra and structure-scatra sides of Γ_{I}. In many cases, the interaction boundary Γ_{I} is treated as a semi-permeable membrane described by the simplified *Kedem-Katchalsky* Equation (2.71). Even if otherwise treated, let $J_{\mathrm{Sol},i}$ denote the diffusive flux of concentration c_i ($i = 1, \ldots, n_c$) through Γ_{I}. Then, the *Neumann*-like S2I coupling condition on the fluid-scatra interaction boundary $\Gamma_{\mathrm{I}}^{\mathcal{FS}}$ reads

$$-D_i^{\mathcal{FS}} \nabla c_i^{\mathcal{FS}} \cdot \boldsymbol{n}_{\mathrm{I}}^{\mathcal{FS}} = -J_{\mathrm{Sol},i}(c_i^{\mathcal{FS}}, c_i^{\mathcal{SS}}), \tag{2.72}$$

whereas on the structure-scatra interaction boundary $\Gamma_{\mathrm{I}}^{\mathcal{SS}}$ the negative of the diffusive flux $J_{\mathrm{Sol},i}$ is prescribed:

$$-D_i^{\mathcal{SS}} \nabla c_i^{\mathcal{SS}} \cdot \boldsymbol{n}_{\mathrm{I}}^{\mathcal{SS}} = J_{\mathrm{Sol},i}(c_i^{\mathcal{FS}}, c_i^{\mathcal{SS}}). \tag{2.73}$$

2.2.2.3 Couplings

The FSSTI problem is a volume and surface coupled multiphysics problem that brings together the FSI and S2I problems introduced beforehand. Besides the surface couplings of the FSI and S2I problems (cf. Sections 2.2.1.2 and 2.2.2.2), there are inherent FSI to S2I volume couplings by the advection with the fluid and the choice of the (fluid) ALE and structure subproblems as ALE observers of the fluid-scatra and structure-scatra subproblems, respectively. In this thesis, there also is a back-coupling from the S2I to the FSI problems due to scalar dependencies of the growth deformation gradient $\boldsymbol{F}_{\mathrm{Gr}}^{\mathcal{S}}(\boldsymbol{c}^{\mathcal{SS}})$ (cf. Section 2.1.4.3) and the strain-energy density function $\Psi^{\mathcal{S}}(\boldsymbol{c}^{\mathcal{SS}})$ of the structure which will be described in detail in Sections 4.1.1.4 and 4.1.1.5.

2.2.3 Porous medium fluid-scalar transport interaction

Another multiphysics problem considered in this thesis is the volume coupled *porous medium fluid-scalar transport interaction* (PFSTI) problem that brings together the poro-fluid and poro-scatra subproblems as introduced in Section 2.1.6.2. As the underlying porous medium structure was assumed to be undeformeable, the PFSTI problem can be seen as a simplification of a full porous medium subproblem coupled to a poro-scatra subproblem. For a schematic overview of the arrangement of the domains and boundaries of the involved subproblems, see Figure 2.4.

Related models can be found in the thesis by *Vuong* [275] or the publications by *Koshiba et al.* [152], *Prosi et al.*[221], *Yang et al.* [294] or others [1, 29, 45, 146, 210, 255, 267].

Couplings

As the concentrations are transported with the porous medium fluid, the poro-scatra subproblem is inherently volume coupled to the poro-fluid subproblem. Additionally, there is a poro-fluid to poro-scatra surface coupling by the *Kedem-Katchalsky* equations (2.70) as the solute flux $J_{\mathrm{Sol},i}$ of concentration c_i ($i = 1, \ldots, n_c$) depends on the volume flux J_{Vol}. The volume flux J_{Vol} is applied as *Neumann*-like boundary condition to the poro-fluid interaction boundary $\Gamma_{\mathrm{I}}^{\mathcal{PF}}$

$$-\frac{K^{\mathcal{PF}}}{\phi\mu^{\mathcal{PF}}}\nabla p^{\mathcal{PF}} \cdot \boldsymbol{n}_{\mathrm{I}}^{\mathcal{PF}} = J_{\mathrm{Vol}}(p^{\mathcal{PF}}) \tag{2.74}$$

whereas the solute flux $J_{\mathrm{Sol},i}$ of concentration c_i is applied as *Neumann*-like boundary condition to the poro-scatra interaction boundary $\Gamma_{\mathrm{I}}^{\mathcal{PS}}$:

$$\left(K_i^{\mathcal{PS}} c_i^{\mathcal{PS}} \boldsymbol{u}^{\mathcal{PF}} - D_{\mathrm{Eff},i}^{\mathcal{PS}} \nabla c_i^{\mathcal{PS}}\right) \cdot \boldsymbol{n}_{\mathrm{I}}^{\mathcal{PS}} = J_{\mathrm{Sol},i}(c_i^{\mathcal{PF}}, p^{\mathcal{PF}}). \tag{2.75}$$

3 Computational approaches

In this chapter, a brief overview of computational aspects required to numerically solve the single-field and multiphysics problems presented in the previous Section 2 is given. More extensive reviews on the presented aspects can be found in the literature and will be referenced at the beginning of the individual sections. All implementations were done in the multiphysics framework BACI [277].

3.1 Single-field problems

Before the single-field and multiphysics problems are discretized in time and space in terms of the finite element method and one-step-θ scheme, their weak formulations must be established.

A detailed overview of the finite element method and other computational aspects can be found in the textbooks by *Larson* and *Bengzon* [163] or *Zienkiewicz et al.* [302]. The textbooks by *Hughes* [129], *Wriggers* [291] or *Zienkiewicz et al.* [301] deal with the specific finite element treatment of structure problems, whereas details on the finite element treatment of transport problems can be found in the textbooks by *Brezzi* and *Fortin* [20], *Donea* and *Huerta* [67] or *Zienkiewicz et al.* [303] or the exhaustive monograph by *Kuzmin* [161].

3.1.1 Weak formulations

The weak formulations of the single-field problems are established from their governing equations as presented in Section 2.1.

3.1.1.1 Fluid

The *weak formulation* of the fluid problem governed by the incompressible *Navier-Stokes* equations is established from its *strong formulation* as described in Section 2.1.3.3. For both primary unknowns – the fluid velocity $\boldsymbol{u}^{\mathcal{F}}$ and fluid pressure $p^{\mathcal{F}}$ – the establishment of the weak from requires the definition of appropriate solution spaces $\mathcal{S}_{\boldsymbol{u}^{\mathcal{F}}}$ and $\mathcal{S}_{p^{\mathcal{F}}}$:

$$\begin{aligned} \mathcal{S}_{\boldsymbol{u}^{\mathcal{F}}} &= \left\{ \boldsymbol{u}^{\mathcal{F}} \in \left(\mathcal{H}^1(\Omega_t^{\mathcal{F}})\right)^3 \,\middle|\, \boldsymbol{u}^{\mathcal{F}} = \boldsymbol{u}_{\mathrm{D}}^{\mathcal{F}} \text{ on } \Gamma_{\mathrm{D}}^{\mathcal{F}} \right\}, \\ \mathcal{S}_{p^{\mathcal{F}}} &= \left\{ p^{\mathcal{F}} \in \mathcal{L}^2(\Omega_t^{\mathcal{F}}) \right\}, \end{aligned} \tag{3.1}$$

where $\mathcal{L}^2(\Omega^{\mathcal{F}})$ and $\mathcal{H}^1(\Omega^{\mathcal{F}})$ denote the usual Sobolev spaces on $\Omega^{\mathcal{F}}$. The trial spaces $\mathcal{T}_{\boldsymbol{u}^{\mathcal{F}}}$ and $\mathcal{T}_{p^{\mathcal{F}}}$ equal the corresponding solution spaces, but with homogenized *Dirichlet* conditions:

$$\begin{aligned} \mathcal{T}_{\boldsymbol{u}^{\mathcal{F}}} &= \left\{ \delta\boldsymbol{u}^{\mathcal{F}} \in \left(\mathcal{H}^1(\Omega_t^{\mathcal{F}})\right)^3 \;\middle|\; \boldsymbol{u}^{\mathcal{F}} = \boldsymbol{0} \text{ on } \Gamma_{\mathrm{D}}^{\mathcal{F}} \right\}, \\ \mathcal{T}_{p^{\mathcal{F}}} &= \left\{ \delta p^{\mathcal{F}} \in \mathcal{L}^2(\Omega_t^{\mathcal{F}}) \right\}. \end{aligned} \tag{3.2}$$

The weak formulation is derived by multiplying Equations (2.21) and (2.22) with the respective testing functions $\delta\boldsymbol{u}^{\mathcal{F}} \in \mathcal{T}_{\boldsymbol{u}^{\mathcal{F}}}$ and $\delta p^{\mathcal{F}} \in \mathcal{T}_{p^{\mathcal{F}}}$ and integrating them over the fluid domain $\Omega^{\mathcal{F}}(t)$. Further an *integration by parts* of the pressure and viscous terms is performed such that *Neumann* boundary conditions can be employed as *natural boundary conditions*. Denoting the standard $\mathcal{L}^2$-scalar products by with $(\bullet, \bullet)$, the weak formulation of the fluid problem $(\mathcal{F})$ reads: Find $\boldsymbol{u}^{\mathcal{F}} \in \mathcal{S}_{\boldsymbol{u}^{\mathcal{F}}}$ and $p^{\mathcal{F}} \in \mathcal{S}_{p^{\mathcal{F}}}$ such that

$$(\mathcal{F}): \begin{cases} 0 = r^{\mathcal{F}} := & \left(\delta\boldsymbol{u}^{\mathcal{F}}, \varrho^{\mathcal{F}} \frac{\partial}{\partial t}\boldsymbol{u}^{\mathcal{F}}\big|_{\boldsymbol{\chi}}\right)_{\Omega^{\mathcal{F}}(t)} + \left(\delta\boldsymbol{u}^{\mathcal{F}}, \varrho^{\mathcal{F}} \left(\left(\boldsymbol{u}^{\mathcal{F}} - \boldsymbol{u}^{\mathcal{G}}\right) \cdot \boldsymbol{\nabla}\right) \boldsymbol{u}^{\mathcal{F}}\right)_{\Omega^{\mathcal{F}}(t)} \\ & - \left(\boldsymbol{\nabla} \cdot \delta\boldsymbol{u}^{\mathcal{F}}, p^{\mathcal{F}}\right)_{\Omega^{\mathcal{F}}(t)} + \left(\boldsymbol{\nabla}\delta\boldsymbol{u}^{\mathcal{F}}, 2\mu^{\mathcal{F}}(\boldsymbol{u}^{\mathcal{F}})\boldsymbol{\varepsilon}^{\mathcal{F}}(\boldsymbol{u}^{\mathcal{F}})\right)_{\Omega^{\mathcal{F}}(t)} \\ & - \left(\delta\boldsymbol{u}^{\mathcal{F}}, \boldsymbol{t}_{\mathrm{N}}^{\mathcal{F}}\right)_{\Gamma_{\mathrm{N}}^{\mathcal{F}}(t)} - \left(\delta\boldsymbol{u}^{\mathcal{F}}, \boldsymbol{b}^{\mathcal{F}}\right)_{\Omega^{\mathcal{F}}(t)} + \left(\delta p^{\mathcal{F}}, \boldsymbol{\nabla} \cdot \boldsymbol{u}^{\mathcal{F}}\right)_{\Omega^{\mathcal{F}}(t)}, \end{cases} \tag{3.3}$$

for all $\delta\boldsymbol{u}^{\mathcal{F}} \in \mathcal{T}_{\boldsymbol{u}^{\mathcal{F}}}$ and $\delta p^{\mathcal{F}} \in \mathcal{T}_{p^{\mathcal{F}}}$. $r^{\mathcal{F}}$ denotes the *weak residual* of the fluid problem.

Remark. *The solution and trial spaces as well as the weak formulations depend on time t. However, this was neglected in the notation to keep it easy and comprehensible. Throughout this thesis, it is always assumed that all quantities are sufficiently smooth in time.*

3.1.1.2 Structure

The weak formulation of the structure problem is established from its strong formulation as described in Section 2.1.4.4. Therefore, the solution space $\mathcal{S}_{\boldsymbol{d}^{\mathcal{S}}}$ and trial space $\mathcal{T}_{\boldsymbol{d}^{\mathcal{S}}}$ for the structure displacement field $\boldsymbol{d}^{\mathcal{S}}$ read

$$\begin{aligned} \mathcal{S}_{\boldsymbol{d}^{\mathcal{S}}} &= \left\{ \boldsymbol{d}^{\mathcal{S}} \in \left(\mathcal{H}^1(\Omega_0^{\mathcal{S}})\right)^3 \;\middle|\; \boldsymbol{d}^{\mathcal{S}} = \boldsymbol{d}_{\mathrm{D}}^{\mathcal{S}} \text{ on } \Gamma_{\mathrm{D}}^{\mathcal{S}} \right\}, \\ \mathcal{T}_{\boldsymbol{d}^{\mathcal{S}}} &= \left\{ \delta\boldsymbol{d}^{\mathcal{S}} \in \left(\mathcal{H}^1(\Omega_0^{\mathcal{S}})\right)^3 \;\middle|\; \boldsymbol{d}^{\mathcal{S}} = \boldsymbol{0} \text{ on } \Gamma_{\mathrm{D}}^{\mathcal{S}} \right\}. \end{aligned} \tag{3.4}$$

The weak formulation is derived by multiplying Equation (2.39) with a testing function $\delta\boldsymbol{d}^{\mathcal{S}} \in \mathcal{T}_{\boldsymbol{d}^{\mathcal{S}}}$, an integration over the structure domain $\Omega_0^{\mathcal{S}}$ and an integration by parts of the stress term such that *Neumann* boundary conditions can be employed as natural boundary conditions. The weak formulation of the structure problem $(\mathcal{S})$ reads: Find $\boldsymbol{d}^{\mathcal{S}} \in \mathcal{S}_{\boldsymbol{d}^{\mathcal{S}}}$ such that

$$(\mathcal{S}): \begin{cases} 0 = r^{\mathcal{S}} := & \left(\delta\boldsymbol{d}^{\mathcal{S}}, \varrho_0^{\mathcal{S}} \frac{\mathrm{d}^2}{\mathrm{d}t^2}\boldsymbol{d}^{\mathcal{S}}\right)_{\Omega_0^{\mathcal{S}}} + \left(\boldsymbol{\nabla}_0\, \delta\boldsymbol{d}^{\mathcal{S}}, \boldsymbol{F}^{\mathcal{S}}\boldsymbol{S}^{\mathcal{S}}\right)_{\Omega_0^{\mathcal{S}}} \\ & - \left(\delta\boldsymbol{d}^{\mathcal{S}}, \boldsymbol{T}_{\mathrm{N}}^{\mathcal{S}}\right)_{\Gamma_{\mathrm{N}}^{\mathcal{S}}} - \left(\delta\boldsymbol{d}^{\mathcal{S}}, \boldsymbol{b}_0^{\mathcal{S}}\right)_{\Omega_0^{\mathcal{S}}}, \end{cases} \tag{3.5}$$

for all $\delta\boldsymbol{d}^{\mathcal{S}} \in \mathcal{T}_{\boldsymbol{d}^{\mathcal{S}}}$. $r^{\mathcal{S}}$ denotes the weak residual of the structure problem.

Remark. *The ALE problem is treated as a stationary pseudo-structure, cf. Section 2.2.1.1. Thus, the weak formulation $(\mathcal{G})$ and the weak residual $r^{\mathcal{G}}$ of the ALE problem read analog to the weak formulation $(\mathcal{S})$ and weak residual $r^{\mathcal{S}}$ of the structure problem, respectively.*

3.1.1.3 Scalar transport

The weak formulations of the fluid-scatra and structure-scatra problems are established from their strong formulations as described in Section 2.1.5.2. The solution spaces $\mathcal{S}_{c_i^{\mathcal{FS}}}$ and $\mathcal{S}_{c_i^{\mathcal{SS}}}$ and trial spaces $\mathcal{T}_{c_i^{\mathcal{FS}}}$ and $\mathcal{T}_{c_i^{\mathcal{SS}}}$ for the primary unknowns – all concentrations of the fluid-scatra problem $c_i^{\mathcal{FS}}$ and the structure-scatra problem $c_i^{\mathcal{SS}}$ $(i = 1, \dots, n_c)$ – read

$$\begin{aligned}
\mathcal{S}_{c_i^{\mathcal{FS}}} &= \left\{ c_i^{\mathcal{FS}} \in \mathcal{H}^1(\Omega_t^{\mathcal{FS}}) \;\middle|\; c_i^{\mathcal{FS}} = c_{i,\mathrm{D}}^{\mathcal{FS}} \text{ on } \Gamma_{\mathrm{D}}^{\mathcal{FS}} \right\}, \\
\mathcal{S}_{c_i^{\mathcal{SS}}} &= \left\{ c_i^{\mathcal{SS}} \in \mathcal{H}^1(\Omega_t^{\mathcal{SS}}) \;\middle|\; c_i^{\mathcal{SS}} = c_{i,\mathrm{D}}^{\mathcal{SS}} \text{ on } \Gamma_{\mathrm{D}}^{\mathcal{SS}} \right\}, \\
\mathcal{T}_{c_i^{\mathcal{FS}}} &= \left\{ \delta c_i^{\mathcal{FS}} \in \mathcal{H}^1(\Omega_t^{\mathcal{FS}}) \;\middle|\; c_i^{\mathcal{FS}} = 0 \text{ on } \Gamma_{\mathrm{D}}^{\mathcal{FS}} \right\}, \\
\mathcal{T}_{c_i^{\mathcal{SS}}} &= \left\{ \delta c_i^{\mathcal{SS}} \in \mathcal{H}^1(\Omega_t^{\mathcal{SS}}) \;\middle|\; c_i^{\mathcal{SS}} = 0 \text{ on } \Gamma_{\mathrm{D}}^{\mathcal{SS}} \right\}.
\end{aligned} \tag{3.6}$$

The weak formulation of the fluid-scatra problem is derived by multiplying Equation (2.46) with the respective testing functions $\delta c_i^{\mathcal{FS}} \in \mathcal{T}_{c_i^{\mathcal{FS}}}$, their integration over the fluid-scatra domain $\Omega^{\mathcal{FS}}(t)$ and taking their sum. An integration by parts of the advective and diffusive terms is performed such that *Neumann* boundary conditions can be employed as natural boundary conditions. The weak formulation of the fluid-scatra problem $(\mathcal{FS})$ reads: Find $c_i^{\mathcal{FS}} \in \mathcal{S}_{c_i^{\mathcal{FS}}}$ $(i = 1, \dots, n_c)$ such that

$$(\mathcal{FS}) : \begin{cases} 0 = r^{\mathcal{FS}} := \sum_{i=1}^{n_c} \Big(\Big(\delta c_i^{\mathcal{FS}}, \frac{\partial}{\partial t} c_i^{\mathcal{FS}}\big|_{\boldsymbol{\chi}} \Big)_{\Omega^{\mathcal{FS}}(t)} + \big(\delta c_i^{\mathcal{FS}}, \big(\boldsymbol{u}^{\mathcal{F}} - \boldsymbol{u}^{\mathcal{G}} \big) \cdot \nabla c_i^{\mathcal{FS}} \big)_{\Omega^{\mathcal{FS}}(t)} \\ \qquad + \big(\nabla \delta c_i^{\mathcal{FS}}, D_i^{\mathcal{FS}} \nabla c_i^{\mathcal{FS}} \big)_{\Omega^{\mathcal{FS}}(t)} + \big(\delta c_i^{\mathcal{FS}}, q_{\mathrm{N}}^{\mathcal{FS}} \big)_{\Gamma_{\mathrm{N}}^{\mathcal{FS}}(t)} \Big), \end{cases} \tag{3.7}$$

for all $\delta c_i^{\mathcal{FS}} \in \mathcal{T}_{c_i^{\mathcal{FS}}}$.

The weak formulation of the structure-scatra problem is derived by multiplying Equation (2.49) with the respective testing functions $\delta c_i^{\mathcal{SS}} \in \mathcal{T}_{c_i^{\mathcal{SS}}}$, their integration over the structure-scatra domain $\Omega^{\mathcal{SS}}(t)$ and taking their sum. An integration by parts of the diffusive terms is performed such that *Neumann* boundary conditions can be employed as natural boundary conditions. The weak formulation of the structure-scatra problem $(\mathcal{SS})$ reads: Find $c_i^{\mathcal{SS}} \in \mathcal{S}_{c_i^{\mathcal{SS}}}$, $i = 1, \dots, n_c$ such that

$$(\mathcal{SS}) : \begin{cases} 0 = r^{\mathcal{SS}} := \sum_{i=1}^{n_c} \Big(\Big(\delta c_i^{\mathcal{SS}}, \frac{\partial}{\partial t} c_i^{\mathcal{SS}}\big|_{\boldsymbol{\chi}} \Big)_{\Omega^{\mathcal{SS}}(t)} + \big(\delta c_i^{\mathcal{SS}}, c_i^{\mathcal{SS}} \boldsymbol{\nabla} \cdot \boldsymbol{u}^{\mathcal{S}} \big)_{\Omega^{\mathcal{SS}}(t)} \\ \qquad + \big(\nabla \delta c_i^{\mathcal{SS}}, D_i^{\mathcal{SS}} \nabla c_i^{\mathcal{SS}} \big)_{\Omega^{\mathcal{SS}}(t)} + \big(\delta c_i^{\mathcal{SS}}, q_{\mathrm{N}}^{\mathcal{SS}} \big)_{\Gamma_{\mathrm{N}}^{\mathcal{SS}}(t)} \\ \qquad - \big(\delta c_i^{\mathcal{SS}}, \varkappa_i^{\mathcal{SS}}(\boldsymbol{c}^{\mathcal{SS}}) \big)_{\Omega^{\mathcal{SS}}(t)} \Big), \end{cases} \tag{3.8}$$

for all $\delta c_i^{\mathcal{SS}} \in \mathcal{T}_{c_i^{\mathcal{SS}}}$. $r^{\mathcal{FS}}$ and $r^{\mathcal{SS}}$ denote the weak residuals of the fluid-scatra and structure scalar problems, respectively.

Remark. *Even though the strong formulations of the fluid-scatra and structure-scatra problems seem quite different, their weak formulations differ only in the advective and reactive term and the choice of the ALE observer. Hence, both formulations can be solved within the same computational scalar transport framework.*

3.1.1.4 Porous medium fluid and scalar transport

The weak formulations of the poro-scatra and poro-scatra problems are established from their strong formulations as described in Section 2.1.6.2. The solution spaces $\mathcal{S}_{p^{\mathcal{PF}}}$ and $\mathcal{S}_{c_i^{\mathcal{PS}}}$ and trial spaces $\mathcal{T}_{p^{\mathcal{PF}}}$ and $\mathcal{T}_{c_i^{\mathcal{PS}}}$ for their primary unknowns – the poro-fluid pressure $p^{\mathcal{PF}}$ and poro-scatra concentrations $c_i^{\mathcal{PS}}$ $(i = 1, \dots, n_c)$ – read

$$\begin{aligned}
\mathcal{S}_{p^{\mathcal{PF}}} &= \left\{ p^{\mathcal{PF}} \in \mathcal{H}^1(\Omega_t^{\mathcal{PF}}) \;\middle|\; p^{\mathcal{PF}} = p_{\mathrm{D}}^{\mathcal{PF}} \text{ on } \Gamma_{\mathrm{D}}^{\mathcal{PF}} \right\}, \\
\mathcal{S}_{c_i^{\mathcal{PS}}} &= \left\{ c_i^{\mathcal{PS}} \in \mathcal{H}^1(\Omega_t^{\mathcal{PS}}) \;\middle|\; c_i^{\mathcal{PS}} = c_{i,\mathrm{D}}^{\mathcal{PS}} \text{ on } \Gamma_{\mathrm{D}}^{\mathcal{PS}} \right\}, \\
\mathcal{T}_{p^{\mathcal{PF}}} &= \left\{ \delta p^{\mathcal{PF}} \in \mathcal{H}^1(\Omega_t^{\mathcal{PF}}) \;\middle|\; p^{\mathcal{PF}} = 0 \text{ on } \Gamma_{\mathrm{D}}^{\mathcal{PF}} \right\}, \\
\mathcal{T}_{c_i^{\mathcal{PS}}} &= \left\{ \delta c_i^{\mathcal{PS}} \in \mathcal{H}^1(\Omega_t^{\mathcal{PS}}) \;\middle|\; c_i^{\mathcal{PS}} = 0 \text{ on } \Gamma_{\mathrm{D}}^{\mathcal{PS}} \right\}.
\end{aligned} \tag{3.9}$$

The weak formulation of the poro-fluid problem is derived by multiplying Equation (2.55) with a testing functions $\delta p^{\mathcal{PF}} \in \mathcal{T}_{p^{\mathcal{PF}}}$, their integration over the poro-fluid domain $\Omega^{\mathcal{PF}}$ and an integration by parts such that *Neumann* boundary conditions can be employed as natural boundary conditions. The weak formulation of the poro-fluid $(\mathcal{PF})$ problem reads: Find $p^{\mathcal{PF}} \in \mathcal{S}_{p^{\mathcal{PF}}}$ such that

$$(\mathcal{PF}) : \begin{cases} 0 = r^{\mathcal{PF}} := & \left(\nabla \delta p^{\mathcal{PF}}, \frac{K^{\mathcal{PF}}}{\phi \mu^{\mathcal{PF}}} \nabla p^{\mathcal{PF}} \right)_{\Omega^{\mathcal{PF}}} + \left(\delta p^{\mathcal{PF}}, q_{\mathrm{N}}^{\mathcal{PF}} \right)_{\Gamma_{\mathrm{N}}^{\mathcal{PF}}} \\ & + \left(\delta p^{\mathcal{PF}}, \frac{K^{\mathcal{PF}}}{\phi \mu^{\mathcal{PF}}} \boldsymbol{\nabla} \cdot \boldsymbol{b}^{\mathcal{PF}} \right)_{\Omega^{\mathcal{PF}}}, \end{cases} \tag{3.10}$$

for all $\delta p^{\mathcal{PF}} \in \mathcal{T}_{p^{\mathcal{PF}}}$.

The weak formulation of the poro-scatra problem is derived by multiplying Equation (2.59) with the respective testing functions $\delta c_i^{\mathcal{PS}} \in \mathcal{T}_{c_i^{\mathcal{PS}}}$, their integration over the poro-scatra domain $\Omega^{\mathcal{PS}}$ and taking their sum. An integration by parts of the advective and diffusive terms is performed such that *Neumann* boundary conditions can be employed as natural boundary conditions. The weak formulation of the poro-scatra problem $(\mathcal{PS})$ reads: Find $c_i^{\mathcal{PS}} \in \mathcal{S}_{c_i^{\mathcal{PS}}}$ $(i = 1, \dots, n_c)$ such that

$$(\mathcal{PS}) : \begin{cases} 0 = r^{\mathcal{PS}} := \sum_{i=1}^{n_c} \Big(& \left(\delta c_i^{\mathcal{PS}}, \frac{\partial}{\partial t} c_i^{\mathcal{PS}} \right)_{\Omega^{\mathcal{PS}}} - \left(\nabla \delta c_i^{\mathcal{PS}}, K_i^{\mathcal{PS}} c_i^{\mathcal{PS}} \boldsymbol{u}^{\mathcal{PF}} \right)_{\Omega^{\mathcal{PS}}} \\ & + \left(\nabla \delta c_i^{\mathcal{PS}}, D_{\mathrm{Eff},i}^{\mathcal{PS}} \nabla c_i^{\mathcal{PS}} \right)_{\Omega^{\mathcal{PS}}} + \left(\delta c_i^{\mathcal{PS}}, q_{\mathrm{N}}^{\mathcal{PS}} \right)_{\Gamma_{\mathrm{N}}^{\mathcal{PS}}} \\ & - \left(\delta c_i^{\mathcal{PS}}, \varkappa_i^{\mathcal{PS}} \left(\boldsymbol{c}^{\mathcal{PS}} \right) \right)_{\Omega^{\mathcal{PS}}} \Big), \end{cases} \tag{3.11}$$

for all $\delta c_i^{\mathcal{PS}} \in \mathcal{T}_{c_i^{\mathcal{PS}}}$. $r^{\mathcal{PF}}$ and $r^{\mathcal{PS}}$ denote the weak residuals of the poro-fluid and poro-scatra problems, respectively.

Remark. *The weak formulation of* Darcy*'s law $(\mathcal{PF})$ can be seen as a special case of the weak formulation of the porous medium scalar transport problem $(\mathcal{PS})$ by considering the poro-fluid pressure $p^{\mathcal{PF}}$ as a stationary, non-advective, non-reactive "concentration $p^{\mathcal{PS}}$" with effective diffusion coefficient $D_{\mathrm{Eff},p} = \frac{K^{\mathcal{PF}}}{\phi \mu^{\mathcal{PF}}}$. Doing so, the advection of the other concentrations with the poro-fluid can interestingly be interpreted as chemotaxation, where $\nabla p^{\mathcal{PF}}$ is the chemoattractant. Hence, the presented poro-fluid problem can be solved within a scalar transport framework.*

3.1.2 Spatial discretization

The weak formulations of the single-field problems $(\mathcal{F})$, $(\mathcal{S})$, $(\mathcal{G})$, $(\mathcal{FS})$, $(\mathcal{SS})$, $(\mathcal{PF})$ and $(\mathcal{PS})$ are spatially discretized by means of the *Galerkin finite element method* with an *equal-order interpolation* of all primary unknowns. As the finite element formulations of all single-field problems read similar, the finite element method is presented in an abstract manner. Spatially discrete quantities are indicated by the subscript $(\bullet)_{\mathrm{h}}$

Following the standard procedure of the finite element method, the domain $\Omega^{(\bullet)}$ of each of the single-field problems is approximated by $n_{\mathrm{ele}}^{(\bullet)}$ disjunct *finite elements* $\Omega_{\mathrm{h},e}^{(\bullet)}$, i.e.

$$\Omega^{(\bullet)} \approx \bigcup_{e=1}^{n_{\mathrm{ele}}^{(\bullet)}} \Omega_{\mathrm{h},e}^{(\bullet)} \,, \tag{3.12}$$

which are spanned by $n_{\mathrm{node}}^{(\bullet)}$ distinct *nodes*. Trilinear *Lagrange* polynomials $N_k^{(\bullet)}$ over the $n_{\mathrm{node}}^{(\bullet)}$ element nodes are used as *ansatz functions* for the unknown primary variables $\boldsymbol{y} \in \{\boldsymbol{u}^{\mathcal{F}}; p^{\mathcal{F}}; \boldsymbol{d}^{\mathcal{S}}; \boldsymbol{d}^{\mathcal{G}}; \boldsymbol{c}^{\mathcal{FS}}; \boldsymbol{c}^{\mathcal{SS}}; \boldsymbol{u}^{\mathcal{PF}}; \boldsymbol{c}^{\mathcal{PS}}\}$ of the single-field problems, i.e.

$$\boldsymbol{y}(t,\cdot) \approx \sum_{k=1}^{n_{\mathrm{node}}^{(\bullet)}} \boldsymbol{y}_{\mathrm{h},k}(t) N_k^{(\bullet)}(\cdot), \tag{3.13}$$

where $\boldsymbol{y}_{\mathrm{h},k}$ denotes the k-th entry of the vectors $\boldsymbol{y}_{\mathrm{h}}$ of *nodal ansatz coefficients*. Using the $n_{\mathrm{node}}^{(\bullet)}$ *Lagrange* polynomials $N_k^{(\bullet)}$ also as *test functions* yields the spatially discrete but temporal continuous, semi-discrete problem for the continuous ansatz coefficients $\boldsymbol{y}_{\mathrm{h}}(t)$, which can be written as an *initial value problem* (IVP) of the form

$$(\mathrm{IVP}): \begin{cases} \frac{\mathrm{d}}{\mathrm{d}t}\boldsymbol{y}_{\mathrm{h}}(t) - \boldsymbol{f}_{\mathrm{h}}(t, \boldsymbol{y}_{\mathrm{h}}(t)) = \boldsymbol{0}, \\ \boldsymbol{y}_{\mathrm{h}}(0) = \boldsymbol{y}_{\mathrm{h},0}. \end{cases} \tag{3.14}$$

Here, the *initial condition* is denoted by $\boldsymbol{y}_{\mathrm{h},0}$ and the nonlinear function $\boldsymbol{f}_{\mathrm{h}}$ corresponds to the spatially discrete version of the weak formulation of the problem under consideration. The integrals in the spatially discrete problem are numerically integrated by the application of the *Gauß quadrature rule*.

To overcome numerical instabilities arising from the chosen equal-order finite element approximation of the fluid problem, *residual-based stabilizations* are applied. Namely, the *Streamline-Upwind Petrov-Galerkin* (SUPG) [67], *Pressure-Stabilized Petrov-Galerkin* (PSPG) [130] and a *grad-div* stabilization [57] are used. The stabilization parameters of the fluid problem are chosen according to [10]. The advection dominated fluid-scatra problem is stabilized using the *Galerkin least-squares* (GLS) method [67]. Additionally, the $YZ\beta$ discontinuity-capturing method is applied [12, 145] to also stabilize steep concentration gradients occurring close to no-slip boundaries of the fluid [161]. The stabilization parameter of the fluid-scatra problem is chosen according to [47]. Further, additional backflow stabilizations on the *Neumann* boundaries $\Gamma_{\mathrm{N}}^{\mathcal{F}}$ and $\Gamma_{\mathrm{N}}^{\mathcal{FS}}$ of the fluid and fluid-scatra problems are applied to deal with spontaneous backflows through *Neumann* boundaries [106].

Remark. *The element nodes that belong to a Dirichtlet boundary* $\Gamma_{\mathrm{D}}^{(\bullet)}$ *would have to be excluded from the sum and explicitly dealt with in the approximation given by Equation* (3.13)*. For details on the rigorous inclusion of* Dirichlet *boundary condition in the finite element method, see the textbooks by* Donea *and* Huerta *[67] or* Hughes *[129].*

3.1.3 Temporal discretization

The temporal discretization of the initial value problem (IVP) is done by the one-step-θ scheme which is a two-stage implicit Runge-Kutta method. The one-step-θ scheme results in an approximating sequence $\{\boldsymbol{y}_{\mathrm{h}}^n\}_{n=0,1,\dots,n_T}$ to the solution $\boldsymbol{y}_{\mathrm{h}}(t)$ of the time continuous initial value problem (IVP) by successively finding the root of the nonlinear *discrete residual* $\boldsymbol{r}_{\mathrm{h}}^{n+1}$ of the fluid:

$$\boldsymbol{r}_{\mathrm{h}}^{n+1}(t^{n+1}, \boldsymbol{y}_{\mathrm{h}}^{n+1}) := \boldsymbol{y}_{\mathrm{h}}^{n+1} - \boldsymbol{y}_{\mathrm{h}}^{n} - \Delta t \left(\theta \boldsymbol{f}_{\mathrm{h}}(t^{n+1}, \boldsymbol{y}_{\mathrm{h}}^{n+1}) + (1-\theta)\boldsymbol{f}_{\mathrm{h}}(t^{n}, \boldsymbol{y}_{\mathrm{h}}^{n})\right) = 0, \tag{3.15}$$

for each $n = 0, 1, \dots, n_T$, where $t^n = n\Delta t$ and $\boldsymbol{y}_{\mathrm{h}}^n = \boldsymbol{y}_{\mathrm{h}}(t^n)$. The (constant) *time step size* is denoted by Δt and n_T *time steps* are performed. If not stated otherwise, the *scheme coefficient* $\theta = \frac{1}{2}$ is used such that the utilized method is equivalent to the *Crank-Nicolson* scheme with a second-order accuracy. The one-step-θ scheme is implicit and therefore requires to use an appropriate method to solve Equation (3.15) for the unknowns $\boldsymbol{y}_{\mathrm{h}}^{n+1}$.

Remark. *A detailed review of Runge-Kutta methods and their analysis can be found in the textbooks by* Butcher *[28] or* Lambert *[162]. The one-step-*θ *scheme with* $\theta = \frac{1}{2}$ *is stable, introduces no damping and is of second-order accuracy. As the one-step-*θ *scheme is implicit, it is computationally expensive to solve for the unknowns* $\boldsymbol{y}_{\mathrm{h}}^{n+1}$*. However, compared to other implicit time integration schemes, the evaluation of the one-step-*θ *scheme is cheap, as it is a two-stage method requiring only a single evaluation of* $\boldsymbol{f}_{\mathrm{h}}$ *for each evaluation of the discrete residual* $\boldsymbol{r}_{\mathrm{h}}^{n+1}$ *when re-using the evaluation of* $\boldsymbol{f}_{\mathrm{h}}(t^n, \boldsymbol{y}_{\mathrm{h}}^n)$ *from the prior time step. Another suitable time integration scheme would be the* generalized-α *scheme which allows for a user specified damping of high-frequencies [44, 140].*

3.1.4 *Newton*'s method

To find the root $\boldsymbol{y}_{\mathrm{h}}^{n+1}$ of the nonlinear discrete residual $\boldsymbol{r}_{\mathrm{h}}^{n+1}$ given by Equation (3.15) the *Newton's method* is applied. Hence, the *linearized system*

$$\begin{aligned} &\frac{\partial}{\partial \boldsymbol{y}} \boldsymbol{r}_{\mathrm{h}}^{n+1}(t^{n+1}, \boldsymbol{y})\Big|_{\boldsymbol{y}=\boldsymbol{y}_{\mathrm{h},j}^{n+1}} \Delta \boldsymbol{y}_{\mathrm{h},j+1}^{n+1} = -\boldsymbol{r}_{\mathrm{h}}^{n+1}(t^{n+1}, \boldsymbol{y}_{\mathrm{h},j}^{n+1}) \\ \Rightarrow \left(\mathbf{1} - \Delta t\theta \boldsymbol{\nabla} \boldsymbol{f}_{\mathrm{h}}(t^{n+1}, \boldsymbol{y}_{\mathrm{h},j}^{n+1})\right) \Delta \boldsymbol{y}_{\mathrm{h},j+1}^{n+1} &= -\boldsymbol{y}_{\mathrm{h},j}^{n+1} + \boldsymbol{y}_{\mathrm{h}}^{n} + \Delta t\big(\theta \boldsymbol{f}_{\mathrm{h}}(t^{n+1}, \boldsymbol{y}_{\mathrm{h},j}^{n+1}) \\ &\qquad + (1-\theta)\boldsymbol{f}_{\mathrm{h}}(t^{n}, \boldsymbol{y}_{\mathrm{h}}^{n})\big) \end{aligned} \tag{3.16}$$

must be solved for the update increment $\Delta \boldsymbol{y}_{\mathrm{h},j+1}^{n+1}$ for each *Newton step* $j = 0, 1, \dots$, followed by the incremental update

$$\boldsymbol{y}_{\mathrm{h},j+1}^{n+1} = \boldsymbol{y}_{\mathrm{h},j}^{n+1} + \Delta \boldsymbol{y}_{\mathrm{h},j+1}^{n+1} \tag{3.17}$$

until a convergence criteria is matched. In this thesis, *Newton* iterations are stopped if the 2-norm of the discrete residual $\|\boldsymbol{r}_{\mathrm{h}}^{n+1}(t^{n+1}, \boldsymbol{y}_{\mathrm{h},j}^{n+1})\|$ and the 2-norm of the increment vector $\|\Delta\boldsymbol{y}_{\mathrm{h},j+1}^{n+1}\|$ divided by the root of the number of degrees of freedom n_{DOF} are below given error tolerances.

Solving Equation (3.16) for each *Newton* step i and each time step n requires an efficient method for inverting the sparse, but $n_{\mathrm{DOF}} \times n_{\mathrm{DOF}}$-dimensional matrix on the left-hand side. Therefore, a parallel preconditioned *generalized minimal residual* method [234] with field-specific algebraic multigrid preconditioning is used [235, 270]. An introduction into algebraic multigrid methods can be found in the textbook by *Briggs et al.* [21] or in the theses by *Mayr* [192] or *Wiesner* [285].

3.2 Multiphysics problems

Multiphysics problems combine single-field subproblems by appropriate coupling conditions like those presented in Section 2.2. Hence, the weak formulations of the single-field subproblems and their numerical treatment as presented in the previous Section 3.1 can be reused when they are enriched by the respective coupling conditions. For simplicity, it is assumed that surface and volume coupled problems have matching grids such that the exchange of quantities between the subproblems it straightforward. However, this assumption is not mandatory and can be dropped, e.g., by using appropriate interpolation or projection methods, such as *collocation* or *mortar* methods, see [15, 74, 150, 153, 288] and references therein.

To computationally solve multiphysics (and multi-field) problems, there are in general three solution approaches – *field elimination*, *monolithic* and *partitioned* approaches [278]. In a *field elimination* approach a continuous or discretized subproblem is analytically solved for its unknowns and its solution plugged into the coupling conditions. As a consequence, the subproblem is eliminated and the size of the multiphysics problems is reduced. However, this approach is generally restricted to simple subproblems where an analytical relation of the unknowns with respect to the other subproblems can actually be derived.

A *monolithic* approach corresponds to the idea of applying *Newton*'s method (cf. Section 3.1.4) to the *full* multiphysics problem. Hence, the individual single-field subproblems as well as their couplings are solved simultaneously which in general leads to a fast converging and robust approach. In practice, however, a monolithic approach must not always be the method of choice to solve a multiphysics problem at hand. A monolithic approach requires to often solve the (linear) *monolithic system*, i.e., the linearized system given by Equation (3.16) of the discretized full multiphysics problems. The associated *monolithic system matrix* has a dimension corresponding to at least the added up dimensions of the subproblems. To invert such a potentially high-dimensional matrix, algebraic multigrid-preconditioned generalized minimal residual methods as for the single-field problems can be employed. However, monolithic system matrixes which result from multiphysics problems often have challenging block-structures such that problem-specific algebraic multigrid block preconditioners are usually required [95, 273]. Therefore, a monolithic approach in general involves sophisticate methods to solve the monolithic system and often comes along with a challenging implementation.

Partitioned approaches exploit the idea to solve multiphysics problems by a fixed-point iteration of the subproblems. The most straightforward method of doing so is by an *iteratively staggered* partitioned approach where each subproblem is successively solved and the other subproblems updated until all couplings between the subproblems are resolved. Such an iteratively staggered approach can be seen as a block *Jacobi*-like method applied to the monolithic system with zero off-diagonal blocks. Thus, it is possible to fasten the convergence of iteratively staggered partitioned approaches by utilizing relaxation methods, such as the *Aitken* Δ^2 relaxation [137, 157]. Nevertheless, relaxed iteratively staggered approaches are usually outperformed by monolithic approaches and may also come along with stability issues, such as the well studied added-mass effect of FSI problems [32, 86, 87]. However, these drawbacks disappear in the case of *one-way* or "loosely" coupled subproblems which are adequately addressed by a *sequentially staggered* partitioned scheme. In a sequentially staggered scheme the subproblems are solved (and the other subproblems updated) in a suitable order which respects their couplings. The strength of partitioned approaches relies on their simplicity. They are relatively easy to implement as only the coupling variables must be transferred between the (completely reusable) implementations of the single-field subproblems. Further, smaller (but more) linear systems must be solved compared to a monolithic approach. An illustration of the presented solution approaches for multiphysics problems is given in Figure 3.1.

In the case of large multiphysics problems, such as FSSTI or PFSTI problems (Sections 2.2.2 and 2.2.3), all three approaches can be combined in a more or less arbitrary manner since each subset of subproblems can be solved again by field elimination, monolithic or partitioned approaches. An appropriate choice for the overall solving approach depends on the specific multiphysics problem and is referred to as *solution strategy*.

In this section, the weak formulations and solution strategies for the multiphysics problems presented in Section 2.2 are given. The numerical treatment of FSI problems is well studied and the reader is referred to the textbooks by *Bazilevs et al.* [13] or *Formaggia et al.* [85] or the theses by *Förster* [86], *Küttler* [158], *Mayr* [192] or *Wall* [278] for details. Further details on FSSTI problems can be found in the publications by *Thon et al.* [266] or *Yoshihara et al.* [297].

3.2.1 Fluid-structure interaction

The numerical treatment of FSI problems as introduced in Section 2.2.1 is well studied and is only briefly summarized in this section.

3.2.1.1 Weak formulation

The weak formulation of the FSI problem is established from the weak formulations $(\mathcal{F})$, $(\mathcal{S})$ and $(\mathcal{G})$ of the fluid, structure and ALE problems (Sections 3.1.1.1 and 3.1.1.2) enriched by the FSI coupling conditions as described in Section 2.2.1.2. The kinematic continuity given by Equation (2.64) is enforced weakly via a *Lagrange multiplier field* $\boldsymbol{\Lambda}$ which allows for an interpretation of the *Lagrange* multiplier field as interface tractions. In this thesis, the arbitrary choice of the *Lagrange* multiplier field $\boldsymbol{\Lambda}$ as the interface traction acting onto the structure side $\Gamma_{\mathrm{I}}^{\mathcal{S}}$

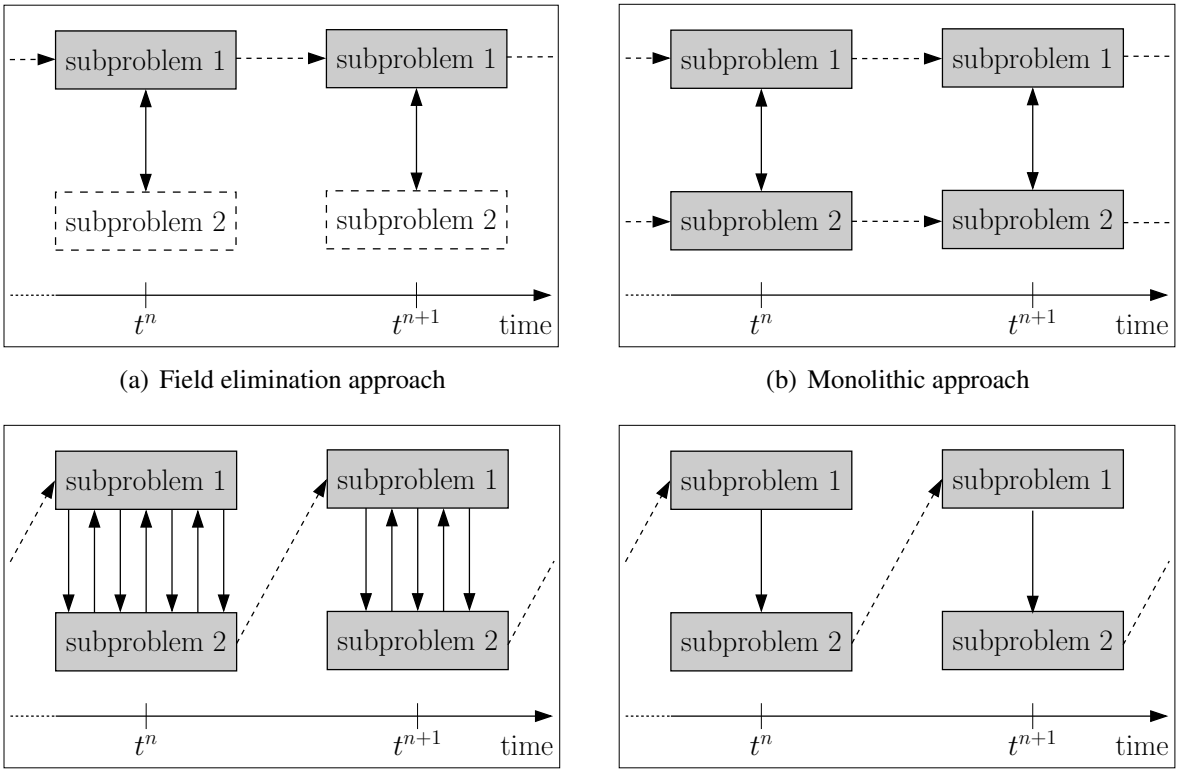

(a) Field elimination approach

(b) Monolithic approach

(c) Iteratively staggered partitioned approach

(d) Sequentially staggered partitioned approach

Figure 3.1 Solution approaches for a multiphysics problem coupling two subproblems 1 and 2 (gray boxes). The arrows indicate the order of the solving of the subproblems, whereby double arrows indicate that the subproblems are solved simultaneously. Dotted arrows indicate a proceeding to the next time step.

of the interaction boundary is made. The solution and trial spaces $\mathcal{S}_{\boldsymbol{\Lambda}}$ and $\mathcal{T}_{\boldsymbol{\Lambda}}$ of the *Lagrange* multiplier field $\boldsymbol{\Lambda}$ are given by

$$\begin{aligned} \mathcal{S}_{\boldsymbol{\Lambda}} &= \left\{ \boldsymbol{\Lambda} \in \left(\mathcal{H}^{-\frac{1}{2}}(\Gamma_{\mathrm{I}}) \right)^3 \right\}, \\ \mathcal{T}_{\boldsymbol{\Lambda}} &= \left\{ \delta\boldsymbol{\Lambda} \in \left(\mathcal{H}^{-\frac{1}{2}}(\Gamma_{\mathrm{I}}) \right)^3 \right\}. \end{aligned} \tag{3.18}$$

The overall weak formulation of the FSI problem $(\mathcal{FSI})$ reads: Find $\boldsymbol{u}^{\mathcal{F}} \in \mathcal{S}_{\boldsymbol{u}^{\mathcal{F}}}, p^{\mathcal{F}} \in \mathcal{S}_{p^{\mathcal{F}}}$, $\boldsymbol{d}^{\mathcal{S}} \in \mathcal{S}_{\boldsymbol{d}^{\mathcal{S}}}, \boldsymbol{d}^{\mathcal{G}} \in \mathcal{S}_{\boldsymbol{d}^{\mathcal{G}}}$ and $\boldsymbol{\Lambda} \in \mathcal{S}_{\boldsymbol{\Lambda}}$ such that

$$(\mathcal{FSI}) : \begin{cases} 0 = & r^{\mathcal{FSI},\mathcal{S}} := r^{\mathcal{S}} - \left(\delta\boldsymbol{d}^{\mathcal{S}}, \boldsymbol{\Lambda} \right)_{\Gamma_{\mathrm{I}}^{\mathcal{S}}}, \\ 0 = & r^{\mathcal{FSI},\mathcal{F}} := r^{\mathcal{F}} + \left(\delta\boldsymbol{u}^{\mathcal{F}}, \boldsymbol{\Lambda} \right)_{\Gamma_{\mathrm{I}}^{\mathcal{F}}}, \\ 0 = & r^{\mathcal{FSI},\mathcal{G}} := r^{\mathcal{G}}, \\ 0 = & r^{\mathrm{Coupl}} := \left(\delta\boldsymbol{\Lambda}, \boldsymbol{d}^{\mathcal{S}} - \boldsymbol{d}^{\mathcal{G}} \right)_{\Gamma_{\mathrm{I}}^{\mathcal{S}}}, \end{cases} \tag{3.19}$$

for all $\delta\boldsymbol{u}^{\mathcal{F}} \in \mathcal{T}_{\boldsymbol{u}^{\mathcal{F}}}, \delta p^{\mathcal{F}} \in \mathcal{T}_{p^{\mathcal{F}}}, \delta\boldsymbol{d}^{\mathcal{S}} \in \mathcal{T}_{\boldsymbol{d}^{\mathcal{S}}}, \delta\boldsymbol{d}^{\mathcal{G}} \in \mathcal{T}_{\boldsymbol{d}^{\mathcal{G}}}$ and $\delta\boldsymbol{\Lambda} \in \mathcal{T}_{\boldsymbol{\Lambda}}$. $r^{\mathcal{FSI},\mathcal{F}}, r^{\mathcal{FSI},\mathcal{S}}$ and $r^{\mathcal{FSI},\mathcal{G}}$ denote the weak residuals of the fluid, structure and ALE subproblems of the FSI problem, respec-

tively. The vector of weak residuals of the FSI problem is denoted by $\boldsymbol{r}^{\mathcal{FSI}} := \left[r^{\mathcal{FSI},\mathcal{S}}, r^{\mathcal{FSI},\mathcal{F}}, r^{\mathcal{FSI},\mathcal{G}}, r^{\mathrm{Coupl}}\right]^T$.

3.2.1.2 Solution strategy

The numerical treatment of FSI problems by partitioned approaches is well studied. Partitioned approaches can lead to inherent instabilities, such as the *added-mass effect* in case of unfavorable density ratios [32, 87, 97] or the *incompressibility dilemma* in case of fully enclosed incompressible fluids [160].

A peculiarity in cardiovascular mechanics is the similar density of fluid $\varrho^{\mathcal{F}}$ and structure $\varrho^{\mathcal{S}}$ which, combined with the incompressibility of the fluid, leads to an increased computational effort of partitioned approaches due to the added-mass effect [87]. Therefore, cardiovascular problems are efficiently addressed by monolithic approaches [114, 157]. In this thesis, the monolithic FSI formulation as described in detail in the publication by *Mayr* [193] is employed.

Monolithic FSI

Analog to the single-field problems, the weak formulation $(\mathcal{FSI})$ of the FSI problem is spatially and temporally discretized in terms of the finite element method and the one-step-θ scheme, respectively. Applying *Newton*'s method (Section 3.1.4) to the discretized FSI problem, the monolithic FSI problem to solve for the incremental structure displacements $\Delta\boldsymbol{d}_{\mathrm{h}}^{\mathcal{S}}$, fluid velocities $\Delta\boldsymbol{u}_{\mathrm{h}}^{\mathcal{F}}$, ALE displacements $\Delta\boldsymbol{d}_{\mathrm{h}}^{\mathcal{G}}$ and *Lagrange* multipliers $\Delta\boldsymbol{\Lambda}_{\mathrm{h}}$ reads

$$\begin{pmatrix} \frac{\partial}{\partial \boldsymbol{d}_{\mathrm{h}}^{\mathcal{S}}}\boldsymbol{r}_{\mathrm{h}}^{\mathcal{FSI},\mathcal{S}} & \boldsymbol{0} & \boldsymbol{0} & \frac{\partial}{\partial \boldsymbol{\Lambda}_{\mathrm{h}}}\boldsymbol{r}_{\mathrm{h}}^{\mathcal{FSI},\mathcal{S}} \\ \boldsymbol{0} & \frac{\partial}{\partial \boldsymbol{u}_{\mathrm{h}}^{\mathcal{F}}}\boldsymbol{r}_{\mathrm{h}}^{\mathcal{FSI},\mathcal{F}} & \boldsymbol{0} & \frac{\partial}{\partial \boldsymbol{\Lambda}_{\mathrm{h}}}\boldsymbol{r}_{\mathrm{h}}^{\mathcal{FSI},\mathcal{F}} \\ \boldsymbol{0} & \boldsymbol{0} & \frac{\partial}{\partial \boldsymbol{d}_{\mathrm{h}}^{\mathcal{G}}}\boldsymbol{r}_{\mathrm{h}}^{\mathcal{FSI},\mathcal{G}} & \boldsymbol{0} \\ \frac{\partial}{\partial \boldsymbol{d}_{\mathrm{h}}^{\mathcal{S}}}\boldsymbol{r}_{\mathrm{h}}^{\mathrm{Coupl}} & \boldsymbol{0} & \frac{\partial}{\partial \boldsymbol{d}_{\mathrm{h}}^{\mathcal{G}}}\boldsymbol{r}_{\mathrm{h}}^{\mathrm{Coupl}} & \boldsymbol{0} \end{pmatrix}_j^{n+1} \begin{pmatrix} \Delta\boldsymbol{d}_{\mathrm{h}}^{\mathcal{S}} \\ \Delta\boldsymbol{u}_{\mathrm{h}}^{\mathcal{F}} \\ \Delta\boldsymbol{d}_{\mathrm{h}}^{\mathcal{G}} \\ \Delta\boldsymbol{\Lambda}_{\mathrm{h}} \end{pmatrix}_{j+1}^{n+1} = - \begin{pmatrix} \boldsymbol{r}_{\mathrm{h}}^{\mathcal{FSI},\mathcal{S}} \\ \boldsymbol{r}_{\mathrm{h}}^{\mathcal{FSI},\mathcal{F}} \\ \boldsymbol{r}_{\mathrm{h}}^{\mathcal{FSI},\mathcal{G}} \\ \boldsymbol{r}_{\mathrm{h}}^{\mathrm{Coupl}} \end{pmatrix}_j^{n+1}, \tag{3.20}$$

where n and j denote the time step and *Newton* step, respectively. To ease the notation the fluid pressure was merged together with the fluid velocities. A structure-handled monolithic approach is utilized where the nodal unknowns of the fluid interaction boundary $\Gamma_{\mathrm{I}}^{\mathcal{F}}$ are condensed from the monolithic system (3.20) [192]. The resulting monolithic system is solved by a preconditioned generalized minimal residual method [234] with a FSI-specific block preconditioning based on algebraic multigrid established by *Gee et al.* [95].

3.2.2 Fluid-structure-scalar transport interaction

The numerical treatment of FSSTI problems as introduced in Section 2.2.2 is given in this section.

3.2.2.1 Weak formulation

The weak formulation of the FSSTI problem is established from the weak formulations $(\mathcal{FSI})$, $(\mathcal{FS})$ and $(\mathcal{SS})$ of the FSI, fluid-scatra and structure scalar problems (Sections 3.2.1.1 and 3.1.1.3) enriched by the S2I couplings as introduced in Section 2.2.2.2. The overall weak formulation $(\mathcal{FSSTI})$ of the FSSTI problem reads: Find $\boldsymbol{u}^{\mathcal{F}} \in \mathcal{S}_{\boldsymbol{u}^{\mathcal{F}}}, p^{\mathcal{F}} \in \mathcal{S}_{p^{\mathcal{F}}}, \boldsymbol{d}^{\mathcal{S}} \in \mathcal{S}_{\boldsymbol{d}^{\mathcal{S}}}, \boldsymbol{d}^{\mathcal{G}} \in \mathcal{S}_{\boldsymbol{d}^{\mathcal{G}}}$, $\boldsymbol{\Lambda} \in \mathcal{S}_{\boldsymbol{\Lambda}}$ and $c_i^{\mathcal{FS}} \in \mathcal{S}_{c_i^{\mathcal{FS}}}, c_i^{\mathcal{SS}} \in \mathcal{S}_{c_i^{\mathcal{SS}}}$ $(i = 1, \ldots, n_c)$ such that

$$(\mathcal{FSSTI}) : \begin{cases} \boldsymbol{0} & = \boldsymbol{r}^{\mathcal{FSI}}(\boldsymbol{c}^{\mathcal{SS}}), \\ 0 & = r^{\mathcal{S2I},\mathcal{FS}} := r^{\mathcal{FS}} - \sum\limits_{i=1}^{n_c} \left(\delta c_i^{\mathcal{FS}}, J_{\mathrm{Sol}}(c_i^{\mathcal{FS}}, c_i^{\mathcal{SS}})\right)_{\Gamma_{\mathrm{I}}^{\mathcal{FS}}}, \\ 0 & = r^{\mathcal{S2I},\mathcal{SS}} := r^{\mathcal{SS}} + \sum\limits_{i=1}^{n_c} \left(\delta c_i^{\mathcal{SS}}, J_{\mathrm{Sol},i}(c_i^{\mathcal{FS}}, c_i^{\mathcal{SS}})\right)_{\Gamma_{\mathrm{I}}^{\mathcal{SS}}}, \end{cases} \tag{3.21}$$

for all $\delta\boldsymbol{u}^{\mathcal{F}} \in \mathcal{T}_{\boldsymbol{u}^{\mathcal{F}}}, \delta p^{\mathcal{F}} \in \mathcal{T}_{p^{\mathcal{F}}}, \delta\boldsymbol{d}^{\mathcal{S}} \in \mathcal{T}_{\boldsymbol{d}^{\mathcal{S}}}, \delta\boldsymbol{d}^{\mathcal{G}} \in \mathcal{T}_{\boldsymbol{d}^{\mathcal{G}}}, \delta\boldsymbol{\Lambda} \in \mathcal{T}_{\boldsymbol{\Lambda}}, \delta c_i^{\mathcal{FS}} \in \mathcal{T}_{c_i^{\mathcal{FS}}}$ and $\delta c_i^{\mathcal{SS}} \in \mathcal{T}_{c_i^{\mathcal{SS}}}$. $r^{\mathcal{S2I},\mathcal{FS}}$ and $r^{\mathcal{S2I},\mathcal{SS}}$ denote the weak residuals of the fluid-scatra and structure-scatra subproblems of the S2I problem, respectively.

3.2.2.2 Solution strategy

To efficiently solve the weak formulation $(\mathcal{FSSTI})$ of the FSSTI problem a suitable solution strategy taking into account the specific couplings between the single-fields must be exploited. As discussed in the previous Section 3.2.1, the FSI subproblem is addressed by a monolithic approach due to the strong coupling between the fluid, structure and ALE subproblems by the FSI coupling conditions. Analog, the S2I subproblem is solved monolithically too. In the context of this thesis, the coupling of the S2I to the FSI subproblem is solely in terms of a structure-scatra concentration-dependent growth and change of the constitutive equation of the structure. Both processes take place on a much larger time scale compared to the time scale of the FSI subproblem such that this coupling is just loosely and hence adequately addressed by a sequentially staggered partitioned approach. Hence, the natural choice for solving the overall FSSTI problem in this thesis is by a sequentially staggered scheme coupling the monolithic FSI with the monolithic S2I subproblem.

Monolithic S2I

The weak formulation of the S2I subproblem is spatially and temporally discretized in terms of the finite element method and the one-step-θ scheme, respectively. Applying *Newton*'s method

(Section 3.1.4) to the discretized S2I subproblem, the monolithic S2I subproblem to solve for the incremental concentrations of the fluid-scatra $\Delta \boldsymbol{c}_h^{\mathcal{FS}}$ and structure-scatra $\Delta \boldsymbol{c}_h^{\mathcal{SS}}$ reads [297]

$$\begin{pmatrix} \frac{\partial}{\partial \boldsymbol{c}_{\mathrm{h}}^{\mathcal{FS}}} \boldsymbol{r}_{\mathrm{h}}^{\mathcal{S}2\mathcal{I},\mathcal{FS}} & \frac{\partial}{\partial \boldsymbol{c}_{\mathrm{h}}^{\mathcal{SS}}} \boldsymbol{r}_{\mathrm{h}}^{\mathcal{S}2\mathcal{I},\mathcal{FS}} \\ \frac{\partial}{\partial \boldsymbol{c}_{\mathrm{h}}^{\mathcal{FS}}} \boldsymbol{r}_{\mathrm{h}}^{\mathcal{S}2\mathcal{I},\mathcal{SS}} & \frac{\partial}{\partial \boldsymbol{c}_{\mathrm{h}}^{\mathcal{SS}}} \boldsymbol{r}_{\mathrm{h}}^{\mathcal{S}2\mathcal{I},\mathcal{SS}} \end{pmatrix}_{j}^{n+1} \begin{pmatrix} \Delta \boldsymbol{c}_{\mathrm{h}}^{\mathcal{FS}} \\ \Delta \boldsymbol{c}_{\mathrm{h}}^{\mathcal{SS}} \end{pmatrix}_{j+1}^{n+1} = - \begin{pmatrix} \boldsymbol{r}_{\mathrm{h}}^{\mathcal{S}2\mathcal{I},\mathcal{FS}} \\ \boldsymbol{r}_{\mathrm{h}}^{\mathcal{S}2\mathcal{I},\mathcal{FS}} \end{pmatrix}_{j}^{n+1} , \tag{3.22}$$

where n and j denote the time step and *Newton* step, respectively. The monolithic system (3.22) is solved for the unknown step increments $\Delta \boldsymbol{c}_h^{\mathcal{FS}}$ and $\Delta \boldsymbol{c}_h^{\mathcal{SS}}$ by a preconditioned generalized minimal residual method [234] with block *Gauß-Seidel* preconditioning that utilizes algebraic multigrid for the approximated block inverses.

3.2.3 Porous medium fluid-scalar transport interaction

The numerical treatment of PFSTI problems as introduced in Section 2.2.3 is given in this section.

3.2.3.1 Weak formulation

The weak formulation of the PFSTI problem is established from the weak formulations $(\mathcal{PF})$ and $(\mathcal{PS})$ of the poro-fluid and poro-scatra subproblems (Sections 3.1.1.4) enriched by the PFSTI couplings as introduced in Section 2.2.3. The overall weak formulation $(\mathcal{PFSTI})$ of the PFSTI problem reads: Find $p^{\mathcal{PF}} \in \mathcal{S}_{p^{\mathcal{PF}}}$ and $c_i^{\mathcal{PS}} \in \mathcal{S}_{c_i^{\mathcal{PS}}}$ $(i = 1, \ldots, n_c)$ such that

$$(\mathcal{PFSTI}) : \begin{cases} 0 & = r^{\mathcal{PF}} + \left(\delta p^{\mathcal{PF}}, J_{\mathrm{Vol}}(p^{\mathcal{PF}})\right)_{\Gamma_{\mathrm{I}}^{\mathcal{PF}}} , \\ 0 & = r^{\mathcal{PS}} + \sum_{i=1}^{n_c} \left(\delta c_i^{\mathcal{PS}}, J_{\mathrm{Sol}}(c_i^{\mathcal{PS}}, p^{\mathcal{PF}})\right)_{\Gamma_{\mathrm{I}}^{\mathcal{PS}}} , \end{cases} \tag{3.23}$$

for all $\delta p^{\mathcal{PF}} \in \mathcal{T}_{p^{\mathcal{PF}}}$ and $\delta c_i^{\mathcal{PS}} \in \mathcal{T}_{c_i^{\mathcal{PS}}}$.

3.2.3.2 Solution strategy

The poro-fluid subproblem can be embedded and solved in a multi-concentration scalar transport framework (cf. remark in Section 3.1.1.4). Doing so, the PFSTI problem is monolithically solved by the monolithic poro-scatra approach presented in Section 3.1.1.4. The weak formulations of all subproblems are spatially and temporally discretized in terms of the finite element method and the one-step-θ scheme, respectively.

4 Multiphysics approach for atherosclerosis

In the previous Chapters 2 and 3 abstract mathematical single-field and multiphysics problems were derived from basic continuum mechanical principles and their numerical treatments were addressed. In this chapter, the abstract FSSTI *problem* (see Section 2.2.2) is extended to a multiphysics *model* of atherosclerosis which incorporates major processes of all time scales of the disease and their interactions. Here, focus lies on the development of a predictive biomechanical model of the short time scale cardiovascular mechanics and its influence to and from the long time scale atherosclerotic processes. In contrast to the cardiovascular mechanics, however, little focus lies on a quantitative modeling of the inflammatory and immunological processes within the artery wall which will be addressed separately in the subsequent Chapter 5. Furthermore, the advective transport within the artery wall by the transmural flow is neglected in this chapter and will be addressed in Chapter 6.

In this chapter, a *multiphysics model* of the cardiovascular mechanics and the transport and penetration of LDL is developed which includes a pulsatile blood flow, a compliant artery wall, a WSS-dependent penetration of LDL and a growth and remodeling of the artery wall, cf. Section 1.2. A simple phenomenological model of the inflammatory and immunological processes is employed to represent the long time scale foam cell accumulation triggering a novel growth and remodeling formulation for the artery wall. The developed model is calibrated to and computationally solved for a murine-specific case reproducing important cardiovascular quantities from the literature. Moreover, the case study is used to investigate the interlacement of the different time scales. In particular, the question of the influence of pulsatile blood flow and vessel compliance on the onset of atherosclerosis are addressed.

The structure of this chapter is as follows: In Section 4.1 the mathematical multiphysics model for atherosclerosis is established. Section 4.2 gives further details on the numerical treatment of the model. A murine-specific computational case study of the model is performed in Section 4.3, where the convergence and validity of the results is evaluated and the consequences of common model reductions are investigated. The computational results are discussed in Section 4.4 and critically reflected in Section 4.5. Finally, a brief summary of this chapter is given in Section 4.6. This chapter is a revised version of the previously published work by *Thon et al.* [266].

4.1 Multiphysics model

To reproduce the atherosclerotic process in a mathematical model, reasonable simplifications and model assumptions have to be made.

Simplified model

The main interest of this chapter is to study the mechanobiological influence of the cardiovascular mechanics driven by the hemodynamics on the atherosclerotic process and *vice versa*. In this chapter, the following model assumptions based on key processes described in Section 1.1 are considered for simplicity:

- The hemodynamics is governed by the pulsatile blood flow interacting with the elastic artery wall.
- LDL molecules are transported by advection and diffusion in the lumen and solely by diffusion in the artery wall.
- The initiator of the atherosclerotic inflammation is the migration of LDL through the endothelium into the artery wall.
- The endothelium has an increased permeability with respect to LDL at regions of low wall shear stresses.
- In the artery wall LDL triggers a series of inflammatory and immunological processes which lead to the production of foam cells.
- The accumulation of foam cells in the artery wall leads to a thickening of the artery wall with an induced change of its mechanical properties.
- The growth of the artery wall is considered to be stress free in the reference configuration.

The simplified model of atherosclerosis is mathematically represented by an extension of the FSSTI problem as described in Section 2.2.2. Therein, *Dirichlet* and *Neumann* conditions have to be specified such that the *in vivo* setup of atherosclerosis is matched as close as possible. Further, a rheological and pressure model for blood, a constitutive, growth and remodeling law for the artery wall, and penetration and reaction models for the inflammatory and immunological processes have to be introduced. The multiphysics model is subdivided into a FSI submodel for the cardiovascular mechanics (Section 4.1.1) and a S2I submodel for the transport and interaction of species (Section 4.1.2). A schematic overview of the simplified model and the affiliation of its main aspects to the submodels is given in Figure 4.1.

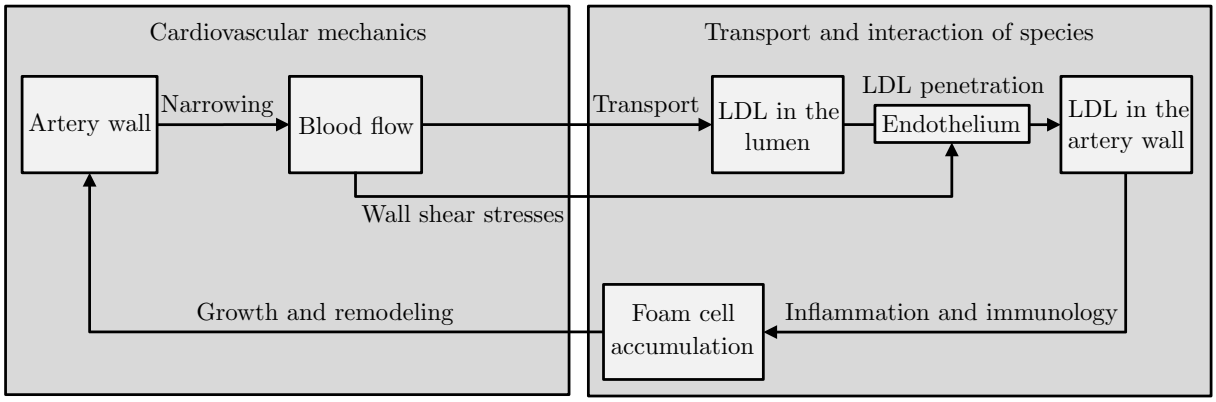

Figure 4.1 Schematic overview of the simplified model of atherosclerosis and affiliation of its main aspects to the submodels of the multiphysics model.

Domain overview

In the context of atherosclerosis in mice (cf. Section 1.1.8), a special focus lies on the aortic sinus, aortic arch and its bifurcations where atherosclerotic plaques are commonly located [98, 99, 167, 185, 232]. Hence, the region of the aortic arch and its surrounding is considered as overall computational domain Ω. The computational domain Ω can be subdivided into the domain of the lumen and the domain of the artery wall. Within the lumen the computational domains of the fluid $\Omega^{\mathcal{F}}$, ALE observer $\Omega^{\mathcal{G}}$ and fluid-scatra $\Omega^{\mathcal{FS}}$ are located. Within the artery wall, the domains of the structure $\Omega^{\mathcal{S}}$ and structure-scatra $\Omega^{\mathcal{SS}}$ are situated.

As introduced beforehand, the affiliation of a quantity $(\bullet)$ to the five computational domains is placed as a superscript, i.e., the quantity is denoted by $(\bullet)^{\mathcal{F}}$, $(\bullet)^{\mathcal{S}}$, $(\bullet)^{\mathcal{G}}$, $(\bullet)^{\mathcal{FS}}$ or $(\bullet)^{\mathcal{SS}}$. Names of quantities are indicated as subscript. Each computational domain contains an inlet boundary Γ_{In} and $n_{\mathrm{Out}} \geq 1$ outlet boundaries $\Gamma_{\mathrm{Out},i}$, $i = 1, \ldots, n_{\mathrm{Out}}$. The endothelium corresponding to the fluid-structure interface and (fluid-scatra)-(structure-scatra) interface is denoted by Γ_{End}. The boundary connecting the outer artery wall with the surrounding tissue is denoted by Γ_{Wall}. A schematic overview of the different domains and boundaries of the multiphysics model is given in Figure 4.2.

4.1.1 Cardiovascular mechanics

The cardiovascular mechanics is commonly modeled by FSI methods [52, 62, 152, 197, 295], cf. Section 2.2.1. Here, it is described by an incompressible non-*Newton*ian fluid (Section 4.1.1.1) including embedded three-element Windkessel models (Section 4.1.1.2) coupled with a hyperelastic solid undergoing finite deformations (Section 4.1.1.3) and a species concentration-dependent anisotropic growth (Section 4.1.1.4) and change of its constitutive equation (Section 4.1.1.5).

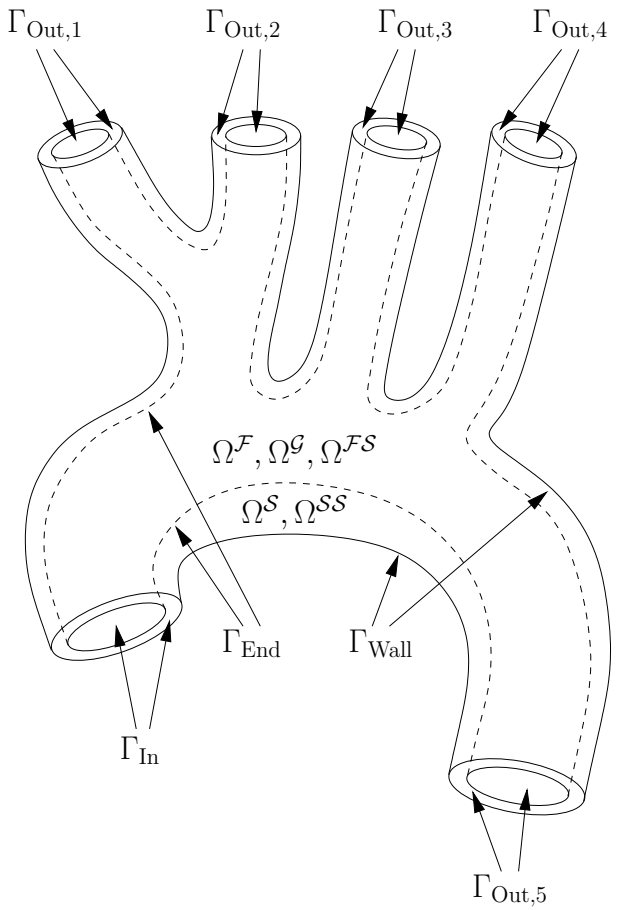

Figure 4.2 Schematic overview of the domains and boundaries of the multiphysics FSSTI model: fluid domain $\Omega^{\mathcal{F}}$, structure domain $\Omega^{\mathcal{S}}$, ALE observer domain $\Omega^{\mathcal{G}}$, fluid-scatra domain $\Omega^{\mathcal{FS}}$, structure-scatra domain $\Omega^{\mathcal{SS}}$, inlet boundary Γ_{In}, outlet boundaries $\Gamma_{\mathrm{Out},i}$ $(i = 1, \ldots, 5)$, endothelium boundary Γ_{End} and outer artery wall boundary Γ_{Wall}.

4.1.1.1 Blood flow

Blood is modeled as an incompressible non-Newtonian fluid. Thus, the blood flow on the deformable domain $\Omega^{\mathcal{F}}(t)$ is governed by the incompressible *Navier-Stokes* equations in an ALE frame, see Section 2.1.3:

$$\begin{aligned} &\varrho^{\mathcal{F}} \frac{\partial}{\partial t} \boldsymbol{u}^{\mathcal{F}}\big|_{\boldsymbol{\chi}} + \varrho^{\mathcal{F}} \left((\boldsymbol{u}^{\mathcal{F}} - \boldsymbol{u}^{\mathcal{G}}) \cdot \boldsymbol{\nabla} \right) \boldsymbol{u}^{\mathcal{F}} + \nabla p^{\mathcal{F}} - 2\mu^{\mathcal{F}}(\boldsymbol{u}^{\mathcal{F}}) \boldsymbol{\nabla} \cdot \boldsymbol{\varepsilon}^{\mathcal{F}}\big(\boldsymbol{u}^{\mathcal{F}}\big) = \boldsymbol{0}, \\ &\boldsymbol{\nabla} \cdot \boldsymbol{u}^{\mathcal{F}} = 0. \end{aligned} \tag{4.1}$$

Blood exhibits a shear-thinning property, i.e., a decrease of its viscosity when its strain-rate increases [38, 43, 178]. The rheological *Carreau-Yasuda* model is used to account for the shear-

thinning property of blood [4, 17, 43, 100]

$$\mu^{\mathcal{F}}(\boldsymbol{u}^{\mathcal{F}}) = \mu_{\infty}^{\mathcal{F}} + \frac{\mu_{0}^{\mathcal{F}} - \mu_{\infty}^{\mathcal{F}}}{\left(1 + \left(\kappa^{\mathcal{F}}\, \dot{\gamma}^{\mathcal{F}}(\boldsymbol{u}^{\mathcal{F}})\right)^{b^{\mathcal{F}}}\right)^{a^{\mathcal{F}}}}, \tag{4.2}$$

where $\mu_{\infty}^{\mathcal{F}}, \mu_{0}^{\mathcal{F}}, \kappa^{\mathcal{F}}, a^{\mathcal{F}}$ and $b^{\mathcal{F}}$ are constants and $\dot{\gamma}^{\mathcal{F}}(\boldsymbol{u}^{\mathcal{F}}) = \sqrt{2\ \mathrm{tr}\left(\boldsymbol{\varepsilon}^{\mathcal{F}}(\boldsymbol{u}^{\mathcal{F}})^2\right)}$ is the shear-rate of the fluid. On $\Gamma_{\mathrm{In}}^{\mathcal{F}}$ the following *Dirichlet* condition is applied

$$\boldsymbol{u}^{\mathcal{F}}(t, \boldsymbol{x}) = -Q_{\mathrm{In}}^{\mathcal{F}}(t)\ g^{\mathcal{F}}(t, \boldsymbol{x})\ \boldsymbol{n}_{\mathrm{In}}^{\mathcal{F}}, \tag{4.3}$$

where the scalar-valued function $g^{\mathcal{F}}(t, \boldsymbol{x})$ corresponds to the applied velocity profile and $Q_{\mathrm{In}}^{\mathcal{F}}(t)$ to the total volume influx. $Q_{\mathrm{In}}^{\mathcal{F}}(t)$ is a T_{Cycl}-periodical function, to regard the pulsatile nature of blood flow with a cardiac cycle duration of T_{Cycl}. The Windkessel effect of succeeding arteries has to be accounted for to achieve a physiological range for the blood pressure $p^{\mathcal{F}}$. Therefore, time varying pressures $p_{\mathrm{WK},i}^{\mathcal{F}}$ from the underlying Windkessel submodels (Section 4.1.1.2) are applied as tractions on each of the outflow boundaries $\Gamma_{\mathrm{Out},i}^{\mathcal{F}}$:

$$\boldsymbol{\sigma}^{\mathcal{F}} \boldsymbol{n}_{\mathrm{Out},i}^{\mathcal{F}} = -p_{\mathrm{WK},i}^{\mathcal{F}}\ \boldsymbol{n}_{\mathrm{Out},i}^{\mathcal{F}}, \tag{4.4}$$

where $\boldsymbol{\sigma}^{\mathcal{F}} = -p^{\mathcal{F}}\mathbf{1} + 2\mu^{\mathcal{F}}\left(\boldsymbol{u}^{\mathcal{F}}\right)\boldsymbol{\varepsilon}^{\mathcal{F}}\left(\boldsymbol{u}^{\mathcal{F}}\right)$ is the *Cauchy* stress tensor of the fluid. On $\Gamma_{\mathrm{End}}^{\mathcal{F}}$ the FSI coupling condition is applied [193]

$$\boldsymbol{u}^{\mathcal{F}} = \boldsymbol{u}^{\mathcal{G}}, \tag{4.5}$$

which enforces the kinematic continuity of the fluid and ALE submodels in combination with a no-slip boundary condition on the fluid across the endothelium.

Remark. *A non-*Newton*ian rheological model for the shear-thinning property of blood is an important factor in hemodynamics [38]. However, a large variety of rheological models for the shear-thinning property of blood exists, see [43, 142] and references therein. For a comparison of* Newton*ian with different non-*Newton*ian viscosity models for blood, see [38, 100, 245, 293]. The* Carreau-Yasuda *model was chosen as it allows for a good approximation of the WSS at low velocities [142]. Hence, as there is a large period with almost no inlet flux in the diastole of the cardiac cycle, the* Carreau-Yasuda *model is well-suited to estimate the WSS in aortic arches. At the same time, it is not as complex as other well-performing models, such as the* Generalized Power Law *[142].*

4.1.1.2 Blood pressure

To achieve a physiological pressure range of the fluid and to physiologically split the total flux to the different bifurcations, separate three-element Windkessel submodels [139, 211, 281, 292] are used on each of the outflow boundaries $\Gamma_{\mathrm{Out},i}^{\mathcal{F}}$ to determine the Windkessel pressures $p_{\mathrm{WK},i}^{\mathcal{F}}$:

$$C_i^{\mathcal{F}} \frac{\mathrm{d}}{\mathrm{d}t} p_{\mathrm{WK},i}^{\mathcal{F}}(t) + \frac{1}{R_{\mathrm{P},i}^{\mathcal{F}}} p_{\mathrm{WK},i}^{\mathcal{F}}(t) = C_i^{\mathcal{F}} R_{\mathrm{C},i}^{\mathcal{F}} \frac{\mathrm{d}}{\mathrm{d}t} Q_{\mathrm{Out},i}^{\mathcal{F}}(t) + \left(1 + \frac{R_{\mathrm{C},i}^{\mathcal{F}}}{R_{\mathrm{P},i}^{\mathcal{F}}}\right) Q_{\mathrm{Out},i}^{\mathcal{F}}(t), \tag{4.6}$$

where $Q^{\mathcal{F}}_{\mathrm{Out},i}(t) = \int_{\Gamma^{\mathcal{F}}_{\mathrm{Out},i}} \boldsymbol{u}^{\mathcal{F}}(t) \cdot \boldsymbol{n}^{\mathcal{F}}_{\mathrm{Out},i}\, \mathrm{d}s$ is the current outflux through $\Gamma^{\mathcal{F}}_{\mathrm{Out},i}$. The constants $R^{\mathcal{F}}_{\mathrm{C},i}$, $R^{\mathcal{F}}_{\mathrm{P},i}$ and $C^{\mathcal{F}}_i$ correspond to the *characteristic resistance*, *peripheral resistance* and *artery compliance* of the successive artery network, respectively. They have to be fitted to the specific case to produce physiologically meaningful results, see Section 4.3.1.

4.1.1.3 Artery wall

The artery wall is a multi-component structure that also contains a fluid phase [29, 267, 294]. Here, its mechanical response is modeled through an anisotropic hyperelastic material law [131], while a movement of species within the artery tissue is still allowed, see Section 4.1.2.2. Hence, the frequently used approach of modeling the artery wall as a solid [52, 59, 81, 152, 197] is used which is governed by the balance of linear momentum on $\Omega^{\mathcal{S}}_0$, see Section 2.1.4

$$\varrho^{\mathcal{S}}_0 \frac{\mathrm{d}^2}{\mathrm{d}t^2} \boldsymbol{d}^{\mathcal{S}} - \boldsymbol{\nabla} \cdot \left(\boldsymbol{F}^{\mathcal{S}} \boldsymbol{S}^{\mathcal{S}}(\boldsymbol{C}^{\mathcal{S}}) \right) = \boldsymbol{0}. \tag{4.7}$$

To incorporate the effect of the tissue surrounding the aorta, a spring and dashpot combination on $\Gamma^{\mathcal{S}}_{\mathrm{Wall}}$ [179, 197] is applied:

$$\boldsymbol{F}^{\mathcal{S}}\ \boldsymbol{S}^{\mathcal{S}} \boldsymbol{N}^{\mathcal{S}}_{\mathrm{Wall}} = -k^{\mathcal{S}}_{\mathrm{Wall}} \boldsymbol{d}^{\mathcal{S}} - c^{\mathcal{S}}_{\mathrm{Wall}} \boldsymbol{u}^{\mathcal{S}}, \tag{4.8}$$

where the constants $k^{\mathcal{S}}_{\mathrm{Wall}}$ and $c^{\mathcal{S}}_{\mathrm{Wall}}$ are the spring stiffness and dashpot viscosity of the surrounding tissue, respectively. To respect the influence of the succeeding aortic tissue on all boundaries $\Gamma^{\mathcal{S}}_{\mathrm{Out},i}$ sliding springs and dashpots acting only in the direction of the surface normal and allowing a free movement in the boundary plane are applied:

$$\boldsymbol{F}^{\mathcal{S}}\ \boldsymbol{S}^{\mathcal{S}} \boldsymbol{N}^{\mathcal{S}}_{\mathrm{Out},i} = \boldsymbol{N}^{\mathcal{S}}_{\mathrm{Out},i} \cdot \left(-k^{\mathcal{S}}_{\mathrm{Out}} \boldsymbol{d}^{\mathcal{S}} - c^{\mathcal{S}}_{\mathrm{Out}} \boldsymbol{u}^{\mathcal{S}} \right) \boldsymbol{N}^{\mathcal{S}}_{\mathrm{Out},i}, \tag{4.9}$$

where $k^{\mathcal{S}}_{\mathrm{Out}}$ and $c^{\mathcal{S}}_{\mathrm{Out}}$ are the spring stiffness and dashpot viscosity of the succeeding aortic tissue, respectively. On the boundary $\Gamma^{\mathcal{S}}_{\mathrm{In}}$, a zero displacement *Dirichlet* condition is applied. On $\Gamma^{\mathcal{S}}_{\mathrm{End}}$ the FSI coupling condition is applied [193]

$$\boldsymbol{\sigma}^{\mathcal{S}} \boldsymbol{n}^{\mathcal{S}}_{\mathrm{End}} = \boldsymbol{h}^{\mathcal{S}}_{\mathrm{End}} = -\boldsymbol{h}^{\mathcal{F}}_{\mathrm{End}} = -\boldsymbol{\sigma}^{\mathcal{F}} \boldsymbol{n}^{\mathcal{S}}_{\mathrm{End}}, \tag{4.10}$$

which enforces the equilibrium of interface traction of the structure $\boldsymbol{h}^{\mathcal{S}}_{\mathrm{End}}$ and the fluid $\boldsymbol{h}^{\mathcal{F}}_{\mathrm{End}}$ across the endothelium.

Remark. *As stated beforehand, the discussion of the ALE submodel is dropped as it is required only to computationally treat the deforming fluid submodel and does not possess a physical relevance on its own. Details on the ALE submodel and further information on the FSI coupling conditions can be found in Section 2.2.1.*

4.1.1.4 Growth

In addition to the elastodynamics, the non-elastic process of growth due to the accumulation of foam cells in the atherogenesis [279] is considered. It is assumed that the growth of the artery wall is stress free in the reference configuration [242] and hence a multiplicative split of the deformation gradient $\boldsymbol{F}^{\mathcal{S}}$ of the structure into an elastic part $\boldsymbol{F}^{\mathcal{S}}_{\mathrm{El}}$ and a growth part $\boldsymbol{F}^{\mathcal{S}}_{\mathrm{Gr}}$ [3, 155] is utilized, see Section 2.1.4.3.

The natural direction of growth is the luminal direction, as it is induced by the accumulation of macrophages and other cells in the intima and the adjacent media. Furthermore, growth of the aorta in the axial or circumferential direction would stretch collagen and elastin fibers within the artery wall and hence introduce additional wall stresses. For a better understanding of the theory of anisotropic growth, it is first assumed that the unit radial direction $\boldsymbol{ra}$, the unit axial direction $\boldsymbol{ax}$ and the unit circumferential direction $\boldsymbol{ci}$ are constants (an assumption that will be dropped in the subsequent discussion). Hence, the following form of the growth deformation gradient is postulated to enforce a growth of the artery wall in the radial direction $\boldsymbol{ra}$ and thus toward the lumen [149]:

$$\boldsymbol{F}^{\mathcal{S}}_{\mathrm{Gr}} = \vartheta(m^{\mathcal{SS}})\ \boldsymbol{ra} \otimes \boldsymbol{ra} + \boldsymbol{ax} \otimes \boldsymbol{ax} + \boldsymbol{ci} \otimes \boldsymbol{ci}, \tag{4.11}$$

where the scalar-valued function $\vartheta(m^{\mathcal{SS}})$ is the *growth factor* and depends on the local concentration of the growth inducing concentration. In this chapter, this concentration is for simplicity the density of macrophages $m^{\mathcal{SS}}$ in the artery wall which are assumed to be foamy.

Remark. *A more precise description for foam cells and its incorporation into the multiphysics framework is given in Chapter 6. At this point a simple definition is chosen as this is in agreement with the simplified model for the inflammatory and immunological processes utilized in this chapter.*

Since the set $\{\boldsymbol{ra}, \boldsymbol{ax}, \boldsymbol{ci}\}$ is an orthonormal basis of $\mathbb{R}^3$, Equation (4.11) can be simplified to

$$\boldsymbol{F}^{\mathcal{S}}_{\mathrm{Gr}} = \boldsymbol{1} + \big(\vartheta(m^{\mathcal{SS}}) - 1\big)\ \boldsymbol{ra} \otimes \boldsymbol{ra}, \tag{4.12}$$

which now only depends on the unit radial direction $\boldsymbol{ra}$. The model of the foam cells is described in Section 4.1.2.2. For the computation of the growth factor $\vartheta(m^{\mathcal{SS}})$, the idea is exploited that the increase in volume $\Delta V_{\mathrm{Gr}}(t)$ due to growth at all times t is proportional to the mass of foam cells $M(m^{\mathcal{SS}}(t))$ at this time. Hence, it is asked for

$$\Delta V_{\mathrm{Gr}}(t) = \alpha^{\mathcal{S}}_m\ M(m^{\mathcal{SS}}(t)), \tag{4.13}$$

where $\alpha^{\mathcal{S}}_m$ is the proportionality constant and corresponds to the amount of volume occupied by a unit of foam cells, i.e., it is the inverse of the statistical mass density of foam cells. It follows

$$V_{\mathrm{Gr}}(t) - V(0) = \alpha^{\mathcal{S}}_m\ M(m^{\mathcal{SS}}(t)), \tag{4.14}$$

which can be expressed in terms of integrals over the corresponding domains

$$\int\limits_{\Omega^{\mathcal{S}}_{\mathrm{Gr}}(t)} 1\ \mathrm{d}V_{\mathrm{Gr}} - \int\limits_{\Omega^{\mathcal{S}}_0} 1\ \mathrm{d}V = \alpha^{\mathcal{S}}_m \int\limits_{\Omega^{\mathcal{S}}(t)} m^{\mathcal{SS}}(t)\ \mathrm{d}v, \tag{4.15}$$

where $\mathrm{d}V_{\mathrm{Gr}}, \mathrm{d}V$ and $\mathrm{d}v$ denote an integration over the corresponding growth, material and spatial configurations, respectively. All integrals can be pulled-back to the material configuration such that

$$\int_{\Omega_0^{\mathcal{S}}} J_{\mathrm{Gr}}^{\mathcal{S}}(t)\,\mathrm{d}V - \int_{\Omega_0^{\mathcal{S}}} 1\,\mathrm{d}V = \alpha_m^{\mathcal{S}} \int_{\Omega_0^{\mathcal{S}}} J^{\mathcal{S}}(t) m^{\mathcal{SS}}(t)\,\mathrm{d}V, \tag{4.16}$$

where $J_{\mathrm{Gr}}^{\mathcal{S}}(t) = \det\left(\boldsymbol{F}_{\mathrm{Gr}}^{\mathcal{S}}(t)\right) \overset{(4.12)}{=} \vartheta(m^{\mathcal{SS}}(t))$ is the Jacobian of the growth deformation gradient $\boldsymbol{F}_{\mathrm{Gr}}^{\mathcal{S}}(t)$ at time t. Since (4.16) also holds locally, a result similar to [149] is achieved:

$$\vartheta\left(m^{\mathcal{SS}}(t)\right) = 1 + \alpha_m^{\mathcal{S}} J^{\mathcal{S}}(t) m^{\mathcal{SS}}(t). \tag{4.17}$$

In an atherosclerosis specific setup the unit radial direction $\boldsymbol{ra}$ at time t is equal to the unit outer normal $\boldsymbol{n}_{\mathrm{End}}^{\mathcal{S}}(t)$ of the deformed surface $\Gamma_{\mathrm{End}}^{\mathcal{S}}(t)$. Hence, the radial direction does change due to the hemodynamics and preceded growth. Thus, Equation (4.12) is not valid in an atherosclerotic context and an incremental definition of the growth part $\boldsymbol{F}_{\mathrm{Gr}}^{\mathcal{S}}$ of the deformation gradient [104, 149] must be used. Let therefore t, τ be instances in time with $\tau < t$, where in the interval $[\tau; t]$ the growth direction is assumed to be constant. Consequently, the growth part $\boldsymbol{F}_{\mathrm{Gr}}^{\mathcal{S}}(t)$ of the deformation gradient at time t is computed by

$$\boldsymbol{F}_{\mathrm{Gr}}^{\mathcal{S}}(t) = \Delta\boldsymbol{F}_{\mathrm{Gr}}^{\mathcal{S}}(\tau, t)\ \boldsymbol{F}_{\mathrm{Gr}}^{\mathcal{S}}(\tau), \tag{4.18}$$

where $\boldsymbol{F}_{\mathrm{Gr}}^{\mathcal{S}}(\tau)$ is the growth history part of the deformation gradient at time τ and $\Delta\boldsymbol{F}_{\mathrm{Gr}}^{\mathcal{S}}(\tau, t)$ is the incremental growth deformation gradient from τ to t. The incremental growth deformation gradient is computed by

$$\Delta\boldsymbol{F}_{\mathrm{Gr}}^{\mathcal{S}}(\tau, t) = \mathbf{1} + \frac{\vartheta(m^{\mathcal{SS}}(t)) - \vartheta(m^{\mathcal{SS}}(\tau))}{\vartheta(m^{\mathcal{SS}}(\tau))}\ \boldsymbol{n}_{\mathrm{End}}^{\mathcal{S}}(t) \otimes \boldsymbol{n}_{\mathrm{End}}^{\mathcal{S}}(t). \tag{4.19}$$

This incremental growth deformation gradient corresponds to a growth of the structure in the current radial direction $\boldsymbol{n}_{\mathrm{End}}^{\mathcal{S}}(t)$ by the factor $(\vartheta(t) - \vartheta(\tau))/\vartheta(\tau)$ compared to the state at time τ.

Remark. *Iff the direction of growth is constant for all times t, the incremental growth deformation gradient-based formulation, i.e., equations* (4.18) *and* (4.19) *are equivalent to the representation in Equation* (4.12)*.*

4.1.1.5 Remodeling and constitutive laws

In the previous section, a growth model for the artery wall representing the increase of volume due to the deposition of foam cells was derived. Along with growth also the change of mechanical properties of the artery wall is considered since foam cells feature a very different mechanical behavior compared to healthy aortic tissue. Thus, an increasing accumulation of foam cells $m^{\mathcal{SS}}$ locally and gradually changes the constitutive law of the structure toward the one of foam cells. The strain-energy density function $\Psi^{\mathcal{S}}$ of the hyperelastic structure is therefore computed as a

convex combination of the strain-energy density function $\Psi^{\mathcal{S}}_{\mathrm{Ao}}$ of healthy aortic tissue and the strain-energy density function $\Psi^{\mathcal{S}}_{\mathrm{FC}}$ of foam cells

$$\Psi^{\mathcal{S}} = \lambda(m^{\mathcal{SS}})\Psi^{\mathcal{S}}_{\mathrm{Ao}} + (1 - \lambda(m^{\mathcal{SS}}))\Psi^{\mathcal{S}}_{\mathrm{FC}}, \tag{4.20}$$

where $\lambda(m^{\mathcal{SS}}) \in]0; 1]$ is the *remodeling factor*. It is a nonlinear function depending on the local concentration $m^{\mathcal{SS}}$ and describes the ratio between the two extrema. To be more precise, the remodeling factor λ describes the fraction of volume of healthy aortic tissue compared to the overall (grown) volume. Since the change of overall volume relative to the initial volume is given by the growth factor $\vartheta(m^{\mathcal{SS}})$, the remodeling factor is calculated by

$$\lambda(m^{\mathcal{SS}}) = \frac{1}{\vartheta(m^{\mathcal{SS}})} \overset{(4.17)}{=} \frac{1}{1 + \alpha^{\mathcal{S}}_m J^{\mathcal{S}} m^{\mathcal{SS}}}. \tag{4.21}$$

Consequently, at a position without foam cells, i.e., $m^{\mathcal{SS}} = 0$ the remodeling factor is $\lambda = 1$ which corresponds to healthy aortic material. In contrast, a large amount of foam cells, i.e., $m^{\mathcal{SS}} \to \infty$ results in $\lambda = 0$ and hence in the mechanical properties that were assumed for foam cells.

Since artery tissue is nearly incompressible [31, 64], an additive split for both strain-energy functions into a volumetric and isochoric part [123, 208] is used. For the specific choices of the volumetric parts $\Psi^{\mathcal{S}}_{\mathrm{Vol}}$, see [65, 207]. The artery wall can be seen as a ground material which is reinforced by fibers representing the collagen and elastin fibers. Hence, for the isochoric part of the healthy aortic tissue $\Psi^{\mathcal{S}}_{\mathrm{Ao}}$ the four-fiber family model is used, see [78, 112, 131, 230]

$$\Psi^{\mathcal{S}}_{\mathrm{Ao}} = \frac{c^{\mathcal{S}}_{0,\mathrm{Ao}}}{2}\left(\overline{I}_{\boldsymbol{C}^{\mathcal{S}}} - 3\right) + \sum_{k=1}^{4} \frac{c^{\mathcal{S}}_{1,k}}{4c^{\mathcal{S}}_{2,k}}\left(e^{\left(c^{\mathcal{S}}_{2,k}((\varpi^{\mathcal{S}}_k)^2-1)^2\right)} - 1\right), \tag{4.22}$$

where the constants $c^{\mathcal{S}}_{0,\mathrm{Ao}}, c^{\mathcal{S}}_{1,k}$ and $c^{\mathcal{S}}_{2,k}$ are aortic tissue specific material parameters. Here, $\overline{I}_{\boldsymbol{C}^{\mathcal{S}}} = (J^{\mathcal{S}})^{-2/3}\mathrm{tr}(\boldsymbol{C}^{\mathcal{S}})$ is the first modified invariant of the right *Cauchy-Green* deformation tensor $\boldsymbol{C}^{\mathcal{S}}$ and $\varpi^{\mathcal{S}}_k$ is the stretch of the k-th fiber family, respectively. The stretch $\varpi^{\mathcal{S}}_k$ is calculated by the total *Cauchy-Green* tensor $\boldsymbol{C}^{\mathcal{S}}$, see [236], and hence by $\varpi^{\mathcal{S}}_k = \sqrt{\boldsymbol{M}^T_k\, \boldsymbol{C}^{\mathcal{S}}\, \boldsymbol{M}_k}$ where $\boldsymbol{M}_k = [0, \sin(\delta_k), \cos(\delta_k)]^T$ is the direction of the k-th fiber represented in the coordinate system spanned by the radial, axial and axes. The directions of the fibers are parameterized by the orientation angles $\delta^{\mathcal{S}}_1$, $\delta^{\mathcal{S}}_2$, $\delta^{\mathcal{S}}_3$ and $\delta^{\mathcal{S}}_4$, which are material specific constants.

The mechanical behavior of atherosclerotic plaques is more comparable to a fluid than to a solid [182]. Therefore, a visco-hyperelastic *Maxwell*-like material, i.e., a spring and dashpot in series like approach is utilized as constitutive equation of foam cells [115, 144, 203, 298]. The relaxation time of the viscous dashpot is $\tau^{\mathcal{S}}_{\mathrm{FC}}$ [203]. For the isochoric part of the strain-energy density function $\Psi^{\mathcal{S}}_{\mathrm{FC}}$ a modified neo-Hookean law is used: [9]

$$\Psi^{\mathcal{S}}_{\mathrm{FC}} = \frac{c^{\mathcal{S}}_{0,\mathrm{FC}}}{2}\left(\overline{I}_{\boldsymbol{C}^{\mathcal{S}}} - 3\right), \tag{4.23}$$

where the constant $c^{\mathcal{S}}_{0,\mathrm{FC}}$ is a material specific parameter.

Remark. *A large variety of constitutive laws for healthy and atherosclerotic aortic tissues exists, see [125, 230] and references therein. Here, the four-fiber family model is utilized as it respects the complex, inhomogeneous and anisotropic structure of which the artery wall is build, cf. Figure 1.1 or [123]. Further, the chosen constitutive law comes with a large variety of parameter sets for different aortic regions and ages of humans which were gained by fits to experimental results [230].*

Remark. *If more species induce a growth and remodeling of the artery wall, the presented laws can be generalized in a straightforward manner. The growth factor ϑ defined in Equation* (4.17) *can be generalized to $\vartheta\left(\boldsymbol{c}^{\mathcal{SS}}\right) = 1 + J^{\mathcal{S}} \sum_i \alpha_i^{\mathcal{S}} c_i^{\mathcal{SS}}$, where $\boldsymbol{c}^{\mathcal{SS}}$ is the vector of concentrations $c_i^{\mathcal{SS}}$ of all growth inducing species i and $\alpha_i^{\mathcal{S}}$ are the corresponding growth parameters. The generalization of the remodeling process governed by Equation* (4.21) *reads $\Psi^{\mathcal{S}} = \frac{1}{\vartheta(\boldsymbol{c}^{\mathcal{SS}})} \Psi_{\mathrm{Ao}}^{\mathcal{S}} + \frac{J^{\mathcal{S}}}{\vartheta(\boldsymbol{c}^{\mathcal{SS}})} \sum_i \alpha_i^{\mathcal{S}} c_i^{\mathcal{SS}} \Psi_i^{\mathcal{S}}$, where the sum again is over all growth (and remodeling) inducing species i.*

4.1.2 Transport and interaction of species

All species are modeled by a continuum approach, i.e., they are described as concentrations. The general framework of species in atherosclerosis model is given by the advection-diffusion-reaction equation [29, 152, 177, 276], see Section 2.1.5. The transport of LDL in the lumen is dominated by advection, whereas in the artery wall it is assumed to be solely driven by diffusion (an assumption that is dropped in Chapter 6). In addition, species in the artery wall are produced and degraded by a simplistic reaction model $\boldsymbol{\varkappa}^{\mathcal{SS}}$ for the inflammatory and immunological processes. The complex heterogeneous structure of the artery wall is neglected and the fluid-wall model [221, 305] is employed, where the endothelium is considered to be the only transport barrier, cf. Section 1.2.1. The endothelium is treated as a semi-permeable membrane leading to a significant discontinuity between the concentrations in the blood and in the artery wall. Thus, the transport and interaction of species is modeled by a S2I method coupling the advection dominated fluid-scatra (Section 4.1.2.1) and the diffusive and reactive structure-scatra (Section 4.1.2.2) in terms of a WSS-dependent version of the *Kedem-Katchalsky* equation (Section 4.1.2.3).

4.1.2.1 Transport of LDL with blood flow

The transport of LDL with blood is modeled by the advection-diffusion equation in an ALE frame, where the motion of the ALE observer is the same as for the fluid submodel, cf. Section 2.1.5. Hence, the dynamics of the scalar-valued concentration $\ell^{\mathcal{FS}}$ of LDL within the deformable fluid-scatra domain $\Omega^{\mathcal{FS}}(t)$ is described by:

$$\frac{\partial}{\partial t} \ell^{\mathcal{FS}}\big|_{\boldsymbol{\chi}} + (\boldsymbol{u}^{\mathcal{F}} - \boldsymbol{u}^{\mathcal{G}}) \cdot \nabla \ell^{\mathcal{FS}} - \boldsymbol{\nabla} \cdot \left(D_{\ell}^{\mathcal{FS}} \nabla \ell^{\mathcal{FS}}\right) = 0. \tag{4.24}$$

On the inflow boundary $\Gamma_{\mathrm{In}}^{\mathcal{FS}}$ the concentration of LDL $\ell_{\mathrm{In}}^{\mathcal{FS}}$ is prescribed by a *Dirichlet* condition:

$$\ell^{\mathcal{FS}} = \ell_{\mathrm{In}}^{\mathcal{FS}}. \tag{4.25}$$

On the outflow boundaries $\Gamma^{\mathcal{FS}}_{\mathrm{Out},i}$ symmetry conditions are used

$$\nabla \ell^{\mathcal{FS}} \cdot \boldsymbol{n}^{\mathcal{FS}}_{\mathrm{Out},i} = 0. \tag{4.26}$$

The flux of LDL through the endothelium $\Gamma^{\mathcal{FS}}_{\mathrm{End}}$ is described by

$$\left(-D^{\mathcal{FS}}_{\ell} \nabla \ell^{\mathcal{FS}} + (\boldsymbol{u}^{\mathcal{F}} - \boldsymbol{u}^{\mathcal{G}}) \ell^{\mathcal{FS}}\right) \cdot \boldsymbol{n}^{\mathcal{FS}}_{\mathrm{End}} = -J_{\mathrm{Sol}}(\ell^{\mathcal{FS}}, \ell^{\mathcal{SS}}), \tag{4.27}$$

where $J_{\mathrm{Sol}}(\ell^{\mathcal{FS}}, \ell^{\mathcal{SS}})$ is the solute flux. The submodel of the solute flux is described in detail in Section 4.1.2.3. It is important to note that in this chapter it is assumed that the artery wall is a solid. Hence, using Equation (4.5) reduces the flux condition to:

$$-D^{\mathcal{FS}}_{\ell} \nabla \ell^{\mathcal{FS}} \cdot \boldsymbol{n}^{\mathcal{FS}}_{\mathrm{End}} = -J_{\mathrm{Sol}}(\ell^{\mathcal{FS}}, \ell^{\mathcal{SS}}). \tag{4.28}$$

4.1.2.2 Species interaction in artery wall

The transport and interaction of species in the artery wall is modeled by the diffusion-reaction equation in an ALE frame, where the motion of the ALE observer is the same as for the structure submodel, cf. Section 2.1.5. Hence, the dynamic of the concentration $\ell^{\mathcal{SS}}$ of LDL in the deforming structure-scatra domain $\Omega^{\mathcal{SS}}(t)$ is described by:

$$\underbrace{\frac{\partial}{\partial t} \ell^{\mathcal{SS}}\big|_{\boldsymbol{x}}}_{\substack{\text{time derivative of LDL} \\ \text{(in ALE frame)}}} + \underbrace{\ell^{\mathcal{SS}} \boldsymbol{\nabla} \cdot \boldsymbol{u}^{\mathcal{S}}}_{\substack{\text{transport of LDL} \\ \text{with deforming} \\ \text{artery wall}}} - \underbrace{\boldsymbol{\nabla} \cdot \left(D^{\mathcal{SS}}_{\ell} \nabla \ell^{\mathcal{SS}}\right)}_{\text{diffusion of LDL}} - \underbrace{\varkappa^{\mathcal{SS}}_{\ell}(\boldsymbol{c}^{\mathcal{SS}})}_{\substack{\text{inflammatory and} \\ \text{immunological} \\ \text{processes of LDL}}} = 0, \tag{4.29}$$

The reaction term $\varkappa^{\mathcal{SS}}_{\ell}(\boldsymbol{c}^{\mathcal{SS}})$ is a function depending on the vector of concentrations $\boldsymbol{c}^{\mathcal{SS}}$ of all species considered in the artery wall. In this chapter, a simplistic reaction model for the inflammatory and immunological process in the artery wall is employed that mimics an atherosclerosis-like behavior. The reaction model considers two species only: "LDL" and "foam cells". Here, LDL does not literally represent low-density lipoproteins but more general a composite of all species involved in the inflammatory and immunological processes, such as native LDL, modified LDL, native HDL, modified HDL, VCAM-1 and MCP-1. In contrast, foam cells must be understood as composite of final growth inducing products of the complex immunological processes, such as monocytes, macrophages, smooth muscle cells, foam cells and necrotic core. The governing equation for the concentration of foam cells $m^{\mathcal{SS}}$ in the structure-scalar domain $\Omega^{\mathcal{SS}}$ is in analogy to Equation (4.29).

It is assumed that there are healing processes which result in the degradation of the concentration $\ell^{\mathcal{SS}}$ of LDL. Furthermore, foam cells are produced if the concentration of LDL $\ell^{\mathcal{SS}}$ exceeds a given threshold $\ell^{\mathcal{SS}}_{\mathrm{Thres}}$. Hence, the reactive term of LDL is

$$\varkappa^{\mathcal{SS}}_{\ell}(\boldsymbol{c}^{\mathcal{SS}}) = -d^{\mathcal{SS}}_{\ell}\, \ell^{\mathcal{SS}} - \gamma^{\mathcal{SS}}_{\ell} \left(\ell^{\mathcal{SS}} - \ell^{\mathcal{SS}}_{\mathrm{Thres}}\right)_{+}, \tag{4.30}$$

where the constants $d_\ell^{\mathcal{SS}}$ and $\gamma_\ell^{\mathcal{SS}}$ are the degradation and reaction rate of LDL, respectively. The index $(\bullet)_+$ denotes the positive branch of $(\bullet)$, i.e., it is zero when its argument is negative. Foam cells are a product of LDL and are not degraded. The reactive term of foam cells reads

$$\varkappa_m^{\mathcal{SS}}(\boldsymbol{c}^{\mathcal{SS}}) = \gamma_\ell^{\mathcal{SS}}\left(\ell^{\mathcal{SS}} - \ell_{\mathrm{Thres}}^{\mathcal{SS}}\right)_+. \tag{4.31}$$

On the boundaries $\Gamma_{\mathrm{In}}^{\mathcal{SS}}$ and $\Gamma_{\mathrm{Out},i}^{\mathcal{SS}}$ symmetry conditions are used:

$$\begin{aligned} \nabla\ell^{\mathcal{SS}} \cdot \boldsymbol{n}_{\mathrm{In}}^{\mathcal{SS}} = 0 = \nabla\ell^{\mathcal{SS}} \cdot \boldsymbol{n}_{\mathrm{Out},i}^{\mathcal{SS}}, \\ \nabla m^{\mathcal{SS}} \cdot \boldsymbol{n}_{\mathrm{In}}^{\mathcal{SS}} = 0 = \nabla m^{\mathcal{SS}} \cdot \boldsymbol{n}_{\mathrm{Out},i}^{\mathcal{SS}}. \end{aligned} \tag{4.32}$$

It is assumed that the artery wall is impervious at its outer boundary $\Gamma_{\mathrm{Wall}}^{\mathcal{SS}}$ and hence no-flux conditions

$$\begin{aligned} -D_\ell^{\mathcal{SS}}\nabla\ell^{\mathcal{SS}} \cdot \boldsymbol{n}_{\mathrm{Wall}}^{\mathcal{SS}} = 0, \\ -D_m^{\mathcal{SS}}\nabla m^{\mathcal{SS}} \cdot \boldsymbol{n}_{\mathrm{Wall}}^{\mathcal{SS}} = 0 \end{aligned} \tag{4.33}$$

are imposed. The diffusive influx of LDL through $\Gamma_{\mathrm{End}}^{\mathcal{SS}}$, i.e., the endothelium is given by

$$-D_\ell^{\mathcal{SS}}\nabla\ell^{\mathcal{SS}} \cdot \boldsymbol{n}_{\mathrm{End}}^{\mathcal{SS}} = J_{\mathrm{Sol}}(\ell^{\mathcal{FS}}, \ell^{\mathcal{SS}}), \tag{4.34}$$

whereas foam cells cannot migrate through the endothelium:

$$-D_m^{\mathcal{SS}}\nabla m^{\mathcal{SS}} \cdot \boldsymbol{n}_{\mathrm{End}}^{\mathcal{SS}} = 0. \tag{4.35}$$

Remark. *It is highlighted again that the multiphysics model in this section neglects the advective transport of LDL through the endothelium and within the artery wall driven by transmural pressure gradients. To consider these effects either a full fluid-porous-structure interaction approach must be chosen for the cardiovascular mechanics [275] or the multiphysics model has to be enriched by a flow model on the structure-scatra domain [152]. The latter will be done in Section 6.1.2.1.*

Remark. *A quantitative model for inflammatory and immunological processes in early atherosclerosis is developed in Section 5 and incorporated into a model of concentrations of key species in the artery wall in Section 6.1.2.2. For simplicity, however, a simplistic reaction model for the inflammatory and immunological processes is used in this chapter.*

4.1.2.3 LDL transport through endothelium

The endothelium is frequently modeled as semi-permeable membrane described by the equations of *Kedem* and *Katchalsky* [29, 126, 145, 148, 221, 264, 294], where the applicability of the *Kedem-Katchalsky* equations was investigated by *Thomas* and *Mikulecky* [264]. Details on the *Kedem-Katchalsky* equations can be found in Section 2.2.2.1. It was assumed that the artery wall is a solid and hence the second *Kedem-Katchalsky* equation that describes the solute fluxes reduces to [29, 126]

$$J_{\mathrm{Sol}}\left(\ell^{\mathcal{FS}}, \ell^{\mathcal{SS}}\right) = P_\ell\left(\ell^{\mathcal{FS}} - \ell^{\mathcal{SS}}\right). \tag{4.36}$$

This neglection of the advective mass transport through the endothelium lies in agreement with observations in the literature [126, 268]. It is well-accepted that the localization of atherosclerosis correlates with hemodynamic factors, such as low wall shear stresses [118, 154, 216, 227]. The wall shear stresses $\boldsymbol{\tau}^{\mathcal{F}}$ of the fluid acting on the endothelium Γ_{End}, are calculated by removing the normal parts of the tractions

$$\boldsymbol{\tau}^{\mathcal{F}} = \boldsymbol{\sigma}^{\mathcal{F}}\, \boldsymbol{n}^{\mathcal{F}}_{\mathrm{End}} - \left(\left(\boldsymbol{n}^{\mathcal{F}}_{\mathrm{End}}\right)^{T} \boldsymbol{\sigma}^{\mathcal{F}} \boldsymbol{n}^{\mathcal{F}}_{\mathrm{End}} \right)\, \boldsymbol{n}^{\mathcal{F}}_{\mathrm{End}}. \tag{4.37}$$

The WSS dependency of the endothelium is on a much larger time scale than the cardiovascular mechanics. It is considered by adapting the diffusive permeability P_ℓ by a function s depending on the norm of the time-averaged WSS $<\boldsymbol{\tau}^{\mathcal{F}}>_t$:

$$J_{\mathrm{Sol}}\left(\ell^{\mathcal{FS}}, \ell^{\mathcal{SS}}, \boldsymbol{\tau}^{\mathcal{F}}\right) = P_\ell\; s(\|<\boldsymbol{\tau}^{\mathcal{F}}>_t\|)\left(\ell^{\mathcal{FS}} - \ell^{\mathcal{SS}}\right), \tag{4.38}$$

where time-average of the WSS $\boldsymbol{\tau}^{\mathcal{F}}$ at time t is defined as

$$<\boldsymbol{\tau}^{\mathcal{F}}>_t = \frac{1}{T_{\mathrm{Cycl}}} \int\limits_{t-T_{\mathrm{Cycl}}}^{t} \boldsymbol{\tau}^{\mathcal{F}}(s)\, \mathrm{d}s. \tag{4.39}$$

The function $s(\|<\boldsymbol{\tau}^{\mathcal{F}}>_t\|)$ is called the *(diffusive) permeability scaling factor* (PSF). For the shape of the PSF s the approach in [29] is followed:

$$s(\|<\boldsymbol{\tau}^{\mathcal{F}}>_t\|) = \frac{1}{\ln(2)} \ln\left(1 + \zeta_\tau \frac{\gamma_\tau}{\|<\boldsymbol{\tau}^{\mathcal{F}}>_t\| + \gamma_\tau}\right), \tag{4.40}$$

where the constants ζ_τ and γ_τ are free model parameters which have to be fitted to the specific geometry, see Section 4.3.1. The PSF is a monotonically decreasing function with respect to WSS resulting in an increased permeability of the endothelium with respect to LDL at regions of low WSS.

Remark. *One could also include other hemodynamic factors like the oscillatory shear index or the relative residence time [118, 216, 245] into the calculation of the PSF $s(\bullet)$. In contrast to the utilized PSF, however, the OSI and relative residence time are normalized quantities where no clear reference value exists (cf. Section 4.3.1). Therefore, they cannot be employed in a straightforward manner to adjust the endothelial permeability.*

4.1.3 Initial conditions and prestressing

To achieve a well-defined initial value problem, specific initial conditions have to be stated. For the cardiovascular mechanics model, zero initial conditions are used and the prescribed fluid influx $Q^{\mathcal{F}}_{\mathrm{In}}(t)$ is smoothly increased to its physiological level. The aim of this model is to utilize geometries stemming from *in vivo* medical imaging that do not represent a stress-free configuration. Hence, a prestressing according to [96] is applied to the structure field. Therein, the

Windkessel submodels on the outflow boundaries lead to a physiological diastolic pressure of the fluid field and hence to physiological loading of the structure comparable to the *in vivo* state.

For the concentrations in the artery wall, zero initial conditions are prescribed. For initial condition of the concentration in the blood, constant concentrations equal to values prescribed on the inflow boundary $\Gamma_{\mathrm{In}}^{\mathcal{FS}}$ are utilized.

4.2 Numerical procedure

The presented model of atherosclerosis is an adapted FSSTI problem and thus can be computationally treated as described in detail in Section 3.2.2. Therein, the weak formulations of the individual single-field models were established, spatially discretized in terms of the finite element method, temporally discretized in terms of the one-step-θ scheme and stability issues arising in the advection dominated fields were dealt with by residual-based stabilizations. This section gives a brief summary of the solution strategy for the multiphysics model and details on the requirements and generation of the utilized finite element mesh.

4.2.1 Solution strategy

A suitable solver strategy is exploited that takes into account the specific couplings between the individual fields as described in Section 3.2.2.2: The FSSTI model is addressed by a sequentially staggered scheme coupling the monolithic FSI and monolithic S2I submodels. Additionally, the fluid submodel is also coupled to the Windkessel submodels. The evolution of the multiple Windkessel pressures $p_{\mathrm{WK},i}^{\mathcal{F}}$ is described by *linear* ODEs, which allow deriving analytic relationships $p_{\mathrm{WK},i}^{\mathcal{F}}(Q_{\mathrm{Out},i}^{\mathcal{F}})$ between the Windkessel pressures $p_{\mathrm{WK},i}^{\mathcal{F}}$ and the outfluxes $Q_{\mathrm{Out},i}^{\mathcal{F}}$ through the different outflow boundaries $\Gamma_{\mathrm{Out},i}^{\mathcal{F}}$ [211]. Hence, the Windkessel submodels can be eliminated (cf. Figure 3.1) by expressing the interface traction on the fluid (cf. Equation (4.4)) directly by the integrated quantity $Q_{\mathrm{Out},i}^{\mathcal{F}}$ of the velocity unknowns $\boldsymbol{u}^{\mathcal{F}}$. Thus, no additional field for the Windkessel submodels and no additional unknowns for the Windkessel pressures are introduced. An illustration of the overall solver strategy of the multiphysics model for atherosclerosis including the corresponding coupling variables is given in Figure 4.3.

4.2.2 Finite element mesh

The finite element mesh for the spatial discretization is generated using Trelis (Csimsoft) such that it satisfies the following properties:

- It is conforming on the FSSTI interface Γ_{End}.
- In the fluid domain $\Omega^{\mathcal{F}}$ a boundary refinement is introduced to better resolve velocity gradients and concentrations ℓ and m near the FSSTI interface $\Gamma_{\mathrm{End}}^{\mathcal{F}}$.

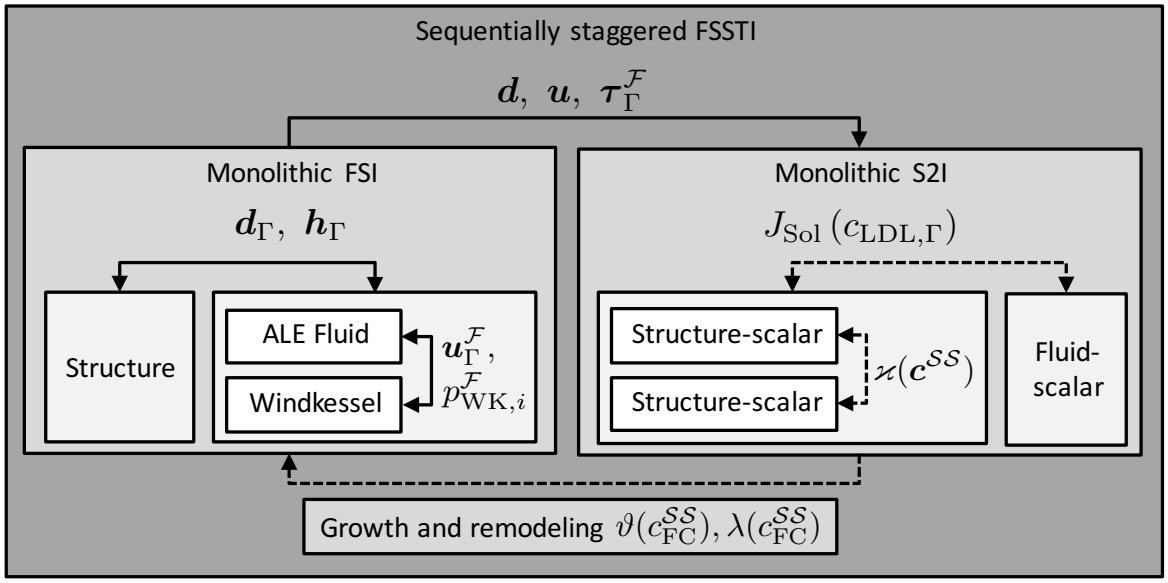

Figure 4.3 Schematic overview of solver strategy of the multiphysics model including the coupling variables between the fields. Simple and double arrows mark one-way and two-way couplings, respectively. Dotted arrows denote weak couplings, whereas solid arrows represent strong couplings. The subscript $(\bullet)_\Gamma$ indicates a surface coupled quantity $(\bullet)$, whereas without explicit subscript a volume coupled quantity is denoted.

- The structure domain $\Omega^{\mathcal{S}}$ is meshed using hexahedral elements such that F-bar element technology can be employed [58, 66].

The lumen of patient-specific geometries of aortic arches are difficult to mesh with hexahedral elements only. Hence, a tetrahedral dominated mesh with a hexahedral boundary layer is employed, where the tetrahedral and hexahedral elements of the fluid mesh are connected by pyramid shaped elements.

The generation of such a finite element mesh of a patient-specific lumen requires the use of an appropriate strategy as follows: First, the segmented geometry is reduced by the thickness of the fluid boundary layer leaving the geometry of the inner lumen. Subsequently, the (inner lumen)-(boundary layer) interface is meshed using quadrilateral surface elements with a *characteristic element length* h. The volume of the inner lumen is meshed using tetrahedral and pyramid shaped elements also with a characteristic element length h. The boundary layer is created by successive offsets of the quadrilateral meshed surface such that it consists of hexahedral elements with thicknesses of $\frac{h}{2}$, $\frac{h}{4}$, $\frac{h}{8}$ and $\frac{h}{16}$ toward the direction of the FSSTI interface Γ_{End}. The structure domain $\Omega^{\mathcal{S}}$ is adjacent to the FSSTI interface $\Gamma_{\mathrm{End}}^{\mathcal{F}}$ with constant thickness T. Its mesh is generated by another offset of the FSSTI interface $\Gamma_{\mathrm{End}}^{\mathcal{F}}$ with 6 element layers with an equidistant thickness. The finite element meshes of the ALE domain $\Omega^{\mathcal{G}}$ and the fluid-scatra domain $\Omega^{\mathcal{FS}}$ equal the fluid mesh. The finite element mesh of the structure-scatra domain $\Omega^{\mathcal{SS}}$ is equal to the structure mesh.

4.3 Computational case study and results

In this section the presented mathematical and computational model is calibrated to a murine-specific case, the computational results of the case study are given and the results compared with various literature. The geometry of the case study is a murine-specific reconstruction of the lumen of a non-atherosclerotic mouse (type C57BL/6J), see Figure 4.4. It was segmented from an *in vivo* magnetic resonance angiography from medical partners. The measurement was taken on a horizontal bore 7T small animal scanner (Discovery MR901, GE Healthcare) applying an ECG-triggered 3D gradient echo sequence achieving an in-plane resolution of $59\ \mu\mathrm{m}$ with a slice thickness of $250\ \mu\mathrm{m}$. The segmentation was performed in a semi-automatic fashion using Mimics (Materialise). Nevertheless, the achieved resolution did not allow for an exact segmentation of the artery wall. Thus, as only a small part of the artery tree is considered, the variation of the wall thickness is neglected and a constant wall thickness T is employed.

The discretization for the performed case study of the murine-specific geometry is visualized in Figure 4.4. A detailed summary of the utilized mesh as described in Section 4.2.2 with a characteristic element length $h = 0.06\ \mathrm{mm}$ (for comparison: the radius of the inflow boundary $\Gamma_{\mathrm{In}}^{\mathcal{F}}$ is $R_{\mathrm{In}} = 0.57\ \mathrm{mm}$) and a constant artery wall thickness $T = 0.08\ \mathrm{mm}$ [284] is given in Table 4.1. A mesh convergence analysis is performed in Section 4.3.3.

4.3.1 Model parameters

Due to a lack of suitable *in vivo* data, an exemplary set of key physiological data of mice from the literature is used to derive from it a set of model parameters for the given patient-specific geometry. The experimental results in [143] are utilized providing a complete set of physiological data – the mean volume influx $<Q_{\mathrm{In}}^{\mathcal{F}}>$, the length of the cardiac cycle T_{Cycl}, the diastolic pressure ${p_{\mathrm{dia}}}^{\mathcal{F}}$ and the systolic pressure ${p_{\mathrm{sys}}}^{\mathcal{F}}$ – from a single source. However, this data set is just one possible choice representing the mice studied in [143] where the systolic pressure ${p_{\mathrm{sys}}}^{\mathcal{F}}$ seems to be low compared to other studies [6, 282]

First, an overview of the parameters which have to be calibrated to the specific geometry is given and afterward the remaining parameters taken from the literature are listed, see Tables 4.3 and 4.4.

For the prescribed inflow velocities on $\Gamma_{\mathrm{In}}^{\mathcal{F}}$ given by Equation (4.3) the velocity profile $g^{\mathcal{F}}(t, \boldsymbol{x})$ and the total volume influx $Q_{\mathrm{In}}^{\mathcal{F}}(t)$ need to be specified. For the inflow profile $g^{\mathcal{F}}(t, \boldsymbol{x})$ a ninth order polynomial-shaped function is utilized [243], which is superimposed by a *Womersley* profile respecting the influence of the oscillatory influx on the velocity profile [138]. The temporal shape of the volume influx $Q_{\mathrm{In}}^{\mathcal{F}}(t)$ is taken from [211] and is scaled such that the length of the cardiac cycle T_{Cycl} and the time-averaged influx $<Q_{\mathrm{In}}^{\mathcal{F}}>$ fits to the murine physiology [6, 76, 143]: $T_{\mathrm{Cycl}} = 0.1\ \mathrm{s}$, $<Q_{\mathrm{In}}^{\mathcal{F}}> = 16.2\ \frac{\mathrm{ml}}{\mathrm{min}} = 270\ \frac{\mathrm{mm}^3}{\mathrm{s}}$. The resulting prescribed influx $Q_{\mathrm{In}}^{\mathcal{F}}(t)$ is plotted in Figure 4.5.

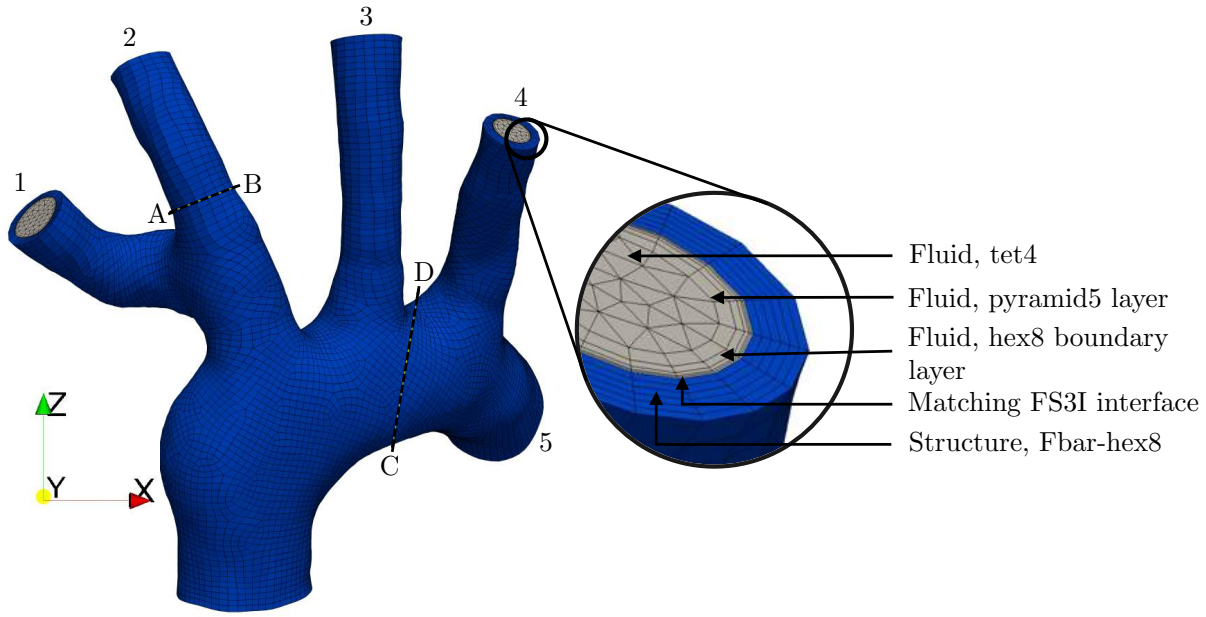

Figure 4.4 Conforming FSSTI mesh consisting of tetrahedral, hexahedral and pyramid shaped finite elements with a characteristic element length $h = 0.06$ mm. Gray represents the finite element mesh used for the fluid domain $\Omega^{\mathcal{F}}$, ALE domain $\Omega^{\mathcal{G}}$ and fluid-scatra domain $\Omega^{\mathcal{FS}}$. Blue represents the finite element mesh used for the structure domain $\Omega^{\mathcal{S}}$ and structure-scatra domain $\Omega^{\mathcal{SS}}$. The numbers indicate the numbering of the outlet boundaries and the lines AB and CD are the profile lines used in the mesh convergence analysis.

Table 4.1 Number of finite elements, number of nodes, degrees of freedom (DOF) per node and total DOF of the fluid domain $\Omega^{\mathcal{F}}$, structure domain $\Omega^{\mathcal{S}}$, ALE domain $\Omega^{\mathcal{G}}$, fluid-scatra domain $\Omega^{\mathcal{FS}}$ structure-scatra domain $\Omega^{\mathcal{SS}}$ and combinations of the mesh with a characteristic element length $h = 0.06$ mm.

Domains	# Finite elements	# Nodes	# DOF per node	# DOF
$\Omega^{\mathcal{F}}$	Tet4 315896, Pyr5 9523, Hex8 47615	108986	4	435944
$\Omega^{\mathcal{S}}$	Hex8 57138	67298	3	201894
$\Omega^{\mathcal{G}}$	Tet4 315896, Pyr5 9523, Hex8 47615	108986	3	326958
$\Omega^{\mathcal{FS}}$	Tet4 315896, Pyr5 9523, Hex8 47615	108986	1	108986
$\Omega^{\mathcal{SS}}$	Hex8 57138	67298	2	134596
$\Omega^{\mathcal{F}} \cup \Omega^{\mathcal{S}} \cup \Omega^{\mathcal{G}}$	430172	176284	5.47	964796
$\Omega^{\mathcal{FS}} \cup \Omega^{\mathcal{SS}}$	430172	176284	1.38	243582
All	430172	176284	6.85	1208378

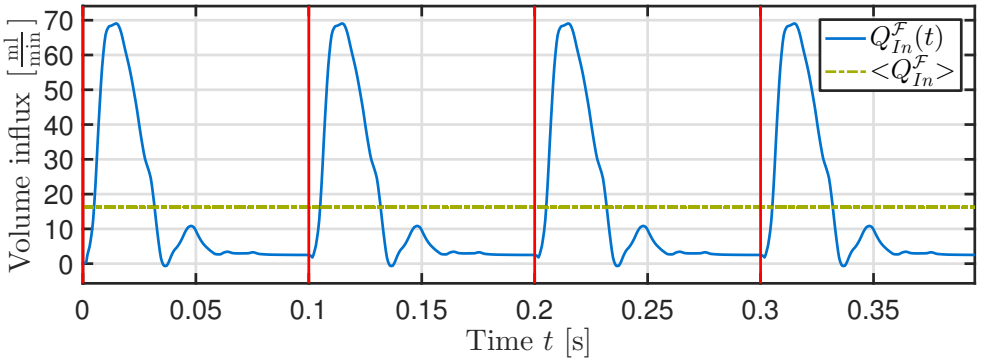

Figure 4.5 Prescribed fluid volume influx $Q^{\mathcal{F}}_{\mathrm{In}}(t)$ through $\Gamma^{\mathcal{F}}_{\mathrm{In}}$ and time-averaged influx $<Q^{\mathcal{F}}_{\mathrm{In}}>$ over time t. The volume influx is periodic with a periodicity of $T_{\mathrm{Cycl}} = 0.1$ s.

Table 4.2 Parameters for the calibration of the three-element Windkessel submodels and calibrated results. Approximated portion of volume outflux $\%Q^{\mathcal{F}}_{\mathrm{Out},i}$ and resulting characteristic resistance $R^{\mathcal{F}}_{\mathrm{C},i}$, peripheral resistance $R^{\mathcal{F}}_{\mathrm{P},i}$ and artery compliance $C^{\mathcal{F}}_i$ of each of the five three-element Windkessel submodels. All units are in mm, s, Pa.

i	$\%Q^{\mathcal{F}}_{\mathrm{Out},i}$	$R^{\mathcal{F}}_{\mathrm{C},i}$	$R^{\mathcal{F}}_{\mathrm{P},i}$	$C^{\mathcal{F}}_i$
1	11.36 %	16.93 $\frac{\mathrm{Pa\,s}}{\mathrm{mm}^3}$	384.18 $\frac{\mathrm{Pa\,s}}{\mathrm{mm}^3}$	$4.29 \cdot 10^{-4}$ $\frac{\mathrm{mm}^3}{\mathrm{Pa}_3}$
2	8.97 %	19.56 $\frac{\mathrm{Pa\,s}}{\mathrm{mm}^3}$	426.39 $\frac{\mathrm{Pa\,s}}{\mathrm{mm}^3}$	$3.29 \cdot 10^{-4}$ $\frac{\mathrm{mm}^3}{\mathrm{Pa}_3}$
3	12.73 %	12.00 $\frac{\mathrm{Pa\,s}}{\mathrm{mm}^3}$	369.63 $\frac{\mathrm{Pa\,s}}{\mathrm{mm}^3}$	$4.81 \cdot 10^{-4}$ $\frac{\mathrm{mm}^3}{\mathrm{Pa}_3}$
4	7.55 %	21.49 $\frac{\mathrm{Pa\,s}}{\mathrm{mm}^3}$	441.62 $\frac{\mathrm{Pa\,s}}{\mathrm{mm}^3}$	$2.86 \cdot 10^{-4}$ $\frac{\mathrm{mm}^3}{\mathrm{Pa}}$
5	59.39 %	4.67 $\frac{\mathrm{Pa\,s}}{\mathrm{mm}^3}$	69.73 $\frac{\mathrm{Pa\,s}}{\mathrm{mm}^3}$	$21.50 \cdot 10^{-4}$ $\frac{\mathrm{mm}^3}{\mathrm{Pa}}$

The parameters of each of the five three-element Windkessel submodels must be fitted to the murine physiology and the specific geometry. For the murine physiology, a diastolic pressure $p^{\mathcal{F}}_{\mathrm{dia}} = 77$ mmHg $= 10265.8$ Pa and a systolic pressure $p^{\mathcal{F}}_{\mathrm{sys}} = 100$ mmHg $= 13332.2$ Pa are assumed as measured in [143]. The compliance of the geometry is approximated by a simulation of the structure submodel, where only a hydrostatic pressure is applied. The geometry is first prestressed to the diastolic pressure p_{dia} and afterward the pressure is further increased to the systolic pressure $p^{\mathcal{F}}_{\mathrm{sys}}$. Then the compliance of the given geometry can be approximated by

$$C_{\mathrm{geo}} \approx \frac{V^{\mathcal{F}}_{\mathrm{sys}} - V^{\mathcal{F}}_{\mathrm{dia}}}{p^{\mathcal{F}}_{\mathrm{sys}} - p^{\mathcal{F}}_{\mathrm{dia}}} = 11.86 \cdot 10^{-4} \, \frac{\mathrm{mm}^3}{\mathrm{Pa}}, \tag{4.41}$$

where $V^{\mathcal{F}}_{\mathrm{sys}}$ and $V^{\mathcal{F}}_{\mathrm{dia}}$ are the volume of the lumen measured at the systolic and diastolic pressure level, respectively. Furthermore, the approximated portions of volume outflux $\%Q^{\mathcal{F}}_{\mathrm{Out},i}$ through each of the five outflow boundaries $\Gamma^{\mathcal{F}}_{\mathrm{Out},i}$ is approximated by the ratio of the surface area of $\Gamma^{\mathcal{F}}_{\mathrm{Out},i}$ to the total surface area of all five outflow boundaries. Following the approach in [292] and [139], Windkessel parameters as given in Table 4.2 are achieved.

The growth parameter $\alpha^{\mathcal{S}}_m$ in Equation (4.17) corresponds to the amount of unite volume occupied by a unit scalar of foam cells. Following the approach in [90], a constant mass density $\varrho^{\mathcal{S}}$ of the

artery wall – which in advanced states consists of both, healthy and atherosclerotic aortic tissue – is applied. Hence, it follows:

$$\alpha_m^{\mathcal{S}} = \frac{1}{\varrho_0^{\mathcal{S}}} = 1.0 \cdot 10^3 \, \frac{\mathrm{mm}^3}{\mathrm{g}}. \tag{4.42}$$

The remaining parameters of the FSI submodel are independent of the specific geometry and are taken from the literature. However, no complete data set based on murine experiments exists such that the used parameters for the *Carreau-Yasuda* model, the surrounding tissue and the constitutive laws are based on human experiments. An overview of fitted as well as the remaining parameters of the FSI submodel is found in Table 4.3.

For the calibration of the permeability scaling factor $s(\|<\boldsymbol{\tau}^{\mathcal{F}}>\|)$ in Equation (4.40) the argumentation of *Cheng et al.* [40] is followed that endothelial cells are primed to the present flow condition. Therefore, the approach by *Calvez et al.* [29] is generalized. The two model parameters ζ_τ and γ_τ of the monotonically decreasing function are determined such that the following two conditions are fulfilled:

1. The permeability scaling factor vanishes, when the norm $\|\boldsymbol{\tau}^{\mathcal{F}}\|$ of the wall shear stresses is equal to the reference value $\|\overline{\boldsymbol{\tau}}^{\mathcal{F}}\|$. This reference value is approximated by considering a stationary *Poiseuille* flow with an equivalent total volume influx $<Q_{\mathrm{In}}^{\mathcal{F}}>$ through a straight pipe with the same radius R_{In} as the inflow boundary $\Gamma_{\mathrm{In}}^{\mathcal{F}}$. Hence, it is required:

$$\begin{aligned} s(\|\overline{\boldsymbol{\tau}}^{\mathcal{F}}\|) &= 1 \text{ with} \\ \|\overline{\boldsymbol{\tau}}^{\mathcal{F}}\| &= \frac{4}{\pi} \frac{\mu_\infty^{\mathcal{F}} <Q_{\mathrm{In}}^{\mathcal{F}}>}{(R_{\mathrm{In}})^3} = 6.404 \text{ Pa}. \end{aligned} \tag{4.43}$$

2. According to measurements in [117], the local permeability of the endothelium with respect to LDL in regions with high permeability is up to a factor of 25 higher than in regions with low permeability. It is assumed that the harmonic mean of those two extrema corresponds to the case of $s(\|\overline{\boldsymbol{\tau}}^{\mathcal{F}}\|) = 1$. Since the permeability is highest for the case $\|\boldsymbol{\tau}^{\mathcal{F}}\| = 0$, the PSF must fulfill:

$$s(0) = 5. \tag{4.44}$$

The two assumptions lead to

$$\begin{aligned} s(\|<\boldsymbol{\tau}^{\mathcal{F}}>\|) &= \frac{1}{\ln(2)} \ln\left(1 + \frac{\left(1 + \frac{1}{2^{s(0)}-2}\right)\|\overline{\boldsymbol{\tau}}^{\mathcal{F}}\|}{\|<\boldsymbol{\tau}^{\mathcal{F}}>\| + \frac{1}{2^{s(0)}-2}\|\overline{\boldsymbol{\tau}}^{\mathcal{F}}\|}\right) \\ &= \frac{1}{\ln(2)} \ln\left(1 + 31\frac{2.13 \cdot 10^{-1} \text{ Pa}}{\|<\boldsymbol{\tau}^{\mathcal{F}}>\| + 2.13 \cdot 10^{-1} \text{ Pa}}\right), \end{aligned} \tag{4.45}$$

which is plotted in Figure 4.6. An overview of the calibrated and remaining physiological parameters for the S2I submodel is found in Table 4.4.

Table 4.3 Parameters of FSI submodel. Parameters are sorted by the first appearance in the model. All units are in mm, g, s, Pa.

Parameter	Description	Value	Source
$\varrho^{\mathcal{F}}$	Mass density of blood	$1.05 \cdot 10^{-3}\ \frac{\mathrm{g}}{\mathrm{mm}^3}$	[142]
$\mu_\infty^{\mathcal{F}}$	Dynamic viscosity of blood for high shear rates	$3.45 \cdot 10^{-3}\ \mathrm{Pa\ s}$	[43]
$\mu_0^{\mathcal{F}}$	Dynamic viscosity of blood for zero shear rates	$5.6 \cdot 10^{-2}\ \mathrm{Pa\ s}$	[43]
$\kappa^{\mathcal{F}}$	Characteristic time of *Carreau-Yasuda* model	$1.902\ \mathrm{s}$	[43]
$b^{\mathcal{F}}$	Parameter of *Carreau-Yasuda* model	1.25	[43]
$a^{\mathcal{F}}$	Parameter of *Carreau-Yasuda* model	0.624	[43]
$Q_{\mathrm{In}}^{\mathcal{F}}(t)$	Influx rate over time	Figure 4.5	[143, 211]
T_{Cycl}	Length of cardiac cycle	$0.1\ \mathrm{s}$	[76]
$<Q_{\mathrm{In}}^{\mathcal{F}}>$	Time-averaged influx rate	$270.0\ \frac{\mathrm{mm}^3}{\mathrm{s}}$	[143]
$C_i^{\mathcal{F}}$	Artery compliances of Windkessel on $\Gamma_{\mathrm{Out},i}^{\mathcal{F}}$	Table 4.2	Table 4.2
$R_{\mathrm{C},i}^{\mathcal{F}}$	Characteristic resistances of Windkessel on $\Gamma_{\mathrm{Out},i}^{\mathcal{F}}$	Table 4.2	Table 4.2
$R_{\mathrm{P},i}^{\mathcal{F}}$	Peripheral resistances of Windkessel on $\Gamma_{\mathrm{Out},i}^{\mathcal{F}}$	Table 4.2	Table 4.2
$\varrho_0^{\mathcal{S}}$	Material mass density of artery wall	$1.0 \cdot 10^{-3}\ \frac{\mathrm{g}}{\mathrm{mm}^3}$	[90]
$k_{\mathrm{Wall}}^{\mathcal{S}}$	Spring stiffness of surrounding tissue	$5.0 \cdot 10^{3}\ \frac{\mathrm{Pa}}{\mathrm{mm}}$	[60, 197]
$c_{\mathrm{Wall}}^{\mathcal{S}}$	Dashpot viscosity of surrounding tissue	$100.0\ \frac{\mathrm{Pa\ s}}{\mathrm{mm}}$	[197]
$k_{\mathrm{Out}}^{\mathcal{S}}$	Spring stiffness of succeeding tissue	$2.0 \cdot 10^{4}\ \frac{\mathrm{Pa}}{\mathrm{mm}}$	[197]
$c_{\mathrm{Out}}^{\mathcal{S}}$	Dashpot viscosity of succeeding tissue	$100.0\ \frac{\mathrm{Pa\ s}}{\mathrm{mm}}$	[197]
$\alpha_m^{\mathcal{S}}$	Growth parameter	$1.0 \cdot 10^{3}\ \frac{\mathrm{mm}^3}{\mathrm{g}}$	Eq. (4.42)
$c_{0,\mathrm{Ao}}^{\mathcal{S}}$	Stiffness of aortic ground material	$47.43 \cdot 10^{3}\ \mathrm{Pa}$	[230]
$c_{1,1}^{\mathcal{S}}$	Stiffness of first fiber	$35.23 \cdot 10^{3}\ \mathrm{Pa}$	[230]
$c_{2,1}^{\mathcal{S}}$	Exponential parameter of first fiber	$7.65 \cdot 10^{-6}$	[230]
$\delta_1^{\mathcal{S}}$	Orientation angle of first fiber	$0°$	[230]
$c_{1,2}^{\mathcal{S}}$	Stiffness of second fiber	$40.84 \cdot 10^{3}\ \mathrm{Pa}$	[230]
$c_{2,2}^{\mathcal{S}}$	Exponential parameter of second fiber	0.1	[230]
$\delta_2^{\mathcal{S}}$	Orientation angle of second fiber	$90°$	[230]
$c_{1,3}^{\mathcal{S}}$	Stiffness of third fiber	$15.21 \cdot 10^{3}\ \mathrm{Pa}$	[230]
$c_{2,3}^{\mathcal{S}}$	Exponential parameter of third fiber	2.58	[230]
$\delta_3^{\mathcal{S}}$	Orientation angle of third fiber	$48.98°$	[230]
$c_{1,4}^{\mathcal{S}}$	Stiffness of fourth fiber	$15.21 \cdot 10^{3}\ \mathrm{Pa}$	[230]
$c_{2,4}^{\mathcal{S}}$	Exponential parameter of fourth fiber	2.58	[230]
$\delta_4^{\mathcal{S}}$	Orientation angle of fourth fiber	$-48.98°$	[230]
$\tau_{\mathrm{FC}}^{\mathcal{S}}$	Relaxation time of lipid material	$47.5 \cdot 10^{-3}\ \mathrm{s}$	[203]
$c_{0,\mathrm{FC}}^{\mathcal{S}}$	Stiffness of lipid material	$10.0 \cdot 10^{3}\ \mathrm{Pa}$	[9]

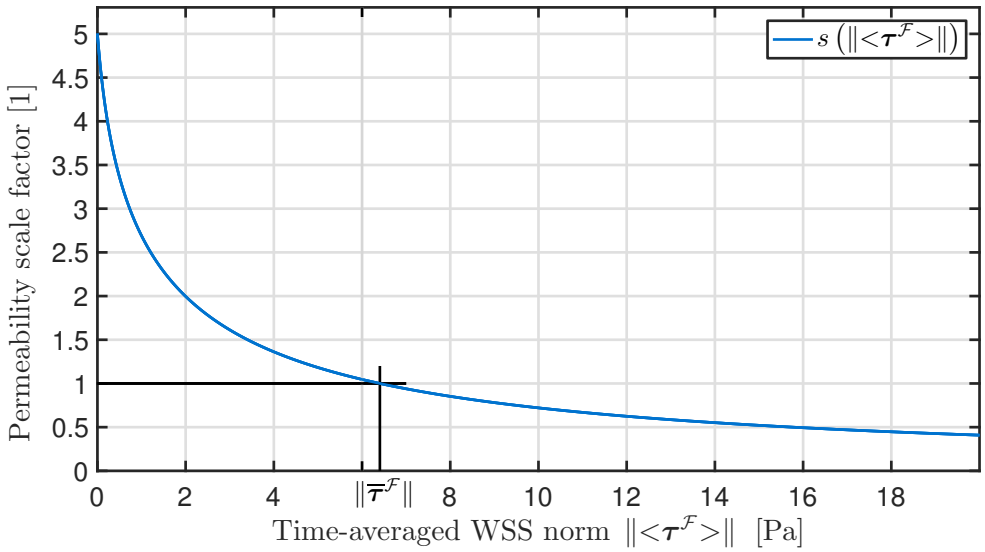

Figure 4.6 Calibrated law for the permeability scaling factor $s(\|<\boldsymbol{\tau}^{\mathcal{F}}>\|)$ plotted over the norm of the time-averaged wall shear stresses $\|<\boldsymbol{\tau}^{\mathcal{F}}>\|$ of the fluid. $\|\overline{\boldsymbol{\tau}}^{\mathcal{F}}\| = 6.404$ Pa is the approximated reference value of the WSS.

Table 4.4 Parameters of S2I submodel. Parameters are sorted by the first appearance in the model. All units are in mm, g, s, Pa.

Parameter	Description	Value	Source
$D_{\ell}^{\mathcal{FS}}$	Diffusivity of LDL in blood	$3.07 \cdot 10^{-5}$ $\frac{\text{mm}^2}{\text{s}}$	[176, 255, 269]
$\ell_{\text{In}}^{\mathcal{FS}}$	Concentration of LDL at $\Gamma_{\text{In}}^{\mathcal{FS}}$	$1.22 \cdot 10^{-6}$ $\frac{\text{g}}{\text{mm}^3}$	[89]
$D_{\ell}^{\mathcal{SS}}$	Diffusivity of LDL in artery wall	$3.5 \cdot 10^{-6}$ $\frac{\text{mm}^2}{\text{s}}$	[29, 255, 267]
$D_{m}^{\mathcal{SS}}$	Diffusivity of foam cells in artery wall	0.0	[90]
P_{ℓ}	Diffusive permeability of endothelium	$1.7 \cdot 10^{-8}$ $\frac{\text{mm}}{\text{s}}$	[268, 294]
ζ_{τ}	Permeability scaling factor parameter	31	Eq. (4.45)
γ_{τ}	Permeability scaling factor parameter	$2.13 \cdot 10^{-1}$ Pa	Eq. (4.45)

4.3.2 Dimensionless parameters

From the parameters in Table 4.3 and Table 4.4 dimensionless parameters are calculated. For the fluid submodel, the *Reynolds* number Re at the inflow boundary is given by

$$Re = \frac{2\varrho^{\mathcal{F}}\|\boldsymbol{u}^{\mathcal{F}}\|R_{\text{In}}}{\mu_{\infty}^{\mathcal{F}}}, \tag{4.46}$$

where $\boldsymbol{u}^{\mathcal{F}}$ is the characteristic velocity. Using the peak velocity at the inflow boundary $\Gamma_{\text{In}}^{\mathcal{F}}$, i.e., $\max_{\boldsymbol{u}^{\mathcal{F}} \in \Gamma_{\text{In}}^{\mathcal{F}}} \|\boldsymbol{u}^{\mathcal{F}}\|$ results in an approximation for the peak *Reynolds* number $Re_{\text{Peak}} = 411.3$. Using the temporal and spatial mean of the velocities on the inflow boundary results in an approximation for the mean *Reynolds* number $Re_{\text{Mean}} = 91.9$. The peak and mean *Reynolds* numbers

are slightly higher than found in the literature [6, 76, 133, 257] The *Womersley* number Wo of the fluid is given by

$$Wo = \sqrt{\frac{2\pi \varrho^{\mathcal{F}} R_{\mathrm{In}}^2}{T_{\mathrm{Cycl}}\, \mu_{\infty}^{\mathcal{F}}}} = 2.49, \tag{4.47}$$

fitting very well to the murine physiology [6, 76, 133, 257]. Since both *Reynolds* numbers Re_{Peak} and Re_{Mean} as well as the *Womersley* number Wo are small, the behavior of the fluid is viscous-dominated and in the laminar regime.

The dimensionless parameter of the transport of LDL with the blood flow governed by the advection-diffusion equation is the Péclet number Pe given by

$$Pe = \frac{2\|\boldsymbol{u}^{\mathcal{F}}\| R_{\mathrm{In}}}{D_{\ell}^{\mathcal{FS}}}. \tag{4.48}$$

Inserting again the peak and mean velocity the range for the *Péclet* number is $Pe \in [9.82 \cdot 10^6; 4.40 \cdot 10^7]$ being in the physiological regime of LDL transport [246]. Hence, the transport with the blood flow is advection dominated, except for regions close to the no-slip fluid-structure interface $\Gamma_{\mathrm{End}}^{\mathcal{F}}$.

4.3.3 Convergence analysis

To prove the validity of the computational results a spatial and temporal convergence analysis is performed. The convergence of the fluid velocities $\boldsymbol{u}^{\mathcal{F}}$ and the ALE displacements $\boldsymbol{d}^{\mathcal{G}}$ is exemplarily checked over two distinct lines AB and CD as indicated in Figure 4.4.

The spatial convergence is analyzed by utilizing the constant time step size $\Delta t = 2.5 \cdot 10^{-4}$ s in combination with meshes as described in Section 4.2.2 with characteristic element lengths h of 0.04 mm, 0.06 mm, 0.09 mm and 0.12 mm. The velocity profiles of the four meshes over the lines AB and CD at the peak of the systolic phase of the fifth cardiac cycle (i.e., $t = 0.412$ s) is plotted in Figure 4.7. The meshes with $h = 0.04$ mm and $h = 0.06$ mm possess qualitatively the same behavior. Quantitatively, the relative $\mathcal{L}^2$-errors of the velocities $\frac{\|\boldsymbol{u}^{\mathcal{F}}_{h=0.04\mathrm{mm}} - \boldsymbol{u}^{\mathcal{F}}_{h=0.06\mathrm{mm}}\|_{\mathcal{L}^2}}{\|\boldsymbol{u}^{\mathcal{F}}_{h=0.06\mathrm{mm}}\|_{\mathcal{L}^2}}$ and the displacements $\frac{\|\boldsymbol{d}^{\mathcal{G}}_{h=0.04\mathrm{mm}} - \boldsymbol{d}^{\mathcal{G}}_{h=0.06\mathrm{mm}}\|_{\mathcal{L}^2}}{\|\boldsymbol{d}^{\mathcal{G}}_{h=0.06\mathrm{mm}}\|_{\mathcal{L}^2}}$ over the lines AB and CD between the two finest meshes are below $1,6\%$.

Additionally to the velocities and displacements, the spatial convergence of the WSS and *von Mises* stresses is exemplarily checked at the four intersection points of the fluid-structure interface $\Gamma_{\mathrm{End}}^{\mathcal{F}}$ and the lines AB and CD. The relative errors of the WSS between the two finest meshes at these four points are below 2.75%. The relative errors of the *von Mises* stresses between the finest two meshes at these four points are below 7.38% but are within the asymptotic range.

To analyze the temporal convergence, the mesh with a characteristic element length $h = 0.06$ mm is utilized with three time step sizes Δt of $1.25 \cdot 10^{-4}$ s, $2.5 \cdot 10^{-4}$ s and $5.0 \cdot 10^{-4}$ s. Again the velocity profiles over the lines AB and CD are analyzed and plotted at time $t = 0.412$ s in Figure

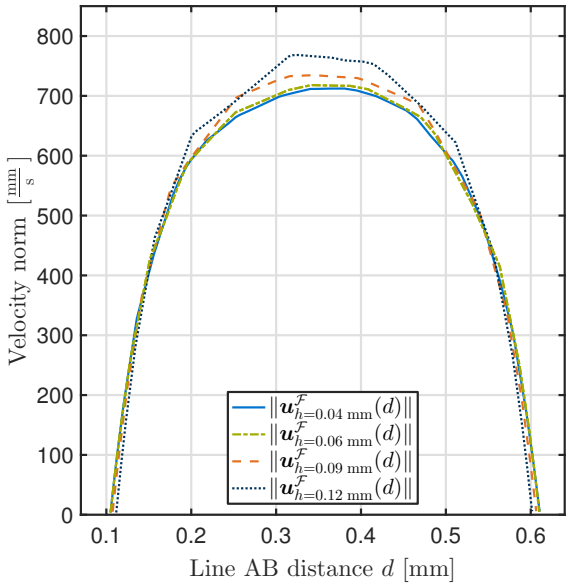

(a) Comparison of the velocity profiles over the line AB (see Figure 4.4) for different meshes with characteristic element lengths h of 0.04 mm, 0.06 mm, 0.09 mm, 0.12 mm and constant time step size $\Delta t = 2.5 \cdot 10^{-4}$ s at time $t = 0.412$ s.

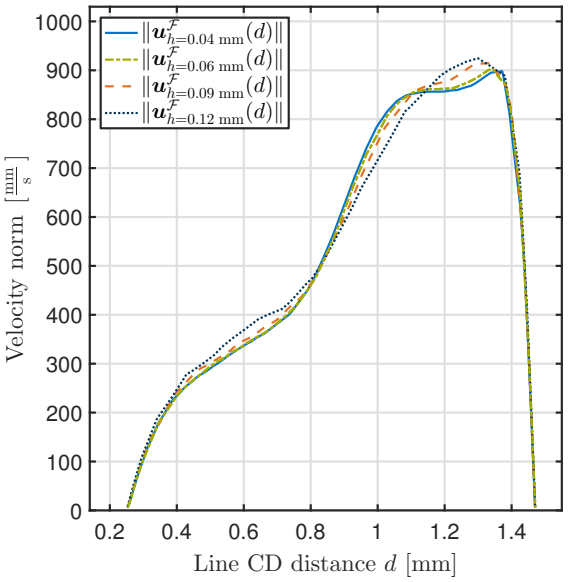

(b) Comparison of the velocity profiles over the line CD (see Figure 4.4) for different meshes with characteristic element lengths h of 0.04 mm, 0.06 mm, 0.09 mm, 0.12 mm and constant time step size $\Delta t = 2.5 \cdot 10^{-4}$ s at time $t = 0.412$ s.

Figure 4.7 Spatial convergence study.

4.8. Temporal convergence is sufficiently reached with a time step size of $\Delta t = 2.5 \cdot 10^{-4}$ s. Quantitatively, the relative L_2-error of the velocities and the displacements over the lines AB and CD between the smallest two time step sizes are below $1,3\%$.

The qualitatively same spatial and temporal convergence behavior was observed for other points and profile lines too. As the wall stress is no quantity of particular interest in the present model, the mesh with a characteristic element length $h = 0.06$ mm in combination with a constant time step size $\Delta t = 2.5 \cdot 10^{-4}$ s is further employed.

4.3.4 Model validation

To show the qualitative validity of the presented mathematical model and its parameters the computational results are compared to cardiovascular measurements and computational results from the literature. The Windkessel submodels determining the pressure of the fluid start with an unphysiological zero pressure and requires approximately four cardiac cycles to reach a periodic state. Hence, in the following the computed results from the seventh simulated cardiac cycle are utilized. Exemplarily, the Windkessel pressure at the outflow boundary $\Gamma_{\text{Out},5}$ over time t is plotted in Figure 4.9. In its periodic state the Windkessel submodel at $\Gamma_{\text{Out},5}$ is oscillating between the diastolic pressure $p_{\text{dia}} \approx 74.0$ mmHg $= 9867.0$ Pa and systolic pressure $p_{\text{sys}} \approx 102.5$ mmHg $= 13660.6$ Pa, being close to the assumed pressure levels [143]. Additionally, the qualitative shape of the pressure over time is in good agreement with the results

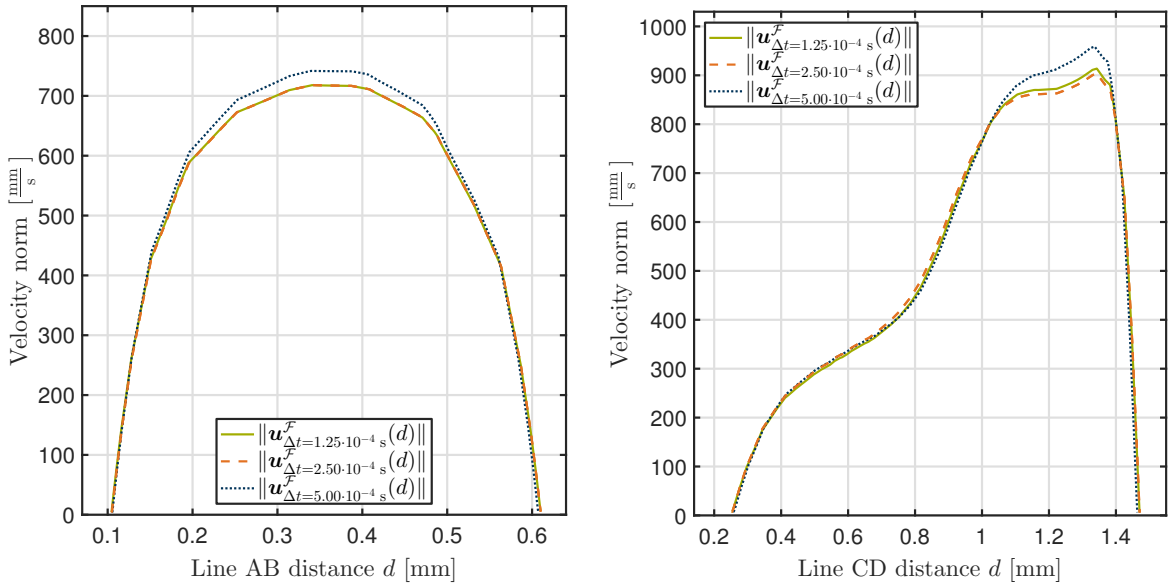

(a) Comparison of the velocity profiles over the line AB (see Figure 4.4) for different time step sizes Δt of $1.25 \cdot 10^{-4}$ s, $2.5 \cdot 10^{-4}$ s, $5.0 \cdot 10^{-4}$ s and a mesh with characteristic element length $h = 0.06$ mm at time $t = 0.412$ s.

(b) Comparison of the velocity profiles over the line CD (see Figure 4.4) for different time step sizes Δt of $1.25 \cdot 10^{-4}$ s, $2.5 \cdot 10^{-4}$ s, $5.0 \cdot 10^{-4}$ s and a mesh with characteristic element length $h = 0.06$ mm at time $t = 0.412$ s.

Figure 4.8 Temporal convergence study.

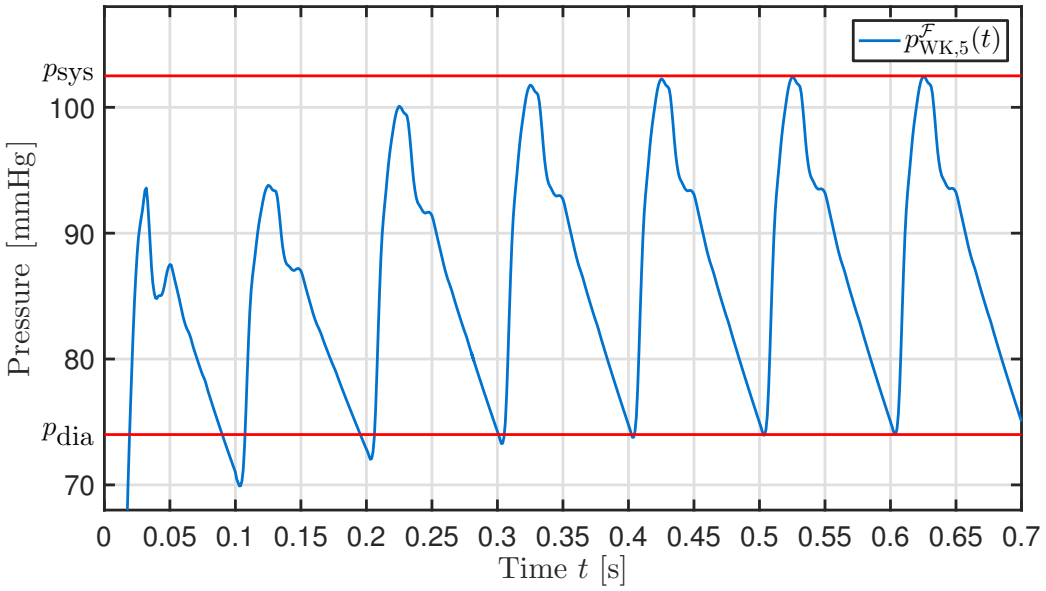

Figure 4.9 Pressure of three-element Windkessel on outflow $\Gamma_{\mathrm{Out},5}$ over time t. After approximately four cardiac cycles the periodic state with the diastolic pressure $p_{\mathrm{dia}} = 74.0$ mmHg and the systolic pressure $p_{\mathrm{sys}} = 102.5$ mmHg is reached.

achieved in [211]. As a result of the fluid pressure and the prestressing of the structure, the structure undergoes a maximal radial enlargement of the inner artery wall of around $14 - 17$ % in the

aortic arch and around $8-12\ \%$ in its branches, which is in good agreement to the measurements in [179]. Due to the pulsatile fluid flow the instantaneous WSS $\boldsymbol{\tau}^{\mathcal{F}}$ changes rapidly over time. But since the WSS-dependent migration of LDL into the artery wall is on a much larger time scale than the cardiac cycle, it is convenient to look at the time-averaged WSS $<\boldsymbol{\tau}>^{\mathcal{F}}$, where the time index is dropped to ease notation. If not explicitly stated otherwise the time-average is taken over the seventh simulated cardiac cycle. The estimated reference WSS $\|\overline{\boldsymbol{\tau}}^{\mathcal{F}}\| = 6.404\ \mathrm{Pa}$ (see Equation (4.43)) lies in perfect agreement with measurements from the literature [40]. The norm of the peak of the computed time-averaged WSS $\|<\boldsymbol{\tau}^{\mathcal{F}}>\|$ is $49.28\ \mathrm{Pa}$ which corresponds to the 7.7 times of the norm of the reference WSS $\|\overline{\boldsymbol{\tau}}^{\mathcal{F}}\|$, both lying in good agreement with computational results from the literature [76, 257]. When the instantaneous WSS $\boldsymbol{\tau}^{\mathcal{F}}$ is used in Equation (4.45), the instantaneous PSF $s(\|\boldsymbol{\tau}^{\mathcal{F}}\|)$ is computed. However, in experiments the long time behavior is measured, which is determined by the mean of the PSF. Therefore, one can computationally investigate three different scenarios: the time-average of the instantaneous PSF $<s(\|\boldsymbol{\tau}^{\mathcal{F}}\|)>$, the PSF of the time-averaged norm of the WSS $s(<\|\boldsymbol{\tau}^{\mathcal{F}}\|>)$ and the PSF of the norm of the time-averaged WSS $s(\|<\boldsymbol{\tau}^{\mathcal{F}}>\|)$. The computational study of these three cases showed that only the latter case is able to match observations from the literature [76, 185]. The second case did produce a qualitatively but not quantitatively correct PSF pattern and the first did result in a more or less homogeneous PSF. In the following $s(\|<\boldsymbol{\tau}^{\mathcal{F}}>\|)$ is called the time-averaged PSF to ease the language. It is visualized in the anterior and posterior view in Figures 4.10(a) and 4.10(b), respectively. The time-averaged PSF varies in the range between 0.18 and 4.74. Hence, the computed scalings differ by a factor of 26.3 showing very good agreement to the measurements in [117].

As visible in Figure 4.10(a) the simulated regions with high endothelial permeability and hence high risk for atherosclerotic driven plaque formation are located at the ascending aorta, near bifurcations and at the bottom and side of the aortic arch. This qualitative phenomena was also observed in experiments [5, 185] and lies in good qualitative agreement with earlier computational results [11, 52, 76, 257]. Moreover, the location of atherosclerotic plaques at these sites is qualitatively corroborated by experimental observations with atherosclerotic mice models, see Figure 4.11.

Remark. *Even if not explicitly considered in the computation of the PSF, the spatial distribution of the OSI* $o(\boldsymbol{\tau}^{\mathcal{F}}) = \frac{1}{2}\left(1 - \frac{\|<\boldsymbol{\tau}^{\mathcal{F}}>\|}{<\|\boldsymbol{\tau}^{\mathcal{F}}\|>}\right)$ *[118, 216, 245] is plotted from two perspectives in Figures 4.10(c) and 4.10(d). An OSI of zero corresponds to regions of non-oscillatory and an OSI of* 0.5 *to regions of highly oscillatory flow. As visible the pattern is comparable to the computed PSF visualized in Figures 4.10(a) and 4.10(b). This supports the theory that the OSI may also be a valid indicator for atherosclerosis plaque localization as is critically discussed in the literature, see [216] and references therein. However, it is not straightforward to use the OSI to adjust the endothelial permeability as there is, in contrast to the utilized PSF, no clear reference value.*

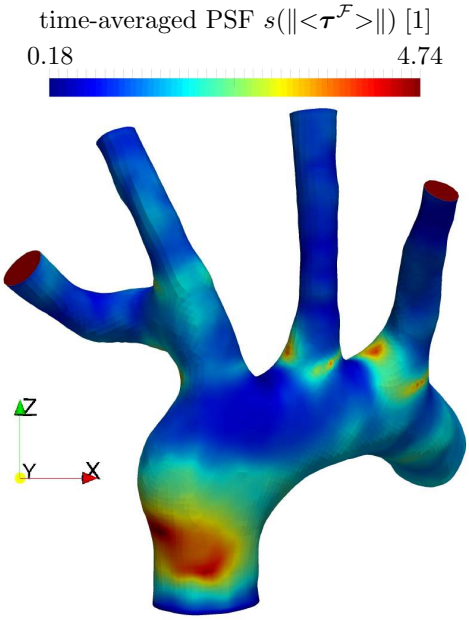

(a) Anterior view of the spatial distribution of time-averaged permeability scaling factor $s(\|<\boldsymbol{\tau}^{\mathcal{F}}>\|)$.

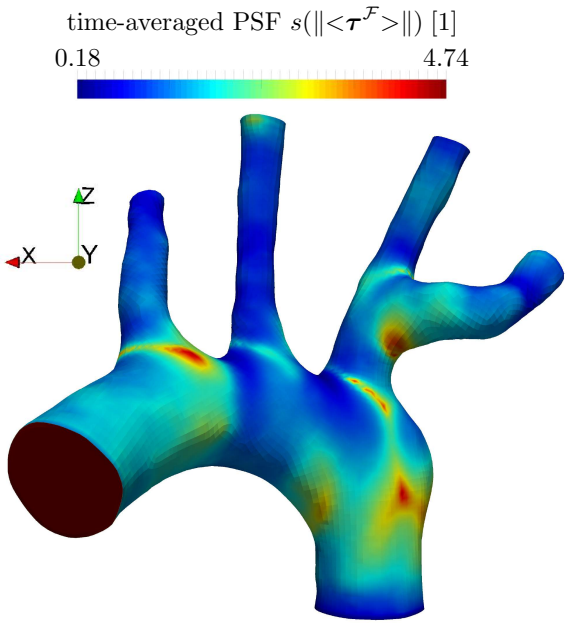

(b) Posterior view of the spatial distribution of time-averaged permeability scaling factor $s(\|<\boldsymbol{\tau}^{\mathcal{F}}>\|)$.

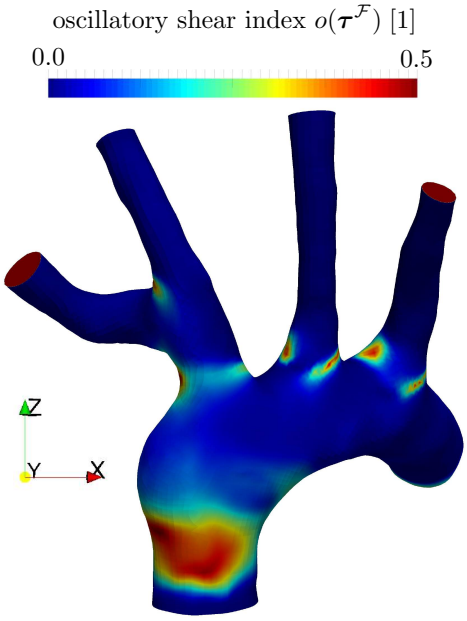

(c) Anterior view of the spatial distribution of oscillatory shear index $o(\boldsymbol{\tau}^{\mathcal{F}})$.

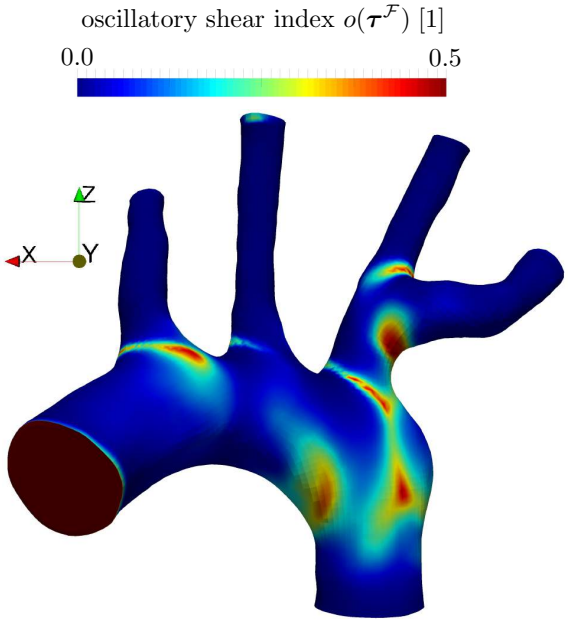

(d) Posterior view of the spatial distribution of oscillatory shear index $o(\boldsymbol{\tau}^{\mathcal{F}})$.

Figure 4.10 Spatial distribution of the time-averaged permeability scaling factor and oscillatory shear index.

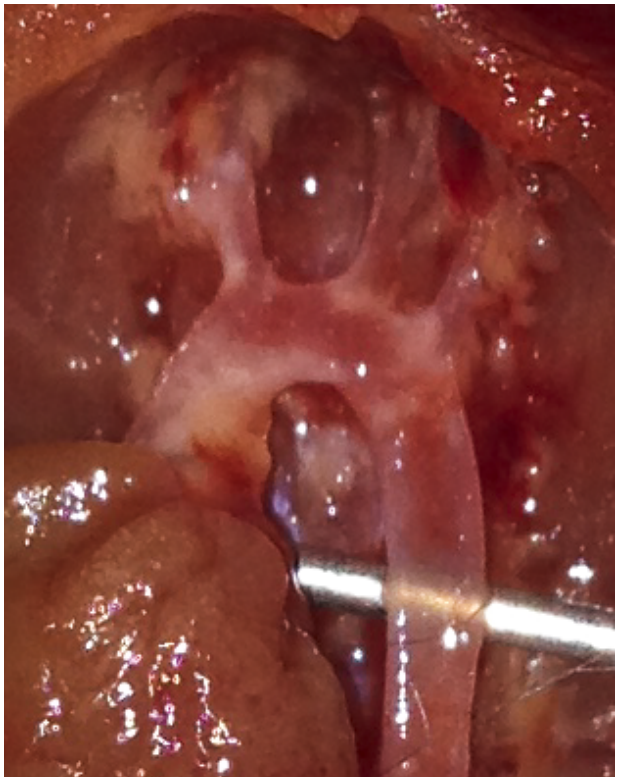

Figure 4.11 Dissection of an aortic arch of a LDL receptor-deficient mouse (type B6.129S7-Ldlrtm1Her/J) with atherosclerotic plaques (white).

4.3.5 Influence of compliance of artery wall and pulsatile flow

The influence of model reductions frequently found in the literature is studied. Therefore, the PSF derived from the multiphysics model with the PSF of reduced models is compared. As model reductions, two simplified versions of the presented model are considered.

The first reduced model is the case of a non-compliant artery wall, resulting in a *rigid wall model*. This simplification is enforced by the addition of the condition $\boldsymbol{d}^{\mathcal{S}} = \mathbf{0}$ compared to the full model. Such types of models are frequently proposed, especially in the context of porous media models of the artery wall, see e.g. [29, 178, 221, 255, 294]. The computed time-averaged PSF $s(\|<\boldsymbol{\tau}^{\mathcal{F}}>\|)$ of the rigid wall model is visualized in Figure 4.12(a). The computed OSI $o(\boldsymbol{\tau}^{\mathcal{F}})$ for the rigid wall model is visualized in Figure 4.12(c).

The second reduced model scenario frequently found in the literature are stationary, *time-averaged flow models* [29, 142, 197, 267, 276]. This simplification is achieved by assuming the influx to be constant in time, i.e., by $Q^{\mathcal{F}}_{\mathrm{In}}(t) = <Q^{\mathcal{F}}_{\mathrm{In}}>$. As consequence, the pressure of the fluid determined by the Windkessel submodels is constant and no displacements can be expected from the loaded *in vivo* state. Hence, the time-averaging of flows implies $\boldsymbol{d}^{\mathcal{S}} = 0$. The computed PSF $s(\|<\boldsymbol{\tau}^{\mathcal{F}}>\|)$ of the time-averaged flow model is visualized in Figure 4.12(b). The computed OSI $o(\boldsymbol{\tau}^{\mathcal{F}})$ for the time-averaged flow model is visualized in Figure 4.12(d).

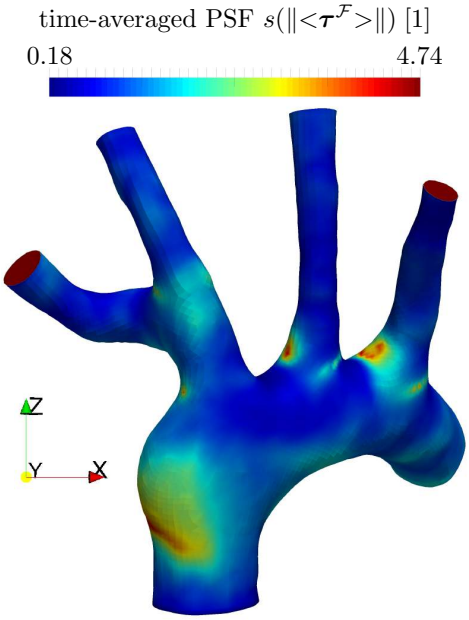

(a) Anterior view of the spatial distribution of time-averaged PSF $s(\|<\boldsymbol{\tau}^{\mathcal{F}}>\|)$ of the rigid wall model.

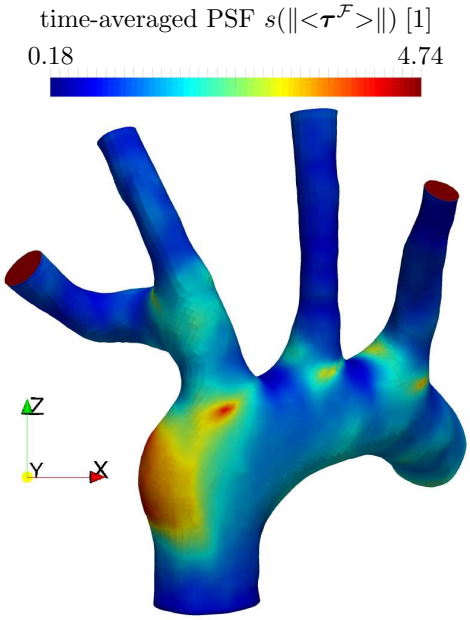

(b) Anterior view of the spatial distribution of time-averaged PSF $s(\|<\boldsymbol{\tau}^{\mathcal{F}}>\|)$ of the time-averaged flow model.

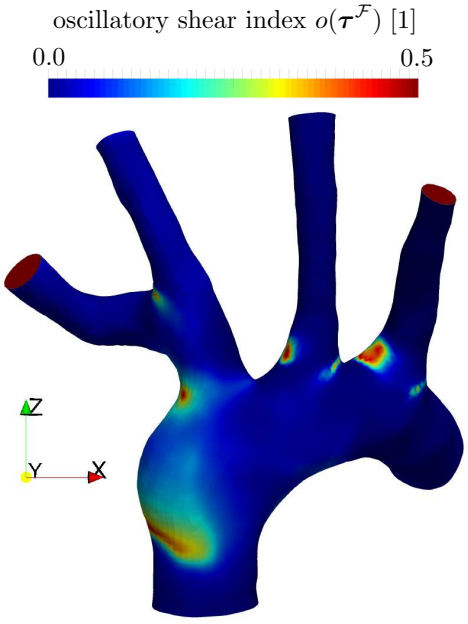

(c) Anterior view of the spatial distribution of the OSI $o(\boldsymbol{\tau}^{\mathcal{F}})$ of the rigid wall model.

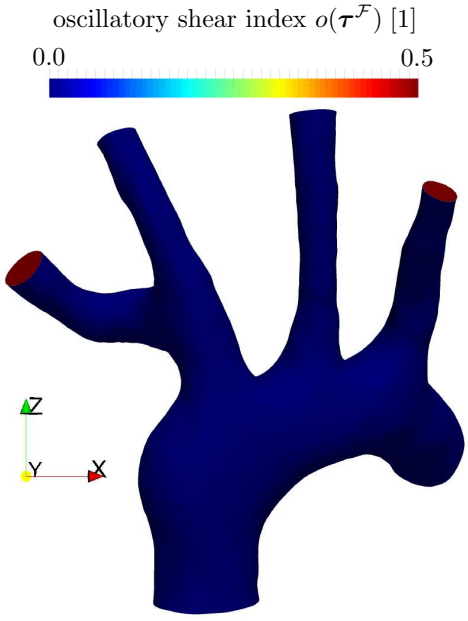

(d) Anterior view of the spatial distribution of the OSI $o(\boldsymbol{\tau}^{\mathcal{F}})$ of the time-averaged flow model.

Figure 4.12 Spatial distribution of time-averaged permeability scaling factor and oscillatory shear index of the rigid and mean-flow model.

4.3.6 Growth and remodeling

To show the capability of the cardiovascular model to adapt to the narrowing of the lumen due to the accumulation of foam cells, the spatial distribution of the PSF is compared at different times. Since inflammatory, immunological, growth and remodeling processes take place on a much larger time scale as the hemodynamics (cf. the orders of the length of the cardiac cycle T_{Cycl} and the diffuse permeability P_ℓ) and as the model is not embedded into a multiscale strategy, some model parameters are increased to accelerate atherosclerosis progression to the duration of a few cardiac cycles. Hence, after the cardiovascular model obtained its periodic state the following adapted model parameters were used: $D_\ell^{\mathcal{SS}} = 6.0 \cdot 10^{-2}\ \frac{\mathrm{mm}^2}{\mathrm{s}}$, $d_\ell^{\mathcal{SS}} = 1.0\ \frac{1}{\mathrm{s}}$, $\gamma_\ell^{\mathcal{SS}} = 0.4\ \frac{1}{\mathrm{s}}$, $\ell_{\mathrm{Thres}}^{\mathcal{SS}} = 2.0 \cdot 10^{-3}\ \ell_{\mathrm{In}}^{\mathcal{FS}}$, $P_\ell = 5.0 \cdot 10^{-4}\ \frac{\mathrm{mm}}{\mathrm{s}}$, $k_{\mathrm{Wall}}^{\mathcal{S}} = 1.0 \cdot 10^{6}\ \frac{\mathrm{Pa}}{\mathrm{mm}}$ and $\alpha_m^{\mathcal{S}} = 4.1 \cdot 10^{10}\ \frac{\mathrm{mm}^3}{\mathrm{g}}$. In Figures 4.13(a) and 4.13(b) the time-averaged PSF of the grown artery wall at different times is visualized. Figures 4.13(c), 4.14(b) and 4.14(c) show the growth and remodeling factors of the grown artery wall at time $t = 1.2$ s.

4.4 Discussion

A methodology to calibrate the multiphysics model to a specific geometry and a given set of key physiological data has been presented. The validation of the model in Section 4.3.4 showed that computed key physiological quantities, such as blood pressure, artery wall displacements and WSS derived from the considered exemplary set of murine physiological data are qualitatively in good agreement with measurements and simulations performed by others. However, there are large inter- and intramouse variations of these quantities depending on the condition, type, age and size of the specific mouse and its geometry, see e.g. [40, 166, 282] and references therein. A quantitative validation of the developed model remains to be done, which is due to a lack of suited *in vivo* data available to us.

The newly developed calibration of the time-averaged WSS-dependent law for the scaling of the endothelial permeability $s(\|<\boldsymbol{\tau}^{\mathcal{F}}>\|)$ to the specific geometry proved to qualitatively predict sites of atherosclerotic plaque formation. The alternative formulations for the time-averaged endothelial PSF $<s(\|\boldsymbol{\tau}^{\mathcal{F}}\|)>$ and $s(<\|\boldsymbol{\tau}^{\mathcal{F}}\|>)$ do not result in physiological results. However, a quantitative validation of the developed PSF remains to be done. Therefore, the *in vivo* plaque locations must be imaged and compared to the predicted locations by the PSF in terms of a suitable metric, see e.g., the work in [59]. A picture of a dissection of a murine aortic arch with atherosclerotic plaques is given in Figure 4.11.

In the literature, models of atherosclerosis with time-averaged flows are commonly utilized. This is often argued by the idea that the growth and remodeling process in atherosclerosis is on a much larger time scale than the hemodynamics and hence also the mean blood flow is a valid indicator for the mechanobiology behind. In contrast to this argument, the comparison of the multiphysics model with the reduced time-averaged flow model introduced in Section 4.3.5, shows a significant difference in the WSS patterns and hence their time-averaged PSF patterns, see Figures 4.10(a) and 4.12(b). This observation is even more valid when comparing the OSI computed by the two models, see Figures 4.10(c) and 4.12(d). This effect is due to the unphysiological averaging of

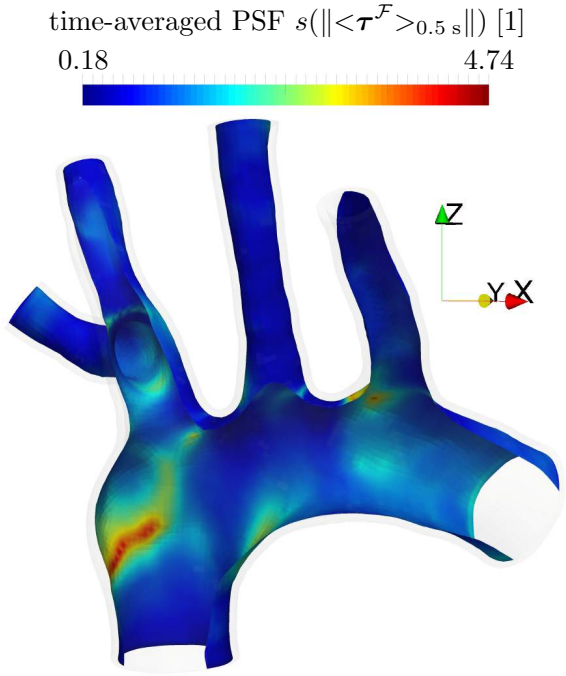

(a) Spatial distribution of time-averaged permeability scaling factor $s(\|<\boldsymbol{\tau}^{\mathcal{F}}>_{0.5\,\mathrm{s}}\|)$ at time $t = 0.5$ s.

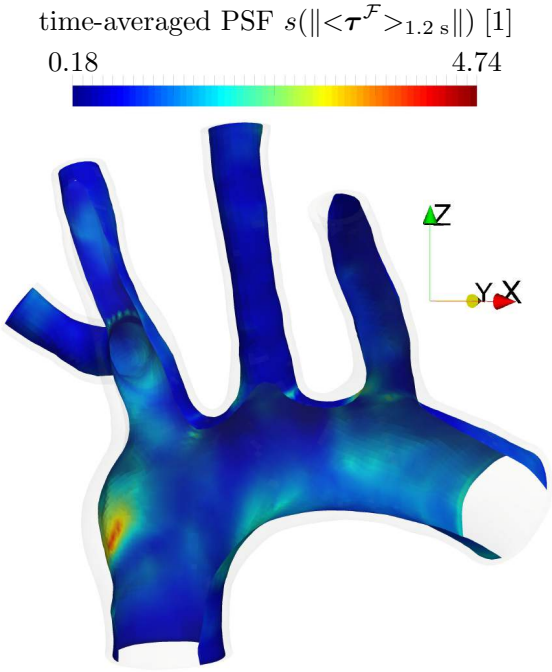

(b) Spatial distribution of time-averaged permeability scaling factor $s(\|<\boldsymbol{\tau}^{\mathcal{F}}>_{1.2\,\mathrm{s}}\|)$ at time $t = 1.2$ s.

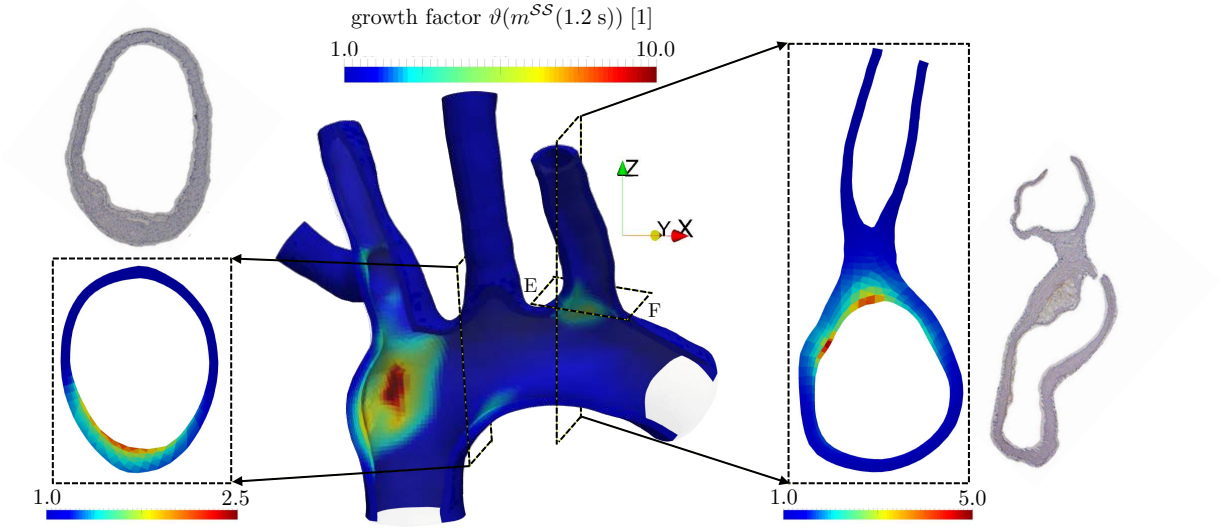

(c) Grown artery wall, spatial distribution of growth factor $\vartheta(m^{\mathcal{SS}}(1.2\ \mathrm{s}))$ at time $t = 1.2$ s and comparison of grown cross sections with aortic cross sections from LDL receptor-deficient mice (type B6.129S7-Ldlrtm1Her/J) with early (left top) and advanced (right) atherosclerotic plaques. The murine cross sections were stained with haematoxylin.

Figure 4.13 Cross sections of spatial distribution of time-averaged permeability scaling factor and growth factor at different times and comparison of grown cross sections with mouse experiments.

the pulsatile nature of blood flow preventing flow recirculations and oscillatory flows frequently occurring in the diastolic phase of the cardiac cycle, where the cardiac output almost vanishes. In the case of time-averaged flows, such oscillatory flows are not observed at all, see Figure 4.12(d). This observation strongly supports the theory that the above described model reduction of neglecting the pulsatile nature of blood flow and hence using a time-averaged flow is misleading, as is stated by others too [76, 152, 178, 255].

In contrast, the comparison of results of the full model with its rigid wall simplification shows that the displacements of the artery wall only have a minor influence on the WSS and PSF patterns, see Figures 4.10(a) and 4.12(a). Similar observations are also made for the computed OSI of the two models, see Figures 4.10(c) and 4.12(c). The case study showed that the time-averaged WSS and OSI and hence the endothelial permeability are only slightly altered by radial enlargements. Hence, the rigid wall model is also capable to properly compute the spatial distribution of the time-averaged PSF and the OSI patterns and hence is also suited to predict the potential plaque formation locations. The difference in the PSF mainly is that the non-compliant artery wall model yields sharper transitions between low and high permeability regions, where in contrast the compliant artery wall does produce broader and more blurred high permeability regions. Similar observations for the WSS patterns in carotid arteries were observed in [62]. However, in [62] a significant influence of the compliant artery wall to the OSI was observed.

Still, a FSI-like approach to model atherosclerosis is indispensable. This is also stated by others [59, 62, 152], but the reason for this conclusion is different. The computational results indicate that not the radial enlargement of the lumen creates the need for a FSI approach, but much more the ability of the model to capture the permanent displacements of the endothelium due to the artery wall thickening. Consequently, a classical FSI approach is not mandatory, but mainly a rigid wall and pulsatile flow model where the vessel lumen adapts to growth and remodeling. Still, a pure computational fluid dynamics simulation is not sufficient since growth and remodeling processes can only be captured physiologically when the specific layout of the artery wall, i.e., a suitable constitutive law is considered. Hence, a FSI-like approach is indispensable to physiologically capture the influences of the long time scale phenomena in atherosclerosis to the cardiovascular mechanics.

To accelerate the development of atherosclerotic plaques to a few cardiac cycles, some parameters of the model were adapted. This was done such that the developed plaques qualitatively match plaques found in experiments with atherosclerotic mice models, see Figure 4.13(c). As indicated in Figures 4.13(a) and 4.13(b), growth successively narrows the lumen and induces a drastic change of the PSF patterns representing the endothelial permeability. To give a quantitative example, the luminal area of cross section EF (cf. Figure 4.13(c)) is reduced by $36,8\%$ compared to the initial state, see Figure 4.14. Even though the results were achieved with a simplistic model for the immunology, this illustrates that the presented model of the cardiovascular mechanics is capable to adjust dynamically to the long time scale atherosclerotic process of growth and remodeling. For the primary high permeability regions with already developed plaques, there are two main trends. On the one hand the endothelial permeability could decrease such that the healing processes outweigh the continuing LDL penetration and hence the atherosclerotic process locally stagnates resulting in a stable plaque. In the contrary case, the endothelial permeability would be too high for the plaque to become stable and the plaque continues to grow. To be able

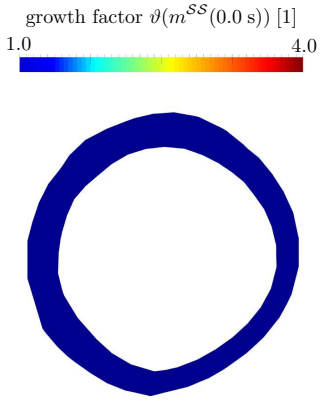

(a) Initial cross section EF and spatial distribution of growth factor $\vartheta(m^{\mathcal{SS}}(0.0\mathrm{s}))$ at time $t = 0.0$ s.

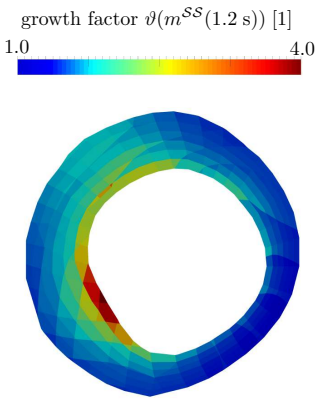

(b) Grown cross section EF and spatial distribution of growth factor $\vartheta(m^{\mathcal{SS}}(1.2\mathrm{s}))$ at time $t = 1.2$ s.

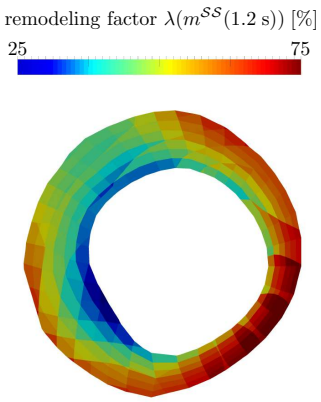

(c) Grown cross section EF and spatial distribution of remodeling factor $\lambda(m^{\mathcal{SS}}(1.2\mathrm{s}))$ at time $t = 1.2$ s.

Figure 4.14 Initial and grown cross section EF (cf. Figure 4.13(c)) and spatial distributions of growth factor and remodeling factor at different times.

to predict the stability outcome of a plaque, a predictive reaction model of key species must be introduced to replace the utilized simplified model. Further, it is inevitable to embed the presented model into a suitable multiscale in time strategy.

4.5 Limitations

The developed multiphysics model is affected by five main limitations. First, the conclusions drawn from the developed mathematical and computational model are based only on a single murine-specific computational case study which is based on a single set of physiological data from the literature. Hence, the murine-specific setup in the multiphysics model only differs in the geometry and geometry-derived model parameters. Still, the computational case study showed that the multiphysics model is well applicable in the context of atherosclerosis. The qualitatively same results are expected also for other murine-specific geometries and derived parameter sets. In further work more murine-specific cases must be investigated to further corroborate the presented conclusions.

Second, the model suffers from a variety of uncertainties which were not yet assessed. The utilized magnetic resonance angiography has a rather coarse spatial resolution (especially through-plane) compared to other imaging techniques like micro computer tomography. Thus, due to the common sequence of imaging, segmentation and simulation, immanent inaccuracies in the segmented geometry of the lumen may result in geometry-driven alterations of computed results, especially of the WSS and PSF patterns [166]. Moreover, some model parameters are only roughly known as they are very difficult to measure (such as the spatial variation of the diffusive permeability) or were not yet measured based on murine experiments (such as the parameters for

the surrounding tissue). A detailed quantification of these uncertainties in the multiphysics model is very challenging and must be individually addressed in future work.

Further, the utilized reaction model is a drastic simplification of the complex inflammatory and immunological processes of atherosclerosis, cf. Section 1.1. Many important processes and key species involved in the development of atherosclerotic plaques were neglected and a simple heuristic reaction model with solely two species (LDL and foam cells) was utilized. The development of a quantitatively validated and predictive reaction model of the formation of early atherosclerotic plaques is addressed in the subsequent Chapter 5. The incorporation of the reaction model into a scalar transport submodel is part of Chapter 6.

The fourth limitation of the proposed model is the neglection of the transmural pressure gradient-driven porous media flow within the artery wall and the induced neglection of the advective solute flux through the endothelium. The mechanical properties, however, are dominated by the media and adventitia layers of the artery wall and these layers mainly consist of a solid phase [294]. Thus, the influence of the fluid phase to the short time scale cardiovascular mechanics can be assumed to be minor. The importance of the advective transport of lipoproteins with the porous media flow to the long time scale atherosclerotic process is controversial, see e.g. [268] and [210], and will be assessed in Chapter 6.

Finally, the expensive computational cost prevents a straightforward application of the multiphysics model to predict the long-term process of atherosclerosis. Hence, the model has to be embedded into a suitable multiscale in time strategy, e.g., similar to [81, 152, 267]. In a multiscale in time strategy, the presented models of cardiovascular mechanics and concentrations in the blood can be utilized to represent the short time scale. In contrast, the model of concentrations in the artery wall (with a predictive reaction model) can be used for the long time scale. As has been shown, the modeling of the short time scale is indispensable and hence the usage of a multiscale in time strategy is unavoidable. A detailed proposal for a multiscale in time strategy based on the developed multiphysics model is given in the final Chapter 7.

4.6 Short summary

This chapter is a revised version of [266]. It is concerned with the development of a novel mathematical model of atherosclerosis which incorporates major processes of all time scales of the disease. Based on basic continuum mechanical principles, a mathematical multiphysics model was developed which incorporates the cardiovascular mechanics including the interaction of blood and artery wall, transport of LDL to and through the endothelium, inflammatory and immunological processes within the artery wall as well as a novel growth and remodeling formulation for the artery wall. Thereby, the interlacement of the different time scales of atherosclerosis is respected such that the short time scale cardiovascular mechanics is capable to dynamically adjust to changes occurring in the long time scale and *vice versa*.

The model was calibrated to an exemplary physiological data set and a murine-specific geometry such that it reproduced important cardiovascular quantities, such as the blood pressure, radial displacements and WSS. The developed law for the up- and downscaling of the endothelial

permeability with respect to LDL is a good indicator for potential sites of atherosclerotic plaque formation. The analysis of model reductions corroborates the theory that neglecting the short time scale of cardiovascular mechanics by time-averaging flows or neglecting the deformation of the artery wall is misleading in the context of atherosclerosis.

5 Quantification of early atherosclerotic plaque formation

The previous Chapter 4 focused on the development of a computational multiphysics approach for atherosclerosis. Thereby, only little focus was put on the inflammatory and immunological processes in the artery wall that lead to the development of atherosclerotic plaques. Simplistic reaction models for LDL $\varkappa_\ell^{\mathcal{SS}}$ and foam cells $\varkappa_m^{\mathcal{SS}}$ were introduced and their parameters trimmed such that they mimicked a physiological atherosclerosis-like behavior. However, when the presented multiphysics approach shall become predictive and clinically relevant, the complex inflammatory and immunological processes must be addressed by a suitable quantified and predictive mathematical model. Indeed, there is a growing number of studies that model inflammatory and immunological processes in the artery wall that cause the development of atherosclerotic plaques, see [215] and references therein. However, only few of these models even use parameters that are obtained from experimental results and none of these models is able to forecast the formation of atherosclerotic plaques in the artery wall.

In this chapter, a *non-spatial* but *parameterized* mathematical ODE model of the early stages of atherosclerosis is developed and analyzed. The model is constructed componentwise where each component is strongly informed by existing sets of *in vitro* experiments. Therefore, ODE submodels are developed which are least-squares fitted to various *in vitro* experimental results from the literature. Subsequently, the submodels are used to construct a parameterized *combined model* of the formation of early atherosclerotic plaques. A local sensitivity analysis of the combined model with respect to its parameters is performed that identifies critical parameters and processes. Further, a systematic analysis of the long-term outcome of the model is presented which produces a characterization of stable and unstable model plaques based on prescribed rates of recruitment of low-density lipoproteins, high density lipoproteins and macrophages.

The structure of this chapter is as follows: In Section 5.1, three mathematical submodels are developed that are validated against *in vitro* experiments. The submodels are merged to create a combined model that describes the formation of early atherosclerotic plaques as they may occur *in vivo*. Section 5.2 gives details on the performed sensitivity and stability analysis of the combined model. In Section 5.3, all computational results are presented, and they are discussed in Section 5.4. Finally, a brief summary of this chapter is given in Section 5.5.

In this chapter, all quantities belong to concentrations in the artery wall. The respective superscript $\mathcal{SS}$ is omitted for clarity. This chapter is a revised version of the previously published work by *Thon et al.* [265].

5.1 Models

This section is concerned with the development of a quantitative mathematical ODE model of the formation of early atherosclerotic plaques. For an overview of important inflammatory and immunological processes in early atherosclerosis, see Section 1.1.

The chosen modeling approach is similar to the biologists' experimental approach where the bigger picture of atherosclerosis is put together from many smaller observations and findings that are gained from *in vitro* experiments. Analog, *in vitro* experimental results from the literature are used to successively construct a quantified and predictive mathematical model. Therefore, a series of three simpler submodels is developed that describe the modification of LDL by endothelial cells and macrophages (Section 5.1.1.1), the protection that HDL offers against the oxidative modification of LDL (Section 5.1.1.2) and the cholesterol cycle and reverse cholesterol transport in macrophages (Section 5.1.1.3). Supplemented by a law for the apoptosis of macrophages, the three submodels are merged to create a combined model that describes formation of early atherosclerotic plaques as they may occur *in vivo* (Section 5.1.2). The combined model is a quantitative and deterministic system of ODEs that describe the coupled inflammatory, lipid and macrophage dynamics within the artery wall. The combined model tracks the number of LDL particles, the extent of their modification, the total number of HDL particles as well as the total number of macrophages and the extent of their intracellular cholesterol burden. A schematic overview of the considered key species and their interactions is shown in Figure 5.1.

In all models, a continuum approach is used where the concentration of each species is represented as a function of time only. Concentrations are either in units of mass per unit volume or number per unit volume where the representative volume will be either the volume determined by the petri dish (for *in vitro* experiments) or the volume of the plaque (for *in vivo* experiments).

Where a species in a model exists in many states, it will be assumed that the different states can be binned so that different classes in the model have functionally distinct roles. For example, LDL has many degrees and different types of oxidative modification [252]. In the models, however, LDL is divided into two classes which are labeled, native LDL and modified LDL. The distinction is that only modified LDL creates an immune reaction that leads to inflammation. The analog holds for HDL. Analog, only those macrophages are modeled that ingest and store lipids to a significant extent, as this is the behavior of the macrophages observed in the *in vitro* experiments that are used to find parameters. Macrophages *in vivo* exhibit a wide variety of phenotypes [201], but modeling that phenotypic diversity is beyond the capability of the available data.

The time-dependent behavior of species is modeled by systems of ODEs. If specific experimental data exist, relationships are chosen which best represent the data. In contrast, linear relationships are used if no experimental data exist and there is nothing to indicate that the relationship must be nonlinear. The results of the mathematical submodels are least-squares fitted to various experimental measurements from the literature to find values of the unknown parameters. Due to a lack of uniform data experimental results gained from cells or lipids from different animal models cannot be distinguished. All quantities are converted to the *International System of Units* (SI units) from the experiment-specific units used in the literature which are often non-SI units. Table 5.1 shows the values used for the conversions in this thesis.

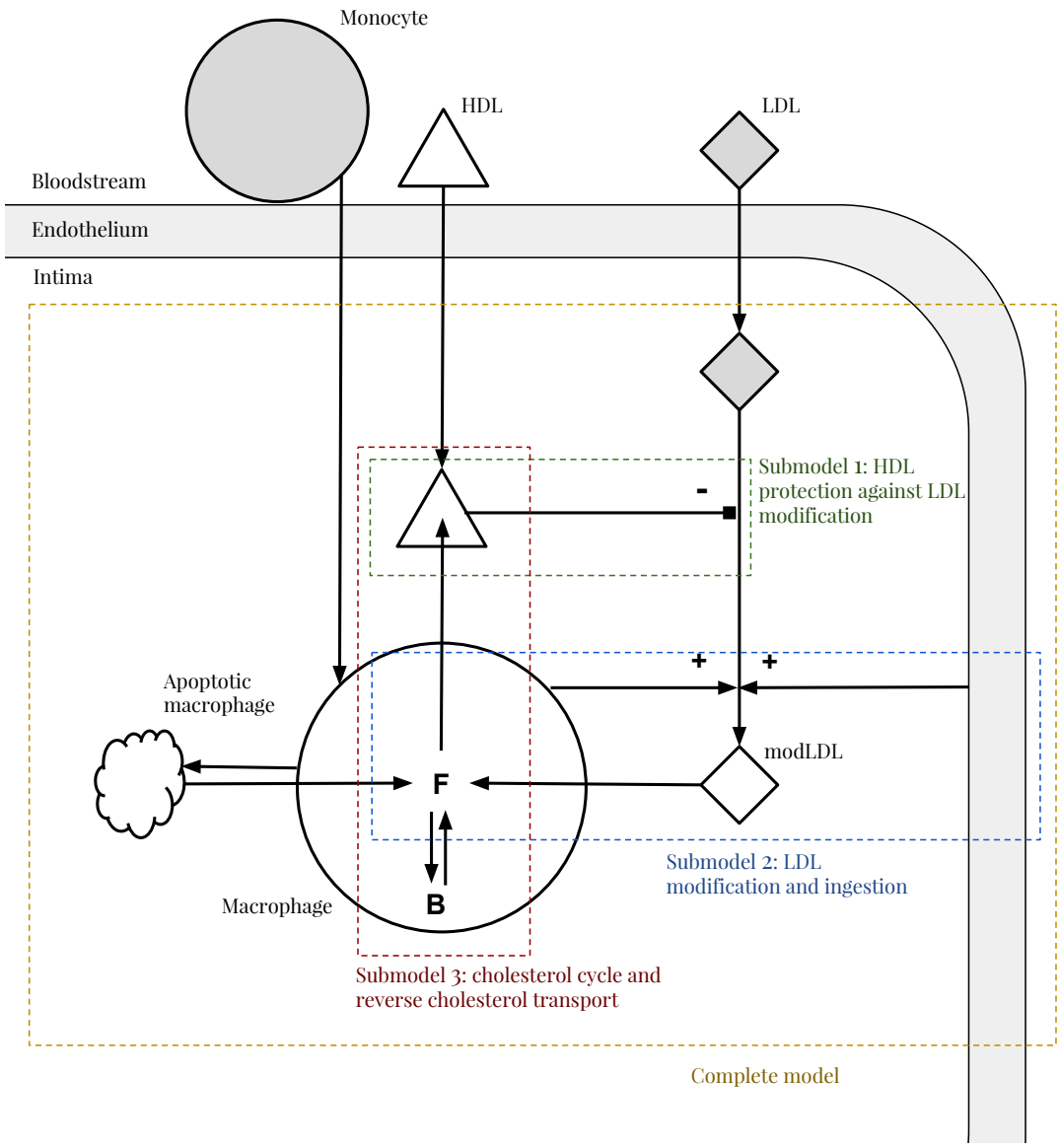

Figure 5.1 Overview of key inflammatory and immunological processes in early atherosclerotic plaques that are considered in the submodels and the combined model. It is assumed that monocytes (circle, gray), LDL (diamond, gray) and HDL (triangle) enter the vessel wall at a constant rate which reflect their concentrations in blood and the magnitude of wall shear stress exerted on the endothelium by blood flow. Monocytes differentiate into macrophages (circle, white), consume modified LDL (diamond, white) and apoptotic macrophages (cloud) and gain free cholesterol (F) as a result, export cholesterol to HDL and undergo apoptosis. Free cholesterol is converted to esterified cholesterol (B) and stored in lipid droplets, so free cholesterol is within an essential and cytotoxic limit. LDL is oxidatively modified by macrophages and the endothelium, whereas HDL counteracts LDL oxidation. The processes considered in each submodel of *in vitro* systems are encircled by green (submodel $\boxed{1}$), blue (submodel $\boxed{2}$) and red (submodel $\boxed{3}$) frames. The processes considered in the combined model are encircled by a yellow frame.

Table 5.1 Overview of values of key quantities in SI units.

Symbol	Description	Value	Source
N_{A}	Avogadro constant	$6.022 \cdot 10^{23}\ \frac{1}{\mathrm{Mol}}$	
ρ_1	Number of cell proteins per cell volume	$3.0 \cdot 10^{15}\ \frac{1}{\mathrm{mm}^3}$	[196]
ρ_2	Molecular weight of cell proteins	$5.3 \cdot 10^{4}\ \frac{\mathrm{g}}{\mathrm{Mol}}$	[181]
M_b	Molecular weight of cholesterol ester	$6.48 \cdot 10^{2}\ \frac{\mathrm{g}}{\mathrm{Mol}}$	[263]
V_b	Volume per mass of cholesterol ester	$1.06 \cdot 10^{3}\ \frac{\mathrm{mm}^3}{\mathrm{g}}$	[263]
M_f	Molecular weight of free cholesterol	$3.87 \cdot 10^{2}\ \frac{\mathrm{g}}{\mathrm{Mol}}$	[263]
V_f	Volume per mass of free cholesterol	$1.02 \cdot 10^{3}\ \frac{\mathrm{mm}^3}{\mathrm{g}}$	[263]
ρ_3	Molecular weight of apolipoprotein B-100	$5.49 \cdot 10^{5}\ \frac{\mathrm{g}}{\mathrm{Mol}}$	[225]
ρ_4	Volume of murine macrophage	$2.10 \cdot 10^{-6}\ \mathrm{mm}^3$	[194]
R_m	Radius of murine macrophage	$7.94 \cdot 10^{-3}\ \mathrm{mm}$	$= \sqrt[3]{\frac{3\rho_4}{4\pi}}$
ρ_5	Macrophages per cell protein mass	$1.80 \cdot 10^{9}\ \frac{1}{\mathrm{g}}$	$= \frac{N_A}{\rho_1\rho_2\rho_4}$
R_ℓ	Radius of LDL	$1.1 \cdot 10^{-5}\ \mathrm{mm}$	[146]
M_ℓ	Molecular weight of LDL	$2.93 \cdot 10^{6}\ \frac{\mathrm{g}}{\mathrm{Mol}}$	[53, 225]
ρ_6	Fraction of cholesterol ester of LDL mass	38.3%	[263]
ρ_7	Fraction of free cholesterol of LDL mass	8.8%	[263]
ρ_8	LDL particles per LDL cholesterol mass	$4.36 \cdot 10^{17}\ \frac{1}{\mathrm{g}}$	$= \frac{N_A}{M_\ell(\rho_6+\rho_7)}$
ρ_9	Apolipoprotein B-100 fraction of LDL protein mass	95%	[225]
ρ_{10}	LDL particles per LDL protein mass	$1.04 \cdot 10^{18}\ \frac{1}{\mathrm{g}}$	$= \frac{N_A\rho_9}{\rho_3}$
R_h	Radius of HDL	$4.72 \cdot 10^{-6}\ \mathrm{mm}$	[151]
M_h	Molecular weight of HDL	$2.92 \cdot 10^{5}\ \frac{\mathrm{g}}{\mathrm{Mol}}$	[151]
ρ_{11}	Cholesterol ester molecules per HDL particle	110.1	[151]
ρ_{12}	Free cholesterol molecules per HDL particle	27.7	[151]
ρ_{13}	HDL particles per HDL cholesterol mass	$7.34 \cdot 10^{18}\ \frac{1}{\mathrm{g}}$	$= \frac{N_A}{M_b\rho_{11}+M_f\rho_{12}}$
ρ_{14}	HDL particles per HDL protein mass	$4.22 \cdot 10^{18}\ \frac{1}{\mathrm{g}}$	[151]

All values are converted to mm, g and Mol.

5.1.1 Submodels of *in vitro* systems

In this section, three mathematical submodels that describe various *in vitro* experiments are developed. All parameters of the submodels are either experiment-specific (i.e., are specified by the experimental procedure) or estimated by a least-squares fit to the measured experimental results.

5.1.1.1 LDL modification and ingestion

Native LDL gets oxidatively modified by endothelial cells and macrophages and both, native LDL and modified LDL, gets ingested by macrophages. The submodel of the LDL modification and

ingestion is based on *in vitro* experiments by *Henriksen et al.* [116] and *Leake et al.* [165]. It is subsequently denoted as submodel $\boxed{1}$.

Experimental setups

The modification of LDL by endothelial cells and the ingestion of modified LDL by macrophages were investigated *in vitro* in [116] using a two-stage experimental setup. First, specified initial concentrations of native LDL $\ell_{\mathrm{Mod},0}$ were modified by exposure to cultured endothelial cell monolayers e_{Mod} for specified time periods T_{Mod}. (Here the subscript "Mod" indicates quantities of the modification stage of the experimental setup.) Subsequently, the mixtures of native and modified LDL, that had been created in the first step, were reduced to specified initial concentrations $\ell_{\mathrm{Ing},0}$ and exposed to specified densities of macrophages m_{Ing} for specified time periods T_{Ing} to allow the macrophages to ingest the LDL. (The subscript "Ing" indicates quantities of the ingestion stage of the experimental setup.) Among other things, the ingested LDL per macrophage was measured for various experiment-specific values of $\ell_{\mathrm{Mod},0}$, e_{Mod}, T_{Mod}, $\ell_{\mathrm{Ing},0}$, m_{Ing} and T_{Ing} as shown in Table 5.2.

Additionally, measurements in [165] are used where the modification and ingestion of LDL by macrophages were investigated. This study used experimental protocols similar to [116], but the modification of LDL in the first stage was done using specified densities of macrophages m_{Mod} instead of endothelial cell monolayers. Also, in the second stage a high concentration of fetal calf serum was added preventing the oxidative modification of LDL by macrophages. In [165], the ingested LDL per macrophage in the second stage was measured for various experiment-specific values of $\ell_{\mathrm{Mod},0}$, m_{Mod}, T_{Mod}, $\ell_{\mathrm{Ing},0}$, m_{Ing} and T_{Ing} as shown in Table 5.2.

Mathematical submodel

The experimental observations in [116] and [165] are driven by the ingestion of native and modified LDL by macrophages and by the modification of native LDL by endothelial cells and macrophages. In these experiments, the ingestion of native and modified LDL, concentrations ℓ and $\tilde{\ell}$ per macrophage saturates as LDL concentrations increase (see [116], Figure 7 and 8 and [165], Figure 4). The modification of native LDL by macrophages and endothelial cells is described by linear relationships in their concentrations ℓ, m and e, respectively, as no experimental data exist which indicates otherwise. In the experiments, a lag phase for the modification of native LDL of $3 - 8$ h was observed (see [116], Figure 2, [165], Figure 1a and 1b, [200], Figure 1b). This lag phase is accounted for by a reduction of 4 h of the experimental time period T_{Mod}.

The mathematical submodel is formulated in the same units that are used in the experiments: time $[t] = \mathrm{h}$, concentration of native LDL $[\ell_{\mathrm{Mod}}] = [\ell_{\mathrm{Ing}}] = \frac{\mu\mathrm{g\ lipid\ protein}}{\mathrm{ml}}$, concentration of modified LDL $[\tilde{\ell}_{\mathrm{Mod}}] = [\tilde{\ell}_{\mathrm{Ing}}] = \frac{\mu\mathrm{g\ lipid\ protein}}{\mathrm{ml}}$, concentration of total ingested LDL $[a_{\mathrm{Ing}}] = \frac{\mu\mathrm{g\ lipid\ protein}}{\mathrm{ml}}$, density of macrophages $[m_{\mathrm{Mod}}] = [m_{\mathrm{Ing}}] = \frac{\mathrm{mg\ cell\ protein}}{\mathrm{ml}}$ and density of endothelial cells $[e_{\mathrm{Mod}}] = \frac{\mathrm{mm}^2}{\mathrm{ml}}$. The submodel consists of two sequential system of ODEs and associated initial conditions. As in the experiments described in [116, 165], the first system corresponds to

Table 5.2 Experiment-specific parameters of the mathematical submodel of LDL modification and ingestion (submodel $\boxed{1}$) in analogy to the experimental setups in [116] and [165].

Experiment \ Quantity	Modification stage				Ingestion stage			
	T_{Mod} [h]	$\ell_{\mathrm{Mod},0}\left[\frac{\mu\mathrm{g\ lipid\ protein}}{\mathrm{ml}}\right]$	$m_{\mathrm{Mod}}\left[\frac{\mathrm{mg\ cell\ protein}}{\mathrm{ml}}\right]$	$e_{\mathrm{Mod}}\left[\frac{\mathrm{mm}^2}{\mathrm{ml}}\right]$	T_{Ing} [h]	$\ell_{\mathrm{Ing},0}\left[\frac{\mu\mathrm{g\ lipid\ protein}}{\mathrm{ml}}\right]$	$m_{\mathrm{Ing}}\left[\frac{\mathrm{mg\ cell\ protein}}{\mathrm{ml}}\right]$	$q_{\ell,m}\left[\frac{\mathrm{ml}}{\mathrm{h\ (mg\ cell\ protein)}}\right]$
[116], Fig. 1, $e_{\mathrm{Mod}} = 0$	24	200	0	0	$0-20$	10	$4.16 \cdot 10^{-2}$ *	$1.18 \cdot 10^{-1}$ **
[116], Fig. 1, $e_{\mathrm{Mod}} = 1413.7$	24	200	0	1413.7	$0-20$	10	$4.16 \cdot 10^{-2}$ *	$1.18 \cdot 10^{-1}$ **
[116], Fig. 2, $e_{\mathrm{Mod}} = 0$	$0-46$	200	0	0	5	8.5	$4.16 \cdot 10^{-2}$ *	$1.18 \cdot 10^{-1}$ **
[116], Fig. 2, $e_{\mathrm{Mod}} = 1413.7$	$0-46$	200	0	1413.7	5	8.5	$4.16 \cdot 10^{-2}$ *	$1.18 \cdot 10^{-1}$ **
[116], Fig. 5, $e_{\mathrm{Mod}} = 0$	26	200	0	0	5	$0-40$	$4.16 \cdot 10^{-2}$ *	$1.18 \cdot 10^{-1}$ **
[116], Fig. 5, $e_{\mathrm{Mod}} = 1413.7$	26	200	0	1413.7	5	$0-40$	$4.16 \cdot 10^{-2}$ *	$1.18 \cdot 10^{-1}$ **
[165], Fig. 1a, $m_{\mathrm{Mod}} = 0$	$0-24$	100	0	0	24	10	$5.54 \cdot 10^{-1}$ *	0
[165], Fig. 1a, $m_{\mathrm{Mod}} = 1.11$	$0-24$	100	1.11 *	0	24	10	$5.54 \cdot 10^{-1}$ *	0
[165], Fig. 4, $m_{\mathrm{Mod}} = 0$	24	100	0	0	24	$0-50$	$5.54 \cdot 10^{-1}$ *	0
[165], Fig. 4, $m_{\mathrm{Mod}} = 1.11$	24	100	1.11 *	0	24	$0-50$	$5.54 \cdot 10^{-1}$ *	0

Parameters indicated by * are estimated using ρ_5 from Table 5.1. Parameters indicated by ** are estimated by least-squares fitting to the experimental results. All values are given in the units of submodel $\boxed{1}$.

the oxidative modification of native LDL by macrophages and endothelial cells (modification stage)

$$\begin{aligned}
\frac{\mathrm{d}}{\mathrm{d}t}\ell_{\mathrm{Mod}}(t) &= -\underbrace{\mu_\ell \frac{(\ell_{\mathrm{Mod}})^{n_\ell}}{(\xi_\ell)^{n_\ell}+(\ell_{\mathrm{Mod}})^{n_\ell}} m_{\mathrm{Mod}}}_{\substack{\text{ingestion of native LDL}\\ \text{by macrophages}}} - \underbrace{q_{\ell,m}\ell_{\mathrm{Mod}}m_{\mathrm{Mod}}}_{\substack{\text{modification of native}\\ \text{LDL by macrophages}}} - \underbrace{q_{\ell,e}\ell_{\mathrm{Mod}}e_{\mathrm{Mod}}}_{\substack{\text{modification of native}\\ \text{LDL by endothelial cells}}}, \\
\frac{\mathrm{d}}{\mathrm{d}t}\tilde{\ell}_{\mathrm{Mod}}(t) &= -\underbrace{\mu_{\tilde{\ell}} \frac{(\tilde{\ell}_{\mathrm{Mod}})^{n_{\tilde{\ell}}}}{(\xi_{\tilde{\ell}})^{n_{\tilde{\ell}}}+(\tilde{\ell}_{\mathrm{Mod}})^{n_{\tilde{\ell}}}} m_{\mathrm{Mod}}}_{\substack{\text{ingestion of modified LDL}\\ \text{by macrophages}}} + \underbrace{q_{\ell,m}\ell_{\mathrm{Mod}}m_{\mathrm{Mod}}}_{\substack{\text{modification of native LDL}\\ \text{by macrophages}}} + \underbrace{q_{\ell,e}\ell_{\mathrm{Mod}}e_{\mathrm{Mod}}}_{\substack{\text{modification of native LDL}\\ \text{by endothelial cells}}}, \\
\ell_{\mathrm{Mod}}(4\mathrm{h}) &= \ell_{\mathrm{Mod},0}, \quad \tilde{\ell}_{\mathrm{Mod}}(4\mathrm{h}) = 0, \quad t \in [4\mathrm{h}; T_{\mathrm{Mod}}]
\end{aligned} \tag{5.1}$$

and the second system to the ingestion of LDL by macrophages (ingestion stage)

$$\frac{\mathrm{d}}{\mathrm{d}t}\ell_{\mathrm{Ing}}(t) = -\underbrace{\mu_\ell \frac{(\ell_{\mathrm{Ing}})^{n_\ell}}{(\xi_\ell)^{n_\ell}+(\ell_{\mathrm{Ing}})^{n_\ell}} m_{\mathrm{Ing}}}_{\substack{\text{ingestion of native LDL}\\ \text{by macrophages}}} - \underbrace{q_{\ell,m}\ell_{\mathrm{Ing}}m_{\mathrm{Ing}}}_{\substack{\text{modification of native LDL}\\ \text{by macrophages}}}, \tag{5.2}$$

$$
\begin{aligned}
\frac{\mathrm{d}}{\mathrm{d}t}\tilde{\ell}_{\mathrm{Ing}}(t) &= -\underbrace{\mu_{\tilde{\ell}}\frac{(\tilde{\ell}_{\mathrm{Ing}})^{n_{\tilde{\ell}}}}{(\xi_{\tilde{\ell}})^{n_{\tilde{\ell}}}+(\tilde{\ell}_{\mathrm{Ing}})^{n_{\tilde{\ell}}}}m_{\mathrm{Ing}}}_{\substack{\text{ingestion of modified LDL}\\ \text{by macrophages}}} + \underbrace{q_{\ell,m}\ell_{\mathrm{Ing}}m_{\mathrm{Ing}}}_{\substack{\text{modification of native LDL}\\ \text{by macrophages}}}, \\
\frac{\mathrm{d}}{\mathrm{d}t}a_{\mathrm{Ing}}(0) &= +\underbrace{\mu_{\ell}\frac{(\ell_{\mathrm{Ing}})^{n_{\ell}}}{(\xi_{\ell})^{n_{\ell}}+(\ell_{\mathrm{Ing}})^{n_{\ell}}}m_{\mathrm{Ing}}}_{\substack{\text{ingestion of native LDL}\\ \text{by macrophages}}} + \underbrace{\mu_{\tilde{\ell}}\frac{(\tilde{\ell}_{\mathrm{Ing}})^{n_{\tilde{\ell}}}}{(\xi_{\tilde{\ell}})^{n_{\tilde{\ell}}}+(\tilde{\ell}_{\mathrm{Ing}})^{n_{\tilde{\ell}}}}m_{\mathrm{Ing}}}_{\substack{\text{ingestion of modified LDL}\\ \text{by macrophages}}}, \\
\ell_{\mathrm{Ing}}(0) &= \ell_{\mathrm{Ing},0}\underbrace{\frac{\ell_{\mathrm{Mod}}(T_{\mathrm{Mod}})}{\ell_{\mathrm{Mod}}(T_{\mathrm{Mod}})+\tilde{\ell}_{\mathrm{Mod}}(T_{\mathrm{Mod}})}}_{\substack{\text{fraction of native LDL at end}\\ \text{of first experimental stage}}}, \\
\tilde{\ell}_{\mathrm{Ing}}(0) &= \ell_{\mathrm{Ing},0}\underbrace{\frac{\tilde{\ell}_{\mathrm{Mod}}(T_{\mathrm{Mod}})}{\ell_{\mathrm{Mod}}(T_{\mathrm{Mod}})+\tilde{\ell}_{\mathrm{Mod}}(T_{\mathrm{Mod}})}}_{\substack{\text{fraction of modified LDL at end}\\ \text{of first experimental stage}}}, \\
a_{\mathrm{Ing}}(0) &= 0, \quad t \in [0; T_{\mathrm{Ing}}],
\end{aligned}
\tag{5.2}
$$

where $T_{\mathrm{Mod}}, \ell_{\mathrm{Mod},0}, m_{\mathrm{Mod}}, e_{\mathrm{Mod}}, T_{\mathrm{Ing}}, \ell_{\mathrm{Ing},0}$ and m_{Ing} are experiment-specific parameters of the submodel (see Table 5.2). The remaining constants $q_{\ell,m}, q_{\ell,e}, \mu_{\ell}, \xi_{\ell}, n_{\ell}, \mu_{\tilde{\ell}}, \xi_{\tilde{\ell}}$ and $n_{\tilde{\ell}}$ are the unknown parameters of submodel $\boxed{1}$. They are estimated by least-squares fitting the simulated ingestion of native and modified LDL per macrophage in the ingestion phase $\frac{a_{\mathrm{Ing}}(T_{\mathrm{Ing}})}{m_{\mathrm{Ing}}}$ is fitted to the experimental results in [116] and [165].

5.1.1.2 HDL protection against LDL modification

The native HDL offers a protection against the oxidative modification of native LDL. The submodel of HDL protection against LDL modification is based on *in vitro* experiments by *Mackness et al.* [187]. It is subsequently denoted as submodel $\boxed{2}$.

Experimental setup

The HDL protection against the oxidative modification of LDL by copper sulfate was investigated *in vitro* in [187]. Specified initial concentrations of native LDL ℓ_0 and HDL h_0 were exposed to specified concentrations of copper sulfate ς for specified time periods T_{Mod}. Among other things, the lipid peroxide content per lipoprotein particle was measured for various experiment-specific values of ℓ_0, h_0, ς and T_{Mod} as shown in Table 5.3.

Mathematical submodel

The experimental observations in [187] are driven by the modification of native LDL and native HDL by copper sulfate as well as by the inhibition of LDL modification by native HDL. The protection that HDL gives against modification of native LDL by copper sulfate saturates as the

Table 5.3 Experiment-specific parameters of the mathematical submodel of HDL protection against LDL modification (submodel 2) in analogy to the experimental setups in [187].

Experiment \ Quantity	T_{Mod} [h]	ℓ_0 $[\frac{\text{mg protein}}{\text{ml}}]$	h_0 $[\frac{\text{mg protein}}{\text{ml}}]$	ς $[\frac{\mu\text{Mol}}{\text{ml}}]$
[187], Fig. 4, $\ell_0 = 0, h_0 = 1.5$	$0-24$	0	1.5	5
[187], Fig. 4, $\ell_0 = 1.5, h_0 = 0$	$0-24$	1.5	0	5
[187], Fig. 4, $\ell_0 = 1.5, h_0 = 1.5$	$0-24$	1.5	1.5	5
[187], Fig. 5	6	1.5	$0-2$	5

All values are given in the units of submodel 2.

concentration of HDL h increases (see [187], Figure 5). The modification of native LDL and native HDL by copper sulfate is described by linear relationships in their concentrations ℓ, h and ς, respectively, as no experimental data exist which indicates otherwise. The lipid peroxide quantities are used as a measure of the concentrations of modified LDL and modified HDL. Therefore, each mg of $\mathrm{lipid\ protein}$ of modified LDL and modified HDL as given in [187] is converted to $N_{\tilde{\ell}}$ nMol and $N_{\tilde{h}}$ nMol of lipid peroxide, respectively.

The mathematical submodel is formulated in the following units: time $[t] = \mathrm{h}$, concentration of native LDL $[\ell] = \frac{\text{mg protein}}{\text{ml}}$, concentration of modified LDL $[\tilde{\ell}] = \frac{\text{mg protein}}{\text{ml}}$, concentration of native HDL $[h] = \frac{\text{mg protein}}{\text{ml}}$, concentration of modified HDL $[\tilde{h}] = \frac{\text{mg protein}}{\text{ml}}$ and concentration of copper sulfate $[\varsigma] = \frac{\mu\text{Mol}}{\text{ml}}$. The submodel consists of a system of four ODEs and associated initial conditions

$$\begin{aligned}
\frac{\mathrm{d}}{\mathrm{d}t}\ell(t) &= -\underbrace{q_{\ell,\varsigma}\ell\varsigma}_{\substack{\text{modification of native}\\ \text{LDL by copper sulfate}}} \cdot \underbrace{\frac{(k_h)^{n_h}}{(k_h)^{n_h} + h^{n_h}}}_{\substack{\text{inhibition of modi-}\\ \text{fication by native HDL}}} = -\frac{\mathrm{d}}{\mathrm{d}t}\tilde{\ell}(t), \\
\frac{\mathrm{d}}{\mathrm{d}t}h(t) &= -\underbrace{q_{h,\varsigma}h\varsigma}_{\substack{\text{modification of native}\\ \text{HDL by copper sulfate}}} \cdot \underbrace{\frac{(k_h)^{n_h}}{(k_h)^{n_h} + h^{n_h}}}_{\substack{\text{inhibition of modi-}\\ \text{fication by native HDL}}} = -\frac{\mathrm{d}}{\mathrm{d}t}\tilde{h}(t), \qquad (5.3) \\
\ell(0) &= \ell_0, \quad \tilde{\ell}(0) = 0, \quad h(0) = h_0, \quad \tilde{h}(0) = 0, \quad t \in [0; T_{\mathrm{Mod}}],
\end{aligned}$$

where $T_{\mathrm{Mod}}, \ell_0, h_0$ and ς are experiment-specific parameters (see Table 5.3). The remaining constants $N_{\tilde{\ell}}, N_{\tilde{h}}, q_{\ell,\varsigma}, q_{h,\varsigma}, k_h$ and n_h are the unknown parameters of submodel 2. They are estimated by least-squares fitting of the simulated lipid peroxide content per lipoprotein $\frac{N_{\tilde{\ell}}\tilde{\ell}(T_{\mathrm{Mod}})}{\ell_0}$ and the reduction of lipid peroxide content due to the presence of HDL to the experimental results in [187].

5.1.1.3 Cholesterol cycle and reverse cholesterol transport

Macrophages ingest native and modified LDL and store its cholesterol content as intracellular free and esterified cholesterol. Free and esterified cholesterol are in a dynamic equilibrium due to hydrolysis and esterification. Further, macrophages are able to offload their free cholesterol content to native HDL. The submodel of cholesterol cycle and reverse cholesterol transport is based on *in vitro* experiments by *Brown et al.* [24, 25]. It is subsequently denoted as submodel $\boxed{3}$.

Experimental setup

The ingestion of cholesterol by macrophages and the cholesterol cycle within macrophages was investigated *in vitro* in [24]. Specified concentrations of modified LDL $\tilde{\ell}_0$ were incubated in a dish in the presence of specified densities of macrophages m for specified time periods T_{Cho}. Among other things, the intracellular free cholesterol and cholesterol ester per macrophage were measured for various experiment-specific values of $\tilde{\ell}_0, m$ and T_{Cho} as shown in Table 5.4.

Using this study [24] as a basis, the cholesterol efflux from macrophages to HDL was investigated in [25] using a multi-staged experimental setup. First, specified densities of macrophages m were loaded with free and esterified cholesterol by incubation with LDL. Subsequently, the concentrations of intracellular free cholesterol f_0 and esterified cholesterol b_0 per macrophage were measured. After specified time periods T_h, specified concentrations of HDL h_0 were added. After a total time period of T_{Cho} the intracellular free and esterified cholesterol per macrophage as well as the excreted cholesterol per macrophage was measured for various experiment-specific values of m, f_0, b_0, h_0, T_h and T_{Cho} as shown in Table 5.4. In both studies, the modification of LDL by macrophages was prevented by high concentrations of fetal calf serum.

Mathematical submodel

The experimental observations in [24] and [25] are driven by the ingestion of modified LDL by macrophages, the free cholesterol-cholesterol ester cycle within macrophages and the off-loading of free cholesterol from macrophages to HDL. The ingestion of modified LDL per macrophage saturates as the concentration of modified LDL $\tilde{\ell}$ increases (see [116], Figure 7). Each $\mu\mathrm{g\ lipid\ protein}$ of ingested modified LDL can be identified with $N_f\ \mathrm{nMol}$ of incorporated intracellular cholesterol particles which are hydrolyzed to free cholesterol [25]. The cholesterol cycle of free cholesterol and cholesterol ester within macrophages shows a buffer-like behavior (see [24], Figure 1 and [25], Figure 1 and 4). Hence, it is assumed that there exists a concentration of free cholesterol f_{Min} which is favored by macrophages as well as a maximum concentration of free cholesterol f_{Max} possible within macrophages [25]. As suggested in [25], these concentrations f_{Min} and f_{Max} affect only the rate k_f of esterification and not the rate k_b of hydrolysis. The delivery of free cholesterol from macrophages to native HDL saturates as the concentration of HDL h increases (see [25], Figure 2), but only takes place when concentration of intracellular free cholesterol f is bigger than f_{Min} (see [25], Figure 1b). In accordance with the results in [25], it is assumed that native HDL is never saturated by the cholesterol it takes up and so the action of HDL does not decline through lipid loading due to reverse cholesterol transport. Additionally, a

Table 5.4 Experiment-specific parameters of the mathematical submodel of cholesterol cycle and reverse cholesterol transport (submodel $\boxed{3}$) in analogy to the experimental setups in [24] and [25].

Experiment \ Quantity	T_{Cho} [h]	T_h [h]	$h_0 \left[\frac{\text{µg lipid protein}}{\text{ml}}\right]$	$\tilde{\ell}_0 \left[\frac{\text{µg lipid protein}}{\text{ml}}\right]$	$f_0 \left[\frac{\text{nMol}}{\text{ml}}\right]$	$b_0 \left[\frac{\text{nMol}}{\text{ml}}\right]$	$m \left[\frac{\text{mg cell protein}}{\text{ml}}\right]$
[24], Fig. 1a & 1b, $\tilde{\ell}_0 = 0$	$0-96$	0	0	0	56	0	$4.16 \cdot 10^{-1}$ *
[24], Fig. 1a & 1b, $\tilde{\ell}_0 = 25$	$0-96$	0	0	25	56	0	$4.16 \cdot 10^{-1}$ *
[25], Fig. 1a, 1b & 1c, $h_0 = 0$	$0-72$	0	0	0	183	342	$6.93 \cdot 10^{-1}$ *
[25], Fig. 1a, 1b & 1c, $T_h = 0$	$0-24$	0	250	0	183	342	$6.93 \cdot 10^{-1}$ *
[25], Fig. 1a, 1b & 1c, $T_h = 24$	$0-48$	24	250	0	183	342	$6.93 \cdot 10^{-1}$ *
[25], Fig. 1a, 1b & 1c, $T_h = 48$	$0-72$	48	250	0	183	342	$6.93 \cdot 10^{-1}$ *
[25], Fig. 2a, $T_{\mathrm{Cho}} = 8$	8	0	$0-267$	0	212	405	$6.93 \cdot 10^{-1}$ *
[25], Fig. 2a, $T_{\mathrm{Cho}} = 24$	24	0	$0-267$	0	212	405	$6.93 \cdot 10^{-1}$ *
[25], Fig. 4	24	0	$0-250$	0	177 **	456 **	1.39 *
[25], Fig. 7a & 7b, $h_0 = 0$	$0-6$	0	0	0	190	488	$6.93 \cdot 10^{-1}$ *
[25], Fig. 7a & 7b, $h_0 = 200$	$0-6$	0	200	0	190	488	$6.93 \cdot 10^{-1}$ *

Parameters indicated by * are estimated using ρ_5 from Table 5.1. Parameters indicated by ** are estimated by least-squares fitting to the experimental results. All values are given in the units of submodel $\boxed{3}$.

constant efflux of intracellular free cholesterol from macrophages independent of native HDL (see [24], Figure 1a and [25], Figure 1c) occurs *in vitro*.

The mathematical submodel is formulated in the following units: time $[t] = \mathrm{h}$, concentration of modified LDL $[\tilde{\ell}_0] = \frac{\text{µg lipid protein}}{\text{ml}}$, concentration of native HDL $[h] = \frac{\text{µg lipid protein}}{\text{ml}}$, density of macrophages $[m] = \frac{\text{mg cell protein}}{\text{ml}}$, concentration of total intracellular free cholesterol $[f] = \frac{\text{nMol}}{\text{ml}}$, concentration of total intracellular cholesterol ester $[b] = \frac{\text{nMol}}{\text{ml}}$ and concentration of total cholesterol excreted from cells $[r] = \frac{\text{nMol}}{\text{ml}}$. The submodel consists of a system of three ODEs and associated initial conditions

$$
\begin{aligned}
h(t) &= h_0 \mathcal{H}(t - T_h) \\
\frac{\mathrm{d}}{\mathrm{d}t} f(t) &= +N_f \underbrace{\mu_{\tilde{\ell}} \frac{\left(\tilde{\ell}_0\right)^{n_{\tilde{\ell}}}}{\left(\xi_{\tilde{\ell}}\right)^{n_{\tilde{\ell}}} + \left(\tilde{\ell}_0\right)^{n_{\tilde{\ell}}}} m}_{\text{ingestion of modified LDL}} - \underbrace{k_f \frac{\frac{f}{m} - f_{\mathrm{Min}}}{f_{\mathrm{Max}} - \frac{f}{m}} \left(\frac{f}{m} - f_{\mathrm{Min}}\right) m}_{\text{esterification of free cholesterol}}
\end{aligned}
\tag{5.4}
$$

$$
\begin{aligned}
&+ \underbrace{k_b b}_{\substack{\text{hydrolysis of}\\ \text{cholesterol ester}}} - \underbrace{\left(c_f + \mu_f \frac{h^{n_f}}{(\xi_f)^{n_f} + h^{n_f}}\right)\left(\frac{f}{m} - f_{\mathrm{Min}}\right) m}_{\text{cholesterol efflux from macrophages to HDL}},\\
\frac{\mathrm{d}}{\mathrm{d}t} b(t) &= + \underbrace{k_f \frac{\frac{f}{m} - f_{\mathrm{Min}}}{f_{\mathrm{Max}} - \frac{f}{m}}\left(\frac{f}{m} - f_{\mathrm{Min}}\right) m}_{\text{esterification of free cholesterol}} - \underbrace{k_b b}_{\substack{\text{hydrolysis of}\\ \text{cholesterol ester}}},\\
\frac{\mathrm{d}}{\mathrm{d}t} r(t) &= + \underbrace{\left(c_f + \mu_f \frac{h^{n_f}}{(\xi_f)^{n_f} + h^{n_f}}\right)\left(\frac{f}{m} - f_{\mathrm{Min}}\right) m}_{\text{cholesterol efflux from macrophages to HDL}},\\
f(0) &= f_0 m, \quad b(0) = b_0 m, \quad r(0) = 0, \quad t \in [0; T_{\mathrm{Cho}}],
\end{aligned}
\tag{5.4}
$$

where the function $\mathcal{H}$ denotes the Heaviside step function and $T_{\mathrm{Cho}}, T_h, h_0, \tilde{\ell}_0$, f_0, b_0 and m, are experiment-specific parameters (see Table 5.4). The constants $\mu_{\tilde{\ell}}, \xi_{\tilde{\ell}}, n_{\tilde{\ell}}$ are the same as those introduced in submodel $\boxed{1}$. The values of these parameters determined by the fitting of submodel $\boxed{1}$ are used, see Table 5.7. The remaining constants $N_f, f_{\mathrm{Min}}, f_{\mathrm{Max}}, k_f, k_b, c_f, \mu_f, \xi_f$ and n_f are the unknown parameters of submodel $\boxed{3}$. They are estimated using a least-squares fit of the simulated concentration of intracellular free cholesterol $\frac{f(T_{\mathrm{Cho}})}{m}$, intracellular cholesterol ester $\frac{b(T_{\mathrm{Cho}})}{m}$ and excreted cholesterol $\frac{r(T_{\mathrm{Cho}})}{m}$ per macrophage to the experimental results in [24] and [25]. The results in [24] are converted into the correct units for the submodel using the molecular weights of free cholesterol $M_f = 3.87 \cdot 10^2 \ \frac{\mathrm{g}}{\mathrm{Mol}}$ and cholesterol ester $M_b = 6.48 \cdot 10^2 \ \frac{\mathrm{g}}{\mathrm{Mol}}$ [263]. Additionally, doubled results from [25], Figure 2 are used in order to be consistent with other measurements of the same experiment, i.e., [25], Figure 1c, 4 and 7b.

5.1.2 Combined model of early atherosclerotic plaque formation

The purpose of the combined mathematical model is to predict the development of early stages of atherosclerotic plaques as they may occur *in vivo*. It is based on the previous submodels of *in vitro* systems that quantified the modification and ingestion of LDL by macrophages and endothelial cells, the protective action of HDL against LDL modification, the cholesterol cycle within macrophages and reverse cholesterol transport from macrophages. Hence, it is assumed that the previous assumptions underlying the submodels and parameters of the *in vitro* systems are valid in an *in vivo* setting too. This modeling approach is philosophically the same as by experimental scientists and relies on the idea that results from *in vitro* studies can be used to inform the understanding of what goes on *in vivo*.

It it assumed that the protection against LDL modification that HDL provides is independent of the source of modification, as no experimental data exist which indicates otherwise. Hence, it is assumed that the protection HDL gives against oxidative modification of LDL by copper is also valid for endothelial cell and macrophage mediated modification. Following [46] the rates of modification of native HDL by macrophages and endothelial cells are 7.6 times smaller than the rates that LDL is modified by macrophages and endothelial cells. Modified HDL no longer takes part in the reverse cholesterol transport [204].

In contrast to the *in vitro* systems where the experiments were run in hours or days, the disease progression *in vivo* happens on a much longer time scale. Hence, the fate of macrophages *in vivo* is of particular interest. Macrophages can undergo necrosis, proliferation, emigration and apoptosis. But as rates of necrosis, proliferation and emigration are small in early stages of atherosclerosis (see [180, 220, 228]), the only fate of macrophages considered in the model is apoptosis. The rate of macrophage apoptosis is dependent on the concentration of free cholesterol within macrophages (see [296], Figure 4a), which is approximated by the average concentration $\frac{f}{m}$ of intracellular free cholesterol per macrophage. As it is implausible to assume an unlimited rate of macrophages apoptosis and it is in accordance with the results in [296], it is assumed that the rate of apoptosis saturates (with an exponent of $n_m = 2$) as the concentration of free cholesterol f increases. In [296] the initial population of macrophages $m(t)$ decays exponentially over the time period of the experiment $T_{\mathrm{Apo}} = 9\ \mathrm{h}$. This gives:

$$m(T_{\mathrm{Apo}}) = m_0 \exp\left(-\mu_m \frac{\left(\frac{f_0}{m_0}\right)^{n_m}}{(\xi_m)^{n_m} + \left(\frac{f_0}{m_0}\right)^{n_m}} T_{\mathrm{Apo}} \right), \tag{5.5}$$

where $\frac{f_0}{m_0}$ is the experiment-specific average intracellular free cholesterol of the macrophage population. The unknown parameters μ_m and ξ_m are least-squares fitted to the measurements of *Yao et al.* [296], Figure 4a. The total intracellular free and esterified cholesterol is not affected by apoptosis as it can be assumed that all apoptotic macrophages are cleared by other non-apoptotic macrophages by efferocytosis which is assumed to be not defective [237].

The concentrations of native LDL ℓ, native HDL h and the density of macrophages m in plaques are determined by recruitment from the bloodstream. Hence, rates of recruitment of native LDL r_ℓ, of native HDL r_h and of macrophages r_m (per unit area of plaque surface) are introduced into the combined model. Monocytes in the blood contain a concentration of free cholesterol f_{In} [296] that remains within each monocyte-derived macrophage when it migrates into a plaque.

The radial thickness of the plaques is denoted by H. A thickness of $H = 10\ \mu\mathrm{m}$ is used which is the width of the intima [221, 294] as early stages of atherosclerosis are considered. The factor $\frac{1}{H}$ is introduced to account for effects of processes which take place on plaque surface (such as the inward flux of lipids and cells from the blood and the modification of LDL and HDL by endothelial cells) on volume-averaged concentrations.

Mathematical model

The combined model is formulated in the following units: time $[t] = \mathrm{h}$, concentration of native LDL $[\ell] = \frac{1}{\mathrm{mm}^3}$, concentration of modified LDL $[\tilde{\ell}] = \frac{1}{\mathrm{mm}^3}$, concentration of native HDL $[h] = \frac{1}{\mathrm{mm}^3}$, concentration of total intracellular free cholesterol $[f] = \frac{1}{\mathrm{mm}^3}$, concentration of total intracellular cholesterol ester $[b] = \frac{1}{\mathrm{mm}^3}$ and density of macrophages $[m] = \frac{1}{\mathrm{mm}^3}$. The combined model consists of a system of six ODEs and associated initial conditions

$$
\begin{aligned}
\frac{\mathrm{d}}{\mathrm{d}t}\ell(t) =& -\underbrace{\mu_\ell \frac{\ell^{n_\ell}}{(\xi_\ell)^{n_\ell}+\ell^{n_\ell}} m}_{\substack{\text{ingestion of native LDL}\\ \text{by macrophages}}} - \underbrace{\left(q_{\ell,m}\ell m + \frac{q_{\ell,e}}{H}\ell\right)}_{\substack{\text{modification of native LDL}\\ \text{by macrophages and}\\ \text{endothelial cells}}} \cdot \underbrace{\frac{(k_h)^{n_h}}{(k_h)^{n_h}+h^{n_h}}}_{\substack{\text{inhibition of}\\ \text{modification by HDL}}} + \underbrace{\frac{r_\ell}{H}}_{\substack{\text{recruitment}\\ \text{of native LDL}}}, \\
\frac{\mathrm{d}}{\mathrm{d}t}\tilde{\ell}(t) =& -\underbrace{\mu_{\tilde{\ell}} \frac{\tilde{\ell}^{n_{\tilde{\ell}}}}{(\xi_{\tilde{\ell}})^{n_{\tilde{\ell}}}+\tilde{\ell}^{n_{\tilde{\ell}}}} m}_{\substack{\text{ingestion of modified LDL}\\ \text{by macrophages}}} + \underbrace{\left(q_{\ell,m}\ell m + \frac{q_{\ell,e}}{H}\ell\right)}_{\substack{\text{modification of native LDL}\\ \text{by macrophages and}\\ \text{endothelial cells}}} \cdot \underbrace{\frac{(k_h)^{n_h}}{(k_h)^{n_h}+h^{n_h}}}_{\substack{\text{inhibition of}\\ \text{modification by HDL}}}, \\
\frac{\mathrm{d}}{\mathrm{d}t}h(t) =& -\underbrace{q_{h,m}hm}_{\substack{\text{modification of HDL}\\ \text{by macrophages}}} - \underbrace{\frac{q_{h,e}}{H}h}_{\substack{\text{modification of HDL}\\ \text{by endothelial cells}}} + \underbrace{\frac{r_h}{H}}_{\substack{\text{recruitment}\\ \text{of HDL}}}, \\
\frac{\mathrm{d}}{\mathrm{d}t}f(t) =& + N_f \underbrace{\mu_\ell \frac{\ell^{n_\ell}}{(\xi_\ell)^{n_\ell}+\ell^{n_\ell}} m}_{\substack{\text{ingestion of native LDL}\\ \text{by macrophages}}} + N_f \underbrace{\mu_{\tilde{\ell}} \frac{\tilde{\ell}^{n_{\tilde{\ell}}}}{(\xi_{\tilde{\ell}})^{n_{\tilde{\ell}}}+\tilde{\ell}^{n_{\tilde{\ell}}}} m}_{\substack{\text{ingestion of modified LDL}\\ \text{by macrophages}}} - \underbrace{k_f \frac{(f-f_{\mathrm{Min}}m)^2}{f_{\mathrm{Max}}m-f}}_{\substack{\text{esterification of}\\ \text{free cholesterol}}} \\
&+ \underbrace{k_b b}_{\substack{\text{hydrolysis of}\\ \text{cholesterol ester}}} - \underbrace{\mu_f \frac{h^{n_f}}{(\xi_f)^{n_f}+h^{n_f}}(f-f_{\mathrm{Min}}m)}_{\text{cholesterol efflux from macrophages to HDL}} + \underbrace{\frac{r_m}{H} f_{\mathrm{In}}}_{\substack{\text{recruitment of}\\ \text{macrophages}}}, \\
\frac{\mathrm{d}}{\mathrm{d}t}b(t) =& + \underbrace{k_f \frac{(f-f_{\mathrm{Min}}m)^2}{f_{\mathrm{Max}}m-f}}_{\substack{\text{esterification of}\\ \text{free cholesterol}}} - \underbrace{k_b b}_{\substack{\text{hydrolysis of}\\ \text{cholesterol ester}}}, \\
\frac{\mathrm{d}}{\mathrm{d}t}m(t) =& -\underbrace{\mu_m \frac{f^{n_m}}{(\xi_m m)^{n_m}+f^{n_m}} m}_{\text{apoptosis of macrophages}} + \underbrace{\frac{r_m}{H}}_{\substack{\text{recruitment of}\\ \text{macrophages}}}, \\
&\ell(0)=0, \quad \tilde{\ell}(0)=0, \quad h(0)=0, \quad f(0)=f_0 m_0, \\
&b(0)=b_0 m_0, \quad m(0)=m_0, \quad t\in[0;\infty[,
\end{aligned}
\tag{5.6}
$$

where all parameters except the initial conditions f_0, b_0, m_0 and the rates of recruitment r_ℓ, r_h, r_m have been introduced previously.

The initial conditions describe the normal, non-inflamed state of the artery wall determined by the prior condition of the subject. It is assumed that the initial intracellular free cholesterol f_0 per macrophage is 50% higher than the free cholesterol f_{In} of recruited macrophages. Assuming that macrophages and intracellular cholesterols are in a steady-state, it follows

$$
\begin{aligned}
f_0 &= 1.5 f_{\mathrm{In}}, \\
m_0 &= \frac{r_m}{H} \frac{(\xi_m)^{n_m}+(f_0)^{n_m}}{\mu_m (f_0)^{n_m}}, \\
b_0 &= \frac{k_f}{k_b} \frac{(f_0-f_{\mathrm{Min}})^2}{f_{\mathrm{Max}}-f_0}.
\end{aligned}
\tag{5.7}
$$

Table 5.5 Ranges of rates of recruitment for the combined mathematical model.

Parameter	Description	Range	Source
r_ℓ	Rate of native LDL influx	$3 \cdot 10^6 - 3 \cdot 10^9 \ \frac{1}{\text{h mm}^2}$ *	[205, 221, 268, 272]
r_h	Rate of native HDL influx	$4 \cdot 10^7 - 4 \cdot 10^9 \ \frac{1}{\text{h mm}^2}$ *	[205, 221, 251, 268]
r_m	Rate of macrophage recruitment	$400 - 2800 \ \frac{1}{\text{h mm}^2}$	[2, 141]

Parameters indicated by * are estimated using ρ_8 and ρ_{13} from Table 5.1. All values are given in the units of the combined mathematical model.

The initial conditions for the concentrations of lipids are set to zero as the lipids rapidly reach a non-zero equilibrium. It is important to note that the long-term behavior of the combined model is independent of the specific choice of initial conditions.

The rates of recruitment of native LDL r_ℓ, native HDL r_h and macrophages r_m into the plaque in reality are strongly dependent on the particular plaque under consideration, including the wall shear stress, where the plaque forms, and the diet, lifestyle and physiology of the individual who carries the plaque.

The simplified version of the second *Kedem-Katchalsky* equation presented in Section 4.1.2.3 can be used to calculate a rough estimate for the recruitment rates of LDL r_ℓ and HDL r_h. For the condition of a healthy subject this estimate shows that the recruitment rates of LDL and HDL can vary by an order of up to 100 [205, 221, 268]. However, in LDL receptor-deficient mice on a high fat-diet this order can even increase up to 1000 due to the very high LDL profile in blood [272]. The rate of macrophage recruitment is approximated by the experimental results in [141] and [2]. An overview of the ranges of these rates of recruitment is given in Table 5.5.

Remark. *The mathematical submodels that describe the* in vitro *systems are special cases of the combined model of early atherosclerotic plaque formation.*

Remark. *To keep the notation comprehensible, the symbols f and b have the following definitions: Stand-alone f and b represent the (time-dependent) total concentrations of intracellular free and esterified cholesterol per volume, respectively. However, with an index, such as $f_0, f_{\text{Min}}, f_{\text{Max}}, f_{\text{In}}$ and b_0 they denote (constant) quantities of unit intracellular cholesterol per macrophage.*

5.2 Methods

This section gives the methods that are required to analyze the combined model. A sensitivity analysis of the combined model with respect to its parameters is performed that identifies crucial parameters and processes and that suggests future experimental investigations (Section 5.2.1). Further, the combined model with the least-squares fitted parameters is used to forecast the stability of the model plaque based on prescribed recruitment rates of LDL, HDL and macrophages into the artery wall (Section 5.2.2).

5.2.1 Sensitivity analysis of combined model

Most of the parameters of the combined model are estimated by least-squares fits of the submodels to the respective *in vitro* experiments. The estimated parameters have a degree of uncertainty due to the different experimental setups and measurement methods, different animals used as experimental models and measurement errors. Additionally, the conversion from the various units of measurement in the experimental studies (especially "mass of cell protein" to "amount of cells" via ρ_5 from Table 5.1) to a unified SI unit system introduces another source of uncertainty for some parameters.

To quantify the effect of uncertainties in the parameters on the results of the combined model, a local sensitivity analysis in terms of a metabolic control analysis [300] is performed. Therefore, the normalized partial derivatives of all concentrations with respect to all parameters p of the combined model (see Tables 5.5 and 5.7) at time $T_{\mathrm{AC}} = 25$ weeks are compared. As in [300], the partial derivatives are estimated by using forward finite difference approximations with a sufficiently small variation parameter $\varepsilon = 0.1\%$. Hence, the metabolic control coefficient $\mathrm{MCC}(\ell, p)$ of LDL ℓ with respect to the model parameter p is computed by

$$\mathrm{MCC}(\ell, p) = \frac{1}{\ell_p(T_{\mathrm{AC}})} \frac{\partial}{\partial p} \ell_p(T_{\mathrm{AC}}) \approx \frac{1}{\ell_p(T_{\mathrm{AC}})} \frac{\ell_{p+\varepsilon\%}(T_{\mathrm{AC}}) - \ell_p(T_{\mathrm{AC}})}{\varepsilon}, \tag{5.8}$$

where $\ell_{p+\varepsilon\%}$ denotes the concentration of LDL ℓ computed with the parameter p perturbed by ε percent. The metabolic control coefficients of all other species are computed in the same way. As a basis for the perturbation of the recruitment rates $r_\ell = 3 \cdot 10^7 \ \frac{1}{\mathrm{h\ mm^2}}, r_h = 4 \cdot 10^8 \ \frac{1}{\mathrm{h\ mm^2}}$ and $r_m = 1000 \ \frac{1}{\mathrm{h\ mm^2}}$ are used. For all other parameters the values stated in Table 5.7 are utilized.

5.2.2 Stability analysis of combined model

The long-term outcome for the plaque of the combined model is strongly dependent on the three recruitment rates of LDL r_ℓ, of HDL r_h and of macrophages r_m, which characterize the physiology and diet of the plaque's host and its position within the cardiovascular system. They vary by up to three orders of magnitude (see Table 5.5) resulting in qualitatively different predicted developments of the model plaque. Hence, a focus is put on these three recruitment rates and a systematic analysis of the stability of the combined model is performed. Therefore, the following proposition is used:

Proposition 1. Let $\ell(t), \tilde{\ell}(t), h(t), f(t), b(t), m(t)$ $(t \geq 0)$ be the unique and smooth solution of the initial value problem defined by Equations (5.6) and (5.7) with strictly positive parameters fulfilling $f_{\mathrm{Min}} \leq f_{\mathrm{In}} < f_{\mathrm{Max}}$ and $f_{\mathrm{Min}} \leq f_0 < f_{\mathrm{Max}}$. Then the solution satisfies:

(a) $\ell(t), \tilde{\ell}(t), h(t), f(t), b(t), m(t) \geq 0$ for all $t \geq 0$.

(b) $m(t) \in \Bigg[\underbrace{\frac{r_m}{H} \frac{(\xi_m)^{n_m} + (f_{\mathrm{Max}})^{n_m}}{\mu_m (f_{\mathrm{Max}})^{n_m}}}_{=:m_{\mathrm{Min}}}, \underbrace{\frac{r_m}{H} \frac{(\xi_m)^{n_m} + (f_{\mathrm{Min}})^{n_m}}{\mu_m (f_{\mathrm{Min}})^{n_m}}}_{=:m_{\mathrm{Max}}} \Bigg]$ and $\frac{f(t)}{m(t)} \in [f_{\mathrm{Min}}, f_{\mathrm{Max}}]$ for all $t \geq 0$.

(c) $\ell(t), h(t), f(t), m(t)$ are bounded. If additionally $\frac{r_\ell}{H} < \mu_{\tilde{\ell}} m_{\mathrm{Min}}$, then $\tilde{\ell}(t)$ is bounded too.

Proof. See Appendix A.

The long-term outcome of the combined model is analyzed by numerically determining the steady-state solutions for the concentrations of macrophages $\widehat{m} \in [m_{\mathrm{Min}}; m_{\mathrm{Max}}]$ and total intracellular free cholesterol per macrophage $\frac{\widehat{f}}{\widehat{m}} \in [f_{\mathrm{Min}}; f_{\mathrm{Max}}]$ for the full physiological spectrum of rates of recruitment r_ℓ, r_h and r_m (see Table 5.5). Additionally, the boundedness of the concentration of the total intracellular cholesterol ester $b(t)$ with respect to the recruitment rates is investigated numerically in order to assess the severity and risk of plaques.

5.3 Results

In this section all results gained from the models in Section 5.1 and the methods in Section 5.2 are presented. All numerical computations were performed using MATLAB (The MathWorks Inc., Natick, Massachusetts, USA, 2000).

5.3.1 Model parameters

The mathematical submodels of LDL modification and ingestion, HDL protection against LDL modification, cholesterol cycle and reverse cholesterol transport and macrophage apoptosis are numerically solved and their parameters least-squares fitted to the respective experimental results. An overview of the sources of these studies, the number of different experiments in each study and the number of data points from each study that were used in the least-squares fitting of the unknown parameters is given in Table 5.6. The fitted parameters and the remaining parameters of the combined model are given in Table 5.7. The least-squares fits of the mathematical submodels of *in vitro* systems to the experimental results in [24, 25, 116, 165, 187, 296] are shown in Figure 5.2, 5.3, 5.4, 5.5, 5.6 and 5.7.

5.3.2 Analysis of combined model

The local sensitivity analysis of the combined mathematical model is analyzed as described in Section 5.2.1. The results of the performed metabolic control analysis are independent of the chosen variation parameter $\varepsilon = 0.1\%$. The metabolic control coefficients of native LDL, modified LDL, HDL, average intracellular free and esterified cholesterol per macrophage and macrophages with respect to all model parameters of the combined model are visualized in Figure 5.8.

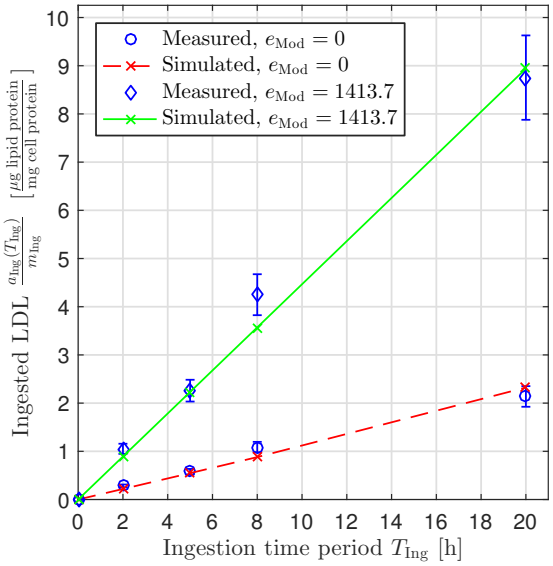

(a) Least-squares fits of simulated ingestion of native LDL and endothelial cell modified LDL to experimental results in [116], Fig. 1 for varying ingestion time periods T_{Ing}.

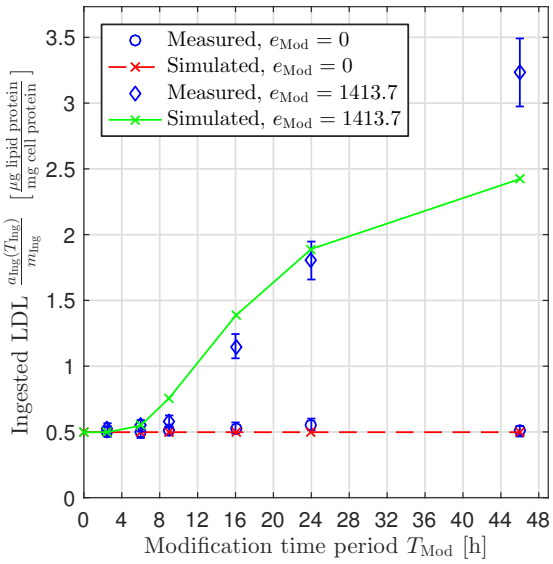

(b) Least-squares fits of simulated ingestion of native LDL and endothelial cell modified LDL to experimental results in [116], Fig. 2 for varying modification time periods T_{Mod}.

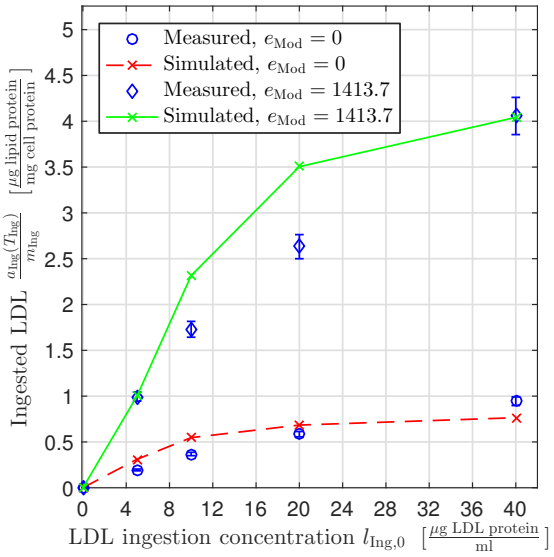

(c) Least-squares fits of simulated ingestion of native LDL and endothelial cell modified LDL to experimental results in [116], Fig. 5 for varying initial LDL ingestion concentrations $\ell_{\text{Ing},0}$.

Figure 5.2 Experimentally measured ingestion of LDL for various experimental setups in [116] and results of the least-squares fitted mathematical submodel of LDL modification and ingestion (submodel $\boxed{1}$).

Table 5.6 Overview of experimental studies, number of different experiments in each study and number of data points from each study that were used for the least-squares fitting of the mathematical submodels of *in vitro* systems.

Source	Experimental setups	Number of data points
[116]	3	34
[165]	2	24
[187]	2	27
[24]	2	20
[25]	6	65
[296]	1	2
Total	16	172

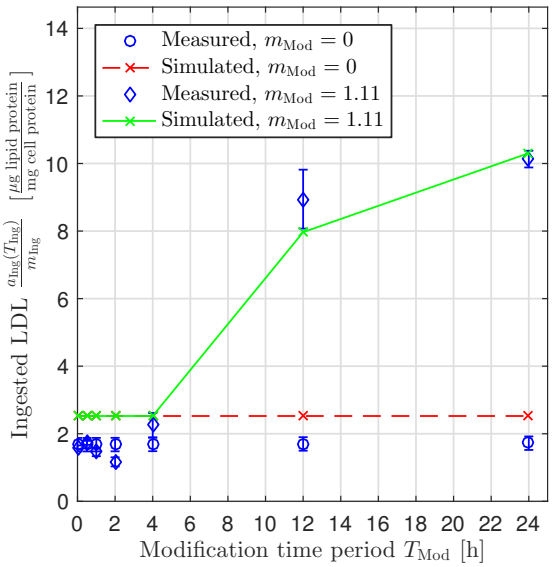

(a) Least-squares fits of simulated ingestion of native LDL and endothelial cell modified LDL to experimental results in [165], Fig. 1*a* for varying modification time periods T_{Mod}.

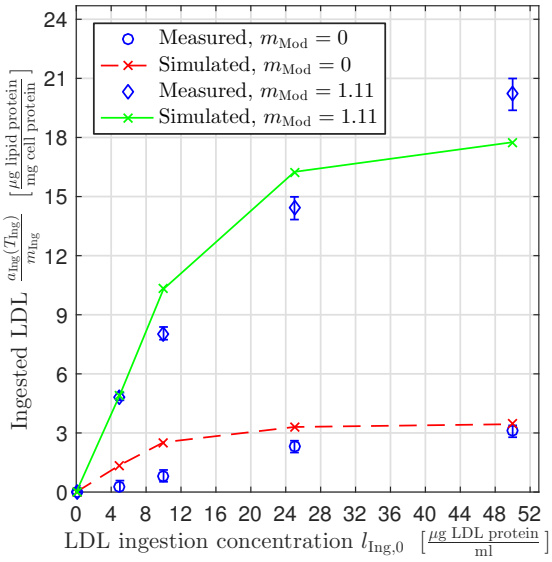

(b) Least-squares fits of simulated ingestion of native LDL and endothelial cell modified LDL to experimental results in [165], Fig. 4 for varying initial LDL ingestion concentrations $\ell_{\mathrm{Ing},0}$.

Figure 5.3 Experimentally measured ingestion of LDL for various experimental setups in [165] and results of the least-squares fitted mathematical submodel of LDL modification and ingestion (submodel $\boxed{1}$).

Table 5.7 Fitted and estimated parameters of the mathematical submodels given in units of the submodel and SI based units.

Parameter	Description	Value in units of the submodels	Value in SI based units	Fitted to / source
$q_{\ell,m}$	Rate of modification of ℓ by m	$1.18 \cdot 10^{-1}$ $\frac{\text{ml}}{\text{h (mg cell protein)}}$	$6.56 \cdot 10^{-5}$ $\frac{\text{mm}^3}{\text{h}}$	[116, 165]
$q_{\ell,e}$	Rate of modification of ℓ by e	$2.48 \cdot 10^{-5}$ $\frac{\text{ml}}{\text{h mm}^2}$	$2.48 \cdot 10^{-2}$ $\frac{\text{mm}}{\text{h}}$	[116, 165]
μ_ℓ	Rate of ingestion of ℓ by m	$1.46 \cdot 10^{-1}$ $\frac{\text{µg lipid protein}}{\text{h (mg cell protein)}}$	$8.44 \cdot 10^{4}$ $\frac{1}{\text{h}}$	[116, 165]
ξ_ℓ	Saturation of ingestion of ℓ by m	5.73 $\frac{\text{µg lipid protein}}{\text{ml}}$	$5.96 \cdot 10^{9}$ $\frac{1}{\text{mm}^3}$	[116, 165]
n_ℓ	Exponent of ingestion of ℓ by m	1.99	1.99	[116, 165]
$\mu_{\tilde{\ell}}$	Rate of ingestion of $\tilde{\ell}$ by m	$7.08 \cdot 10^{-1}$ $\frac{\text{µg lipid protein}}{\text{h (mg cell protein)}}$	$4.09 \cdot 10^{5}$ $\frac{1}{\text{h}}$	[116, 165]
$\xi_{\tilde{\ell}}$	Saturation of ingestion of $\tilde{\ell}$ by m	4.63 $\frac{\text{µg lipid protein}}{\text{ml}}$	$4.82 \cdot 10^{9}$ $\frac{1}{\text{mm}^3}$	[116, 165]
$n_{\tilde{\ell}}$	Exponent of ingestion of $\tilde{\ell}$ by m	1.99	1.99	[116, 165]
$N_{\tilde{\ell}}$	Lipid peroxide per $\tilde{\ell}$	298.49 $\frac{\text{nMol}}{\text{mg lipid protein}}$	$1.73 \cdot 10^{2}$	[187]
$N_{\tilde{h}}$	Lipid peroxide per $\tilde{h}$	63.73 $\frac{\text{nMol}}{\text{mg lipid protein}}$	9.09	[187]
$q_{\ell,\varsigma}$	Rate of lipid peroxidation in ℓ by ς	$1.11 \cdot 10^{-2}$ $\frac{\text{ml}}{\text{h µMol}}$	$1.84 \cdot 10^{-17}$ $\frac{\text{mm}^3}{\text{h}}$	[187]
$q_{h,\varsigma}$	Rate of lipid peroxidation in h by ς	$6.18 \cdot 10^{-2}$ $\frac{\text{ml}}{\text{h µMol}}$	$1.03 \cdot 10^{-16}$ $\frac{\text{mm}^3}{\text{h}}$	[187]
k_h	Saturation of inhibition of modification by h	$2.57 \cdot 10^{-1}$ $\frac{\text{mg lipid protein}}{\text{ml}}$	$1.08 \cdot 10^{12}$ $\frac{1}{\text{mm}^3}$	[187]
n_h	Exponent of inhibition of modification by h	2.59	2.59	[187]
N_f	Number of ingested f per ingested ℓ or $\tilde{\ell}$	10.61 $\frac{\text{nMol}}{\text{µg lipid protein}}$	$6.14 \cdot 10^{3}$	[24, 25]
f_{Min}	Minimum f for esterification	36.43 $\frac{\text{nMol}}{\text{mg cell protein}}$	$1.22 \cdot 10^{10}$	[24, 25]
f_{Max}	Maximum f for esterification	213.70 $\frac{\text{nMol}}{\text{mg cell protein}}$	$7.15 \cdot 10^{10}$	[24, 25]
k_f	Rate of esterification of f	$2.56 \cdot 10^{-2}$ $\frac{1}{\text{h}}$	$2.56 \cdot 10^{-2}$ $\frac{1}{\text{h}}$	[24, 25]
k_b	Rate of hydrolysis of b	$4.33 \cdot 10^{-2}$ $\frac{1}{\text{h}}$	$4.33 \cdot 10^{-2}$ $\frac{1}{\text{h}}$	[24, 25]
c_f	Rate of efflux of f	$3.32 \cdot 10^{-3}$ $\frac{1}{\text{h}}$	$3.32 \cdot 10^{-3}$ $\frac{1}{\text{h}}$	[24, 25]
μ_f	Rate of efflux of f to h	$1.65 \cdot 10^{-1}$ $\frac{1}{\text{h}}$	$1.65 \cdot 10^{-1}$ $\frac{1}{\text{h}}$	[24, 25]
ξ_f	Saturation of efflux of f to h	85.41 $\frac{\text{µg lipid protein}}{\text{ml}}$	$3.60 \cdot 10^{11}$ $\frac{1}{\text{mm}^3}$	[24, 25]
n_f	Exponent of efflux of f to h	$7.37 \cdot 10^{-1}$	$7.37 \cdot 10^{-1}$	[24, 25]
f_{In}	f of recruited m	56.85 $\frac{\text{nMol}}{\text{mg cell protein}}$	$1.90 \cdot 10^{10}$	[24, 296]
μ_m	Rate of apoptosis of m by f	$9.90 \cdot 10^{-2}$ $\frac{1}{\text{h}}$	$9.90 \cdot 10^{-2}$ $\frac{1}{\text{h}}$	[296]
ξ_m	Saturation of apoptosis of m by f	622.8 $\frac{\text{µg}}{\text{mg cell protein}}$	$5.38 \cdot 10^{11}$	[296]
n_m	Exponent of apoptosis of m by f	2.00	2.00	[296]
$q_{h,m}$	Rate of modification of h by m	-	$8.63 \cdot 10^{-6}$ $\frac{\text{mm}^3}{\text{h}}$	$= \frac{q_{\ell,m}}{7.6}$, [46]
$q_{h,e}$	Rate of modification of h by e	-	$3.26 \cdot 10^{-3}$ $\frac{\text{mm}}{\text{h}}$	$= \frac{q_{\ell,e}}{7.6}$, [46]
H	Thickness of early plaque	-	$1.00 \cdot 10^{-2}$ mm	[221, 294]
f_0	Initial f per m	-	$2.85 \cdot 10^{10}$	$= 1.5 f_{\text{In}}$

All units are converted from respective experimental units to the SI based units mm and h using ρ_5, ρ_{10} and ρ_{14} from Table 5.1. Abbreviations: native low-density lipoproteins, ℓ; modified low-density lipoproteins, $\tilde{\ell}$; native high-density lipoproteins, h; modified high-density lipoproteins, $\tilde{h}$; endothelial cells, e; macrophages, m; copper sulfate, ς; intracellular free cholesterol, f; intracellular cholesterol ester, b.

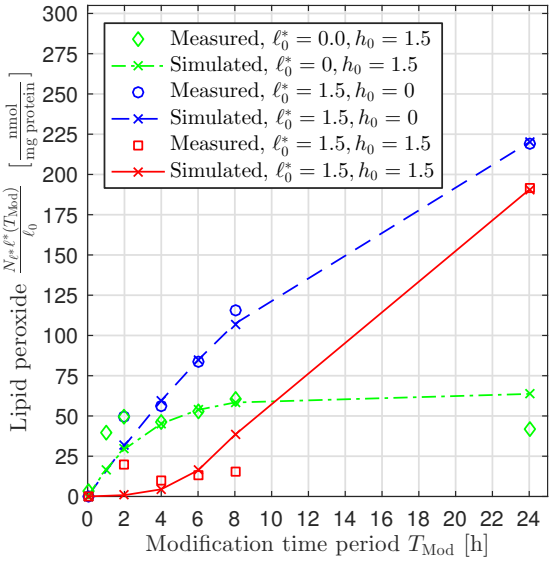

(a) Least-squares fits of simulated lipid peroxide content to experimental results in [187], Fig. 4 for varying modification time periods T_{Mod}.

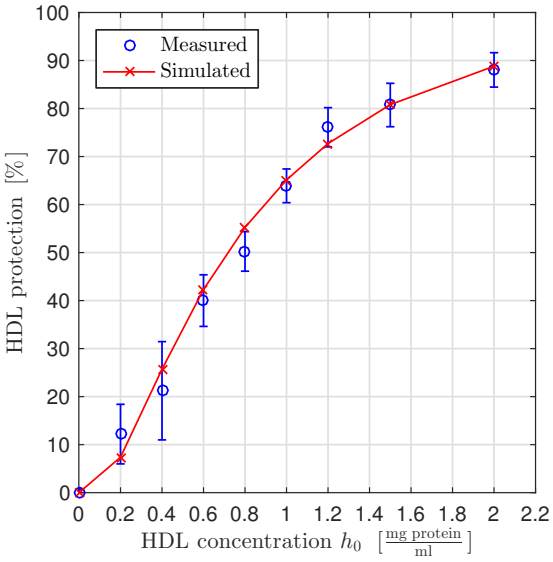

(b) Least-squares fit of simulated reduction of lipid peroxide content to experimental results in [187], Fig. 5 for varying initial HDL concentrations h_0.

Figure 5.4 Experimentally measured lipid peroxide content and HDL protection for various experimental setups in [187] and results of the least-squares fitted mathematical submodel of the HDL protection against LDL modification (submodel 2).

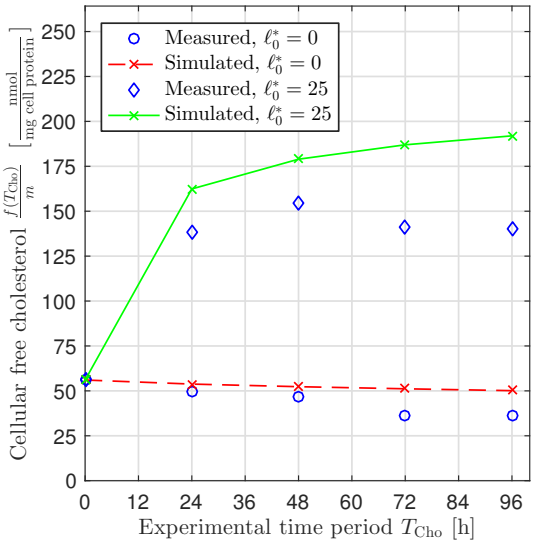

(a) Least-squares fits of simulated intracellular free cholesterol per macrophage $\frac{f(T_{\mathrm{Cho}})}{m}$ to experimental results in [24], Fig. 1a for varying experimental time periods T_{Cho}.

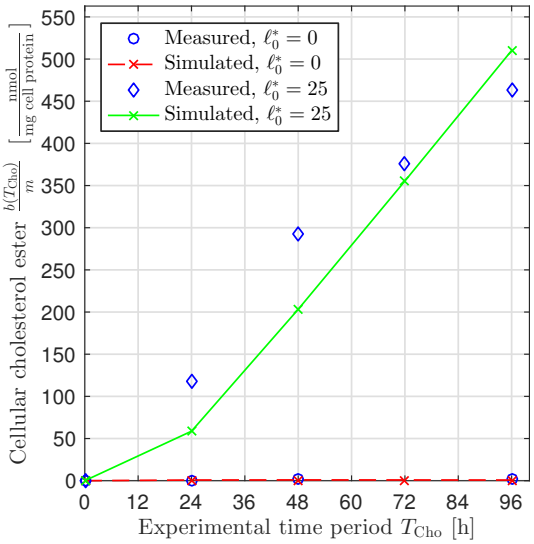

(b) Least-squares fits of simulated intracellular free cholesterol per macrophage $\frac{f(T_{\mathrm{Cho}})}{m}$ to experimental results in [24], Fig. 1b for varying experimental time periods T_{Cho}.

Figure 5.5 Experimentally measured intracellular cholesterols per macrophage for various experimental setups in [24] and results of the least-squares fitted mathematical submodel of cholesterol cycle and reverse cholesterol transport (submodel 3).

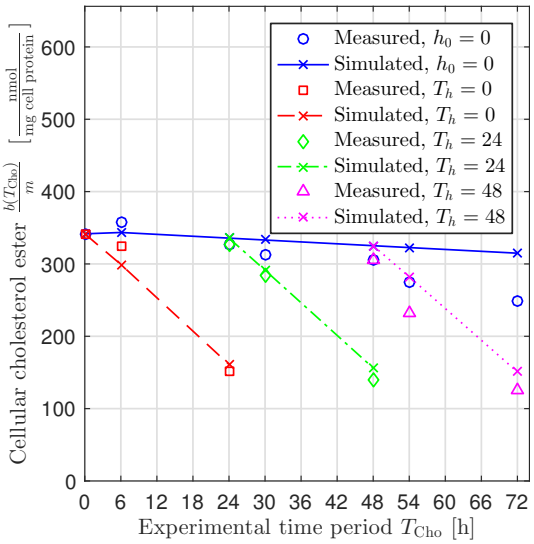

(a) Least-squares fits of simulated intracellular cholesterol ester per macrophage $\frac{b(T_{\text{Cho}})}{m}$ to experimental results in [25], Fig. 1a for varying experimental time periods T_{Cho}.

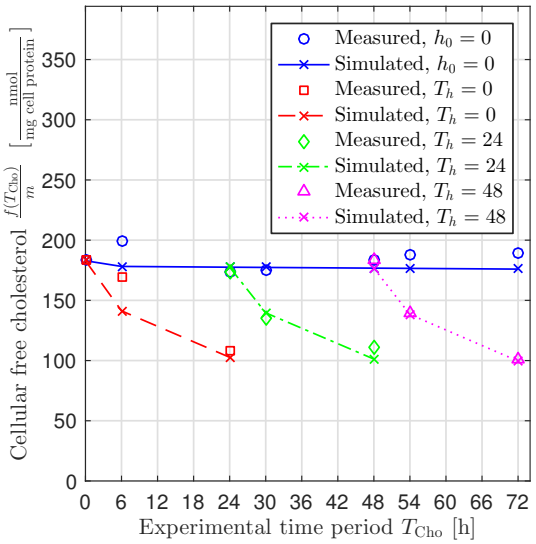

(b) Least-squares fits of simulated intracellular free cholesterol per macrophage $\frac{f(T_{\text{Cho}})}{m}$ to experimental results in [25], Fig. 1b for varying experimental time periods T_{Cho}.

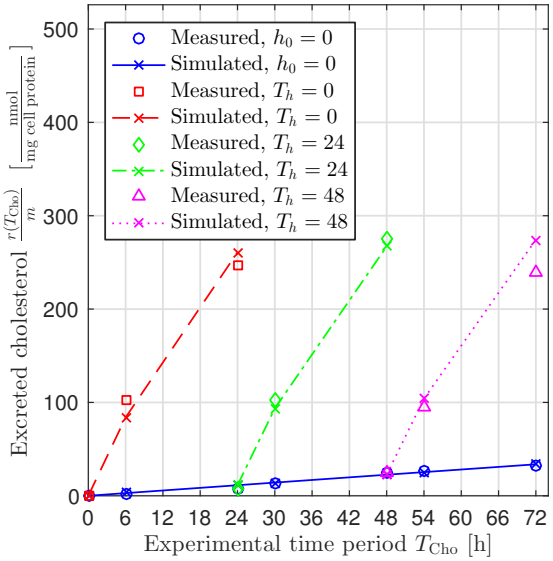

(c) Least-squares fits of simulated excreted cholesterol per macrophage $\frac{r(T_{\text{Cho}})}{m}$ to experimental results in [25], Fig. 1c for varying experimental time periods T_{Cho}.

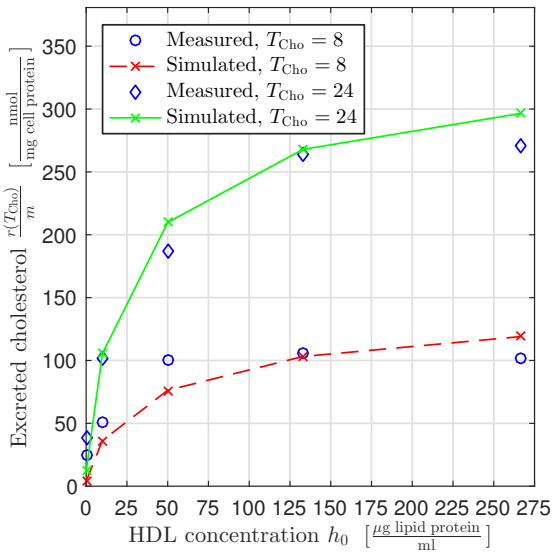

(d) Least-squares fits of simulated excreted cholesterol per macrophage $\frac{r(T_{\text{Cho}})}{m}$ to doubled experimental results in [25], Fig. 2a for varying additions of HDL h_0.

Figure 5.6 Experimentally measured intracellular free cholesterol, intracellular cholesterol ester and excreted cholesterol per macrophage for various experimental setups in [25] and results of the least-squares fitted mathematical submodel of cholesterol cycle and reverse cholesterol transport (submodel $\boxed{3}$).

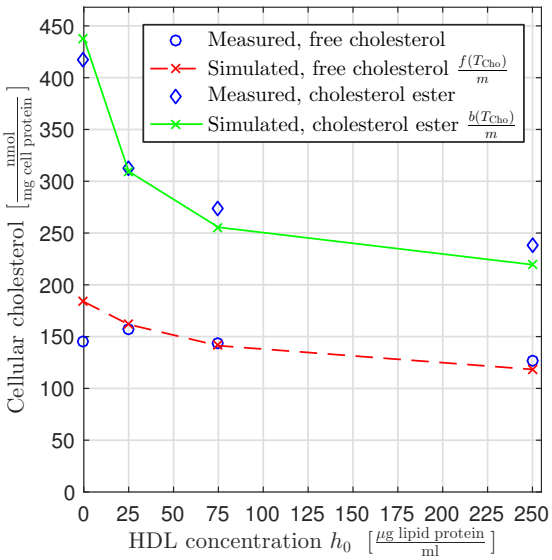

(e) Least-squares fits of simulated intracellular free cholesterol $\frac{f(T_{\text{Cho}})}{m}$ and cholesterol ester $\frac{b(T_{\text{Cho}})}{m}$ per macrophage to experimental results in [25], Fig. 4 for varying additions of HDL h_0.

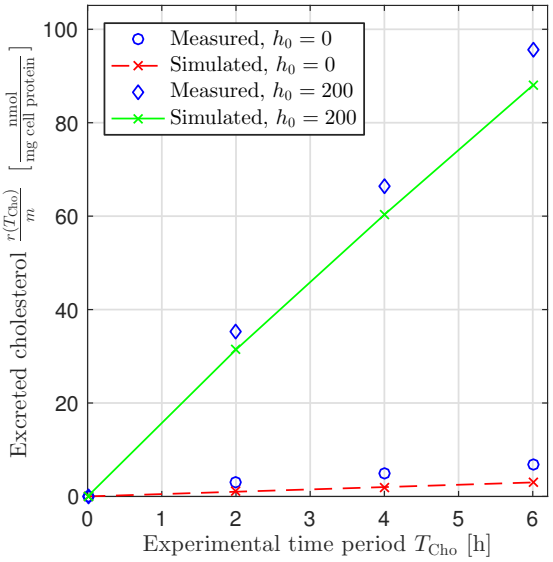

(f) Least-squares fits of simulated excreted cholesterol per macrophage $\frac{r(T_{\text{Cho}})}{m}$ to experimental results in [25], Fig. 7b for varying experimental time periods T_{Cho}.

Figure 5.6 Continued.

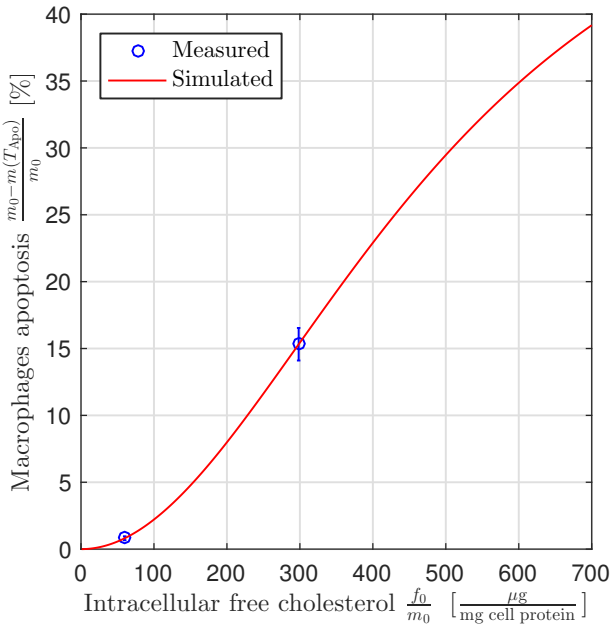

Figure 5.7 Least-squares fit of simulated macrophage apoptosis to experimental results in [296], Fig. 4a.

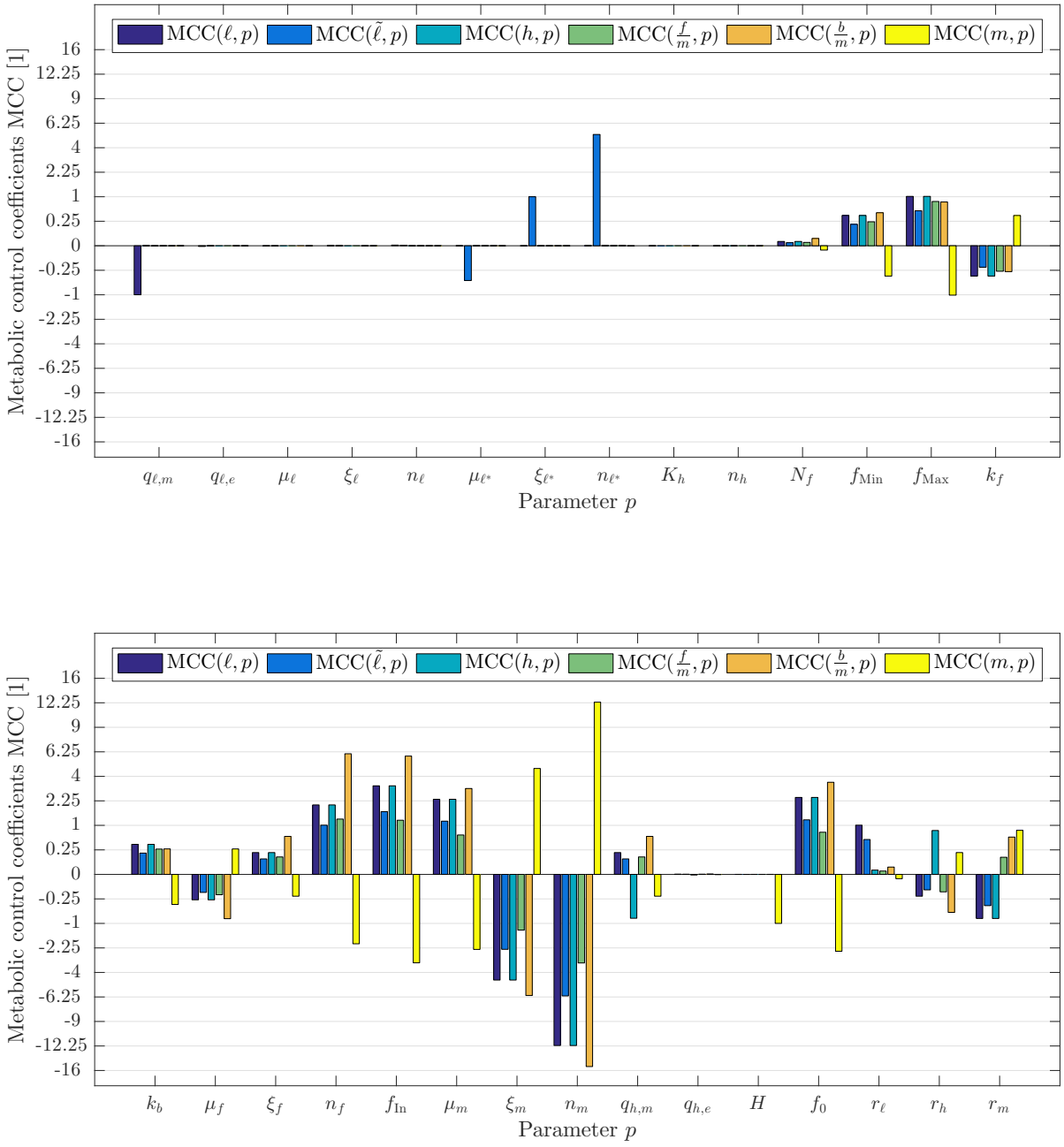

Figure 5.8 Metabolic control analysis of the combined mathematical model. The metabolic control coefficients of native LDL ℓ, modified LDL $\tilde{\ell}$, HDL h, average intracellular free cholesterol per macrophage $\frac{f}{m}$, average intracellular cholesterol ester per macrophage $\frac{f}{m}$ and macrophages m with respect to all parameters p of the combined model are computed as described in Section 5.2.1. For an overview of all parameters of the combined model, see Tables 5.5 and 5.7.

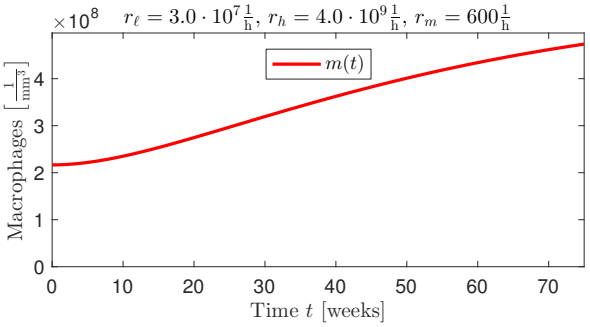

(a) Density of macrophages $m(t)$ over time t with HDL recruitment rate $r_h = 4.0 \cdot 10^9 \ \frac{1}{\mathrm{h}}$.

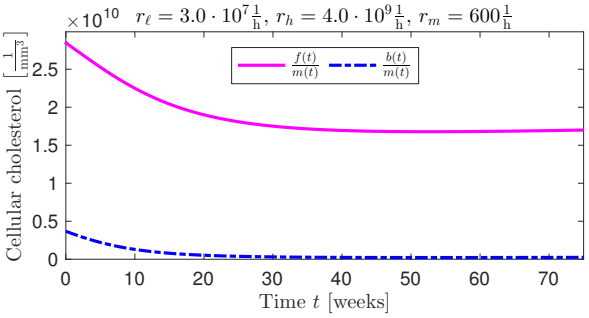

(b) Concentrations of free cholesterol $\frac{f(t)}{m(t)}$ and cholesterol ester $\frac{f(t)}{m(t)}$ per macrophage over time t with HDL recruitment rate $r_h = 4.0 \cdot 10^9 \ \frac{1}{\mathrm{h}}$.

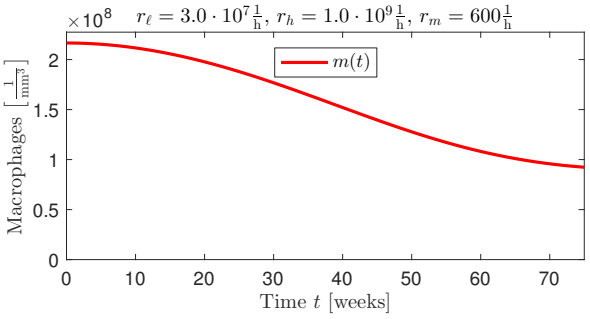

(c) Density of macrophages $m(t)$ over time t with HDL recruitment rate $r_h = 1.0 \cdot 10^9 \ \frac{1}{\mathrm{h}}$.

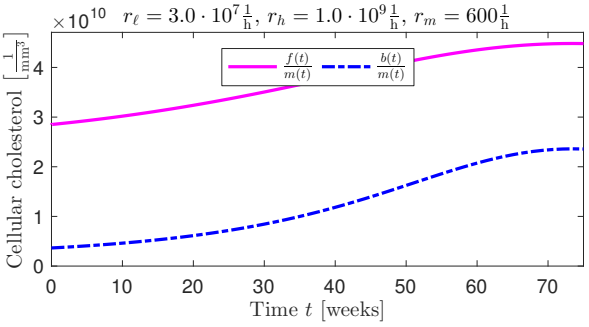

(d) Concentrations of free cholesterol $\frac{f(t)}{m(t)}$ and cholesterol ester $\frac{f(t)}{m(t)}$ per macrophage over time t with HDL recruitment rate $r_h = 1.0 \cdot 10^9 \ \frac{1}{\mathrm{h}}$.

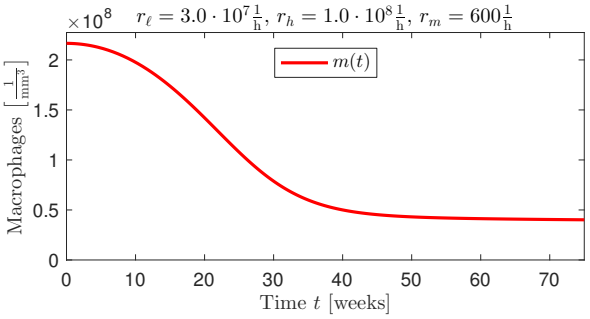

(e) Density of macrophages $m(t)$ over time t with HDL recruitment rate $r_h = 1.0 \cdot 10^8 \ \frac{1}{\mathrm{h}}$.

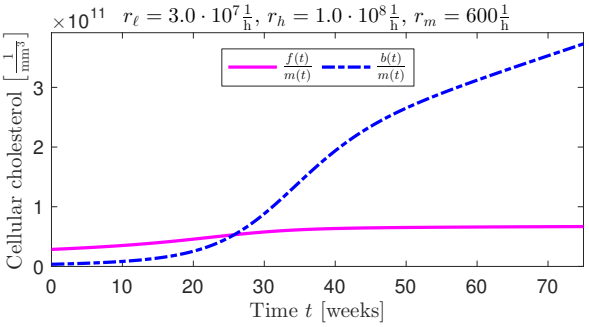

(f) Concentrations of free cholesterol $\frac{f(t)}{m(t)}$ and cholesterol ester $\frac{f(t)}{m(t)}$ per macrophage over time t with HDL recruitment rate $r_h = 1.0 \cdot 10^8 \ \frac{1}{\mathrm{h}}$.

Figure 5.9 Examples of densities of macrophages $m(t)$ and concentrations of intracellular free cholesterol $\frac{f(t)}{m(t)}$ and intracellular cholesterol ester $\frac{b(t)}{m(t)}$ per macrophage over time t predicted by the combined mathematical model. Parameters from Table 5.7, a LDL recruitment rate $r_\ell = 3.0 \cdot 10^7 \ \frac{1}{\mathrm{h}}$, a macrophage recruitment rate $r_m = 600 \ \frac{1}{\mathrm{h}}$ and varying HDL recruitment rates r_h were used.

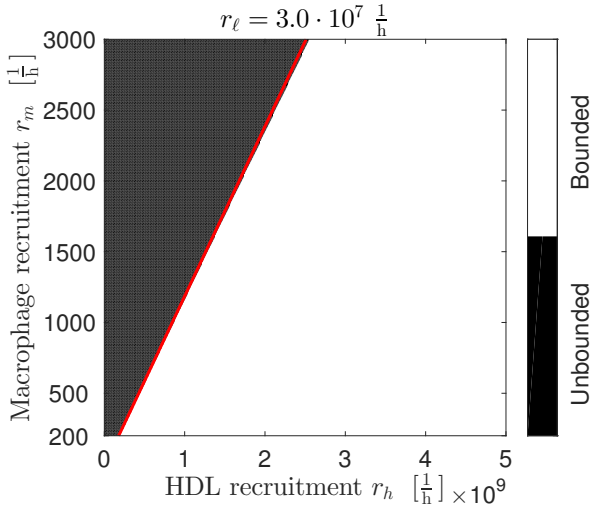

(a) Boundedness of concentration of intracellular cholesterol ester per macrophage for varying r_h and r_m, and fixed $r_\ell = 3.0 \cdot 10^7 \ \frac{1}{\mathrm{h}}$.

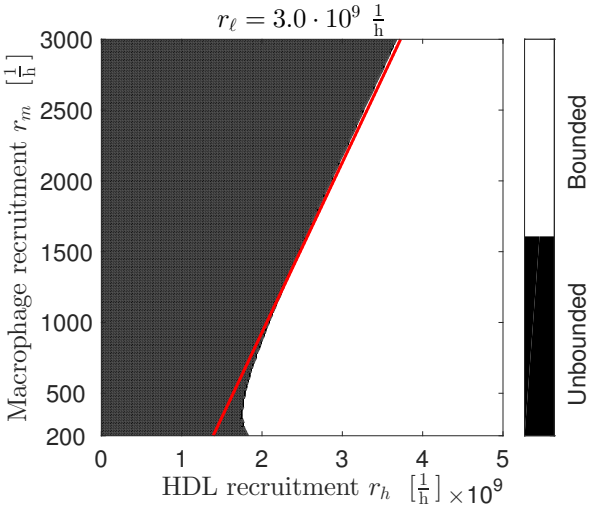

(b) Boundedness of concentration of intracellular cholesterol ester per macrophage for varying r_h and r_m, and fixed $r_\ell = 3.0 \cdot 10^9 \ \frac{1}{\mathrm{h}}$.

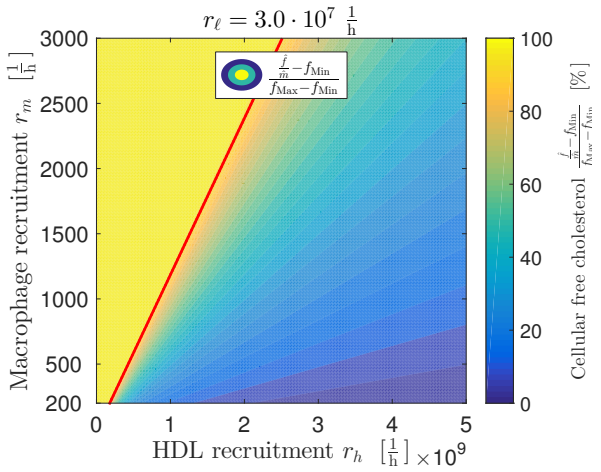

(c) Steady-state concentration of intracellular free cholesterol per macrophage $\frac{\hat{f}}{\hat{m}}$ relative to $[f_{\mathrm{Min}}, f_{\mathrm{Max}}]$ for varying r_h and r_m, and fixed $r_\ell = 3.0 \cdot 10^7 \ \frac{1}{\mathrm{h}}$.

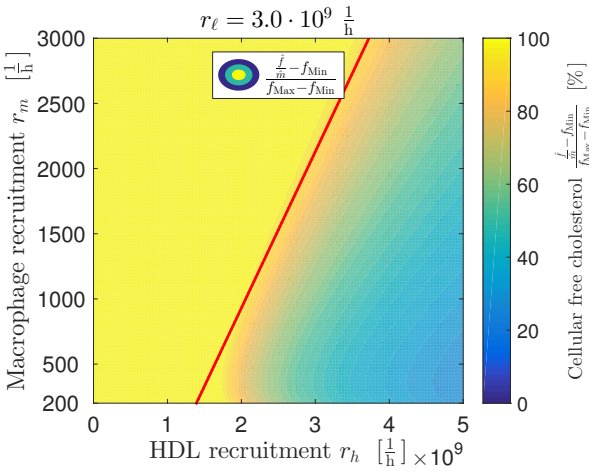

(d) Steady-state concentration of intracellular free cholesterol per macrophage $\frac{\hat{f}}{\hat{m}}$ relative to $[f_{\mathrm{Min}}, f_{\mathrm{Max}}]$ for varying r_h and r_m, and fixed $r_\ell = 3.0 \cdot 10^9 \ \frac{1}{\mathrm{h}}$.

Figure 5.10 Stability analysis of the combined mathematical model. The boundedness of intracellular cholesterol ester, the steady-state concentration of intracellular free cholesterol per macrophages and the steady-state density of macrophages are predicted for varying rates of recruitment of LDL r_ℓ, HDL r_h and macrophages r_m. The red line indicates the boundary between where intracellular cholesterol ester concentrations change from being bounded to unbounded. Its equation is $1.2 \cdot 10^{-6} \ r_h = r_m + 4.9 \cdot 10^{-7} \ r_\ell$.

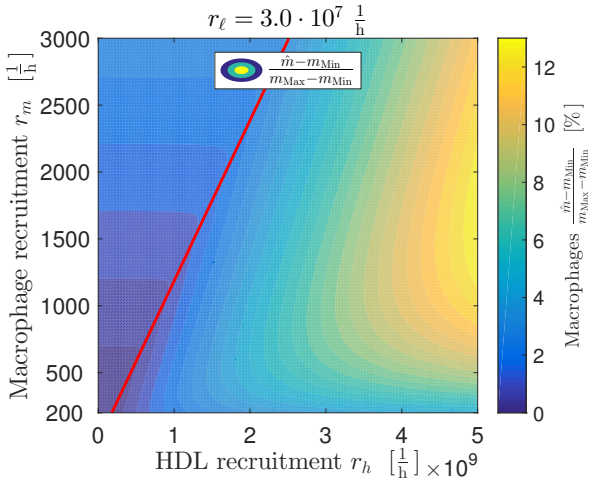

(e) Steady-state density of macrophages $\widehat{m}$ relative to $[m_{\text{Min}}, m_{\text{Max}}]$ for varying r_h and r_m, and fixed $r_\ell = 3.0 \cdot 10^7$ $\frac{1}{\text{h}}$.

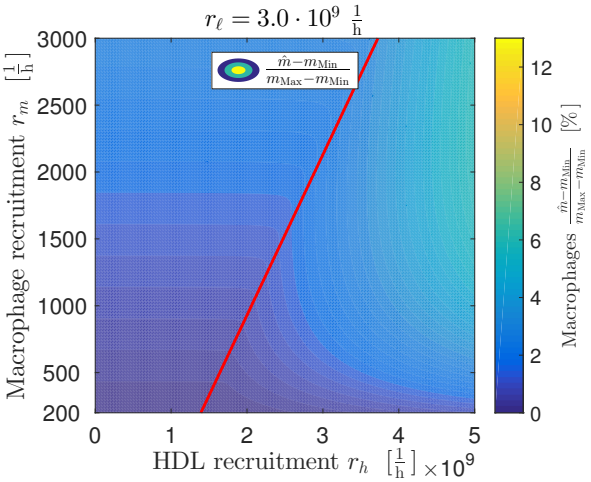

(f) Steady-state density of macrophages $\widehat{m}$ relative to $[m_{\text{Min}}, m_{\text{Max}}]$ for varying r_h and r_m, and fixed $r_\ell = 3.0 \cdot 10^9$ $\frac{1}{\text{h}}$.

Figure 5.10 Continued.

Data from the literature [2, 141, 205, 221, 251, 268] suggest that the three rates of recruitment r_ℓ, r_h, r_m which characterize each individual plaque vary by up to three orders of magnitude (see Table 5.5) and induce qualitatively different long-term outcomes of the combined model. Time-dependent concentrations for three example sets of recruitment rates with qualitatively different long-term outcomes are plotted in Figure 5.9.

The analysis of the long-term outcome of the combined model with respect to the recruitment rates is performed as described in Section 5.2.2. Proposition 1 applies as all its requirements are fulfilled by the combined model with the parameter set from Table 5.7. Hence, the steady-state concentrations of macrophages $\widehat{m}$ and intracellular free cholesterol per macrophage $\frac{\widehat{f}}{\widehat{m}}$ satisfy

$$\begin{aligned} \widehat{m} &\in [m_{\text{Min}}, m_{\text{Max}}] = [1.16 \cdot 10^7, 5.90 \cdot 10^9] \frac{1}{\text{mm}^3}, \\ \frac{\widehat{f}}{\widehat{m}} &\in [f_{\text{Min}}, f_{\text{Max}}] = [1.22 \cdot 10^{10}, 7.15 \cdot 10^{10}] \end{aligned} \tag{5.9}$$

and only the concentration of cholesterol ester b can be unbounded. Hence, the boundedness of intracellular cholesterol ester b, the steady-state concentration of intracellular free cholesterol per macrophages $\frac{\widehat{f}}{\widehat{m}}$ and the steady-state density of macrophages $\widehat{m}$ are computed for the full physiological ranges of recruitment rates of LDL r_ℓ, HDL r_h and macrophages r_m. The considered ranges of the recruitment rates in the stability analysis are $r_\ell \in [3 \cdot 10^6, 3 \cdot 10^9]$ $\frac{1}{\text{h mm}^2}$, $r_h \in [0, 5 \cdot 10^9]$ $\frac{1}{\text{h mm}^2}$ and $r_m \in [200, 3000]$ $\frac{1}{\text{h mm}^2}$ (compare Table 5.5). They are covered by a simple analysis utilizing an equidistant grid of the parameter space. The results for varying r_h and r_m and two different r_ℓ are visualized in Figure 5.10.

5.4 Discussion

Three mathematical submodels of *in vitro* systems were developed and their parameters least-squares fitted to measurements of various experimental setups, see Table 5.6. The fitted submodels show very good agreement with the experimental data, see Figure 5.2, 5.3, 5.4, 5.5, 5.6 and 5.7. The fitted parameters given in Table 5.7 lead to the following observations.

- The ingestion of native and modified LDL follows a very similar saturating kinematic. The rate of ingestion of native LDL μ_ℓ is approximately 5 times smaller than the rate of ingestion of modified LDL $\mu_{\tilde{\ell}}$. This is consistent with values reported in the literature [183, 250].
- Using a density of $1205.2\ \frac{1}{\mathrm{mm}^2}$ [141] of endothelial cells per unit endothelial monolayer area the rate of oxidative modification of native LDL by endothelial cells can be compared to the modification rate by macrophages. The rate of modification of native LDL by macrophages $q_{\ell,m}$ is approximately 3 times smaller than the modification rate by endothelial cells $q_{\ell,e}$.
- Free cholesterol and cholesterol ester are in a buffer-like relationship, where the maximum concentration of intracellular cholesterol f_{Max} is approximately 6 times bigger than the minimum concentration f_{Min}. The rate of esterification of intracellular cholesterol k_f varies as the level of intracellular free cholesterol changes. However, the average rate of esterification of cholesterol k_f is approximately 2 times faster than the rate of hydrolysis k_b. In the absence of a source and acceptor for the intracellular free cholesterol the model suggests that approximately 63.8% of the stored cholesterol is hydrolyzed and re-esterified each day which is moderately higher than 50% as proposed in [25].
- The dynamic of lipids and cholesterols, i.e., of native LDL, modified LDL, HDL, free cholesterol and cholesterol ester adapts very rapidly to the current number of macrophages and is in the order of minutes to hours. In contrast, the fate of macrophages is determined on a much larger time scale in the order of weeks to months. Hence, the long-term outcome for the plaque is driven by the fate of macrophages, which is governed by the short term quasi-equilibrium concentrations of intracellular cholesterols. The concentrations of intracellular cholesterols, however, are governed by the uptake of modified LDL and in particular the efflux to available native HDL which are determined by the very rapid influx through the endothelium and the modification by macrophages.

  Remark. *Due to the short time scale which governs the dynamic of the concentrations of native LDL, modified LDL and HDL it would be justified to take a steady-state assumption for their concentrations, i.e., to assume* $\frac{\mathrm{d}}{\mathrm{d}t}\ell(t) = 0 = \frac{\mathrm{d}}{\mathrm{d}t}\tilde{\ell}(t) = \frac{\mathrm{d}}{\mathrm{d}t}h(t)$ *in the combined model. However, the resulting equations for the steady-state concentrations* $\widehat{\ell}, \widehat{\tilde{\ell}}$ *and* $\widehat{h}$ *cannot be solved analytically. Hence, the concentrations of native LDL, modified LDL and HDL cannot be condensed from the combined model.*

A mathematical model for the early development of atherosclerotic plaques has been derived. It is based on submodels of *in vitro* systems and most importantly is parameterized using data from *in vitro* experimental studies. The combined model includes and quantifies the following biological

processes: oxidative modification of native LDL and HDL by endothelial cells and macrophages, protection that native HDL offers against LDL modification, ingestion of native and modified LDL by macrophages, esterification and hydrolysis of intracellular cholesterols, cholesterol efflux from macrophages to HDL, apoptosis of macrophages as well as the recruitment of native LDL, native HDL and macrophages into the plaque.

The performed sensitivity analysis of the combined model with respect to its parameters reveals that the combined model is especially sensitive to parameters connected to the apoptosis of macrophages (e.g., μ_m, ξ_m, n_m) and to free cholesterol (e.g., $f_{\mathrm{Max}}, f_{\mathrm{In}}, f_0$), see Figure 5.8. The sensitivity of the combined model with respect to free cholesterol-related parameters is high but their estimation is based on a large number of data points, see Table 5.6, and so their value is likely to be reliable. However, the high sensitivity with respect to the parameters of macrophage apoptosis n_m and ξ_m is crucial. This sensitivity is approximately 3 times bigger compared to the sensitivity of other parameters and additionally the parameters of macrophage apoptosis are estimated only on the base of two data points, see Table 5.6. More suitable experimental data from the literature could not be found and hence further experimental work quantifying apoptosis of macrophages in atherosclerotic plaques is recommended. The sensitivity analysis and further investigations reveal that the influence of the rates of ingestion of native LDL as well as HDL protection against native LDL modification is minor to the plaque formation process and plaque outcome in the model. In both cases this is due to the low concentrations of native LDL and HDL compared to the respective saturation coefficients.

The combined model is able to predict three qualitatively different long-term plaque outcomes. They are characterized by the following behaviors:

- *Regressing plaque* or non-atherosclerotic region: all concentrations are bounded and the long-term equilibrium concentrations are characterized by low modified LDL $\widehat{\widetilde{\ell}}$, high macrophages $\widehat{m}$, low intracellular free cholesterol per macrophage $\frac{\widehat{f}}{\widehat{m}}$ and very low intracellular cholesterol ester per macrophage $\frac{\widehat{b}}{\widehat{m}}$. Macrophages exhibit a low rate of apoptosis, and the ingested modified LDL within macrophages is effectively offloaded to native HDL. An example of time-dependent concentrations of macrophage and intracellular cholesterols for a regressing plaque is shown in Figure 5.9(a) and 5.9(b).

- *Stable plaque*: all concentrations are bounded and the long-term equilibrium concentrations are characterized by moderate modified LDL $\widehat{\widetilde{\ell}}$, low macrophages $\widehat{m}$, moderate intracellular free cholesterol per macrophage $\frac{\widehat{f}}{\widehat{m}}$ and low intracellular cholesterol ester per macrophage $\frac{\widehat{b}}{\widehat{m}}$. Macrophages exhibit a moderate rate of apoptosis, and the ingested modified LDL within macrophages is still offloaded to native HDL. An example of time-dependent concentrations of macrophage and intracellular cholesterols for a stable plaque is shown in Figure 5.9(c) and 5.9(d).

- *Unstable plaque*: concentration of intracellular cholesterol ester per macrophage $\frac{b}{m}$ is unbounded, and the remaining long-term equilibrium concentrations are characterized by high modified LDL $\widehat{\widetilde{\ell}}$, very low macrophages $\widehat{m}$ and very high intracellular free cholesterol per macrophage $\frac{\widehat{f}}{\widehat{m}}$. Macrophages exhibit a high rate of apoptosis, and not all the ingested

modified LDL within macrophages is offloaded to native HDL. An example of time-dependent concentrations of macrophage and intracellular cholesterols for an unstable plaque is shown in Figure 5.9(e) and 5.9(f).

The distinction between mathematically stable and unstable model plaques is clear, whereas there is a smooth transition between regressing and stable plaques. The definitions of mathematical stability of model plaques closely align with medical definitions of plaques that become clinically stable or unstable [173, 248, 249].

The recruitment rates of native LDL r_ℓ, native HDL r_h and macrophages r_m which characterize the plaque under consideration show only little influence in the performed local sensitivity analysis, see Figure 5.8. Still, the long-term behavior of the combined model and hence the classification of plaques into the three categories above is determined by them as they can vary by up to three orders of magnitude, cf. Table 5.5. The stability analysis visualized in Figure 5.10 shows that a model plaque is unstable if the recruitment of HDL r_h is low and the recruitment of macrophages r_m is large. More precisely a plaque is unstable if

$$1.2 \cdot 10^{-6}\, r_h < r_m + 4.9 \cdot 10^{-7}\, r_\ell \tag{5.10}$$

holds approximately, see Figure 5.10(a) and Figure 5.10(b). A plaque is regressing if the recruitment rate of macrophages r_m is low and the recruitment rate of HDL r_h is sufficiently large, cf. Figure 5.10(c), 5.10(d), 5.11(e) and 5.11(f). For increasing r_m or decreasing r_h the plaque smoothly transitions from a regressing to a stable atherosclerotic plaque. In general, an increased recruitment rate of LDL r_ℓ results in a less stable atherosclerotic plaque, but the predicted influence of r_ℓ is small compared to r_h and r_m. However, in reality the rate of macrophage recruitment r_m is a function of modified LDL $\tilde{\ell}$ (which, in turn, is strongly dependent on r_ℓ), since it triggers the production of vascular cell adhesion molecules and monocyte chemoattractant proteins by endothelial cells which determine the number of macrophages recruited from the blood [2, 93, 141]. As a consequence, the rate of macrophage recruitment is actually dependent on the LDL recruitment. Therefore, the rate of macrophage recruitment that is used in this model to determine plaque stability is, in effect, the rate of macrophage recruitment at the long-term steady state equilibrium, i.e., $r_m = r_m(\widehat{\tilde{\ell}}(r_\ell))$. As this dependency is not explicitly considered, but r_m is a fixed input parameter of the combined model, the influence of the rate of LDL recruitment r_ℓ is underestimated. The explicit consideration of this dependency as well as the explicit modeling of the driving mechanisms for the recruitment rates of LDL r_ℓ, HDL r_h and macrophages r_m will be addressed in the subsequent Chapter 6. Moreover, the increase of the thickness of the plaque H due to the advancing accumulation of macrophages, nor indeed any other spatially-dependent effects have not been included. Hence, the reduction of the recruitment rates of LDL, HDL and macrophages by the factor $\frac{1}{H}$ which will continually decrease in growing plaques is neglected. This leads to an overestimation of all three rates and must be addressed in future work.

The mathematical stability criterion given by Equation (5.10) is not suitable for the experimental determination of the clinical stability of a given early atherosclerotic plaque *in vivo*. Macrophages within unstable plaques contain a very high concentration of intracellular cholesterol ester, see 5.10(a), 5.10(b), 5.10(c) and 5.10(d). As a consequence, the predicted concentration of intracellular free cholesterol is also high in unstable plaques due to the buffer-like behavior

between free and esterified cholesterol. More precisely the estimated concentration of intracellular free cholesterol in model plaques is close to $f_{\mathrm{Max}} \approx 213.70 \ \frac{\mathrm{nMol}}{\mathrm{mg\ cell\ protein}}$ when a plaque becomes unstable in the long-term. This suggests that a high concentration of intracellular free cholesterol within plaque macrophages is necessary in order for an early plaque to be progression-prone and hence be of type IIb in the classification by the *American Heart Association*, cf. Table 1.1. The relation between intracellular free cholesterol and plaque stability *in vivo* has not yet been investigated experimentally.

This model assumes that macrophages only undergo recruitment and apoptosis and do not experience necrosis, proliferation and emigration from plaques. This assumption is only valid for early stages of the atherosclerotic process, i.e., for atherosclerotic plaques of type I to IIb. In contrast, necrosis, proliferation and emigration are important in intermediate atheroma [170, 220, 228, 258] which lead to a reduction of cholesterol ester within macrophages. If the processes of intermediate-stage plaques are included in the model in addition to recruitment and apoptosis of macrophages, the behavior of intermediate atheroma of type III and IV can be modeled. As for apoptosis, there are very few experimental data suited for parameter estimations for rates of necrosis, proliferation and emigration of macrophages. The extension of the combined model to also represent the behavior and fate of macrophages in late-stage plaques requires further work. In particular, further experiments are required that quantify macrophage behavior in intermediate and advanced plaques.

5.5 Short summary

This chapter is a revised version of [265]. It is concerned with mathematical modeling and quantification of early atherosclerotic plaque formation. Therefore, three novel ODE submodels of *in vitro* systems were derived and parameterized based on existing experimental studies. The submodels closely reproduced experimental results and lead to a quantification of crucial biological processes of atherosclerosis, such as LDL modification and ingestion, HDL protection against LDL modification, cholesterol cycle within macrophages and reverse cholesterol transport from macrophages.

The three submodels that are closely connected to *in vitro* studies were merged to build the basis of a quantified and predictive combined ODE model of the formation of early atherosclerotic plaques which uses the physiological parameters determined by the submodels. A sensitivity analysis of the combined model suggests that further experimental work quantifying the different fates of macrophages as functions of their cholesterol load and the balance between intracellular free cholesterol and cholesterol ester may add valuable insight toward predicting long-term plaque outcomes *in vivo*. Moreover, the combined model was used to classify the stability of early model plaques with respect to prescribed rates of recruitment of native LDL, native HDL and macrophages. The results suggest that a persistent high supply of LDL and macrophages in combination with a lack of HDL *in vivo* render early plaques progression-prone.

6 Spatially resolved model of early atherosclerosis

In the previous Chapter 5, a parameterized set of ODEs was developed that describes the formation of early atherosclerotic plaques. The established combined ODE model (see Section 5.1.2) is able to predict the stability of early model plaques based on the recruitment of low-density lipoproteins r_ℓ, high-density lipoproteins r_h and macrophages r_m, which characterize the physiology and diet of the plaque's host and its position within the cardiovascular system. However, the recruitment rates were *a priori* specified constants that neither adapt to the progression of the plaque, nor can be estimated from measurable or computable *in vivo* inputs in a straightforward manner. In particular, the rate of macrophage recruitment r_m is crucial for the stability of early plaques and their classification into progression-prone and progression-resistant plaques. Still, only scarce work has yet been done concerning the modeling of its dependencies with respect to the current state of plaques in general [27, 45] and the activation of the endothelium in particular. Yet, enhanced by poor availability of quantitative experimental data, the modeling and quantification of macrophage recruitment remains a challenge. In addition, the combined model neglects all spatial aspects, which is reasonable solely for *in vitro* experiments. In contrast, spatial effects, such as the diffusivity of species, their transport with the transmural flow or their inhomogeneous recruitment into the artery wall can have a severe impact on the local disease progression *in vivo*.

In this chapter, models for the recruitment of macrophages as well as the fluxes of LDL and HDL are developed. A quantification of these models based on *in vitro* experimental results allows to estimate the previously constant recruitment rates based on three measurable or computable physiological *in vivo* inputs: the LDL and HDL blood cholesterol concentrations and the WSS the plaque is exposed to. Furthermore, the abstract PFSTI *problem* (see Section 2.2.3) is extended to a *model of key species* of early atherosclerosis which consists of a submodel of the transmural filtration flow within the porous artery wall, non-constant recruitment laws and a spatial generalization of the combined model. A sensitivity analysis of the model of key species with respect to its parameters is performed that identifies crucial parameters and processes. Further, the model's stability is assessed based on the three *in vivo* inputs in order to identify and classify regions of progression-prone and progression-resistant plaques. Moreover, the model is used to assess the importance of the diffusive and advective lipoprotein fluxes through the endothelium and within the artery wall. Finally, the influence of locally varying WSS to the model plaque outcome is investigated.

This chapter is structured as follows: In Section 6.1, the submodels of the recruitment of macrophages, as well as the fluxes of LDL and HDL are developed. Subsequently, a spatial

PFSTI model is established based on the developed recruitment submodels and the previous chapter's combined model. Section 6.2 gives details on the parameterization of the models and the methods to analyze them. In Section 6.3, all computational results are presented, and they are discussed in Section 6.4. Finally, a brief summary of this chapter is given in Section 6.5.

6.1 Models

This section is concerned with the development of a porous medium fluid-scalar transport interaction model that describes the penetration and spatial transport of key species and the inflammatory and immunological processes that occur on the long time scale of atherosclerosis. First, submodels of the recruitment of macrophages and the fluxes of LDL and HDL are developed (Section 6.1.1). Subsequently, the PFSTI model is established based on the submodels of macrophage recruitment, lipoprotein fluxes and the previous chapter's combined model (Section 6.1.2).

6.1.1 Submodels

The submodels in this section are concerned with a detailed modeling of the adhesion of monocytes on endothelial cells *in vitro* (Section 6.1.1.1), the recruitment of macrophages *in vivo* (Section 6.1.1.2) and the fluxes of LDL and HDL through the endothelium (Section 6.1.1.3).

6.1.1.1 Monocyte adhesion *in vitro*

Monocytes migrate from the bloodstream into the artery wall depending on the local flow condition of blood and the current activation of the endothelium, cf. Section 1.1.3. The modeling of the monocyte adhesion *in vitro* is based on experimental results by *Jeng et al.* [141]. It is subsequently denoted as submodel $\boxed{4}$.

Experimental setup

The adhesion of human monocytes on human vein endothelial cells in the absence of flow and their binding under flow conditions *in vitro* was investigated in [141] using a two-stage experimental setup. First, specified initial concentrations of native LDL ℓ_0 and modified LDL $\tilde{\ell}_0$ were incubated with cultured endothelial cell monolayers e on coverslips for specified time periods T_{Mod}. Thereby, the endothelial cells oxidatively modified native LDL [116, 165] and accrued modified LDL activated endothelial cells, increasing their adhesiveness with respect to monocytes [2, 93, 169]. Subsequently, all LDL was removed and monocytes were added for specified time periods T_{Adh}, where they adhered to the endothelial cells. The coverslips were placed in a flow chamber in which the flux was increased step by step, exposing the monocytes to varying WSS levels $\|\boldsymbol{\tau}\|$. Among other things, the number of adhered monocytes m_{Adh} prior to the flow chamber and the number of remaining monocytes after each increase of WSS exposure was counted for various experiment-specific values of $\ell_0, \tilde{\ell}_0, e, T_{\mathrm{Mod}}, T_{\mathrm{Adh}}, \|\boldsymbol{\tau}\|$ as shown in Table 6.1.

Table 6.1 Experiment-specific parameters of the mathematical submodel of monocyte adhesion *in vitro* (submodel 4) in analogy to the experimental setups in [141].

Experiment \ Quantity	Modification stage				Adhesion stage	
	T_{Mod} [h]	$\ell_0 \left[\frac{\mu\mathrm{g\ protein}}{\mathrm{ml}}\right]$	$\tilde{\ell}_0 \left[\frac{\mu\mathrm{g\ protein}}{\mathrm{ml}}\right]$	$e \left[\frac{\mathrm{mm}^2}{\mathrm{ml}}\right]$	T_{Adh} [h]	$\|\boldsymbol{\tau}\| \left[\frac{\mathrm{dyn}}{\mathrm{cm}^2}\right]$
[141], Table 1, $\ell_0 = 0, \tilde{\ell}_0 = 0$	6	0	0	2.68	0.5	$0 - 30.52$
[141], Table 1, $\ell_0 = 25, \tilde{\ell}_0 = 0$	6	25	0	2.68	0.5	$0 - 30.52$
[141], Table 1, $\ell_0 = 0, \tilde{\ell}_0 = 25$	6	0	25	2.68	0.5	$0 - 30.52$

All values are given in the units of submodel 4.

Mathematical submodel

The observations made in the flow chamber experiments in [141] are driven by the modification of native LDL by endothelial cells, the adhesion of monocytes on modified LDL-activated endothelial cells and the detachment of monocytes due to exposure to WSS. As in the previous Section 5.1.1.1, the modification of native LDL by endothelial cells is described by a linear relationship in their concentrations ℓ and e and the initial LDL modification lag phase is accounted for by a reduction of 4 h of the experimental time period T_{Mod}. The activation of endothelial cells by modified LDL saturates as the concentration of modified LDL $\tilde{\ell}$ increases (see [141], Fig. 5 and [93], Fig. 1). Still, monocytes adhere on endothelial cells also in the absence of LDL (see [141], Fig. 3 and [93], Fig. 1). Therefore, the activation of endothelial cells is modeled using a partly vanishing and saturating kinematic. The WSS-dependent detachment of adhered monocytes *in vitro* is also saturating and decreases as the WSS $\|\boldsymbol{\tau}\|$ are increased (see [141], Fig. 1). No experimental data exist that quantify the influence of the monocyte concentration in the bloodstream on the amount of adhering monocytes on the endothelium. Here, it is assumed that it is solely dependent on the activation of the endothelium and that there is a surplus of monocytes at all times such that the number of adhering monocytes is independent of the number of monocytes in the flow chamber.

The mathematical submodel is formulated in the same units that are used in the experiments: time $[t] = \mathrm{h}$, concentration of native LDL $[\ell] = \frac{\mu\mathrm{g\ protein}}{\mathrm{ml}}$, concentration of modified LDL $[\tilde{\ell}] = \frac{\mu\mathrm{g\ protein}}{\mathrm{ml}}$, density of endothelial cells $[e] = \frac{\mathrm{mm}^2}{\mathrm{ml}}$, amount of adhered monocytes $[m] = \frac{1}{0.1452\ \mathrm{mm}^2}$ and level of WSS exposure $[\|\boldsymbol{\tau}\|] = \frac{\mathrm{dyn}}{\mathrm{cm}^2}$. The submodel consists of two sequential system of ODEs and associated initial conditions. The first system corresponds to the

modification of native LDL by endothelial cells (modification stage)

$$\begin{aligned} \frac{\mathrm{d}}{\mathrm{d}t}\ell(t) = -\underbrace{q_{\ell,e}\ell e}_{\substack{\text{modification of native}\\ \text{LDL by endothelial cells}}} &= -\frac{\mathrm{d}}{\mathrm{d}t}\tilde{\ell}(t), \\ \ell(4\mathrm{h}) = \ell_0, \quad \tilde{\ell}(4\mathrm{h}) &= \tilde{\ell}_0, \quad t \in [4\mathrm{h}; T_{\mathrm{Mod}}] \end{aligned} \tag{6.1}$$

and the second system corresponds to the adhesion and detachment of monocytes (adhesion stage)

$$\begin{aligned} \frac{\mathrm{d}}{\mathrm{d}t}m(t) = P_m \underbrace{\left(1 - \delta_m \frac{k_m}{k_m + \tilde{\ell}(T_{\mathrm{Mod}})}\right)}_{\substack{\text{activation of endothelial cells}\\ \text{by modified LDL}}} \underbrace{\left(1 - \delta_\tau \frac{\|\boldsymbol{\tau}\|^{\nu_\tau}}{(\xi_\tau)^{\nu_\tau} + \|\boldsymbol{\tau}\|^{\nu_\tau}}\right)}_{\substack{\text{monocytes remaining bound}\\ \text{on endothelial cells}}}, \\ m(0) = 0, \quad t \in [0; T_{\mathrm{Adh}}], \end{aligned} \tag{6.2}$$

where $q_{\ell,e} = 2.48 \cdot 10^{-5} \frac{\mathrm{ml}}{\mathrm{h\ mm^2}}$ (cf. Table 5.7) and $T_{\mathrm{Mod}}, \ell_0, \tilde{\ell}_0, e, T_{\mathrm{Adh}}, \|\boldsymbol{\tau}\|$ are the experiment-specific parameters, see Table 6.1. The remaining constants $P_m, \delta_m, k_m, \delta_\tau, \xi_\tau$ and ν_τ are the unknown parameters of submodel $\boxed{4}$. They are estimated by least-squares fitting of the simulated number of adhered monocytes $m(T_{\mathrm{Adh}})$ to the experimental results in [141].

6.1.1.2 Macrophage recruitment

The experiments by *Jeng et al.* [141] solely considered the adhesion of monocytes in the absence of flow and their successive detachment under various flow conditions. When monocytes migrate from the bloodstream into the artery wall *in vivo*, however, the attachment of monocytes takes place under pulsatile flow conditions. However, no experimental data exist that allow to quantify the adhesion of monocytes on activated endothelial cells under flow conditions. The submodel of the macrophage recruitment is based on submodel $\boxed{4}$ and the experimental results by *Alon et al.* [2]. It is subsequently denoted as submodel $\boxed{5}$.

Mathematical submodel

The influence of the WSS to the adhesion of T-lymphocytes on VCAM-1 saturated plastic slides was investigated by *Alon et al.* [2]. The experimental results show that the adhesion of cells under flow conditions vanishes when they are exposed to high WSS (see [2], Fig. 1). In this submodel, the vanishing adhesion is accounted for by neglecting the limiting of the saturation kinematic with respect to WSS $\|\boldsymbol{\tau}\|$, i.e., by using $\delta_\tau = 1$ for the *in vivo* setup. Due to the presence of MCP-1 and other monocyte-attracting molecules *in vivo*, it is assumed that each monocyte that adheres and remains bound under heavy flow conditions also migrates into the intima. Further, the considered time scale of atherosclerosis progression is large such that the relatively fast differentiation of monocytes into macrophages [191] is approximated by an instantaneous differentiation. In total, the submodel for the rate of recruitment of macrophages r_m thus reads

$$r_m(\tilde{\ell}, \|\boldsymbol{\tau}\|) = P_m \left(1 - \delta_m \frac{k_m}{k_m + \tilde{\ell}}\right) \frac{(\xi_\tau)^{\nu_\tau}}{(\xi_\tau)^{\nu_\tau} + \|\boldsymbol{\tau}\|^{\nu_\tau}}, \tag{6.3}$$

where all parameters have been introduced previously.

6.1.1.3 LDL and HDL fluxes

Lipoproteins, such as LDL and HDL are transported through the endothelium depending on their concentrations in blood and the local blood flow condition, cf. Section 1.1.2. The submodel of the LDL and HDL fluxes is subsequently denoted as submodel $\boxed{6}$.

Mathematical submodels

As discussed in Sections 2.2.2.1 and 4.1.2.3, the transport of native LDL ℓ through the endothelium is modeled as transport through a semi-permeable membrane described by the equations of *Kedem* and *Katchalsky*. Thus, the total flux of native LDL r_ℓ into the intima is subdivided into a diffusive and an advective flux

$$r_\ell\left(\ell, p, \|\boldsymbol{\tau}\|\right) = \underbrace{P_\ell s_{\mathrm{P}}\left(\|\boldsymbol{\tau}\|\right)\left(\eta_\ell - \ell\right)}_{\text{diffusive flux}} + \underbrace{\left(1-\sigma_{\mathrm{F},\ell}\right)\left(\omega_\ell\eta_\ell + (1-\omega_\ell)\ell\right) J_{\mathrm{Vol}}(p, \|\boldsymbol{\tau}\|)}_{=:r_{\mathrm{Adv},\ell}(\ell,p,\|\boldsymbol{\tau}\|),\ \text{advective flux}}, \tag{6.4}$$

where η_ℓ, $\sigma_{\mathrm{F},\ell}$ and ω_ℓ are the concentration of native LDL in blood, filtration reflection coefficient with respect to LDL and weighting factor for the average LDL concentration within the endothelium layer, respectively. The volume flux through the endothelium J_{Vol} is given by

$$J_{\mathrm{Vol}}(p, \|\boldsymbol{\tau}\|) = L_p s_{\mathrm{L}}(\|\boldsymbol{\tau}\|)\left(\eta_p - p\right), \tag{6.5}$$

where η_p and p correspond to the luminal blood pressure and the subendothelial blood plasma pressure, respectively. The diffusive permeability P_ℓ and hydraulic conductivity L_p are modulated depending on the magnitude of the local WSS $\|\boldsymbol{\tau}\|$ the model plaque is exposed to. For the shape of the diffusive permeability modulation s_{P}, the monotonically decreasing (diffusive) permeability scaling factor from Section 4.1.2.3 is used:

$$s_{\mathrm{P}}\left(\|\boldsymbol{\tau}\|\right) = \frac{1}{\ln(2)} \ln\left(1 + \zeta_\tau \frac{\gamma_\tau}{\|\boldsymbol{\tau}\| + \gamma_\tau}\right). \tag{6.6}$$

In contrast to the diffusive permeability, there is clear experimental data that the hydraulic conductivity L_p increases as endothelial cells are exposed to increased WSS $\|\boldsymbol{\tau}\|$ [36, 240]. Therefore, the hydraulic conductivity is modulated by the following monotonically increasing function from literature [226, 254]

$$s_{\mathrm{L}}(\|\boldsymbol{\tau}\|) = \gamma_p \ln\left(\mu_p\|\boldsymbol{\tau}\| + \xi_p\right), \tag{6.7}$$

which is subsequently called *(hydraulic) conductivity scaling factor* (CSF).

Due to their related structure and size, the transport mechanisms of modified LDL and native HDL are equal to that of native LDL. Hence, the fluxes of modified LDL r_ℓ and HDL r_h are modeled in analogy to Equation (6.4):

$$\begin{aligned} r_{\tilde{\ell}}(\tilde{\ell}, p, \|\boldsymbol{\tau}\|) &= P_{\tilde{\ell}} s_{\mathrm{P}}\left(\|\boldsymbol{\tau}\|\right)\left(\eta_{\tilde{\ell}} - \tilde{\ell}\right) + (1-\sigma_{\mathrm{F},\tilde{\ell}})(\omega_{\tilde{\ell}}\eta_{\tilde{\ell}} + (1-\omega_{\tilde{\ell}})\tilde{\ell}) J_{\mathrm{Vol}}(p, \|\boldsymbol{\tau}\|), \\ r_h\left(h, p, \|\boldsymbol{\tau}\|\right) &= P_h s_{\mathrm{P}}\left(\|\boldsymbol{\tau}\|\right)\left(\eta_h - h\right) + \left(1-\sigma_{\mathrm{F},h}\right)\left(\omega_h\eta_h + (1-\omega_h)h\right) J_{\mathrm{Vol}}(p, \|\boldsymbol{\tau}\|). \end{aligned} \tag{6.8}$$

Remark. *In the multiphysics model from Chapter 4, the WSS $\boldsymbol{\tau}$, concentration of native LDL in blood η_ℓ and luminal blood pressure η_p were denoted by $\boldsymbol{\tau}^{\mathcal{F}}$, $\ell^{\mathcal{FS}}$ and $p^{\mathcal{F}}$. However, in present model of key species, these quantities are considered to be constant (in time) and are therefore denoted by different symbols to avoid confusion.*

6.1.2 Spatially resolved model of key species

The penetration and transport of species as well as immunological and inflammatory processes of atherosclerosis take place in the intima and adjacent media, see Section 1.1. A spatial model of the species must therefore consider both layers and their main transport barriers – the endothelium and the internal elastic lamina, cf. Figure 1.1. However, monocytes actively transmigrate from the intima into the media [189, 239] and the transport rates of lipoproteins through the internal elastic lamina are more than two orders of magnitude faster compared to those through the endothelium [146, 294]. As a consequence, the internal elastic lamina represents solely a minor transport barrier for LDL, HDL and macrophages. The internal elastic lamina is therefore neglected and a fluid-wall model is employed [221, 305], where the endothelium is considered to be the only transport barrier, see Section 1.2.1.

In contrast to the multiphysics model where the artery wall was treated as a non-porous solid (cf. Section 4.1.2), this section considers a pressure gradient-driven transmural flow. All species are modeled by temporal and spatially continuous concentrations with the unit of number per volume. As the species are diffusive, reactive and are transported with the transmural flow, the general framework of the species is given by the porous medium-advection-diffusion-reaction equation (see Section 2.1.6.2). The immunological and inflammatory processes and species transport in atherosclerosis take place on the long time scale of the disease, cf. Section 1.2, where the deformation of the intima and media due to the pulsatile blood flow is dispensable. In total, the model of key species of atherosclerosis in this section is a PFSTI problem (cf. Section 2.2.3) extended by atherosclerosis-specific reactions and boundary conditions.

Using the same notation as introduced in the beginning of Section 4.1, the PFSTI model considers the poro-fluid domain $\Omega^{\mathcal{PF}}$ and the poro-scatra domain $\Omega^{\mathcal{PS}}$. The boundaries are the inlet boundary Γ_{In}, outlet boundary Γ_{Out}, endothelium boundary Γ_{End} and media-adventitia boundary Γ_{Adv}. For a schematic overview of the domains and boundaries of the PFSTI model of key species, see Figure 6.1.

In the subsequent Section 6.1.2.1, the model of the transmural flow is given, whereas Section 6.1.2.2 gives the model of the interaction and transport of species. In the following, the superscript $\mathcal{PS}$ of all species and parameters related to the poro-scatra domain $\Omega^{\mathcal{PS}}$ is omitted to keep the notation comprehensible.

6.1.2.1 Transmural flow

As frequently done in the literature [29, 146, 152, 210, 221, 267], the transmural filtration flow within the artery wall is modeled as a purely pressure gradient-driven incompressible flow. Further,

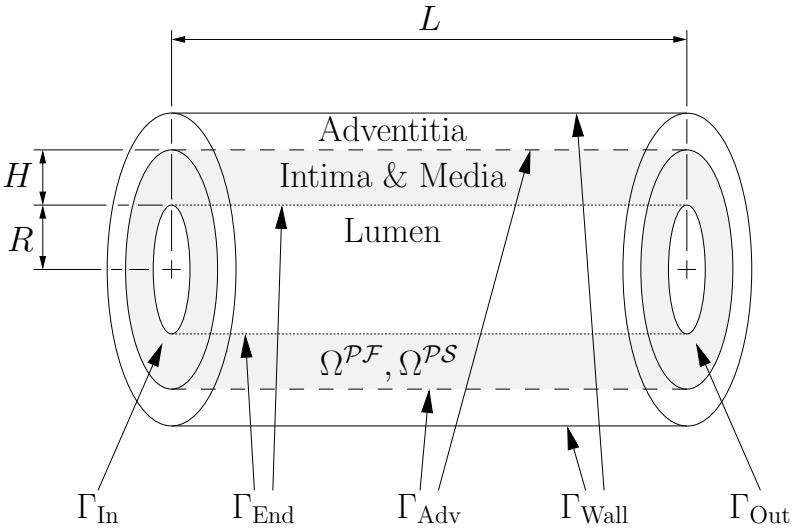

Figure 6.1 Schematic overview of domains (gray) and boundaries of the PFSTI model of key species: poro-fluid domain $\Omega^{\mathcal{PF}}$, poro-scatra domain $\Omega^{\mathcal{PS}}$, inlet boundary Γ_{In}, endothelium boundary Γ_{End}, media-adventitia boundary Γ_{Adv}, outer wall boundary Γ_{Wall} and outlet boundary Γ_{Out}. Both domains are characterized by the lumen radius R, intima-media thickness H and segment length L.

the deformation of the spatial poro-fluid domain $\Omega^{\mathcal{PF}}$ is dispensable in the long time scale which implies a constant porosity ϕ. The transmural flow is thus described by *Darcy*'s law and the incompressibility equation, see Section 2.1.6.2:

$$\begin{aligned} \boldsymbol{u}^{\mathcal{PF}} &= -\frac{K^{\mathcal{PF}}}{\phi\mu^{\mathcal{PF}}}\nabla p^{\mathcal{PF}}, \\ \boldsymbol{\nabla}\cdot\boldsymbol{u}^{\mathcal{PF}} &= 0. \end{aligned} \tag{6.9}$$

Together, both equations yield the *Poisson* equation for the intimal and medial blood plasma pressure $p^{\mathcal{PF}}$ on the fixed spatial domain $\Omega^{\mathcal{PF}}$:

$$-\boldsymbol{\nabla}\cdot\left(\frac{K^{\mathcal{PF}}}{\phi\mu^{\mathcal{PF}}}\nabla p^{\mathcal{PF}}\right) = 0. \tag{6.10}$$

On the media-adventitia boundary $\Gamma^{\mathcal{PF}}_{\mathrm{Adv}}$ a constant pressure corresponding to the adventitial pressure $p^{\mathcal{PF}}_{\mathrm{Adv}}$ is prescribed as *Dirichlet* boundary condition:

$$p^{\mathcal{PF}} = p^{\mathcal{PF}}_{\mathrm{Adv}}. \tag{6.11}$$

The volume flux J_{Vol} through the endothelium boundary $\Gamma^{\mathcal{PF}}_{\mathrm{End}}$ is described by the first *Kedem-Katchalsky* equation without osmotic flux [128, 262], see Section 2.2.2.1:

$$-\frac{K^{\mathcal{PF}}}{\phi\mu^{\mathcal{PF}}}\nabla p^{\mathcal{PF}}\cdot\boldsymbol{n}^{\mathcal{PF}}_{\mathrm{End}} \overset{(6.9)}{=} \boldsymbol{u}^{\mathcal{PF}}\cdot\boldsymbol{n}^{\mathcal{PF}}_{\mathrm{End}} = J_{\mathrm{Vol}}(p^{\mathcal{PF}}, \|\boldsymbol{\tau}\|) = L_p s_{\mathrm{L}}(\|\boldsymbol{\tau}\|)\left(\eta_p - p^{\mathcal{PF}}\right). \tag{6.12}$$

On the inlet and outlet boundaries $\Gamma_{\text{In}}^{\mathcal{PF}}$ and $\Gamma_{\text{Out}}^{\mathcal{PF}}$ no-flux conditions are applied:

$$\begin{aligned} -\frac{K^{\mathcal{PF}}}{\phi\mu^{\mathcal{PF}}}\nabla p^{\mathcal{PF}}\cdot\boldsymbol{n}_{\text{In}}^{\mathcal{PF}} &= 0 \\ -\frac{K^{\mathcal{PF}}}{\phi\mu^{\mathcal{PF}}}\nabla p^{\mathcal{PF}}\cdot\boldsymbol{n}_{\text{Out}}^{\mathcal{PF}} &= 0 \end{aligned} \tag{6.13}$$

6.1.2.2 Interaction and transport of species

The model of the interaction and transport of species is a generalization and extension of the combined model from Section 5.1.2. In addition to the parameterized reaction terms of the combined model, the specific laws for the recruitment of macrophages (submodel $\boxed{5}$, Section 6.1.1.2), as well as the fluxes of LDL and HDL (submodel $\boxed{6}$, Section 6.1.1.3) are employed to replace the *constant* recruitment rates utilized in the combined model. Further, the non-spatial combined model is generalized to the spatial domain $\Omega^{\mathcal{PS}}$ to account for the diffusive and advective transport of species and spatially varying boundary condition due to inhomogeneous WSS distributions.

The general framework of the poro-scatra model is given by the porous medium-advection-diffusion-reaction equation, see Equation (2.59). The porous medium scalar transport models of native LDL ℓ, modified LDL $\tilde{\ell}$ and HDL h on the fixed spatial domain $\Omega^{\mathcal{PS}}$ read

$$\begin{aligned} \frac{\partial}{\partial t}\ell + \underbrace{\boldsymbol{\nabla}\cdot\left(K_\ell \ell \boldsymbol{u}^{\mathcal{PF}}\right)}_{\substack{\text{advection of native}\\ \text{LDL with poro-fluid}}} - \underbrace{\boldsymbol{\nabla}\cdot\left(D_{\text{Eff},\ell}\nabla\ell\right)}_{\substack{\text{diffusion of}\\ \text{native LDL}}} &= -\underbrace{\mu_\ell \frac{\ell^{n_\ell}}{(\xi_\ell)^{n_\ell}+\ell^{n_\ell}} m}_{\substack{\text{ingestion of native}\\ \text{LDL by macrophages}}} - \underbrace{q_{\ell,m}\ell m \frac{(k_h)^{n_h}}{(k_h)^{n_h}+h^{n_h}}}_{\substack{\text{modification of native}\\ \text{LDL by macrophages}\\ \text{and inhibition by HDL}}}, \\ \frac{\partial}{\partial t}\tilde{\ell} + \underbrace{\boldsymbol{\nabla}\cdot\left(K_{\tilde{\ell}} \tilde{\ell} \boldsymbol{u}^{\mathcal{PF}}\right)}_{\substack{\text{advection of modified}\\ \text{LDL with poro-fluid}}} - \underbrace{\boldsymbol{\nabla}\cdot\left(D_{\text{Eff},\tilde{\ell}}\nabla\tilde{\ell}\right)}_{\substack{\text{diffusion of}\\ \text{modified LDL}}} &= -\underbrace{\mu_{\tilde{\ell}} \frac{\tilde{\ell}^{n_{\tilde{\ell}}}}{(\xi_{\tilde{\ell}})^{n_{\tilde{\ell}}}+\tilde{\ell}^{n_{\tilde{\ell}}}} m}_{\substack{\text{ingestion of modified}\\ \text{LDL by macrophages}}} + \underbrace{q_{\ell,m}\ell m \frac{(k_h)^{n_h}}{(k_h)^{n_h}+h^{n_h}}}_{\substack{\text{modification of native}\\ \text{LDL by macrophages}\\ \text{and inhibition by HDL}}}, \\ \frac{\partial}{\partial t}h + \underbrace{\boldsymbol{\nabla}\cdot\left(K_h h \boldsymbol{u}^{\mathcal{PF}}\right)}_{\substack{\text{advection of HDL}\\ \text{with poro-fluid}}} - \underbrace{\boldsymbol{\nabla}\cdot\left(D_{\text{Eff},h}\nabla h\right)}_{\substack{\text{diffusion of HDL}}} &= -\underbrace{q_{h,m} h m}_{\substack{\text{modification of HDL}\\ \text{by macrophages}}}, \end{aligned} \tag{6.14}$$

where the advection of lipoproteins is with the transmural filtration flow governed by the gradient of the blood plasma pressure $p^{\mathcal{PF}}$, see Equation (6.9). In contrast to lipoproteins, macrophages are not transported by advection with the transmural flow due to their several orders of magnitude larger size, cf. Table 5.1. Thus, the models of the concentrations of intracellular free cholesterol f, intracellular cholesterol ester b and the density of macrophages m on the fixed spatial domain $\Omega^{\mathcal{PS}}$

read

$$
\begin{aligned}
\frac{\partial}{\partial t} f - \underbrace{\boldsymbol{\nabla} \cdot (D_{\mathrm{Eff},f} \nabla f)}_{\substack{\text{diffusion of}\\ \text{free cholesterol}}} &= + N_f \underbrace{\mu_\ell \frac{\ell^{n_\ell}}{(\xi_\ell)^{n_\ell} + \ell^{n_\ell}} m}_{\substack{\text{ingestion of native}\\ \text{LDL by macrophages}}} + N_f \underbrace{\mu_{\tilde{\ell}} \frac{(\tilde{\ell})^{n_{\tilde{\ell}}}}{(\xi_{\tilde{\ell}})^{n_{\tilde{\ell}}} + (\tilde{\ell})^{n_{\tilde{\ell}}}} m}_{\substack{\text{ingestion of modified}\\ \text{LDL by macrophages}}} \\
&\quad - \underbrace{k_f \frac{(f - f_{\mathrm{Min}} m)^2}{f_{\mathrm{Max}} m - f}}_{\substack{\text{esterification of}\\ \text{free cholesterol}}} + \underbrace{k_b b}_{\substack{\text{hydrolysis of}\\ \text{cholesterol ester}}} - \underbrace{\mu_f \frac{h^{n_f}}{(\xi_f)^{n_f} + h^{n_f}} (f - f_{\mathrm{Min}} m)}_{\text{cholesterol efflux from macrophages to HDL}}, \\
\frac{\partial}{\partial t} b - \underbrace{\boldsymbol{\nabla} \cdot (D_{\mathrm{Eff},b} \nabla b)}_{\substack{\text{diffusion of}\\ \text{cholesterol ester}}} &= + \underbrace{k_f \frac{(f - f_{\mathrm{Min}} m)^2}{f_{\mathrm{Max}} m - f}}_{\substack{\text{esterification of}\\ \text{free cholesterol}}} - \underbrace{k_b b}_{\substack{\text{hydrolysis of}\\ \text{cholesterol ester}}}, \\
\frac{\partial}{\partial t} m - \underbrace{\boldsymbol{\nabla} \cdot (D_{\mathrm{Eff},m} \nabla m)}_{\substack{\text{diffusion of}\\ \text{macrophages}}} &= - \underbrace{\mu_m \frac{f^{n_m}}{(\xi_m m)^{n_m} + f^{n_m}} m}_{\text{apoptosis of macrophages}}.
\end{aligned}
\tag{6.15}
$$

On the inlet, outlet and media-adventitia boundaries $\Gamma^{\mathcal{PS}}_{\mathrm{In}}$, $\Gamma^{\mathcal{PS}}_{\mathrm{Out}}$ and $\Gamma^{\mathcal{PS}}_{\mathrm{Adv}}$, no-flux conditions are applied. Native LDL and HDL are oxidatively modified by endothelial cells. Further, native LDL ℓ, modified LDL $\tilde{\ell}$, HDL h and macrophages m are recruited according to submodels $\boxed{5}$ and $\boxed{6}$, whereby recruited macrophages contain an amount f_{In} of free cholesterol. Accordingly, the *in*flux boundary conditions on the endothelium boundary $\Gamma^{\mathcal{PS}}_{\mathrm{End}}$ are given by

$$
\begin{aligned}
-\left(K_\ell \ell \boldsymbol{u}^{\mathcal{PF}} - D_{\mathrm{Eff},\ell} \nabla \ell\right) \cdot \boldsymbol{n}^{\mathcal{PS}}_{\mathrm{End}} &= - \underbrace{q_{\ell,e} \ell \frac{(k_h)^{n_h}}{(k_h)^{n_h} + h^{n_h}}}_{\substack{\text{modification of native}\\ \text{LDL by endothelial cells}\\ \text{and inhibition by HDL}}} + \underbrace{r_\ell\left(\ell, p^{\mathcal{PF}}, \|\boldsymbol{\tau}\|\right)}_{\substack{\text{influx of native LDL}\\ \text{from lumen}}}, \\
-\left(K_{\tilde{\ell}} \tilde{\ell} \boldsymbol{u}^{\mathcal{PF}} - D_{\mathrm{Eff},\tilde{\ell}} \nabla \tilde{\ell}\right) \cdot \boldsymbol{n}^{\mathcal{PS}}_{\mathrm{End}} &= + \underbrace{q_{\ell,e} \ell \frac{(k_h)^{n_h}}{(k_h)^{n_h} + h^{n_h}}}_{\substack{\text{modification of native}\\ \text{LDL by endothelial cells}\\ \text{and inhibition by HDL}}} + \underbrace{r_{\tilde{\ell}}(\tilde{\ell}, p^{\mathcal{PF}}, \|\boldsymbol{\tau}\|)}_{\substack{\text{outflux of modified LDL}\\ \text{to lumen}}}, \\
-\left(K_h h \boldsymbol{u}^{\mathcal{PF}} - D_{\mathrm{Eff},h} \nabla h\right) \cdot \boldsymbol{n}^{\mathcal{PS}}_{\mathrm{End}} &= - \underbrace{q_{h,e} h}_{\substack{\text{modification of HDL}\\ \text{by endothelial cells}}} + \underbrace{r_h\left(h, p^{\mathcal{PF}}, \|\boldsymbol{\tau}\|\right)}_{\substack{\text{influx of native HDL}\\ \text{from lumen}}}, \\
-\left(-D_{\mathrm{Eff},f} \nabla f\right) \cdot \boldsymbol{n}^{\mathcal{PS}}_{\mathrm{End}} &= + f_{\mathrm{In}} \underbrace{r_m(\tilde{\ell}, \|\boldsymbol{\tau}\|)}_{\substack{\text{recruitment of}\\ \text{macrophages}}}, \\
-\left(-D_{\mathrm{Eff},b} \nabla b\right) \cdot \boldsymbol{n}^{\mathcal{PS}}_{\mathrm{End}} &= 0, \\
-\left(-D_{\mathrm{Eff},m} \nabla m \cdot\right) \boldsymbol{n}^{\mathcal{PS}}_{\mathrm{End}} &= + \underbrace{r_m(\tilde{\ell}, \|\boldsymbol{\tau}\|)}_{\substack{\text{recruitment of}\\ \text{macrophages}}},
\end{aligned}
\tag{6.16}
$$

where the functions $r_\ell, r_{\tilde{\ell}}, r_h$ and r_m are given by Equations (6.3), (6.4) and (6.8).

6.1.2.3 Initial conditions

To achieve a well-defined initial value problem, the specific initial conditions are stated. A spatially constant initial blood plasma pressure $p_0^{\mathcal{PF}}$ is utilized

$$p^{\mathcal{PF}}(0, \boldsymbol{x}) = p_0^{\mathcal{PF}} \tag{6.17}$$

and spatially constant initial concentrations similar to the combined model (Equation (5.7)) are used

$$\begin{aligned} &\ell(0, \boldsymbol{x}) = 0, \quad \tilde{\ell}(0, \boldsymbol{x}) = \tilde{\ell}_0, \quad h(0, \boldsymbol{x}) = 0, \\ &f(0, \boldsymbol{x}) = f_0 m_0, b(0, \boldsymbol{x}) = b_0 m_0, \quad m(0, \boldsymbol{x}) = m_0, \end{aligned} \tag{6.18}$$

where

$$\begin{aligned} f_0 &= 1.5 f_{\mathrm{In}}, \\ m_0 &= \frac{r_m\left(\tilde{\ell}_0, \|\boldsymbol{\tau}\|\right)}{H} \frac{(\xi_m)^{n_m} + (f_0)^{n_m}}{\mu_m (f_0)^{n_m}}, \\ b_0 &= \frac{k_f}{k_b} \frac{(f_0 - f_{\mathrm{Min}})^2}{f_{\mathrm{Max}} - f_0}. \end{aligned} \tag{6.19}$$

In contrast to the combined model, the initial concentration of modified LDL $\tilde{\ell}_0$ is required to estimate the initial rate of recruitment of macrophages $r_m\left(\tilde{\ell}_0, \|\boldsymbol{\tau}\|\right)$. Therefore, an initial concentration of modified LDL $\tilde{\ell}_0 = 7.2 \cdot 10^{-4}\ \eta_\ell$ based on the experimental results in [117, 268] is utilized.

Remark. *Except for the specific submodels of the recruitment of species, the spatially resolved PFSTI model of key species in this section and the non-spatial combined ODE model from Section 5.1.2 are equivalent in the case of homogeneous concentrations, e.g., induced by high effective diffusion coefficients* $D_{\mathrm{Eff},i} \to \infty,\ \forall i = \ell, \ldots, m$.

6.2 Methods

This section specifies the parameters and methods that are required to analyze and solve the PFSTI model of key species of atherosclerosis. A simplified geometrical setup of the murine physiology of the aortic arch is considered. Therefore, the dimensions corresponding to the example in Section 4.3 are employed: lumen radius $R = 0.57\ \mathrm{mm}$, intima-media thickness $H = \frac{T}{2} = 0.04\ \mathrm{mm}$ and segment length $L = 3R \approx 1.8\ \mathrm{mm}$, cf. Figure 6.1.

First, all unknown parameters of the PFSTI model are estimated in Section 6.2.1. Using a non-spatial extended combined model, uncertainties in the parameters are assessed by a sensitivity analysis and the laws for the recruitment of LDL, HDL and macrophages (submodels $\boxed{5}$ and $\boxed{6}$) are analyzed as described in Sections 6.2.2 and 6.2.3, respectively. The methods that are required to analyze the stability with respect to its parameters are introduced in Section 6.2.4. Subsequently,

the meshing and a validation of the implementation of the spatial PFSTI model are presented in Section 6.2.5. Finally, the influence of spatial lipoprotein transports and inhomogeneous WSS distributions to the atherosclerotic process are investigated as described in Sections 6.2.6.

6.2.1 Model parameters

In this section, a complete set of parameters for the PFSTI model is established, where all parameters are formulated in the SI based units h, mm and g. As the media is the predominant part of the considered intima-media domain (cf. Figure 1.1), parameters corresponding to the media are employed.

The least-squares fitted parameters of the model of the monocyte adhesion *in vitro* (submodel $\boxed{4}$) to the experimental results in [141] read

$$\begin{aligned} P_m &= 443.17 \frac{1}{\mathrm{h}\ 0.1452\ \mathrm{mm}^2} = 3052.13 \frac{1}{\mathrm{h}\ \mathrm{mm}^2}, \quad \delta_m = 68.62\ \%, \\ k_m &= 7.09 \cdot 10^{-3}\ \frac{\mu\mathrm{g\ lipid\ protein}}{\mathrm{ml}} = 7.38 \cdot 10^{6}\ \frac{1}{\mathrm{mm}^3}, \quad \delta_\tau = 40.22\ \%, \\ \xi_\tau &= 1.95\ \frac{\mathrm{dyn}}{\mathrm{cm}^2} = 1.95 \cdot 10^{-1}\ \mathrm{Pa}, \quad \nu_\tau = 1.18, \end{aligned} \tag{6.20}$$

where all values are given in the unit of the experiment *and* SI based units. The conversion from experimental to SI based units is performed using ρ_{10} from Table 5.1. An overview of the least-squares fits of submodel $\boxed{4}$ is given in Figure 6.2(a).

The influx of native LDL through the endothelium described by Equation (6.4) is well studied and thus the required parameters are found in the literature. In contrast, the fluxes of modified LDL and native HDL are yet only poorly investigated. Due to its origin and equal size, it is convenient to use equal parameters for native and modified LDL. In contrast to native LDL, however, the concentration of modified LDL in blood is low [70] and therefore $\eta_{\tilde{\ell}} = 0$ is employed.

HDL has a smaller size compared to LDL. More precisely, LDL and HDL have radii of $R_\ell = 11.0\ \mathrm{nm}$ and $R_h = 4.72\ \mathrm{nm}$, cf. Table 5.1. As a consequence, HDL has an approximately 1.87 times higher diffusive permeability compared to LDL: $P_h = 1.87\ P_\ell = 1.14 \cdot 10^{-4}\ \frac{\mathrm{mm}}{\mathrm{h}}$ [251, 268].

Karner et al. [146] investigated the transport rates of ADP, albumin and LDL through the endothelium and the internal elastic lamina. As ADP and albumin have a smaller and LDL has a larger radius compared to HDL, their filtration reflection coefficients are used to estimate the filtration reflection coefficient $\sigma_{\mathrm{F},h}$ of HDL. To this end, a least-squares fit of the filtration reflection coefficient as given in [146], Table 3 to a saturating function in the particle radius R_i of the form $\sigma_{\mathrm{F},i}(R_i) = \frac{R_i^a}{b^a + R_i^a}$ is performed. The least-squares fit yields $a = 3.006$ and $b = 2.112\ \mathrm{nm}$ and it follows

$$\sigma_{\mathrm{F},i}(R_i) = \frac{R_i^{3.006}}{(2.112\ \mathrm{nm})^{3.006} + R_i^{3.006}}, \tag{6.21}$$

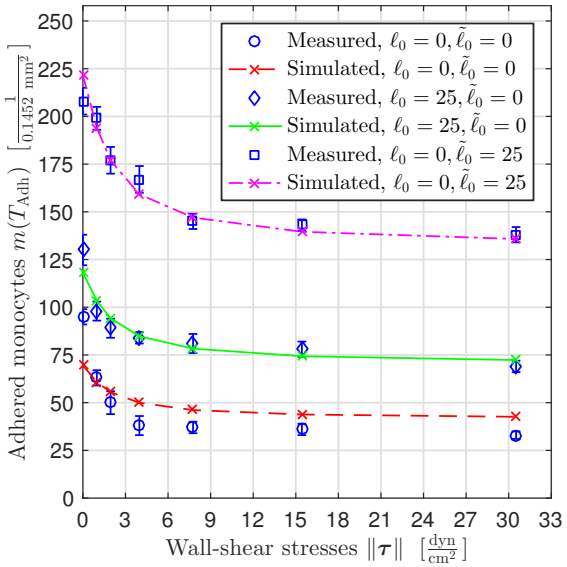

(a) Least-squares fits of simulated monocyte adhesion to experimental results in [141], Table 1 for varying initial concentration of LDL in the modification stage and varying levels of WSS $\|\boldsymbol{\tau}\|$ in the adhesion stage.

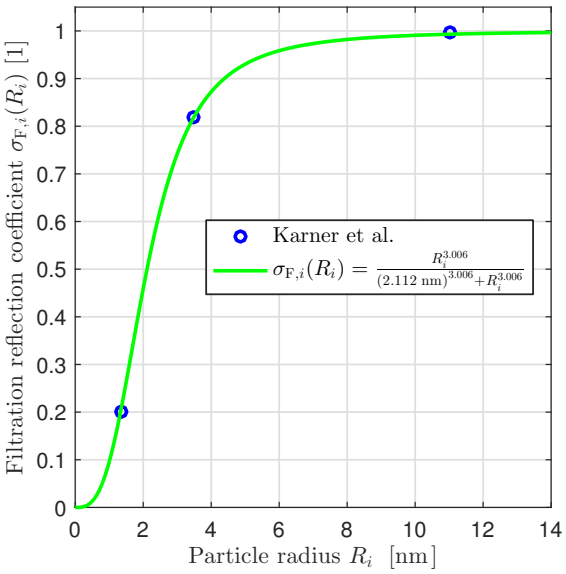

(b) Least-squares fit of filtration reflection coefficient $\sigma_{\mathrm{F},i}$ with respect to particle radius R_i to [146], Table 3.

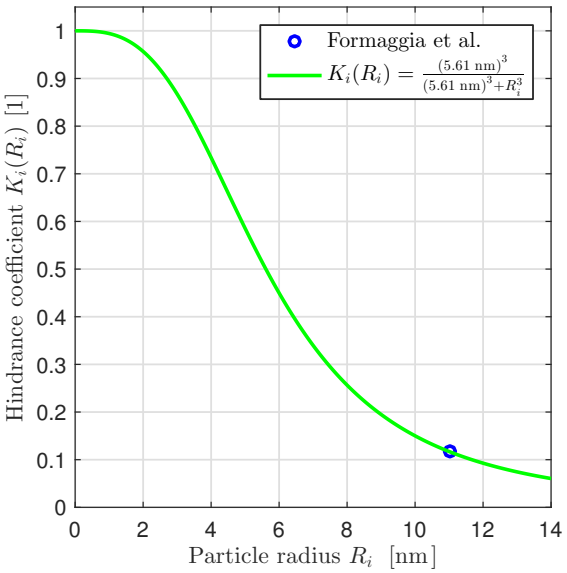

(c) Least-squares fit of hindrance coefficient K_i with respect to particle radius R_i to result in [85].

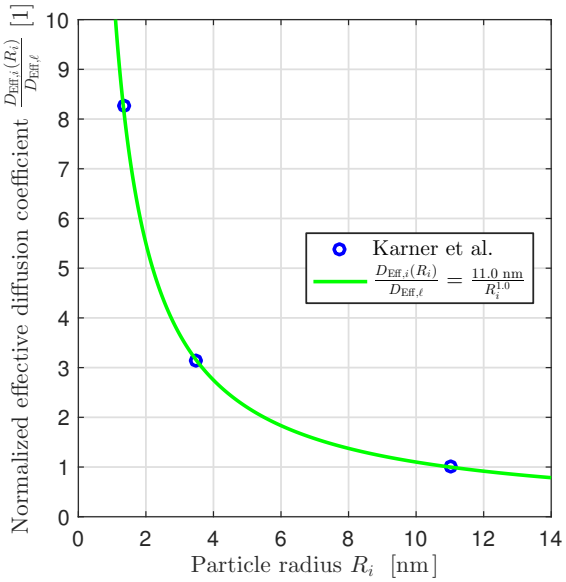

(d) Least-squares fit of effective diffusion coefficient $D_{\mathrm{Eff},i}$ with respect to particle radius R_i to [146], Table 2.

Figure 6.2 Least-squares fits of submodel of monocyte adhesion *in vitro* (submodel 4), filtration reflection coefficient, hindrance coefficient and effective diffusion coefficient to various data.

which is visualized in Figure 6.2(b). Accordingly, the filtration reflection coefficient scales approximately with the volume of particles and for HDL ($R_h = 4.72$ nm) it yields $\sigma_{\mathrm{F},h} = 9.18 \cdot 10^{-1}$.

The hindrance coefficient of LDL in the media is given by $K_\ell = K_{\tilde{\ell}} = 0.117$ [85, 210, 256], respectively. Assuming that the hindrance coefficient scales with the volume of particles (in consistency to the filtration reflection coefficient) and a saturating kinematic (in general it holds $0 \leq K_i(R_i) \leq 1$), it follows

$$K_i(R_i) = \frac{(5.61 \text{ nm})^3}{(5.61 \text{ nm})^3 + R_i^3}, \tag{6.22}$$

which is plotted Figure 6.2(c). Accordingly, the hindrance coefficient of HDL ($R_h = 4.72$ nm) is estimated to $K_h = 6.27 \cdot 10^{-1}$.

An additional unknown parameter is the effective diffusion coefficient of HDL $D_{\mathrm{Eff},h}$ within the artery wall. The effective diffusivity of LDL is measured as $D_{\mathrm{Eff},\ell} = D_{\mathrm{Eff},\tilde{\ell}} = 1.26 \cdot 10^{-2}$ $\frac{\mathrm{mm}^2}{\mathrm{h}}$ [29, 255, 267], but no experimental results exist that allow quantifying the effective diffusivity of HDL. However, *Karner et al.* [146] state the diffusivities of ADP, albumin and LDL in blood plasma. The data in [146] is therefore normalized to the diffusivity of LDL in blood plasma and least-squares fitted to a rational function of the form $\frac{D_{\mathrm{Eff},i}(R_i)}{D_{\mathrm{Eff},\ell}} = \frac{e}{R_i^f}$. The least-squares fit yields $e = 11.0$ nm and $f = 1.0$ such that

$$D_{\mathrm{Eff},i}(R_i) = \frac{11.0 \text{ nm}}{R_i} D_{\mathrm{Eff},\ell}, \tag{6.23}$$

which is visualized in Figure 6.2(d). Here, the effective diffusion coefficients scales with the radius of particles and for HDL ($R_h = 4.72$ nm) it yields $D_{\mathrm{Eff},h} = 2.33$ $D_{\mathrm{Eff},\ell} = 2.94 \cdot 10^{-2}$ $\frac{\mathrm{mm}^2}{\mathrm{h}}$.

The weighting factors $\omega_\ell, \omega_{\tilde{\ell}}$ and ω_h for the average concentrations of native LDL, modified LDL and native HDL within the endothelium layer are estimated as proposed in [85]. Therein, the one-dimensional advection-diffusion equation is solved and volume-averaged over the domain of the endothelium. It follows that

$$\omega_i = \frac{\exp(Pe_i)}{\exp(Pe_i) - 1} - \frac{1}{Pe_i}, \tag{6.24}$$

where Pe_i is the *Péclet* number of species i within the endothelium given by

$$Pe_i = \frac{\|\boldsymbol{u}\|}{P_i}. \tag{6.25}$$

Here, $\|\boldsymbol{u}\|$ and P_i are the transmural filtration velocity and the diffusive permeability of species i, respectively. Using $\|\boldsymbol{u}\| = 6.41 \cdot 10^{-2}$ $\frac{\mathrm{mm}}{\mathrm{h}}$ [85, 195, 294] and $P_\ell = P_{\tilde{\ell}} = 6.12 \cdot 10^{-5}$ $\frac{\mathrm{mm}}{\mathrm{h}}$, $P_h = 1.14 \cdot 10^{-4}$ $\frac{\mathrm{mm}}{\mathrm{h}}$ [251, 268, 294] results in the weighting factors

$$\omega_\ell = \omega_{\tilde{\ell}} = 9.99 \cdot 10^{-1}, \quad \omega_h = 9.98 \cdot 10^{-1}. \tag{6.26}$$

The *Darcy* permeability of the intima and media $K^{\mathcal{PF}}$ must be estimated to fit to the murine physiology, i.e., to the murine intima-media thickness. The *Darcy* permeability is approximated by solving the norm of Equation (6.9) for $K^{\mathcal{PF}}$:

$$K^{\mathcal{PF}} = \frac{\phi \mu^{\mathcal{PF}} \|\boldsymbol{u}\|}{\|\nabla p_{\mathrm{Med}}\|}, \tag{6.27}$$

where $\|\boldsymbol{u}\|$ and $\|\nabla p_{\mathrm{Med}}\|$ correspond to the transmural filtration velocity and pressure gradient the intima and media, respectively. The latter is approximated by the luminal blood pressure $\eta_p = 100\ \mathrm{mmHg}$ [1, 209, 282], the pressure drop across the endothelium $\Delta p_{\mathrm{End}} = 18\ \mathrm{mmHg}$ [262] and the adventitial pressure $p_{\mathrm{Adv}} = 30\ \mathrm{mmHg}$ [1, 209, 294] by: $\|\nabla p_{\mathrm{Med}}\| = \frac{\eta_p - \Delta p_{\mathrm{End}} - p_{\mathrm{Adv}}}{H} = \frac{52\ \mathrm{mmHg}}{0.04\ \mathrm{mm}} = 1.73 \cdot 10^5\ \frac{\mathrm{Pa}}{\mathrm{mm}}$. Assuming a transmural filtration velocity $\|\boldsymbol{u}\| = 6.41 \cdot 10^{-2}\ \frac{\mathrm{mm}}{\mathrm{h}}$ [85, 195, 294], a porosity $\phi = 0.15$ [1, 221] and a dynamic viscosity of blood plasma $\mu^{\mathcal{PF}} = 2.0 \cdot 10^{-7}\ \mathrm{Pa\ h}$ [221, 294] yields a *Darcy* permeability of $K^{\mathcal{PF}} = 1.11 \cdot 10^{-14}\ \mathrm{mm}^2$.

The rates of oxidative modification of HDL by macrophages $q_{h,m}$ and endothelial cells $q_{h,e}$ are crucial, but no experimental results exist that allow quantifying them directly. Hence, the rates of HDL modification are calculated from the rates of LDL modification by considering the different structure and size of LDL and HDL. Therefore, we use

$$q_{h,m} = \frac{q_{\ell,m}}{7.6} \frac{N_{\tilde{\ell}}}{N_{\tilde{h}}}, \quad q_{h,e} = \frac{q_{\ell,e}}{7.6} \frac{N_{\tilde{\ell}}}{N_{\tilde{h}}}, \tag{6.28}$$

where $N_{\tilde{\ell}}$ and $N_{\tilde{h}}$ correspond to the amount of lipid peroxide in modified LDL and HDL, respectively. The factor 7.6 represents the relative difference between the surface areas of LDL and HDL [46]. Using the values of $q_{\ell,m}, q_{\ell,e}, N_{\tilde{\ell}}$ and $N_{\tilde{h}}$ given in Table 5.7 yields $q_{h,m} = 1.64 \cdot 10^{-4}\ \frac{\mathrm{mm}^3}{\mathrm{h}}$ and $q_{h,e} = 6.21 \cdot 10^{-2}\ \frac{\mathrm{mm}}{\mathrm{h}}$.

There is experimental data by *Sill et al.* [240] that quantifies the hydraulic conductivity with respect to the WSS $\|\boldsymbol{\tau}\|$. *Sun et al.* [254] used these experimental results to parameterize the CSF given by Equation (6.7) which leads to: $\gamma_p = 1.31 \cdot 10^{-1}$, $\mu_p = 1.24 \cdot 10^3\ \frac{1}{\mathrm{Pa}}$ and $\xi_p = 1.86 \cdot 10^1$. Therein, the parameter μ_p was scaled such that it fits to a reference WSS value of $\|\overline{\boldsymbol{\tau}}\| = 1.68\ \mathrm{Pa}$. Even though the distribution of the reference WSS value $\|\overline{\boldsymbol{\tau}}\|$ within an animal is more or less uniform [238], it varies significantly in between different animal models [40]. Therefore, the parameter μ_p of the CSF must be adapted to match the physiology of the animal under consideration, i.e., the murine physiology.

The analog also holds for the parameters ξ_τ and γ_τ of the recruitment law of macrophages (Equation (6.3)) and the PSF (Equation (6.6)). The estimated value $\xi_\tau = 1.95 \cdot 10^{-1}\ \mathrm{Pa}$ corresponds to the human physiology with a reference WSS value $\|\overline{\boldsymbol{\tau}}\| = 1.16\ \mathrm{Pa}$ [40]. The parameter γ_τ is linked to a given reference WSS value $\|\overline{\boldsymbol{\tau}}\|$ by $\gamma_\tau = \frac{1}{30}\|\overline{\boldsymbol{\tau}}\|$, see Section 4.3.1. A tabular overview of values for $\|\overline{\boldsymbol{\tau}}\|$, ξ_τ, γ_τ and μ_p for different animal models and the normalized case is given in Table 6.2. The PSF and CSF are visualized in Figure 6.3. In the following, normalized WSS $\frac{\|\boldsymbol{\tau}\|}{\|\overline{\boldsymbol{\tau}}\|}$ values are employed, as frequently done in the literature [29, 45, 146, 254].

An overview of all specific parameters of the PFSTI model is given in Table 6.3. The remaining parameters are given by the values parameterized for the combined model listed in Table 5.7.

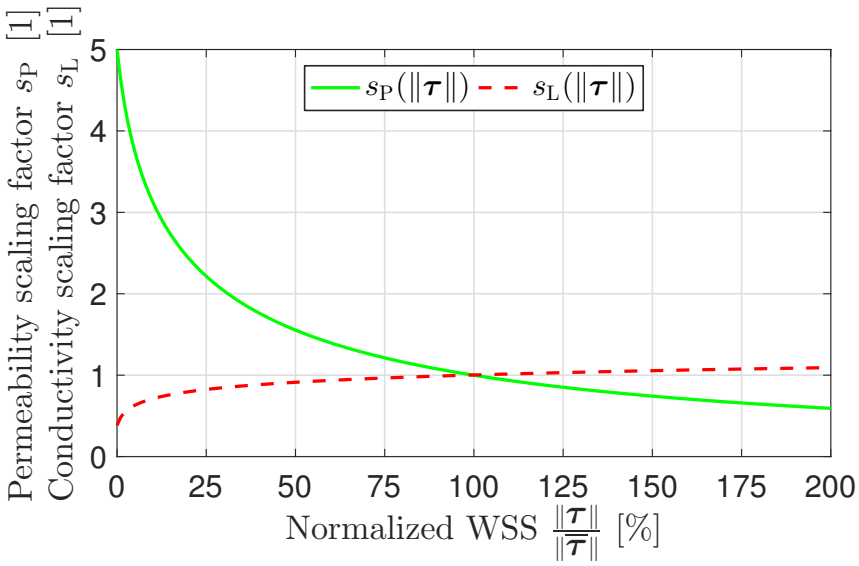

Figure 6.3 Permeability scaling factor $s_P(\|\boldsymbol{\tau}\|)$ and conductivity scaling factor $s_L(\|\boldsymbol{\tau}\|)$ for varying normalized wall shear stresses $\frac{\|\boldsymbol{\tau}\|}{\|\overline{\boldsymbol{\tau}}\|}$.

Table 6.2 Wall shear stress-dependent parameters for different animal models and the normalized case.

Species \ Quantity	$\|\overline{\boldsymbol{\tau}}\|$ [Pa]	ξ_τ [Pa]	γ_τ [Pa]	μ_p $\left[\frac{1}{\text{Pa}}\right]$
Normalized	1	$1.68 \cdot 10^{-1}$	$3.33 \cdot 10^{-2}$	$20.88 \cdot 10^{2}$
Human	1.16	$1.95 \cdot 10^{-1}$	$3.87 \cdot 10^{-2}$	$18.00 \cdot 10^{2}$
Dog	1.61	$2.71 \cdot 10^{-1}$	$5.37 \cdot 10^{-2}$	$12.97 \cdot 10^{2}$
Rabbit	2.38	$4.00 \cdot 10^{-1}$	$7.93 \cdot 10^{-2}$	$8.77 \cdot 10^{2}$
Rat	4.71	$7.92 \cdot 10^{-1}$	$15.70 \cdot 10^{-2}$	$4.43 \cdot 10^{2}$
Mouse	6.52	$10.96 \cdot 10^{-1}$	$21.73 \cdot 10^{-2}$	$3.20 \cdot 10^{2}$
Fitted to / source	[40]	[141]	Eq. (4.45)	[240, 254]

It remains to specify the concentrations of native LDL η_ℓ and HDL η_h in blood and the WSS $\|\boldsymbol{\tau}\|$ the model plaque is exposed to *in vivo*, which characterize the physiology and diet of the plaque's host and its position in the cardiovascular system. These parameters cannot be predetermined to fixed values, but their full ranges must be considered. The WSS $\|\boldsymbol{\tau}\|$ within a murine aortic arch are approximately below $7.7\|\overline{\boldsymbol{\tau}}\|$, cf. Section 4.3.4. In a clinical context, the concentrations of LDL and HDL are measured by determining their cholesterol contents in blood. In humans, the physiological ranges lie approximately in between concentrations of $50 - 250$ $\frac{\text{mg}}{\text{dl}}$ of LDL blood cholesterol and $20 - 80$ $\frac{\text{mg}}{\text{dl}}$ of HDL blood cholesterol [205], which can be transformed into SI units of particles per volume using ρ_8 and ρ_{13} from Table 5.1. In the case of mice with genetic modifications and high-fat diets, the LDL and HDL cholesterol concentrations can rise above 3000 $\frac{\text{mg}}{\text{dl}}$ and 400 $\frac{\text{mg}}{\text{dl}}$, respectively [167, 272]. In general, however, mice show lower total blood cholesterol concentrations compared to humans, where HDL cholesterol is

Table 6.3 Specific parameters of the PFSTI model. Parameters are grouped according to their affiliation. All units are in $\mathrm{mm}, \mathrm{g}, \mathrm{s}$ and Pa.

Parameter	Description	Value	Fitted to / source
R	Lumen radius	$5.7 \cdot 10^{-1}$ mm	Figure 4.4
H	Intima-media thickness	$4.00 \cdot 10^{-2}$ mm	$= \frac{T}{2}$, [84, 124, 146]
L	Segment length	1.8 mm	$\approx 3R$
P_m	Rate of recruitment of m	$3.05 \cdot 10^{3}\ \frac{1}{\mathrm{h\,mm^2}}$	[141]
δ_m	Fraction of saturation of recruitment of m by $\tilde{\ell}$	$68.62\ \%$	[141]
k_m	Saturation of recruitment of m by $\tilde{\ell}$	$7.38 \cdot 10^{6}\ \frac{1}{\mathrm{mm^3}}$	[141]
ξ_τ	Saturation of recruitment of m by $\boldsymbol{\tau}$	Table 6.2	[141]
ν_τ	Exponent of recruitment of m by $\boldsymbol{\tau}$	1.18	[141]
$D_{\mathrm{Eff},m}$	Effective diffusion coefficient of m	$3.6 \cdot 10^{-6}\ \frac{\mathrm{mm^2}}{\mathrm{h}}$	[45, 90]
$D_{\mathrm{Eff},f}$	Effective diffusion coefficient of f	$3.6 \cdot 10^{-6}\ \frac{\mathrm{mm^2}}{\mathrm{h}}$	$= D_m$
$D_{\mathrm{Eff},b}$	Effective diffusion coefficient of b	$3.6 \cdot 10^{-6}\ \frac{\mathrm{mm^2}}{\mathrm{h}}$	$= D_m$
P_ℓ	Diffusive permeability of ℓ	$6.12 \cdot 10^{-5}\ \frac{\mathrm{mm}}{\mathrm{h}}$	[268]
ζ_τ	Permeability scaling factor parameter	31	Eq. (4.45)
γ_τ	Permeability scaling factor parameter	Table 6.2	Eq. (4.45)
$\sigma_{\mathrm{F},\ell}$	Filtration reflection coefficient of ℓ	$9.97 \cdot 10^{-1}$	[146, 255, 294]
ω_ℓ	Weighting factor of ℓ	$9.99 \cdot 10^{-1}$	Eq. (6.26), [85]
L_p	Hydraulic conductivity	$4.26 \cdot 10^{-5}\ \frac{\mathrm{mm}}{\mathrm{Pa\,h}}$	[262]
γ_p	Conductivity scaling factor parameter	$1.31 \cdot 10^{-1}$	[240, 254]
μ_p	Conductivity scaling factor parameter	Table 6.2	[240, 254]
ξ_p	Conductivity scaling factor parameter	$1.86 \cdot 10^{1}$	[240, 254]
$D_{\mathrm{Eff},\ell}$	Effective diffusion coefficient of ℓ	$1.26 \cdot 10^{-2}\ \frac{\mathrm{mm^2}}{\mathrm{h}}$	[29, 255, 267]
K_ℓ	Hindrance coefficient of ℓ	$1.17 \cdot 10^{-1}$	[85, 210]
$P_{\tilde{\ell}}$	Diffusive permeability of $\tilde{\ell}$	$6.12 \cdot 10^{-5}\ \frac{\mathrm{mm}}{\mathrm{h}}$	$= P_\ell$
$\eta_{\tilde{\ell}}$	Concentration of $\tilde{\ell}$ in blood	$0.0\ \frac{1}{\mathrm{mm^3}}$	[70]
$\sigma_{\mathrm{F},\tilde{\ell}}$	Filtration reflection coefficient of $\tilde{\ell}$	$9.97 \cdot 10^{-1}$	$= \sigma_{\mathrm{F},\ell}$
$\omega_{\tilde{\ell}}$	Weighting factor of $\tilde{\ell}$	$9.99 \cdot 10^{-1}$	$=\omega_\ell$
$D_{\mathrm{Eff},\tilde{\ell}}$	Effective diffusion coefficient of $\tilde{\ell}$	$1.26 \cdot 10^{-2}\ \frac{\mathrm{mm^2}}{\mathrm{h}}$	$= D_{\mathrm{Eff},\ell}$
$K_{\tilde{\ell}}$	Hindrance coefficient of $\tilde{\ell}$	$1.17 \cdot 10^{-1}$	$= K_\ell$
P_h	Diffusive permeability of h	$1.14 \cdot 10^{-4}\ \frac{\mathrm{mm}}{\mathrm{h}}$	$=1.87 P_\ell$, [251]
$\sigma_{\mathrm{F},h}$	Filtration reflection coefficient of h	$9.18 \cdot 10^{-1}$	Eq. (6.21), [146]
ω_h	Weighting factor of h	$9.98 \cdot 10^{-1}$	Eq. (6.26), [85]
$q_{h,m}$	Rate of modification of h by m	$1.64 \cdot 10^{-4}\ \frac{\mathrm{mm^3}}{\mathrm{h}}$	$= \frac{q_{\ell,m}}{7.6} \frac{N_{\tilde{\ell}}}{N_{\tilde{h}}}$
$q_{h,e}$	Rate of modification of h by e	$6.21 \cdot 10^{-2}\ \frac{\mathrm{mm}}{\mathrm{h}}$	$= \frac{q_{\ell,e}}{7.6} \frac{N_{\tilde{\ell}}}{N_{\tilde{h}}}$
$D_{\mathrm{Eff},h}$	Effective diffusion coefficient of h	$2.94 \cdot 10^{-2}\ \frac{\mathrm{mm^2}}{\mathrm{h}}$	Eq. (6.23), [146]
K_h	Hindrance coefficient of h	$6.27 \cdot 10^{-1}$	Eq. (6.22), [85]
ϕ	Porosity of media	$1.5 \cdot 10^{-1}$	[1, 221]
$K^{\mathcal{PF}}$	*Darcy* permeability of artery wall	$1.11 \cdot 10^{-14}\ \mathrm{mm^2}$	Eq. (6.27)
$\varrho^{\mathcal{PF}}$	Mass density of blood plasma	$1.05 \cdot 10^{-3}\ \frac{\mathrm{g}}{\mathrm{mm^3}}$	$= \varrho^{\mathcal{F}}$
$\mu^{\mathcal{PF}}$	Dynamic viscosity of blood plasma	$2.0 \cdot 10^{-7}\ \mathrm{Pa\,h}$	[221, 294]
η_p	Luminal blood pressure	$1.33 \cdot 10^{4}\ \mathrm{Pa}$	[1, 209, 282]
p_{Adv}	Adventitial blood plasma pressure	$4.0 \cdot 10^{3}\ \mathrm{Pa}$	[1, 209, 294]

Abbreviations: low-density lipoproteins, ℓ; modified low-density lipoproteins, $\tilde{\ell}$; high-density lipoproteins, h; endothelial cells, e; macrophages, m; intracellular free cholesterol, f; intracellular cholesterol ester, b; wall shear stresses, $\boldsymbol{\tau}$.

Table 6.4 Physiological ranges of LDL η_ℓ and HDL η_h cholesterol concentrations in blood as well as wall shear stress exposure $\|\boldsymbol{\tau}\|$ *in vivo*.

Parameter	Description	Range	Source
η_ℓ	Concentration of LDL cholesterol in blood	$10 - 3000\ \frac{\mathrm{mg}}{\mathrm{dl}}$ *	[167, 205, 272]
η_h	Concentration of HDL cholesterol in blood	$20 - 400\ \frac{\mathrm{mg}}{\mathrm{dl}}$ *	[167, 205, 272]
$\|\boldsymbol{\tau}\|$	WSS exposure	$0\,\% - 770\,\%\|\overline{\boldsymbol{\tau}}\|$	

Parameters indicated by * can be transformed into SI based units using ρ_8 and ρ_{13} from Table 5.1.

the predominant lipoprotein [167]. An overview of the full spectrum of LDL and HDL blood cholesterol concentrations as well as WSS is given in Table 6.4. The ranges of interest, however, lie in the lower ends of the spectrum as these are associated with the development of atherosclerotic plaques in humans.

Remark. *The volume-averaged concentrations of LDL and HDL within the endothelial layer are close to their concentrations in blood. Moreover, the concentrations of native LDL ℓ and HDL h in the intima and media are small compared to the respective concentrations η_ℓ and η_h in blood [19, 54, 195, 268]. Therefore,*

$$\begin{aligned} r_\ell\left(\ell, p, \|\boldsymbol{\tau}\|\right) &\approx \left(P_\ell s\left(\|\boldsymbol{\tau}\|\right) + (1-\sigma_{\mathrm{F},\ell}) L_p\left(\|\boldsymbol{\tau}\|\right)\left(\eta_p - p\right)\right)\eta_\ell, \\ r_h\left(h, p, \|\boldsymbol{\tau}\|\right) &\approx \left(P_h s\left(\|\boldsymbol{\tau}\|\right) + (1-\sigma_{\mathrm{F},h}) L_p\left(\|\boldsymbol{\tau}\|\right)\left(\eta_p - p\right)\right)\eta_h \end{aligned} \tag{6.29}$$

are reasonable approximations to the influx of native LDL r_ℓ [146, 210] and HDL r_h given by Equations (6.4) *and* (6.8)*, respectively. However, as the concentration of modified LDL in blood $\eta_{\tilde{\ell}}$ is small, the analog simplification is not valid for the outflux of modified LDL $r_{\tilde{\ell}}$.*

6.2.2 Sensitivity analysis

The estimated parameters in the previous section have a degree of uncertainty due to their different origins, different animals used as experimental models and measurement errors. Additionally, the conversion from the various units of measurement in the experimental studies to a unified SI unit system introduces another source of uncertainty for some parameters.

To quantify the effect of uncertainties in the parameters on the computational results of the model, a local sensitivity analysis in terms of a metabolic control analysis [300] is performed. However, the computational cost to solve the spatial PFSTI model is large such that a metabolic control analysis using the spatial PFSTI model is not achievable. Therefore, the non-spatial *extended combined model* is exploited which consists of the combined model (Section 5.1.2) enriched by the laws of the macrophage, LDL and HDL recruitments (submodels $\boxed{5}$ and $\boxed{6}$ with fixed $p = \eta_p - \Delta p_{\mathrm{End}} = 82\ \mathrm{mmHg} = 1.09 \cdot 10^4\ \mathrm{Pa}$ [45, 209, 262, 267]). The extended combined model is given in detail in Appendix B. It is important to note that the extended combined model is equivalent to the spatial PFSTI model in the case of large effective diffusion coefficients $D_{\mathrm{Eff},i}$.

The metabolic control analysis is performed in correspondence to Section 5.2.1. Therefore, the metabolic control coefficients $\mathrm{MCC}(i,p)$ of all species i at time $t = 100$ weeks are computed as described by Equation (5.8), where solely the non-spatial parameters p listed in Table 6.3 are regarded. The uncertainties of the remaining non-spatial parameters were previously addressed in Section 5.2.1. The influence of the spatial parameters $D_{\mathrm{Eff},i}$ and K_i is assessed as described in Section 6.2.6. As a basis for the perturbation of LDL cholesterol, HDL cholesterol and WSS, $\eta_\ell = 150\ \frac{\mathrm{mg}}{\mathrm{dl}}$, $\eta_h = 50\ \frac{\mathrm{mg}}{\mathrm{dl}}$ and $\|\boldsymbol{\tau}\| = 10\,\%\|\overline{\boldsymbol{\tau}}\|$ are employed.

Remark. *The extended combined model does* not *solve for an approximation of the medial pressure $p^{\mathcal{PF}}$ and transmural velocity $\boldsymbol{u}^{\mathcal{PF}}$, but a prescribed medial pressure p and velocity $\boldsymbol{u}$ are employed. To avoid confusion, the prescribed medial pressure and velocity of the extended combined model are denoted without superscript $\mathcal{PF}$, whereas their counterparts in the PFSTI model are denoted with superscript.*

6.2.3 Influence of advective fluxes through endothelium

The fluxes of lipoproteins through the endothelium governed by the WSS-dependent *Kedem-Katchalsky* equations in Section 6.1.1.3 are subdivided into diffusive and advective parts which are individually altered by the WSS-dependent PSF and CSF. The advective fluxes are a consequence of the pressure drop $\Delta p_{\mathrm{End}} = \eta_p - p$ across the endothelium and the induced volume flux J_{Vol} of blood plasma through the endothelium, cf. Section 4.5. However, mathematical and computational models frequently model the artery wall as solids (e.g., the multiphysics model in Chapter 4), where the advective fluxes of lipoproteins are neglected as consequence. There is controversy about the impact of this simplifying model assumption with respect to the transport of native LDL through the endothelium [210, 268]. Further, the advective flux of modified LDL and native HDL through the endothelium is not yet assessed at all. Therefore, the laws for the fluxes of native LDL $r_\ell\left(\ell, p, \|\boldsymbol{\tau}\|\right)$, modified LDL $r_{\tilde{\ell}}(\tilde{\ell}, p, \|\boldsymbol{\tau}\|)$ and HDL $r_h\left(h, p, \|\boldsymbol{\tau}\|\right)$ through the endothelium (Equations (6.4) and (6.8)) are analyzed.

First, the three laws relative to the cholesterol concentrations in blood, i.e., $\frac{r_\ell}{\eta_\ell}$, $\frac{r_{\tilde{\ell}}}{\eta_\ell}$ and $\frac{r_h}{\eta_h}$ are studied, where the following physiological ranges for their arguments are considered: According to the measurements in [262], the pressure drop across the endothelium is approximately $\Delta p_{\mathrm{End}} = 18\ \mathrm{mmHg}$. Hence, subendothelial pressures p in between $75-90\ \mathrm{mmHg}$ are considered. In analogy to the medial LDL concentrations measured in [117, 268], $\ell = \tilde{\ell} = 7.2 \cdot 10^{-4}\eta_\ell$ and $h = 7.2 \cdot 10^{-4}\eta_h$ are utilized as lipoprotein concentrations in the media. The remaining parameters are given in Tables 5.7 and 6.3.

Further, the fractions of the advective to the total fluxes of native LDL $\frac{r_{\mathrm{Adv},\ell}}{r_\ell}$, modified LDL $\frac{r_{\mathrm{Adv},\tilde{\ell}}}{r_{\tilde{\ell}}}$ and HDL $\frac{r_{\mathrm{Adv},h}}{r_h}$ are investigated using the same parameters as stated above. Here, $r_{\mathrm{Adv},i}$ denotes the advective flux of a lipoprotein $i = \ell, \tilde{\ell}, h$, cf. Equation (6.4).

6.2.4 Stability analysis

The outcome of the PFSTI model is strongly dependent on blood cholesterol concentrations of LDL η_ℓ and HDL η_h and the WSS $\|\boldsymbol{\tau}\|$ which characterize the physiology and diet of the host and the position of the individual plaque within the cardiovascular system. They can – depending on the species, its predisposition and its diet – vary by several orders of magnitude (cf. Table 6.4) which results in qualitatively different predicted long-term outcomes of the model plaque, cf. Section 5.4. Hence, a focus is put on these three parameters and a systematic analysis of the stability in correspondence to Section 5.2.2 is performed. Due to the high computational cost of the spatial PFSTI model, the stability analysis is performed using the extended combined model (cf. Appendix B) with parameters from Tables 5.7 and 6.3 and a subendothelial pressure $p = 82\ \mathrm{mmHg}$.

The long-term outcome of the extended combined model is analyzed by numerically determining the steady-state values of the concentrations of macrophages

$$\widehat{m} \in [m'_{\mathrm{Min}}, m'_{\mathrm{Max}}] := \left[\frac{P_m\,(1-\delta_m)}{H} \frac{(\xi_\tau)^{\nu_\tau}}{(\xi_\tau)^{\nu_\tau} + \|\boldsymbol{\tau}\|^{\nu_\tau}} \frac{(\xi_m)^{n_m} + (f_{\mathrm{Max}})^{n_m}}{\mu_m (f_{\mathrm{Max}})^{n_m}}, \right. \\ \left. \frac{P_m}{H} \frac{(\xi_\tau)^{\nu_\tau}}{(\xi_\tau)^{\nu_\tau} + \|\boldsymbol{\tau}\|^{\nu_\tau}} \frac{(\xi_m)^{n_m} + (f_{\mathrm{Min}})^{n_m}}{\mu_m (f_{\mathrm{Min}})^{n_m}} \right] \tag{6.30}$$

and total intracellular free cholesterol per macrophage

$$\frac{\widehat{f}}{\widehat{m}} \in [f_{\mathrm{Min}}; f_{\mathrm{Max}}] \tag{6.31}$$

for the ranges of interest of η_ℓ, η_h and $\|\boldsymbol{\tau}\|$. Additionally, the boundedness of the concentration of the total intracellular cholesterol ester $b(t)$ is investigated numerically in order to assess the severity and risk of plaques.

Remark. *Since* $(1-\sigma_{\mathrm{F},i})(1-\omega_i)L_p s_{\mathrm{L}}(\|\boldsymbol{\tau}\|)(\eta_p - p) \leq P_i s_{\mathrm{P}}(\|\boldsymbol{\tau}\|)\ \forall i = \ell, \tilde{\ell}, h$*, the influx rates of native LDL* $r_\ell\,(\ell, p, \|\boldsymbol{\tau}\|)$ *and HDL* $r_h\,(h, p, \|\boldsymbol{\tau}\|)$ *are positive and bounded by positive* constants *and the "influx" rate of modified LDL* $r_{\tilde{\ell}}(\tilde{\ell}, p, \|\boldsymbol{\tau}\|)$ *is strictly negative. In addition, the rate of recruitment of macrophages is bounded by* $0 \leq r_m(\tilde{\ell}, \|\boldsymbol{\tau}\|) \leq P_m$*. Therefore, Proposition 1 from Section 5.2.2 remains valid with slight adaptations for the extended combined model, see Proposition 2 in Appendix B.*

6.2.5 Meshing and implementation validation

The PFSTI model is numerically treated as described in Section 3.2.3. The poro-fluid domain $\Omega^{\mathcal{PF}}$ and poro-scatra domain $\Omega^{\mathcal{PS}}$ of the idealized intima-media geometry utilize equal finite element meshes which are structured as follows: The endothelial boundary Γ_{End} is meshed using quadrilateral elements with *surface element length* h_1. In the radial direction, equidistant layers of hexahedral elements with *radial element length* h_2 are employed. As the deficiency of the finite element mesh lies in the resolution of the steep concentration gradients near the endothelial and media-adventitia boundaries Γ_{End} and Γ_{Adv}, 20 equidistant layers with radial element

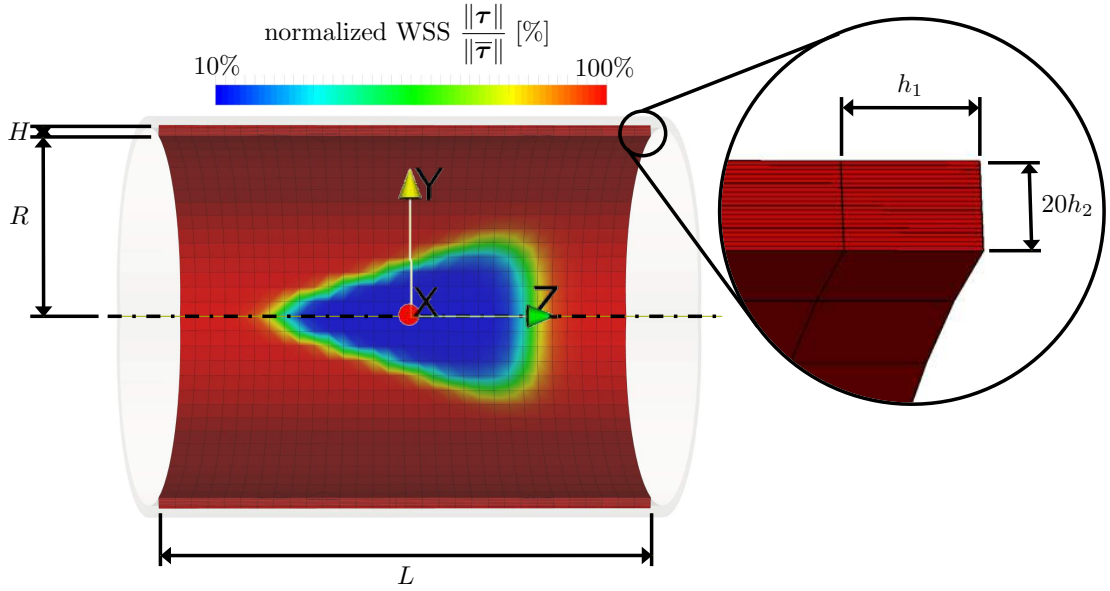

Figure 6.4 Finite element mesh for the PFSTI model with $h_1 = 6.0 \cdot 10^{-2}$ mm and $h_2 = 2.0 \cdot 10^{-3}$ mm and prescribed inhomogeneous normalized WSS pattern $\frac{\|\boldsymbol{\tau}\|}{\|\overline{\boldsymbol{\tau}}\|}(\boldsymbol{x})$.

length $h_2 = 2.0 \cdot 10^{-3}$ mm are utilized. As determined in Section 4.3.3, a surface element length $h_1 = 6.0 \cdot 10^{-2}$ mm is used. In total, a finite element mesh with 36000 hexahedral elements, 39060 nodes and 273420 degrees of freedom is employed. An overview of the finite element mesh for the PFSTI model is given in Figure 6.4.

A validation of the implementation of the complex inflammatory and immunological reactions and boundary conditions of the PFSTI model in BACI is performed. To this end, the results of the PFSTI model with high effective diffusion coefficients $D_{\mathrm{Eff},i}$ solved using BACI are compared to the results of the extended combined model solved using MATLAB. In MATLAB, a stiff solver with adaptive time stepping (MATLAB solver "ode15s") is used. In contrast, a constant time step size $\Delta t = 1$ week $= 168$ h is employed in BACI. Thus, to allow a valid comparison of the results with MATLAB, appropriate initial concentrations $\ell_0, \tilde{\ell}_0, h_0, f_0, b_0, m_0$ are employed for the PFSTI model which correspond to the post-initial concentrations computed with MATLAB.

6.2.6 Influence of transport within artery wall

Within the artery wall LDL and HDL are transported by diffusion and advection with the transmural flow which lead to spatially varying concentration profiles. However, the importance of the transport of lipoproteins *within* the artery wall was not yet investigated. The influence of diffusion on the lipoproteins transport is assessed by a successive reduction of the order of magnitude of the effective diffusion coefficients $D_{\mathrm{Eff},\ell}$, $D_{\mathrm{Eff},\tilde{\ell}}$ and $D_{\mathrm{Eff},h}$ from large values inducing homogeneous concentrations to their values as given in Table 6.3. Subsequently, the importance of the advective transport of lipoproteins within the artery wall is investigated by a comparison of the concentration profiles of the PFSTI model with various hindrance coefficients K_ℓ, $K_{\tilde{\ell}}$ and K_h. As consistent

inhomogeneous initial concentrations are not achievable in the case of physiological diffusion coefficients, a shock-like event in the beginning of the simulation is inevitable. Therefore, numerical dissipation is introduced by using the one-step-θ scheme coefficient $\theta = 0.6$.

6.2.7 Influence of inhomogeneous WSS distribution

In addition to diffusion and advection, the concentrations are locally altered *in vivo* by non-uniform recruitment rates of LDL, HDL and macrophages through the endothelium, e.g., induced by spatially varying WSS distributions. Regional differences in the recruitment rates can locally lead to the formation of plaques whereas other sites remain healthy. Therefore, the PFSTI model is solved and analyzed with a prescribed inhomogeneous normalized WSS distribution given by

$$\frac{\|\boldsymbol{\tau}\|(\boldsymbol{x})}{\|\overline{\boldsymbol{\tau}}\|} = \left(1 - 0.9 \frac{1 - \exp\left(- \frac{1}{1+((6^2(X/\mathrm{mm}-0.57)^2+(5-8Z/\mathrm{mm})^2(Y/\mathrm{mm}-0)^2+2^2(Z/\mathrm{mm}-0))^2)^8} \right)}{1 - \exp\left(-1\right)} \right), \tag{6.32}$$

where X, Y and Z are the coordinates of the vector $\boldsymbol{x} = [X, Y, Z]^T$ in the cartesian coordinate system. The geometrical center of the idealized intima-media geometry (with lumen radius $R = 0.57$ mm, intima-media thickness $H = 0.04$ mm and segment length $L = 1.8$ mm) is at the origin of the coordinate system and the geometry is symmetric with respect to the Z-axis. A visualization of the geometry and the prescribed inhomogeneous normalized WSS distribution $\frac{\|\boldsymbol{\tau}\|(\boldsymbol{x})}{\|\overline{\boldsymbol{\tau}}\|}$ is given in Figure 6.4. In accordance with the WSS pattern in mice (cf. Figure 4.10), a sharp transition from low ($10\,\%\|\overline{\boldsymbol{\tau}}\|$) to high ($100\,\%\|\overline{\boldsymbol{\tau}}\|$) WSS is prescribed.

6.3 Results

In this section all results gained from the models in Section 6.1 and the methods in Section 6.2 are presented. All numerical computations concerning ODE models were performed using MATLAB (The MathWorks Inc., Natick, Massachusetts, USA, 2000). The solving of the spatial PFSTI model was performed using BACI [277].

6.3.1 Sensitivity analysis

The local sensitivity of the extended combined model with respect to its parameters is analyzed as described in Section 6.2.2. The results of the performed metabolic control analysis are independent of the chosen variation parameter $\varepsilon = 0.1\%$. The metabolic control coefficients of all species of the extended combined model with respect to all non-spatial parameters listed in Table 6.3 are visualized in Figure 6.5.

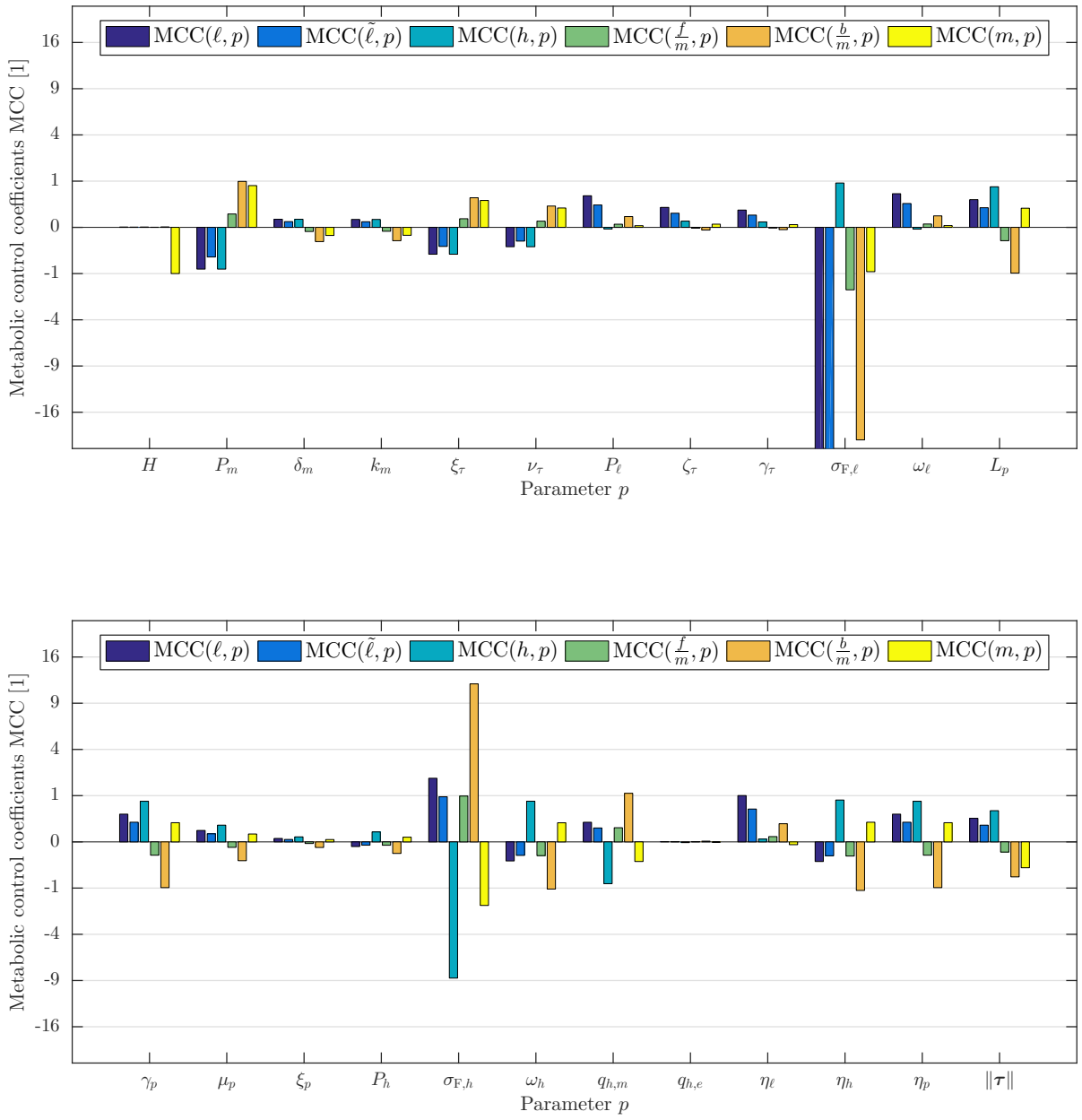

Figure 6.5 Metabolic control analysis of the extended combined model. The metabolic control coefficients of native LDL ℓ, modified LDL $\tilde{\ell}$, HDL h, intracellular free cholesterol per macrophage $\frac{f}{m}$, intracellular cholesterol ester per macrophage $\frac{b}{m}$ and macrophages m with respect to all specific parameters p of the PFSTI model are computed as described in Section 6.2.2. The values of the truncated bars are $\mathrm{MCC}(\ell, \sigma_{\mathrm{F},\ell}) = -175.90$ and $\mathrm{MCC}(\tilde{\ell}, \sigma_{\mathrm{F},\ell}) = -92.68$. For an overview of all parameters, see Tables 5.7 and 6.3.

6.3.2 Lipoprotein fluxes and macrophage recruitment

The submodels for the fluxes of native LDL, modified LDL and HDL (submodel $\boxed{6}$) are analyzed as described in Section 6.2.3. As medial concentrations of native LDL ℓ and HDL h relative to the luminal concentrations η_ℓ and η_h are employed, the results of the relative fluxes of native LDL $\frac{r_\ell}{\eta_\ell}$ and HDL $\frac{r_h}{\eta_h}$ are independent of η_ℓ and η_h, respectively. In contrast, since $\eta_{\tilde{\ell}} = 0$, the relative outflux of modified LDL $\frac{r_{\tilde{\ell}}}{\eta_\ell}$ scales linearly with the medial concentration of modified LDL $\tilde{\ell}$. The fractions of the advective fluxes of native LDL $\frac{r_{\mathrm{Adv},\ell}}{r_\ell}$, modified LDL $\frac{r_{\mathrm{Adv},\tilde{\ell}}}{r_{\tilde{\ell}}}$ and HDL $\frac{r_{\mathrm{Adv},h}}{r_h}$ are independent of the medial and luminal lipoprotein concentrations, cf. remark in Section 6.2.1.

The relative fluxes $\frac{r_i}{\eta_i}$ and fractions of advective fluxes $\frac{r_{\mathrm{Adv},i}}{r_i}$ of native LDL ℓ, modified LDL $\tilde{\ell}$ and HDL h are shown in Figure 6.6. Further, an overview of the estimated rates of recruitment of macrophages (submodel $\boxed{5}$) for various concentrations of modified LDL is given in Figure 6.7.

6.3.3 Stability analysis

The influence of the blood cholesterol concentrations of LDL η_ℓ and HDL η_h and the WSS $\|\boldsymbol{\tau}\|$ to the long-term outcome of model plaques is investigated using the extended combined model as described in Section 6.2.4. Proposition 2 from Appendix B) applies as all its requirements are fulfilled by the extended combined model with the parameter set from Tables 5.7 and 6.3. Hence, the steady-state concentrations of macrophages $\widehat{m}$ and intracellular free cholesterol per macrophage $\frac{\widehat{f}}{\widehat{m}}$ satisfy

$$\begin{aligned} \widehat{m} &\in [m'_{\mathrm{Min}}, m'_{\mathrm{Max}}] = [0.04 \cdot 10^8, 14.96 \cdot 10^8] \, \frac{1}{\mathrm{mm}^3}, \\ \frac{\widehat{f}}{\widehat{m}} &\in [f_{\mathrm{Min}}, f_{\mathrm{Max}}] = \left[1.22 \cdot 10^{10}, 7.15 \cdot 10^{10}\right] \end{aligned} \tag{6.33}$$

and only the concentration of cholesterol ester b can be unbounded. The boundedness of intracellular cholesterol ester b, the steady-state concentration of intracellular free cholesterol per macrophages $\frac{\widehat{f}}{\widehat{m}}$ and the steady-state density of macrophages $\widehat{m}$ are computed for the crucial ranges of η_ℓ, η_h and $\|\boldsymbol{\tau}\|$. As high LDL cholesterol, low HDL cholesterol and regions with low WSS are prone to atherosclerosis, the considered ranges for the stability analysis are $\eta_\ell \in [10, 800] \, \frac{\mathrm{mg}}{\mathrm{dl}}$, $\eta_h \in [20, 100] \, \frac{\mathrm{mg}}{\mathrm{dl}}$ and $\|\boldsymbol{\tau}\| \in [5\,\%, 40\,\%] \|\overline{\boldsymbol{\tau}}\|$, cf. Table 6.4. They are covered by a simple analysis utilizing an equidistant grid of the parameter space. The results for varying blood cholesterol concentrations η_ℓ and η_h and four different WSS levels $\|\boldsymbol{\tau}\|$ are visualized in Figure 6.8.

6.3.4 Spatially resolved model

The validity check of the complex implementation of the spatial PFSTI model in BACI is performed as described in Section 6.2.5, where the parameter set from Tables 5.7 and 6.3 together with $D_{\mathrm{Eff},i} = 1.26 \cdot 10^2 \frac{1}{\mathrm{mm}^2} \; \forall i = \ell, \ldots, m$, $\|\boldsymbol{\tau}\| = 10\,\% \|\overline{\boldsymbol{\tau}}\|$, $\eta_\ell = 150 \, \frac{\mathrm{mg}}{\mathrm{dl}}, \eta_h = 50 \, \frac{\mathrm{mg}}{\mathrm{dl}}$ and

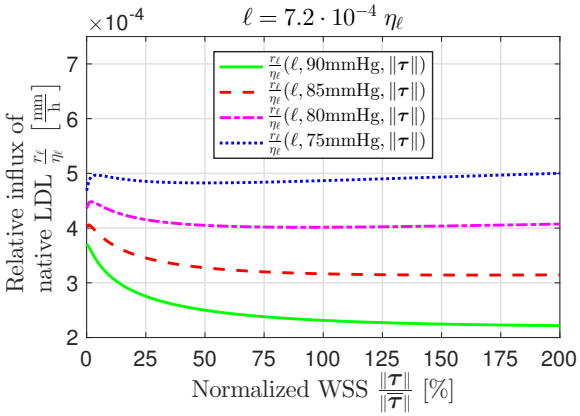

(a) Relative influx of native LDL $\frac{r_\ell}{\eta_\ell}$.

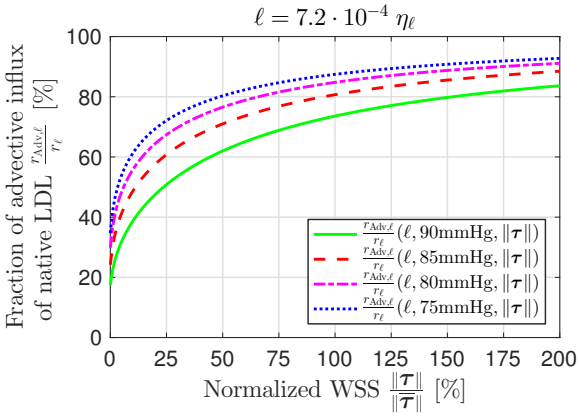

(b) Fraction of advective influx of native LDL $\frac{r_{\text{Adv},\ell}}{r_\ell}$.

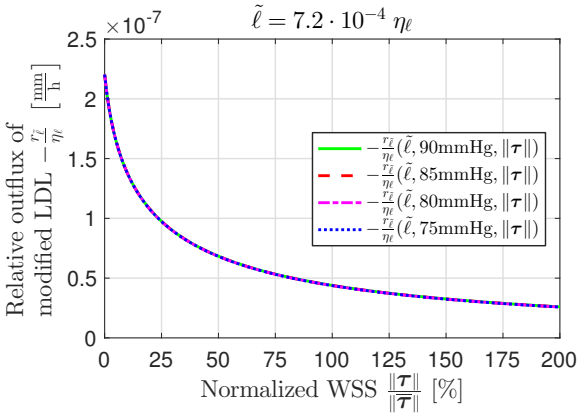

(c) Relative outflux of modified LDL $-\frac{r_{\tilde{\ell}}}{\eta_{\tilde{\ell}}}$.

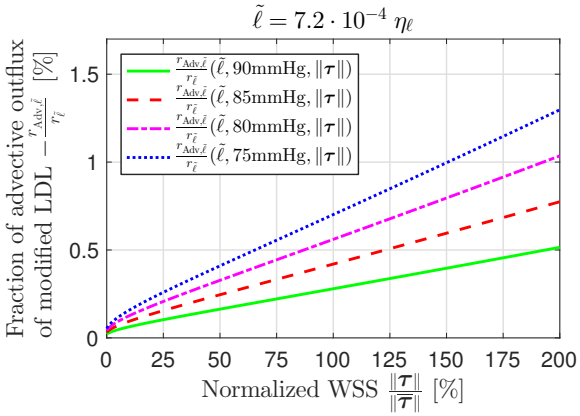

(d) Fraction of advective outflux of modified LDL $-\frac{r_{\text{Adv},\tilde{\ell}}}{r_{\tilde{\ell}}}$.

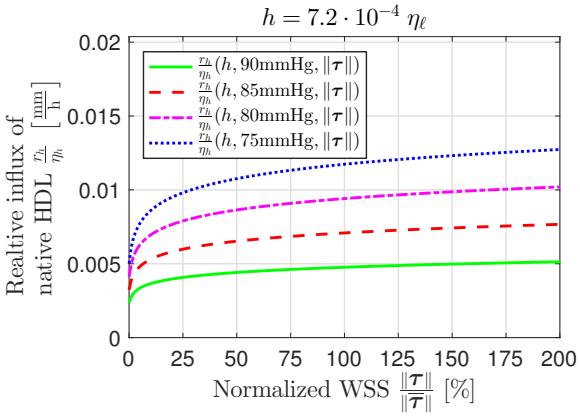

(e) Relative influx of native HDL $\frac{r_h}{\eta_h}$.

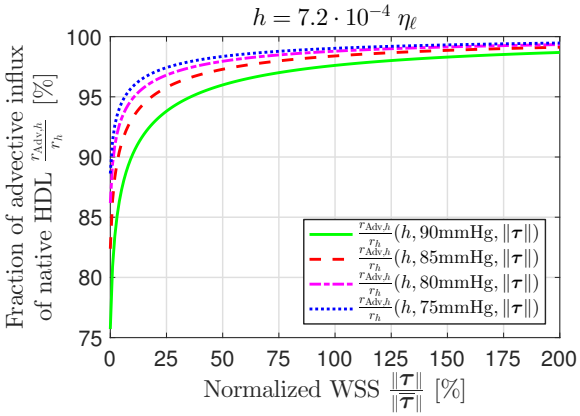

(f) Fraction of advective influx of native HDL $\frac{r_{\text{Adv},h}}{r_h}$.

Figure 6.6 Relative fluxes $\frac{r_i}{\eta_i}$ and fractions of advective fluxes $\frac{r_{\text{Adv},i}}{r_i}$ of native LDL, modified LDL and HDL ($i = \ell, \tilde{\ell}, h$) as predicted by submodel $\boxed{6}$ with varying normalized wall shear stresses $\frac{\|\boldsymbol{\tau}\|}{\|\overline{\boldsymbol{\tau}}\|}$, various medial pressures p and prescribed medial concentrations ℓ, $\tilde{\ell}$ and h.

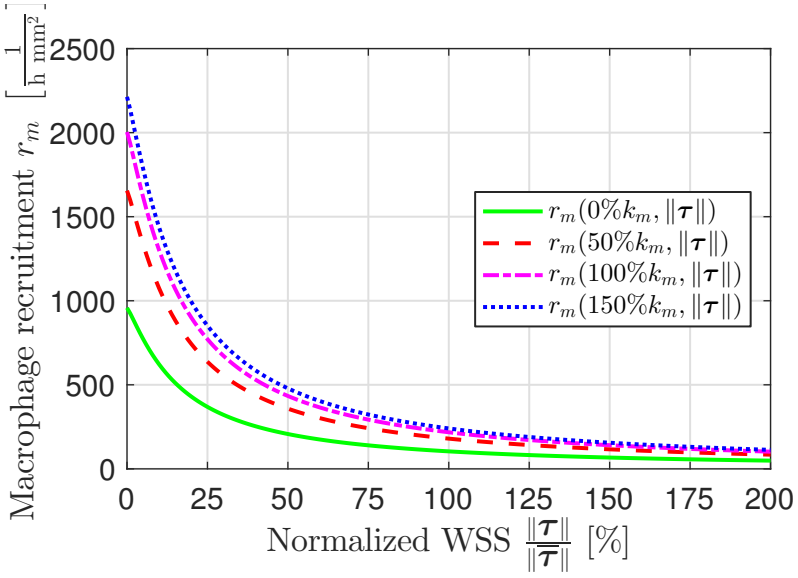

Figure 6.7 Rate of recruitment of macrophages as predicted by the submodel of macrophage recruitment (submodel $\boxed{5}$) with varying normalized wall shear stresses $\frac{\|\boldsymbol{\tau}\|}{\|\overline{\boldsymbol{\tau}}\|}$ and various concentrations of modified LDL $\tilde{\ell}$.

$p = 82$ mmHg are employed. Due to the high effective diffusion coefficients $D_{\text{Eff},i}$, the concentrations are homogeneous throughout the domain $\Omega^{\mathcal{PS}}$ and the results of an arbitrary node are utilized. The comparison of the results of the PFSTI model solved using BACI and the extended combined model solved using MATLAB is shown in Figure 6.9.

The influence of diffusion and advection within the artery wall is assessed as described in Section 6.2.6. Successively reducing the effective diffusion coefficients $D_{\text{Eff},\ell}$, $D_{\text{Eff},\tilde{\ell}}$ and $D_{\text{Eff},h}$ in the PFSTI model results in inhomogeneous concentration profiles of all species along the radial direction, whereby the independence of the utilized element lengths h_1 and h_2 to the computational results is ensured. Denoting the concentration profile of native LDL along the X-axis by $\ell(X)$ (with $X \in [R, R+H] = [0.57 \text{ mm}, 0.61 \text{ mm}]$), the space-averaged concentration of native LDL $\overline{\ell}$ and its center of mass $\overline{X}_{\overline{\ell}}$ are computed by

$$\begin{aligned} \overline{\ell} &= \frac{1}{H} \int_R^{R+H} \ell(X) \, \mathrm{d}X, \\ \overline{X}_{\overline{\ell}} &= \frac{1}{\overline{\ell}} \int_R^{R+H} X \, \ell(X) \, \mathrm{d}X. \end{aligned} \tag{6.34}$$

The average concentrations and centers of mass of the remaining species are computed analogously. The average concentrations of all species $\overline{\ell}, \ldots, \overline{m}$ along the X-axis and the position of their respective centers of mass $\overline{X}_{\overline{\ell}}, \ldots, \overline{X}_{\overline{m}}$ on the X-axis for various effective diffusion coefficients $D_{\text{Eff},\ell}, D_{\text{Eff},\tilde{\ell}}, D_{\text{Eff},h}$ and hindrance coefficients $K_\ell, K_{\tilde{\ell}}, K_h$ are given in Table 6.5. Moreover, the concentration profiles for various hindrance coefficients $K_\ell, K_{\tilde{\ell}}$ and K_h are given in Figure 6.10.

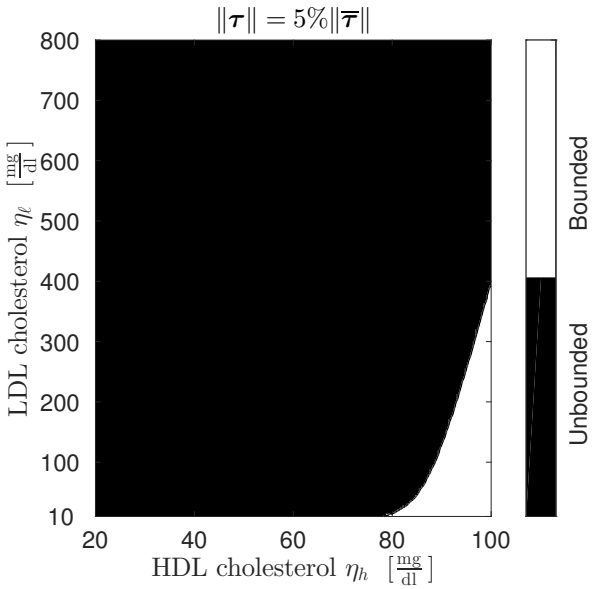

(a) Boundedness of concentration of intracellular cholesterol ester per macrophage for varying η_ℓ and η_h and fixed $\|\boldsymbol{\tau}\| = 5\,\%\|\overline{\boldsymbol{\tau}}\|$.

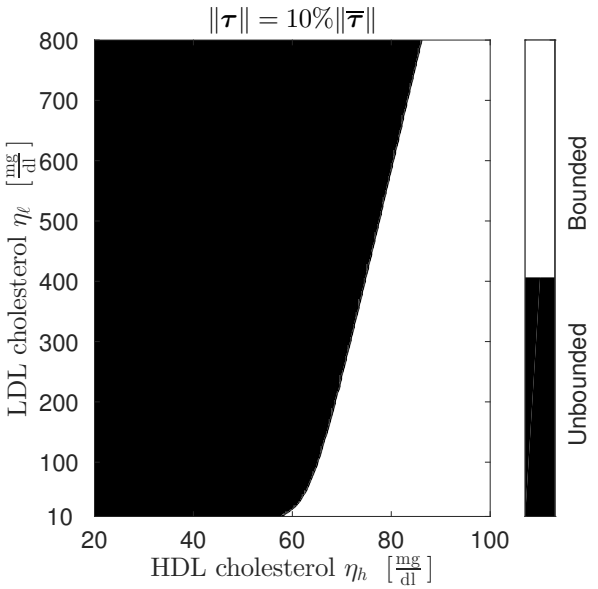

(b) Boundedness of concentration of intracellular cholesterol ester per macrophage for varying η_ℓ and η_h and fixed $\|\boldsymbol{\tau}\| = 10\,\%\|\overline{\boldsymbol{\tau}}\|$.

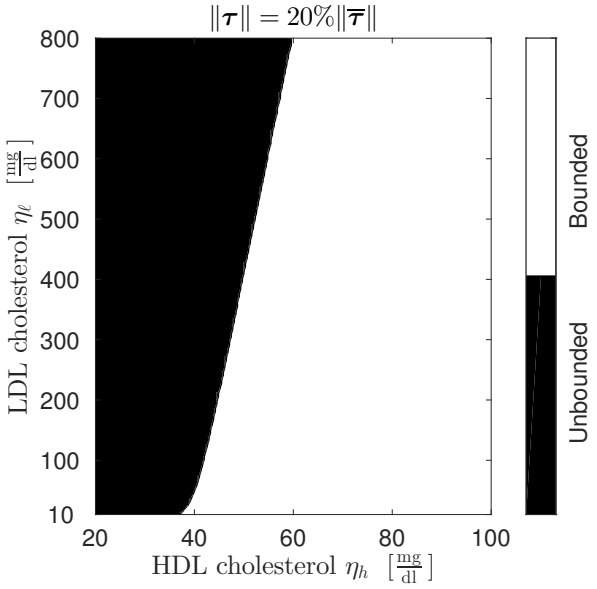

(c) Boundedness of concentration of intracellular cholesterol ester per macrophage for varying η_ℓ and η_h and fixed $\|\boldsymbol{\tau}\| = 20\,\%\|\overline{\boldsymbol{\tau}}\|$.

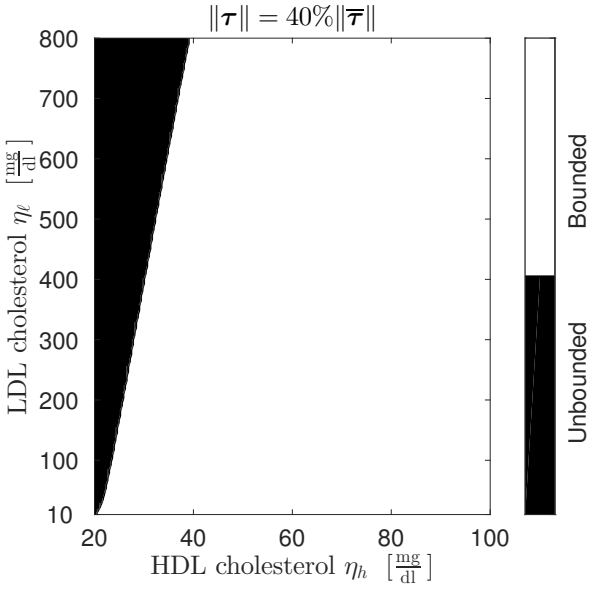

(d) Boundedness of concentration of intracellular cholesterol ester per macrophage for varying η_ℓ and η_h and fixed $\|\boldsymbol{\tau}\| = 40\,\%\|\overline{\boldsymbol{\tau}}\|$.

Figure 6.8 Stability analysis of the extended combined model as described in Section 6.2.4. The boundedness of intracellular cholesterol ester, the steady-state concentration of intracellular free cholesterol per macrophage $\frac{\widehat{f}}{\widehat{m}}$ and the steady-state density of macrophages $\widehat{m}$ are predicted for varying LDL and HDL cholesterol concentrations η_ℓ and η_h and various WSS $\|\boldsymbol{\tau}\|$.

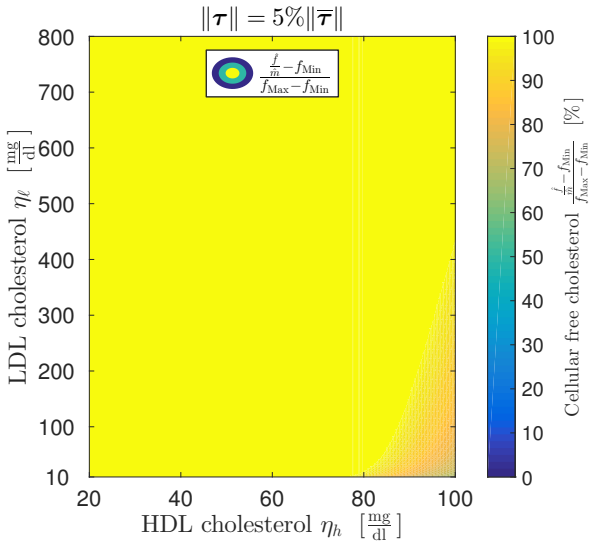

(e) Steady-state concentrations of intracellular free cholesterol per macrophage $\frac{\widehat{f}}{\widehat{m}}$ relative to $[f_{\text{Min}}, f_{\text{Max}}]$ for varying η_ℓ and η_h and fixed $\|\boldsymbol{\tau}\| = 5\%\|\overline{\boldsymbol{\tau}}\|$.

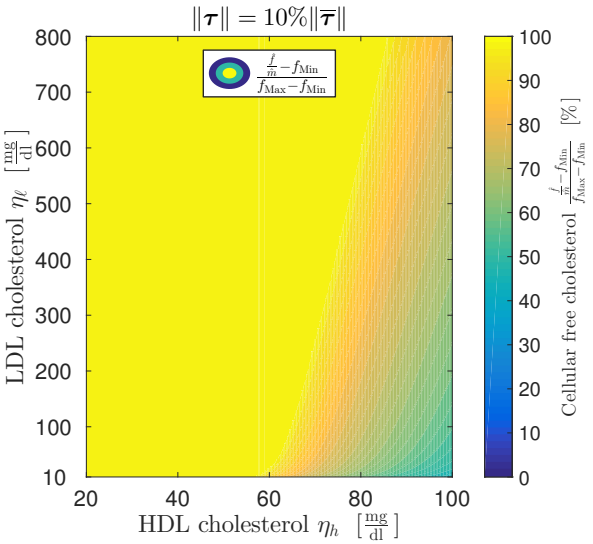

(f) Steady-state concentrations of intracellular free cholesterol per macrophage $\frac{\widehat{f}}{\widehat{m}}$ relative to $[f_{\text{Min}}, f_{\text{Max}}]$ for varying η_ℓ and η_h and fixed $\|\boldsymbol{\tau}\| = 10\%\|\overline{\boldsymbol{\tau}}\|$.

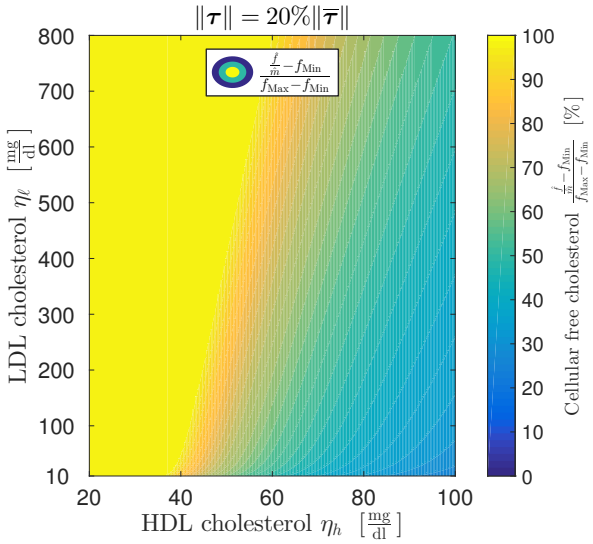

(g) Steady-state concentrations of intracellular free cholesterol per macrophage $\frac{\widehat{f}}{\widehat{m}}$ relative to $[f_{\text{Min}}, f_{\text{Max}}]$ for varying η_ℓ and η_h and fixed $\|\boldsymbol{\tau}\| = 20\%\|\overline{\boldsymbol{\tau}}\|$.

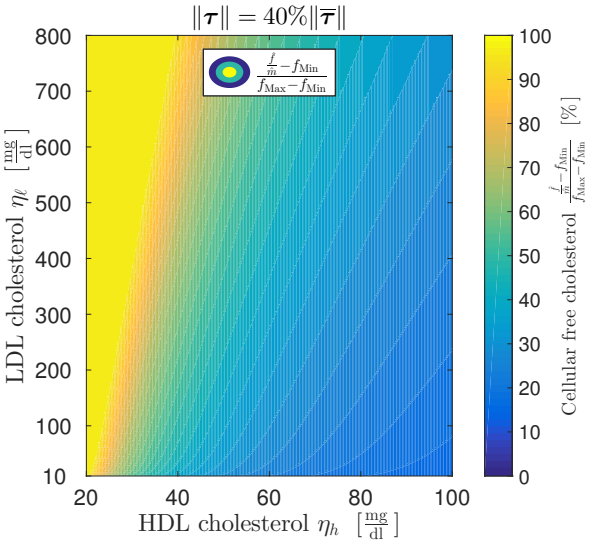

(h) Steady-state concentrations of intracellular free cholesterol per macrophage $\frac{\widehat{f}}{\widehat{m}}$ relative to $[f_{\text{Min}}, f_{\text{Max}}]$ for varying η_ℓ and η_h and fixed $\|\boldsymbol{\tau}\| = 40\%\|\overline{\boldsymbol{\tau}}\|$.

Figure 6.8 Continued.

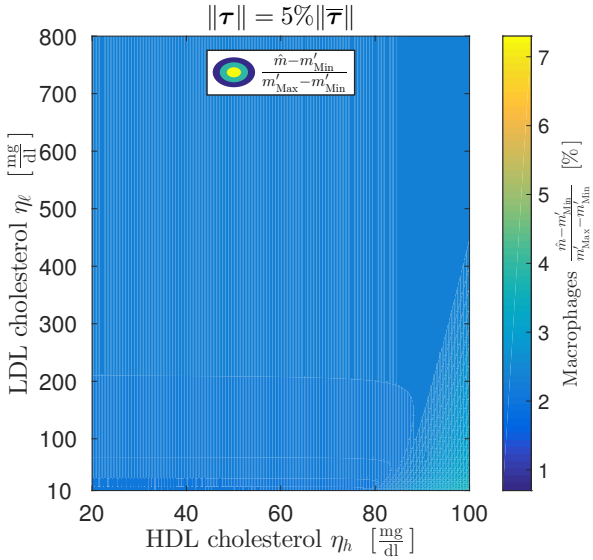

(i) Steady-state densities of macrophages $\widehat{m}$ relative to $[m'_{\text{Min}}; m'_{\text{Max}}]$ for varying η_ℓ and η_h and fixed $\|\boldsymbol{\tau}\| = 5\%\|\overline{\boldsymbol{\tau}}\|$.

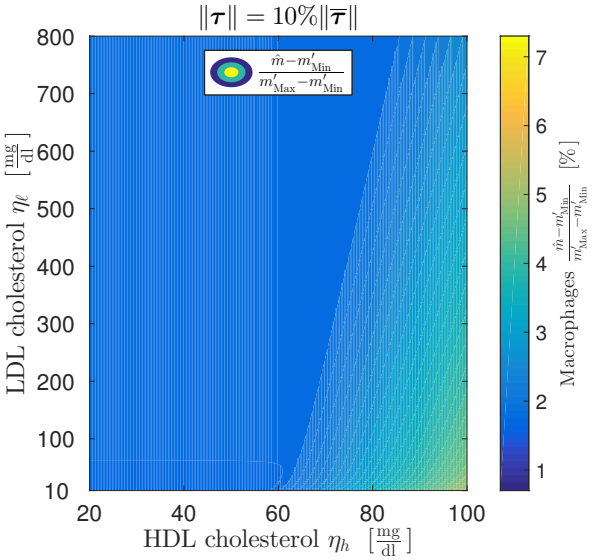

(j) Steady-state densities of macrophages $\widehat{m}$ relative to $[m'_{\text{Min}}; m'_{\text{Max}}]$ for varying η_ℓ and η_h and fixed $\|\boldsymbol{\tau}\| = 10\%\|\overline{\boldsymbol{\tau}}\|$.

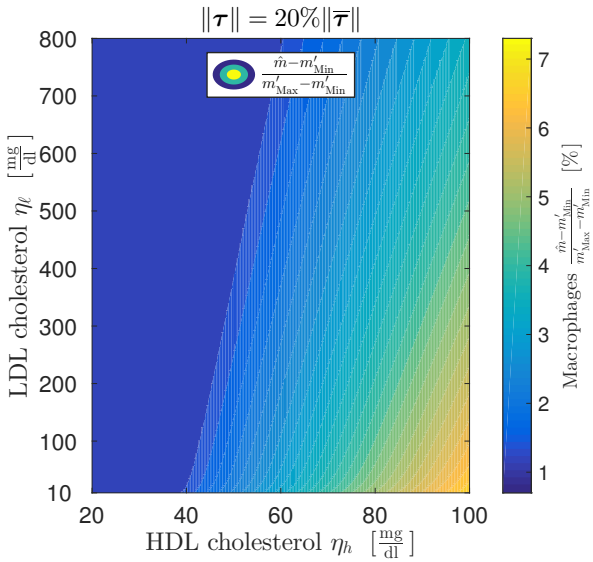

(k) Steady-state densities of macrophages $\widehat{m}$ relative to $[m'_{\text{Min}}; m'_{\text{Max}}]$ for varying η_ℓ and η_h and fixed $\|\boldsymbol{\tau}\| = 20\%\|\overline{\boldsymbol{\tau}}\|$.

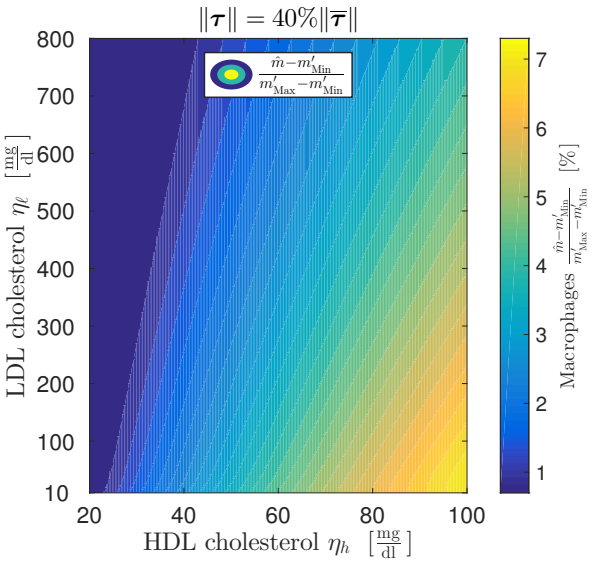

(l) Steady-state densities of macrophages $\widehat{m}$ relative to $[m'_{\text{Min}}; m'_{\text{Max}}]$ for varying η_ℓ and η_h and fixed $\|\boldsymbol{\tau}\| = 40\%\|\overline{\boldsymbol{\tau}}\|$.

Figure 6.8 Continued.

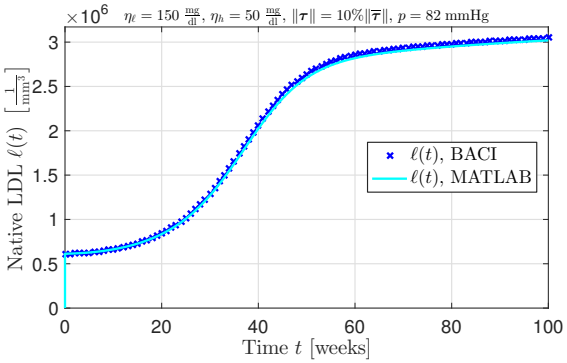

(a) Concentrations of native LDL $\ell(t)$ over time t.

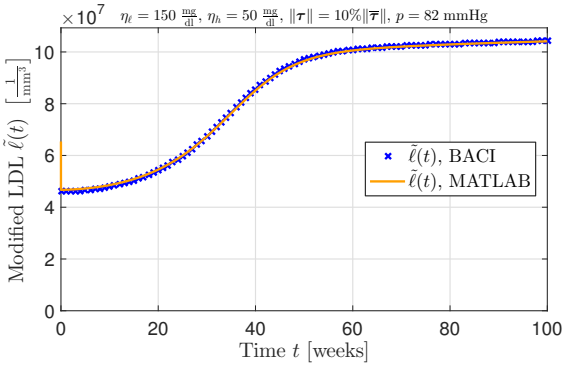

(b) Concentrations of modified LDL $\tilde{\ell}(t)$ over time t.

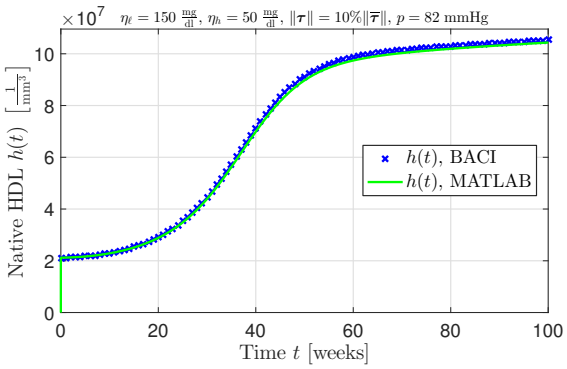

(c) Concentrations of HDL $h(t)$ over time t.

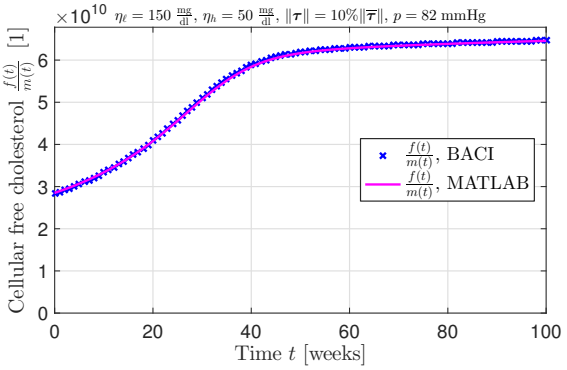

(d) Concentration of intracellular free cholesterol per macrophage $\frac{f(t)}{m(t)}$ relative to $[f_{\text{Min}}, f_{\text{Max}}]$ over time t.

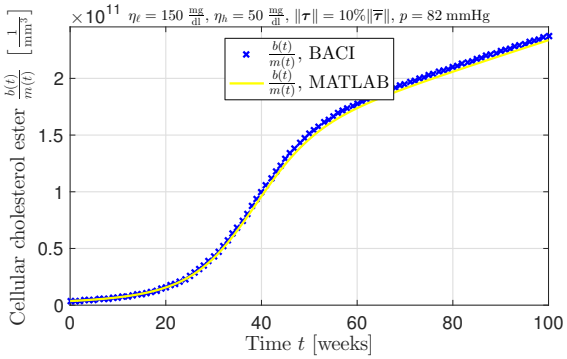

(e) Concentration of intracellular cholesterol ester per macrophage $\frac{b(t)}{m(t)}$ over time t.

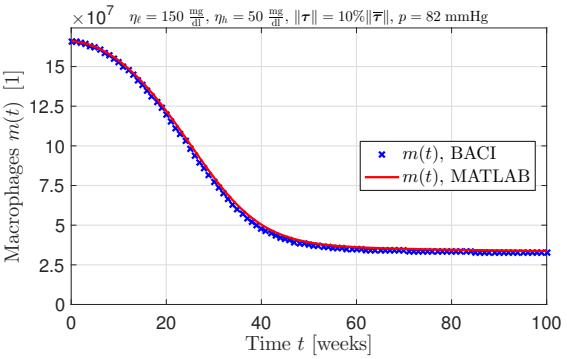

(f) Density of macrophages $m(t)$ relative to $[m'_{\text{Min}}, m'_{\text{Max}}]$ over time t.

Figure 6.9 Comparison of concentrations of native and modified LDL, HDL, intracellular free and esterified cholesterol per macrophage and macrophages over time t computed with MATLAB and BACI as described in Section 6.2.5. Parameters from Tables 5.7 and 6.3, $\eta_\ell = 150\ \frac{\text{mg}}{\text{dl}}$, $\eta_h = 50\ \frac{\text{mg}}{\text{dl}}$, $\|\boldsymbol{\tau}\| = 10\%\|\overline{\boldsymbol{\tau}}\|$ and $p = 82$ mmHg.

Table 6.5 Mean concentrations of native LDL $\overline{\ell}$, modified LDL $\overline{\tilde{\ell}}$, native HDL $\overline{h}$, intercellular free cholesterol $\frac{\overline{f}}{\overline{m}}$, intercellular cholesterol ester $\frac{\overline{f}}{\overline{m}}$ and macrophages $\overline{m}$ and their centers of mass $\overline{X}_{\overline{i}}$ for varying effective diffusivities $D_{\mathrm{Eff},\ell}$ ($= D_{\mathrm{Eff},\tilde{\ell}} = \frac{1}{2.33} D_{\mathrm{Eff},h}$) and hindrance coefficients K_ℓ ($= K_{\tilde{\ell}} = \frac{1}{5.36} K_h$) of native LDL at time $t = 100$ weeks. Parameters from Tables 5.7 and 6.3 and $\eta_\ell = 150\ \frac{\mathrm{mg}}{\mathrm{dl}}$, $\eta_h = 50\ \frac{\mathrm{mg}}{\mathrm{dl}}$ and homogeneous WSS $\|\boldsymbol{\tau}\| = 10\,\%\|\overline{\boldsymbol{\tau}}\|$.

Parameter setup		Mean concentration $\left[\frac{1}{\mathrm{mm}^3}\right]$ or [1]						Center of mass [%] *						Plot
$\frac{1}{1.26} \cdot D_{\mathrm{Eff},\ell}$	K_ℓ	$10^{-6} \cdot \overline{\ell}$	$10^{-7} \cdot \overline{\tilde{\ell}}$	$10^{-7} \cdot \overline{h}$	$10^{-10} \cdot \frac{\overline{f}}{\overline{m}}$	$10^{-11} \cdot \frac{\overline{b}}{\overline{m}}$	$10^{-7} \cdot \overline{m}$	$\overline{X}_{\overline{\ell}}$	$\overline{X}_{\overline{\tilde{\ell}}}$	$\overline{X}_{\overline{h}}$	$\overline{X}_{\frac{\overline{f}}{\overline{m}}}$	$\overline{X}_{\frac{\overline{b}}{\overline{m}}}$	$\overline{X}_{\overline{m}}$	
10^2	0.12 **	3.02	10.41	10.43	6.46	2.33	3.37	50	50	50	50	50	50	Fig. 6.9
10^0	0.12 **	2.67	9.73	9.07	6.15	1.77	3.41	41.3	50.9	40.8	51.4	54.0	48.5	–
10^{-1}	0.12 **	2.66	9.90	9.04	6.27	2.18	3.27	18.6	48.9	17.9	51.3	54.1	48.4	–
10^{-2} **	0	2.58	8.83	8.78	6.39	2.75	3.19	5.51	37.2	5.32	51.3	54.1	48.3	–
10^{-2} **	0.12 **	2.58	8.84	8.78	6.39	2.75	3.19	5.52	37.3	5.33	51.3	54.1	48.3	Fig. 6.10
10^{-2} **	1	2.58	8.94	8.79	6.39	2.75	3.19	5.55	38.1	5.33	51.3	54.1	48.3	Fig. 6.10
10^{-2} **	5	2.59	9.33	8.81	6.39	2.74	3.18	5.71	41.5	5.40	51.3	54.1	48.3	Fig. 6.10
10^{-2} **	25	2.67	9.70	9.04	6.39	2.72	3.11	6.63	55.6	5.79	51.3	54.1	48.3	Fig. 6.10

* $0\,\%$ and $100\,\%$ correspond to the endothelium and media-adventitia boundary, respectively.
** Corresponds to the physiological parameter from Table 6.3.

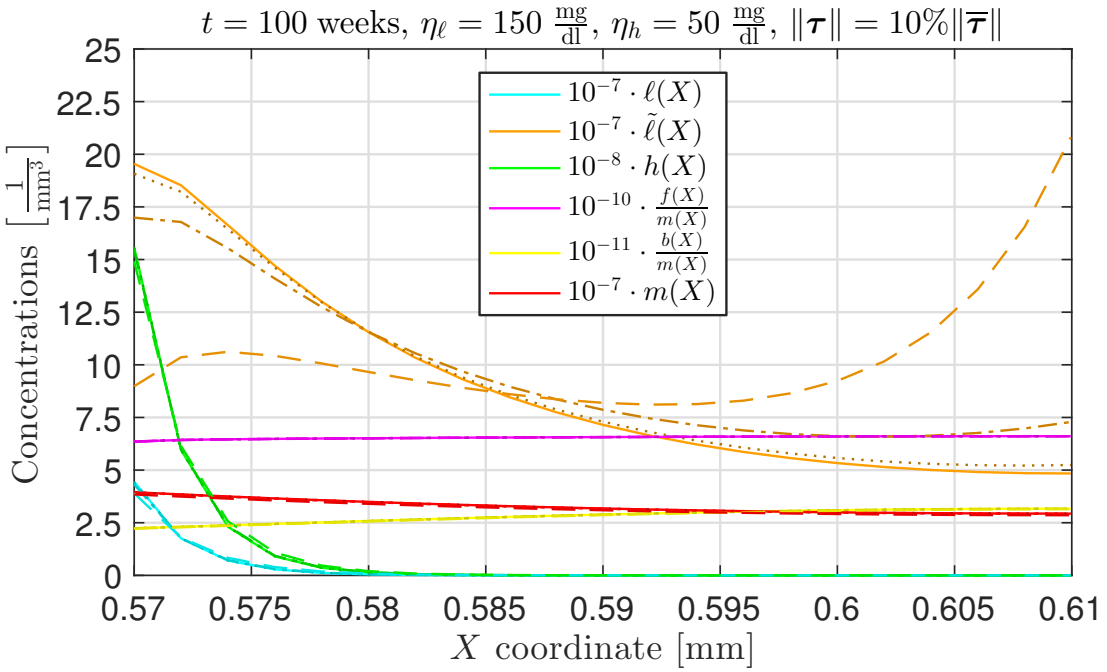

Figure 6.10 Concentration profiles of native LDL ℓ, modified LDL $\tilde{\ell}$, native HDL h, intercellular free cholesterol $\frac{f}{m}$, intercellular cholesterol ester $\frac{b}{m}$ and macrophages m at time $t = 100$ weeks plotted over the X-axis. Parameters from Tables 5.7 and 6.3 and $\eta_\ell = 150\ \frac{\mathrm{mg}}{\mathrm{dl}}$, $\eta_h = 50\ \frac{\mathrm{mg}}{\mathrm{dl}}$, homogeneous WSS $\|\boldsymbol{\tau}\| = 10\,\%\|\overline{\boldsymbol{\tau}}\|$ and $K_\ell = 0.12$ (solid lines), $K_\ell = 1$ (dotted lines), $K_\ell = 5$ (dash-dotted lines) or $K_\ell = 25$ (dash lines) ($K_{\tilde{\ell}} = K_\ell$, $K_h = 5.36 K_\ell$).

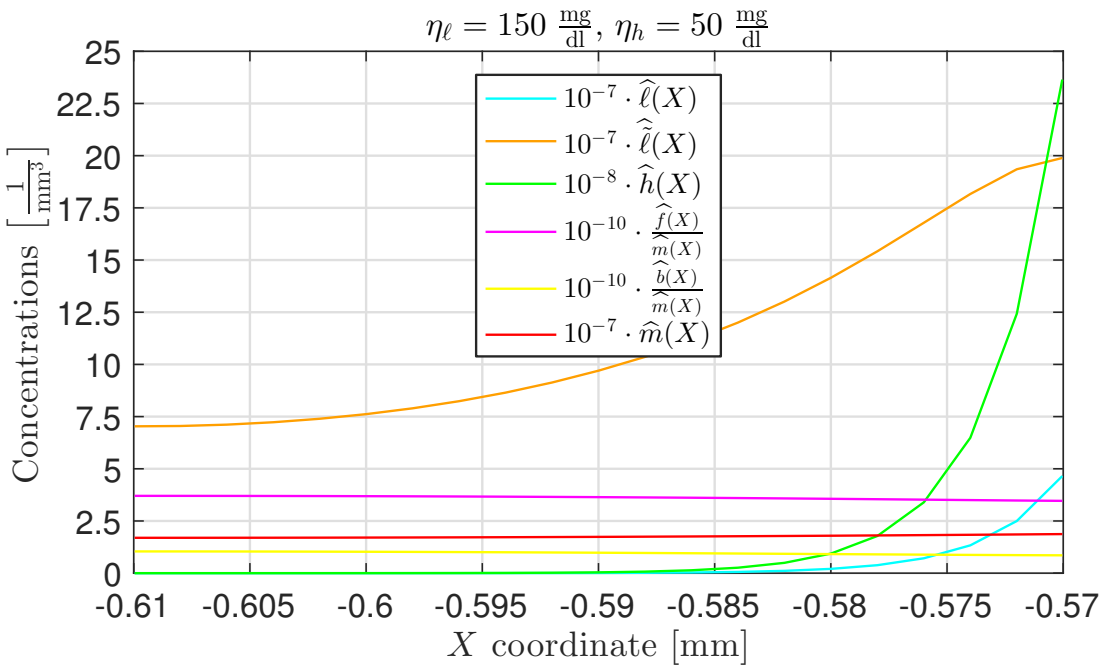

(a) Steady-state concentration profiles of species over the negative X-axis.

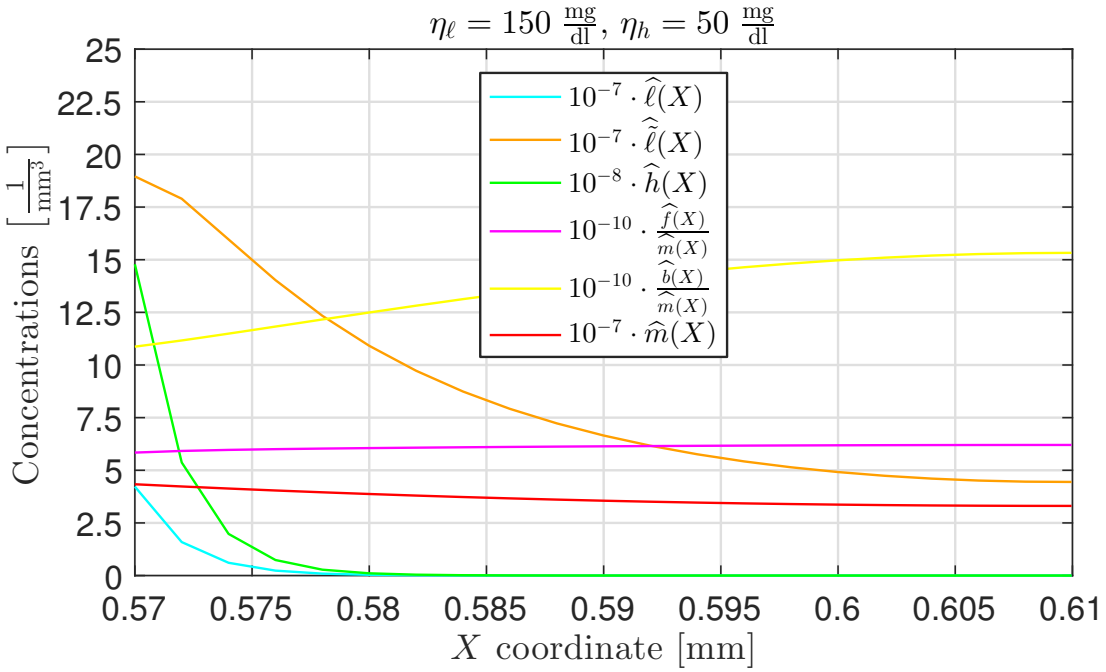

(b) Steady-state concentration profiles of species over the positive X-axis.

Figure 6.11 Steady-state concentration profiles of native LDL $\widehat{\ell}$, modified LDL $\widehat{\tilde{\ell}}$, native HDL $\widehat{h}$, intercellular free cholesterol $\frac{\widehat{f}}{\widehat{m}}$, intercellular cholesterol ester $\frac{\widehat{b}}{\widehat{m}}$ and macrophages $\widehat{m}$ plotted over the positive and negative X-axis. Parameters from Tables 5.7 and 6.3 and $\eta_\ell = 150\ \frac{\text{mg}}{\text{dl}}$, $\eta_h = 50\ \frac{\text{mg}}{\text{dl}}$ and non-homogeneous WSS $\|\boldsymbol{\tau}\|(\boldsymbol{x})$ as given by Equation (6.32).

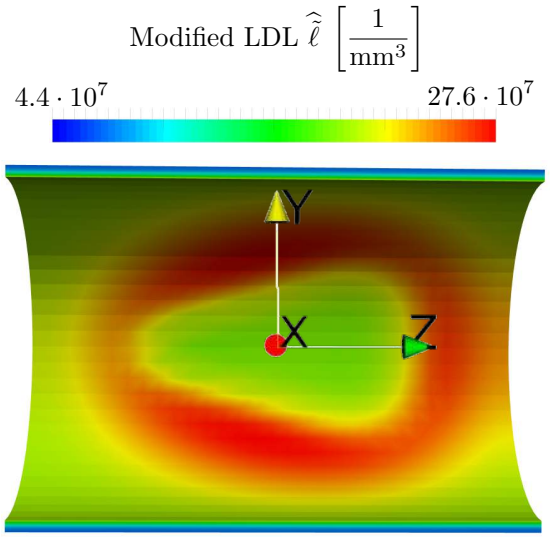

(a) Spatial distribution of steady-state concentration of modified LDL $\widehat{\widetilde{\ell}}$.

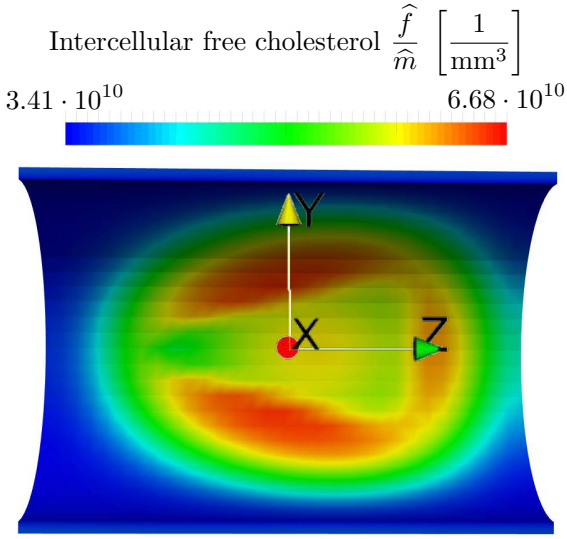

(b) Spatial distribution of steady-state concentration of intercellular free cholesterol $\frac{\widehat{f}}{\widehat{m}}$.

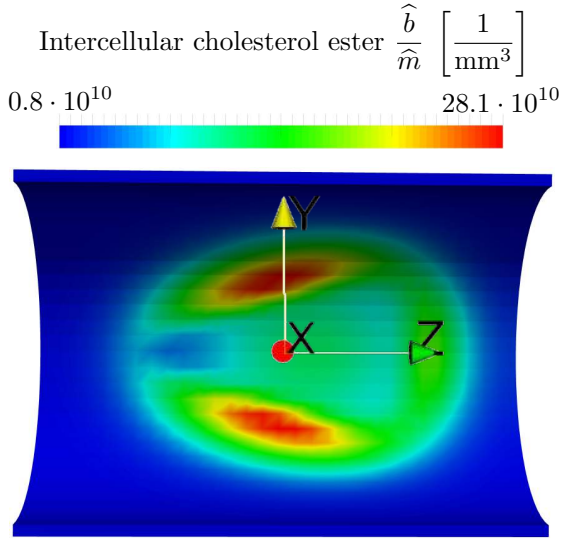

(c) Spatial distribution of steady-state concentration of intercellular cholesterol ester $\frac{\widehat{b}}{\widehat{m}}$.

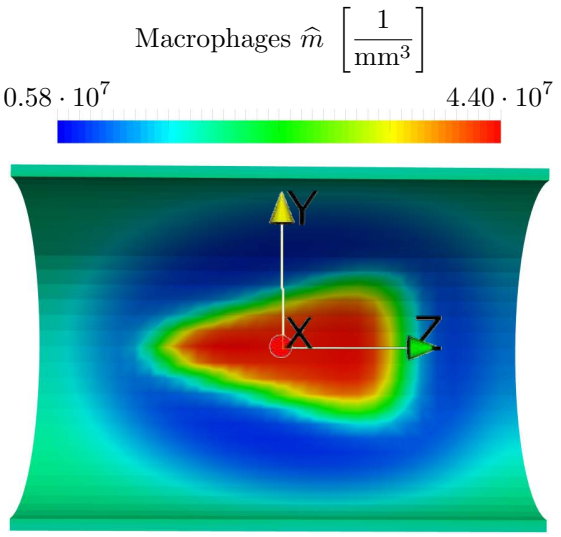

(d) Spatial distribution of steady-state density of macrophages $\widehat{m}$.

Figure 6.12 Spatial distributions of steady-state concentration of modified LDL $\widehat{\widetilde{\ell}}$, intercellular free cholesterol $\frac{\widehat{f}}{\widehat{m}}$, intercellular cholesterol ester $\frac{\widehat{b}}{\widehat{m}}$ and macrophages $\widehat{m}$. Parameters from Tables 5.7 and 6.3 and $\eta_\ell = 150\ \frac{\mathrm{mg}}{\mathrm{dl}}$, $\eta_h = 50\ \frac{\mathrm{mg}}{\mathrm{dl}}$ and non-homogeneous WSS $\|\boldsymbol{\tau}\|(\boldsymbol{x})$ as given by Equation (6.32).

The steady-state concentration profiles of the species $\hat{\ell}(X), \ldots, \hat{m}(X)$ of the PFSTI model with prescribed inhomogeneous WSS given by Equation (6.32) along the negative and positive X-axis are visualized in Figure 6.11. Further, the spatial distributions of the steady-state concentrations of modified LDL $\widehat{\tilde{\ell}}$, intercellular free cholesterol $\frac{\widehat{f}}{\widehat{m}}$, intercellular cholesterol ester $\frac{\widehat{b}}{\widehat{m}}$ and macrophages $\widehat{m}$ at the endothelial boundary $\Gamma_{\mathrm{End}}^{\mathcal{PS}}$ are shown in Figure 6.12.

6.4 Discussion

A parameterized mathematical and computational model of key species of early atherosclerosis was developed. To this end, a mathematical model of the adherence of monocytes on modified LDL-activated endothelial cells *in vitro* was developed and its parameters were estimated by least-squares fitting to experimental results in [141]. The fitted submodel thereby shows very good agreement with experimental data, see Figure 6.2(a). The remaining parameters of the model of key species were specified either by further least-squares fits, estimates based on experimental data or were taken from the literature such that a complete parameter set was obtained.

The parameters of the complete set given by Tables 5.7 and 6.3 are subject to uncertainties arising from various sources. The performed sensitivity analysis of the extended combined model reveals that variations of the filtration reflection coefficients of LDL $\sigma_{\mathrm{F},\ell}$ and HDL $\sigma_{\mathrm{F},h}$ have by far the largest influence to the computational results, see Figure 6.5. While the impact of the filtration reflection coefficient of HDL $\sigma_{\mathrm{F},h}$ is moderate, the effect of $\sigma_{\mathrm{F},\ell}$ is severe even though the literature in general agrees on $\sigma_{\mathrm{F},\ell} \approx 9.97 \cdot 10^{-1}$ [1, 146, 221, 255, 294]. Still, both parameters $\sigma_{\mathrm{F},\ell}$ and $\sigma_{\mathrm{F},h}$ require further attention, especially by experimental communities.

In addition, the recruitment of monocytes *in vivo* requires a special focus in future experimental work. As only very few experimental results exist that consider non-constant flow patterns to assess the influence of complex flows to the endothelium [127], determining a truly valid measure for the local influence of the pulsatile blood flow is currently impossible. Here, the WSS $\|\boldsymbol{\tau}\|$ were employed as indicator for disturbed blood flow [154, 216]. In addition, the specific law for the recruitment of macrophages was derived from experimental results investigating the adherence of monocytes. However, no quantitative data exist that allow estimating the actual rate of monocyte *recruitment* into the intima.

Three laws based on the equations of *Kedem* and *Katchalsky* were developed and parameterized to assess the fluxes of native LDL r_ℓ, modified LDL $r_{\tilde{\ell}}$ and native HDL r_h through the endothelium. The total fluxes are subdivided into diffusive and advective parts which vary depending on the WSS $\|\boldsymbol{\tau}\|$ due to the PSF and CSF, cf. Figure 6.3. As a consequence, the total fluxes and the fractions of the advective fluxes of native LDL, modified LDL and native HDL differ depending on the WSS, see Figure 6.6.

As apparent from Figures 6.6(b), 6.6(d) and 6.6(f), there is great difference in the importance of the advective fluxes with respect to the different lipoproteins. While the total outflux of modified LDL $r_{\tilde{\ell}}$ is hardly counterbalanced by its advective influx, the advective influx of HDL dominates the total influx of native HDL r_h for all relevant WSS and medial pressure regions. The picture of the advective influx of native LDL is ambiguous as it is dominant for low WSS regimes but

minor for high WSS. In total, however, the results indicate that the advective flux of lipoproteins through the endothelium is in general *not* negligible.

Due to their smaller particle size, the amount of penetrating native HDL is – depending on the WSS and subendothelial pressure – approximately 10 to 25 times larger compared to native LDL, see Figures 6.6(a) and 6.6(e). A large concentration of modified LDL $\tilde{\ell} = 7.2 \cdot 10^{-4}\eta_\ell$ was assumed to assess the outflux of modified LDL. Still, the outflux of modified LDL is negligible as it is more than three magnitudes smaller compared to the influx of native LDL and HDL, cf. Figure 6.6(c). Furthermore, it is important to note that the influx of native HDL increases with increasing WSS while the influx of native LDL decreases. Together with a decreasing recruitment of macrophages under high WSS, see Figure 6.7, all three external markers of the combined model (i.e., the constant recruitment rates r_ℓ, r_h and r_m, cf. Section 5.1.2) turn from the tendency of an unbounded (unstable) plaque toward a bounded (stable) plaque with increasing WSS, cf. Figure 5.10. This observation explains the great importance of the local blood flow condition to the onset of atherosclerosis. Thus, the results indicate that the WSS and therefore the location of plaques within the cardiovascular system decisively determine the type of early plaques, i.e., if they are progression-prone (type IIa) or progression-resistant (type IIb), cf. Table 1.1.

Besides the flow-dependent and thus non-modifiable WSS, the cholesterol concentrations of LDL η_ℓ and HDL η_h play an important role in atherogenesis. Depending on the physiology and diet of a plaque's host, they vary by several orders of magnitude (cf. Table 6.4) and induce qualitatively different long-term outcomes of model plaques. The stability analysis of the extended combined model shows that the most crucial determinant of the stability are the WSS $\|\boldsymbol{\tau}\|$ followed by the blood cholesterol concentration of HDL η_h, see Figure 6.8. Solely high blood cholesterol concentrations of LDL η_ℓ significantly influence the long term outcome. However, such LDL cholesterol concentrations do not occur naturally but must be enforced, e.g., by putting genetically modified mice on a high-fat diet. The observations from the stability analysis indicate that the natural resistance of mice against atherosclerosis might be due to their in general high HDL and low LDL blood cholesterol profiles [167]. For the common range of blood cholesterol concentrations in humans [205], plaques at locations with a WSS exposure below approximately $\|\boldsymbol{\tau}\| = 20\,\%\|\overline{\boldsymbol{\tau}}\| = 0.2$ Pa must be considered as progression-prone plaques, i.e., as plaques of type IIa [249].

Based on the assumption of a purely pressure gradient-driven transmural flow, *Darcy*'s law in combination with the first *Kedem-Katchalsky* equation was used to develop a model of the blood plasma pressure and transmural flow in the artery wall. In average, a transmural filtration velocity of $\|\boldsymbol{u}^{\mathcal{PF}}\| = 6.47 \cdot 10^{-2}\ \frac{\mathrm{mm}}{\mathrm{h}}$ is estimated which is in perfect agreement with experimental and computational results in the literature [85, 195, 221, 294]. Using this average velocity value, the *Reynolds* number Re of the transmural filtration flow is calculated to

$$Re = \frac{\varrho^{\mathcal{PF}}\|\boldsymbol{u}^{\mathcal{PF}}\|H}{\mu^{\mathcal{PF}}} = 1.05 \cdot 10^{-6}. \tag{6.35}$$

As the *Reynolds* number is $Re \ll 1$, the application of *Darcy*'s law results in a good approximation to the viscous transmural flow within aortic tissue [14, 85, 164]. Using *Darcy*'s law, an intima-media pressure drop of $\Delta p^{\mathcal{PF}}_{\mathrm{Med}} = 52.4\ \mathrm{mmHg} = 7.0 \cdot 10^3\ \mathrm{Pa}$ is estimated which is in very good agreement to experimental results in [262].

Crucial parameters that were not covered by the performed sensitivity analysis of the extended combined model are the effective diffusivity of native LDL $D_{\text{Eff},\ell}$ and the arising diffusivities of modified LDL $D_{\text{Eff},\tilde{\ell}} = D_{\text{Eff},\ell}$ and native HDL $D_{\text{Eff},h} = 2.33 D_{\text{Eff},\ell}$. No agreement on the value of $D_{\text{Eff},\ell}$ exists in the literature, where almost all orders of magnitude in between $D_{\text{Eff},\ell} = 1.2 \cdot 10^{2} \ \frac{\text{mm}^2}{\text{h}}$ [90] and $D_{\text{Eff},\ell} = 1.8 \cdot 10^{-4} \ \frac{\text{mm}^2}{\text{h}}$ [294] are found. Based on an extensive literature review, in this thesis a frequently found intermediate value $D_{\text{Eff},\ell} = 1.26 \cdot 10^{-2} \ \frac{\text{mm}^2}{\text{h}}$ [29, 255, 267] is utilized. As apparent from the comparison with the results of the non-spatial extended combined model (cf. Figure 6.9), effective diffusion coefficients in the order of magnitude of $D_{\text{Eff},i} = \mathcal{O}(10^2 \frac{\text{mm}^2}{\text{h}})$ result in concentration profiles without spatial variations. With decreasing diffusion coefficients, the concentrations of lipoproteins along the radial direction change from homogeneous concentrations to concentration profiles with steep gradients at the endothelium, see Table 6.5 and Figure 6.10. In contrast, the density of macrophages and their intercellular free and esterified cholesterol contents remain rather homogeneously distributed along the radial direction. Even though the centers of mass shift by the reduction of the diffusivities, the average concentrations of all species $\overline{\ell}, \overline{\tilde{\ell}}, \overline{h}, \overline{f}, \overline{b}, \overline{m}$ are solely little affected by the reduction of the diffusivities ($< 18\,\%$). Thus, the extended combinded model is a valid simplification compared to the PFSTI model when it comes to the analysis of non-spatial phenomena.

The variation of the hindrance coefficients $K_\ell, K_{\tilde{\ell}}$ and K_h reveals that no species is significantly affected ($< 10\,\%$) by the advective transport with the transmural flow within the artery wall, see Table 6.5 and Figure 6.10. Even if the advective transport of lipoproteins is increased by using high hindrance coefficients, solely the concentration profile of modified LDL is significantly altered, whereas the profiles of the remaining species are barely affected. As hindrance coefficients are in general $0 \leq K_i \leq 1$, such fast advective transports are only achieved by an approximately 100 times higher transmural velocity of $\|\boldsymbol{u}^{\mathcal{PF}}\|$, which is far beyond velocities reported in the literature. The advective transport can thus not explain the increase of the LDL profile toward the media-adventitia boundary as observable *in vivo* [19, 54, 195, 268] and the driving mechanism behind remains unknown. In total, the computational results indicate that in case of homogeneous boundary conditions, the effect of diffusion is minor while the influence of the advective transport with the transmural flow within the artery wall is negligible. Still, the model of the transmural flow cannot completely be neglected as it determines the subendothelial pressure $p^{\mathcal{PF}}$ and thus significantly alters the total lipoprotein fluxes $r_\ell, r_{\tilde{\ell}}$ and r_h, see Figure 6.6.

Important spatial phenomena occur when considering inhomogeneous boundary conditions, see Figures 6.11 and 6.12. The steady-state concentration profiles of the PFSTI model with prescribed inhomogeneous WSS pattern (cf. Figure 6.4) along the radial directions are qualitatively different. The negative X-axis corresponds to a region exposed to high WSS $\|\boldsymbol{\tau}\| = \|\overline{\boldsymbol{\tau}}\|$ and thus the atherosclerotic process remains non-critical: the long-term equilibrium concentrations are characterized by moderate modified LDL $\widehat{\overline{\ell}}$, low macrophages $\widehat{m}$ with low intracellular free cholesterol $\frac{\widehat{f}}{\widehat{m}}$ and almost no intracellular cholesterol ester $\frac{\widehat{b}}{\widehat{m}}$, cf. Figure 6.11(a). The negative X-axis corresponds to a region exposed to low WSS $\|\boldsymbol{\tau}\| = 10\,\%\|\overline{\boldsymbol{\tau}}\|$. As a consequence, along the negative X-axis qualitatively similar results as in Figures 6.8(b), 6.8(f), 6.8(j), 6.9 and 6.10 are found. It is important to note, however, that the concentration of intracellular cholesterol ester $\widehat{b}$ remains bounded in the case of inhomogeneous WSS which is not the case for homogeneous boundary conditions. The reason for this arising boundedness of *all* species lies in the diffusion

of the species which blurs the strongly atherosclerotic regions with the surrounding virtually non-atherosclerotic regions. By the smearing of the atherosclerotic region, the area of the plaque drastically increases compared to the area of low WSS (cf. Figures 6.4 and 6.12), whereby the surrounding region next to the low WSS is drawn into an even worse condition than the central plaque region, see Figure 6.12. Another effect of the diffusion-driven smearing is that macrophages are capable to preserve a stable concentration of detrimental modified LDL $\widehat{\widetilde{\ell}}$ comparable to non-atherosclerotic sites, see Figure 6.12(a). However, this comes by the cost of an increased concentration of intracellular free cholesterol $\frac{\widehat{f}}{\widehat{m}}$ and cholesterol ester $\frac{\widehat{b}}{\widehat{m}}$ within macrophages rendering their own state toward apoptotic and necrotic foam cells. Hence, plaques at the low WSS region *and* their surrounding must be considered progression-prone, i.e., as type IIa in the classification by the *American Heart Association* given in Table 1.1.

The developed PFSTI model of key species of early atherosclerosis is able to assess the stability of an early plaque based on the blood cholesterol concentrations of LDL and HDL and the WSS it is exposed to. As discussed in detail in Section 5.4, the model of macrophages must be enriched by their fates of emigration, proliferation and necrosis in order to assess intermediate and advanced plaques. Further, solely a simplified geometrical setup was investigated, where an artificial WSS distribution was prescribed. To consider patient-specific anatomies, the PFSTI model can be embedded into the multiphysics model from Chapter 4 within a suitable multiscale in time strategy, e.g., as described in the subsequent Chapter 7. Within the multiphysics model, the PFSTI model can replace the previously employed simplistic reaction model of the inflammatory and immunological processes, see Section 4.4. Within a patient-specific setup, the time-averaged WSS and luminal pressure from a pulsatile fluid or fluid-structure interaction simulation can be used to achieve locally varying physiological lipoprotein fluxes and macrophage recruitments. To consider the back-coupling to the short time scale due to growth and remodeling of the artery wall, the PFSTI model must be slightly adapted to respect the deforming porous media structure.

6.5 Short summary

This chapter is concerned with the development of a quantified spatially resolved mathematical model of key species of early atherosclerosis and a classification of the stability of early model plaques. Based on basic continuum mechanical principles, a novel model is established that brings together *Darcy*'s law, the previous chapter's combined model as well as submodels of the recruitment of macrophages and fluxes of lipoproteins that were parameterized using existing experimental results.

The model of key species allows to assess a local differentiation of progression-prone and progression-resistant plaques based on three measurable or computable *in vivo* inputs – the WSS a plaque is exposed to and blood cholesterol concentrations of LDL and HDL. An analysis of the model's parameters indicates that the impact of the transmural flow in the artery wall is ambiguous. While the advective flux of lipoproteins through the activated endothelium is decisive, the influence of the advective transport within the artery wall is negligible. Further, the model suggests that regions within cardiovascular systems with an approximate WSS exposure below

20 % below the average WSS as well as their surroundings must be considered as potential regions of progression-prone atherosclerotic plaques.

7 Overall summary and outlook

In this section, the main results of this thesis are briefly recapitulated and an outlook on remaining and possible future work is given.

7.1 Summary of results

In this thesis, various novel mathematical and computational models were developed and parameterized to assess crucial mechanobiological, inflammatory and immunological processes *in silico* that lead to the formation of atherosclerotic plaques and that drive their early stages. The successive modeling, quantification and analysis deepen the understanding of key biological mechanisms as described in the following summary.

As a first step, a mathematical and computational multiphysics fluid-structure-scalar-transport interaction model for atherosclerosis was derived based on basic continuum mechanical principles, and a subsequent discretization in terms of the finite element method and the one-step-θ scheme. The multiphysics model incorporates major processes of all time scales of the disease, such as cardiovascular mechanics including the interaction of blood and artery wall, transport of LDL to and through the endothelium, inflammatory and immunological processes as well as growth and remodeling of the artery wall. The interlacement of the different time scales of atherosclerosis is thereby respected such that the short time scale cardiovascular mechanics dynamically adjusts to changes occurring in the long time scale and *vice versa*. Using the multiphysics model, the importance of the interdependencies of the time scales and the influence of patient-specific anatomies to the atherosclerotic process was assessed. The model was therefore calibrated to an exemplary physiological data set and a murine-specific geometry of the aortic arch such that it reproduced important cardiovascular quantities, such as blood pressure, radial displacements, and wall shear stresses. A methodology for the WSS-dependent up- and downscaling of the endothelial permeability with respect to lipoproteins was developed and proved to be a qualitative indicator for potential sites of atherosclerotic plaque formation. The analysis of the interlacement of the different time scales in the multiphysics model further corroborates the theory that neglecting the short time scale of cardiovascular mechanics, e.g., by time-averaging flows or neglecting the deformation of the artery wall, is misleading in the context of atherosclerosis. Thus, the short time scale of atherosclerosis is indispensable and must therefore be considered in future modeling approaches. As the separation of the time and space scales of atherosclerosis follows the separation of its involved physics, the multiphysics model is an essential step toward multiscale models in time and space.

A quantification of crucial processes of the formation of early atherosclerotic plaques was addressed by a modeling approach similar to the biologists' experimental approach where the bigger picture of atherosclerosis is put together from many smaller observations and findings that are gained from *in vitro* experiments. To this end, several ODE submodels of crucial inflammatory and immunological processes, such as LDL modification and ingestion, HDL protection against LDL modification, cholesterol cycle within macrophages, reverse cholesterol transport from macrophages and macrophage apoptosis were developed. The submodels were parameterized by least-squares fits to existing experimental results from various *in vitro* studies. The fitted submodel closely reproduce the experimental results such that a complete physiological parameter set was found for key biological processes of early atherosclerosis. The submodels that are closely connected to *in vitro* studies build the basis for a quantified and predictive combined mathematical model of early atherosclerotic plaque formation which reuses the physiological parameter set determined by the submodels. A sensitivity analysis of the data-driven combined model suggests that further experimental work quantifying the different fates of macrophages as functions of their cholesterol load, and the balance between intracellular free cholesterol and cholesterol ester may add valuable insight toward predicting long-term plaque outcomes *in vivo*. Moreover, the combined model was used to classify the stability of early model plaques with respect to prescribed rates of recruitment of LDL, HDL and macrophages. The results suggest that a persistent high supply of LDL and macrophages in combination with a lack of HDL *in vivo* render early atherosclerotic plaques progression-prone. Due to its experiment-based derivation and parameterization, the combined model is an important step toward models applicable in a clinical setting.

The stability of early plaques was further addressed by a quantified spatially resolved mathematical and computational model of key species of early atherosclerosis. The model therefore incorporates major spatial aspects of the long time scale of atherosclerosis, such as penetration of macrophages and lipoproteins through the inflammation- and WSS-activated endothelium, transmural flow of blood plasma within the artery wall, transport of macrophages and lipoproteins within the artery wall as well as key inflammatory and immunological processes of early plaques. Based on basic continuum mechanical principles, the developed porous medium fluid-scalar transport interaction model of key species brings naturally together *Darcy*'s law, the combined model, and submodels of the recruitment of macrophages and fluxes of lipoproteins through the endothelium. Analog to the combined model, the submodels of the recruitment of macrophages and fluxes of lipoproteins were parameterized using various existing experimental results. A sensitivity analysis of the model with respect to uncertainties in the parameters recommends further experimental work quantifying the endothelial filtration reflection coefficients of lipoproteins. In addition, the results indicate that the impact of the transmural flow in the artery wall is ambiguous. While the advective flux of lipoproteins through the activated endothelium is decisive, the influence of the advective transport within the artery wall is negligible. Further, a characterization of progression-prone and progression-resistant early plaques based on three measurable or computable *in vivo* inputs – the WSS a plaque is exposed to and blood cholesterol concentrations of LDL and HDL – was achieved. The results indicate that under the common range of blood cholesterol concentrations in humans, regions within the cardiovascular system with an approximate WSS exposure below $1.3\ \mathrm{Pa}$ as well as their surroundings must be considered as potential regions of progression-prone atherosclerotic plaques. As the model of key species of early atherosclerosis allows to assess

the long-term outcome of early plaques based on measurable or computable *in vivo* inputs, it is a decisive step toward determining the stability properties and risks of early plaques within a clinical context.

7.2 Outlook on future work

Three outstanding computational and experimental aspects can be identified that require (further) attention in future research.

From a computational and application perspective, the biggest drawback of the developed multiphysics framework is its high computational cost which prevents the straightforward simulation of long time spans and thus the usage of a physiological model of the inflammatory and immunological processes of atherosclerosis. The developed multiphysics approach, however, naturally respects the separation of the time and space scales inherent with atherosclerosis (cf. Section 1.2.5). The multiphysics FSSTI model, together with the PFSTI model of key species, can therefore build the basis to resolve the problem of different time and space scales within a multiscale in time strategy based on works by *Figueroa et al.* [81], *Koshiba et al.* [152] and *Tomaso et al.* [267].

As the mechanical properties of artery walls are dominated by media and adventitia, the short time scale processes of the cardiovascular mechanics and the induced transport of lipoproteins with the pulsatile blood flow can be addressed by a one-way coupled FSSTI method coupling the quantified FSI (cf. Section 4.1.1) and fluid-scatra submodels (cf. Section 4.1.2.1). In contrast to the multiphysics model, the atherosclerotic processes within the artery wall must *not* be considered simultaneously as they take much more time compared to the duration of few cardiac cycles being in the order of magnitude of seconds. The short time scale must be solved until its periodic state induced by the pulsatile hemodynamics is reached. Subsequently, the PFSTI model can be exploited to compute the long time scale processes of the penetration and transport of species in the artery wall and the accompanied inflammatory and immunological processes. The transition from the short to the long time scale can be accomplished by computing the time-average of all quantities relevant to the large time scale, such as the local time-averaged WSS $<\boldsymbol{\tau}^{\mathcal{F}}>$, blood pressure $<p^{\mathcal{F}}>$, blood LDL concentration $<\ell^{\mathcal{FS}}>$ and blood HDL concentration $<h^{\mathcal{FS}}>$. In addition to the time-averaging, the transmural flow (without osmotic volume flux) within the artery wall (cf. Section 6.1.2.1) can be precomputed prior to the simulation of the long time scale. The quantified poro-scatra submodel (cf. Section 6.1.2.2) can be employed to predict the formation of early plaques taking place on the long time scale being in the order of magnitude of weeks. The long time scale poro-scatra part can be solved as long as the condition of the plaque's host does not significantly change and as long it can be assumed that the relevant time-averaged small time scale quantities are not drastically altered by the back-coupling from the long time scale. As the loss of concentrations within the blood due to the penetration of lipoproteins is negligible compared to the replenishment by the blood flow [247], the most relevant back-coupling from the large time scale is due to growth and remodeling of the artery wall.

The growth and remodeling induced by the accumulation of foam cells can be considered by using the developed laws for the anisotropic growth and remodeling (cf. Sections 4.1.1.4 and 4.1.1.5),

where solely the growth factor and remodeling factor have to be adapted to match the employed poro-scatra part. To this end, it can be assumed that the volume occupied by the macrophage population $m^{\mathcal{PS}}$ is proportional to their (average) intracellular free and esterified cholesterols contents $\frac{f^{\mathcal{PS}}}{m^{\mathcal{PS}}}$ and $\frac{b^{\mathcal{PS}}}{m^{\mathcal{PS}}}$, respectively. Doing so, the growth factor ϑ and remodeling factor λ read

$$\begin{aligned} \vartheta &= \vartheta(f^{\mathcal{PS}}, b^{\mathcal{PS}}) = 1 + \left(\alpha_f \frac{f^{\mathcal{PS}}}{m^{\mathcal{PS}}} + \alpha_b \frac{b^{\mathcal{PS}}}{m^{\mathcal{PS}}} \right) J^{\mathcal{S}} m^{\mathcal{PS}} = 1 + \alpha_f J^{\mathcal{S}} f^{\mathcal{PS}} + \alpha_b J^{\mathcal{S}} b^{\mathcal{PS}}, \\ \lambda &= \lambda(f^{\mathcal{PS}}, b^{\mathcal{PS}}) = \frac{1}{\vartheta(f^{\mathcal{PS}}, b^{\mathcal{PS}})}, \end{aligned} \tag{7.1}$$

where α_f and α_b are the respective proportionality constants. Identifying them with the volume of free and esterified cholesterol molecules, they are estimated to $\alpha_f = 6.55 \cdot 10^{-19}\ \mathrm{mm}^3$ and $\alpha_b = 1.14 \cdot 10^{-18}\ \mathrm{mm}^3$ by using V_f, V_b and N_{A} from Table 5.1. As the growth factor ϑ is associated to the local relative increase of volume, the supremum norm $\|\vartheta - 1\|_\infty = \|\alpha_f J^{\mathcal{S}} f^{\mathcal{PS}} + \alpha_b J^{\mathcal{S}} b^{\mathcal{PS}}\|_\infty$ can be used to determine the end of the validity of the long time scale simulation, i.e., if the cardiovascular mechanics is significantly altered due to local growth and remodeling induced by the accumulation of intracellular cholesterols. The transition from long to short time scale involves to reestablish the equilibrium between all involved physics. This can be done in a sequentially staggered partitioned manner where the growth is applied to the structure submodel within the short time scale FSSTI part and the concentrations are reduced within the long time scale poro-scatra part to assure mass conservation.

Summarizing, it is proposed to utilize a partioned two-way coupled scheme as multiscale in time strategy for atherosclerosis which couples one-way coupled FSSTI and PFSTI models based on the models developed in this thesis. A schematic overview of the suggested multiscale in time strategy including the corresponding coupling variables is given in Figure 7.1. It is important to note, however, that the back-coupling of the long to short time scale by growth and remodeling is solely necessary when investigating the long-term progression of atherosclerosis. If focus lies on the onset of atherosclerotic plaques, a one-way coupled multiscale in time strategy which neglects the growth and remodeling of the artery wall is sufficient too.

The time scale separation in atherosclerosis into short and long time scale is accompanied by the separation of space scales. To assess the large space (and short time) scale FSSTI part a considerable part of the lumen and its adjacent entire artery wall must be considered and thus rather coarse finite element meshes corresponding to the "organ level" size are employed (cf. Section 4.2.2). In contrast, the small space (and long time) scale PFSTI part requires to resolve the intima and media with sufficient accuracy, especially in the radial directions. Therefore, fine finite element meshes corresponding to the intima-media thickness are required to resolve the steep concentration gradients (cf. Section 6.2.5). To simultaneously respect phenomena occurring at different space scales, an appropriate multiscale in space approach must be taken. A simple but convenient approach would be to use interpolation or projection methods, such as volumetric collocation or mortar approaches as, e.g., discussed in the publications by *Farah et al.* [74] or *Krause* and *Zulian* [153]. Such methods have the advantage that spatial effects within both space scales can be fully respected and that the individual implementations of the FSSTI and PFSTI parts must not be interlaced but solely the transfer of exchanged quantities

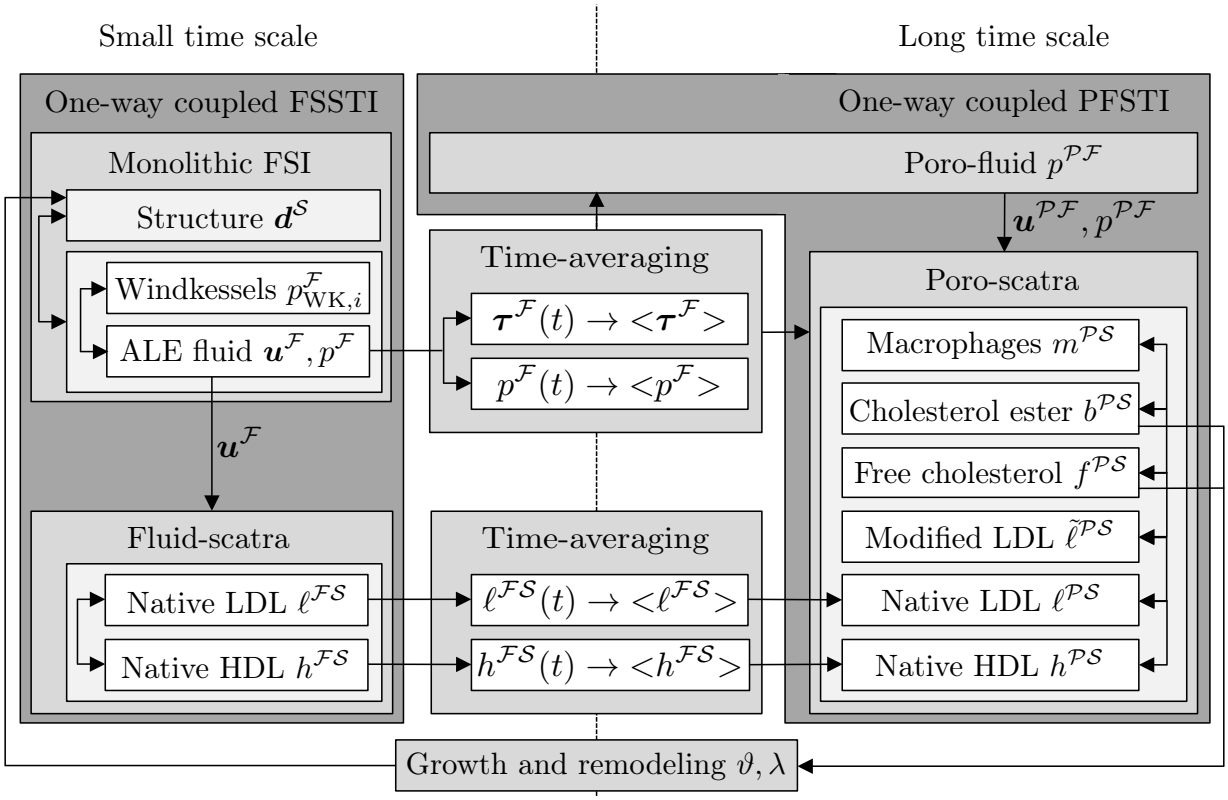

Figure 7.1 Overview of proposed multiscale in time strategy inlcuding the primary unknowns of each model and coupling variables.

must be adapted. However, as the neglection of spatial effects within the artery wall did not drastically alter the space-averaged concentrations, an alternative approach would be to utilize space-averaging methods, such as the *FE*^{2} *method* [71, 79, 92]. The poro-scatra model could therefore be space-averaged to ODE models (cf. the extended combined model in Appendix B) which have to be solved solely on the endothelium boundary. However, such averaging approaches come with the inherent drawback of inducing a uniformly growing artery wall along the radial directions and thus do not allow investigating complex growth related phenomena, such as the *Glagov* remodeling [84, 101, 113, 136, 168].

After having achieved an appropriate multiscale model (in time and space) of early atherosclerosis, the second main issue can be addressed. It remains to quantitatively validate the developed PSF based on multiple experimental *in vivo* data sets. Therefore, *in vivo* plaque locations could be imaged and compared to predicted atherosclerosis-prone regions by the multiscale model in terms of suitable metrics, e.g., similar to the methodology given by *de Wilde et al.* [59]. The chosen approach in this thesis of investigating murine aortic arches has several murine specific advantages (cf. Section 1.1.8). However, the imaging and localization of plaques *in vivo* yet remains a challenge [167]. It could therefore be expedient to switch from a study of *in vivo* murine aortic arches to human carotids which can be assessed in a clinical context using high-resolution ultrasonography [107, 219].

The final outstanding issue for future research must be addressed by experimental biologists. Only little data exist that allow assessing the fates of macrophages [180, 220, 228, 296]. Besides the experiments by *Yao et al.* [296] which were used to quantify macrophage apoptosis (based on solely two data points), the remaining fates, namely macrophage emigration, proliferation and necrosis can yet not be quantified based on experimental results. Thus, it is crucial that biologists further address the fate of macrophages in future experimental work. Once quantifiable experimental data are available, the experimental results can be used to enhance the developed (extended) combined model and model of key species by the additional fates of macrophages. Such enhanced models allow proceeding from the study of early plaques of type IIa or IIb according to the classification by the *American Heart Association* [249] to the investigation of intermediate atheroma of type III and IV.

The analog issue holds for the quantification of processes related to the role of smooth muscle cells in advanced plaques. The oxidative modification of native LDL as well as the ingestion of native and modified LDL by SMCs can be quantified by a straightforward extension of submodel $\boxed{1}$ (cf. Section 5.1.1.1) using the experimental results by *Henriksen et al.* [116], Fig. 7 and 8. However, their probably most important ability to move hapto- and chemotactically is currently not quantifiable from the available experimental data in the literature. As SMCs in general and their chemotaxation in particular are crucial for the formation of fibrous caps and thus the development of plaques of type Va and higher, their further experimental study and quantification is key to assess advanced plaques and their susceptibility to rupture.

The quantification of the various fates of macrophages and the role of SMCs, and their subsequent incorporation in the proposed multiscale model have the ability to significantly increase the knowledge of atherosclerosis and might help to reduce social and economic burdens arising from this burgeoning disease.

A Proof of Proposition 1

In the following Proposition 1 from Section 5.2.2 is proved. To prove the positivity of ℓ, i.e., $\ell(t) \geq 0 \; \forall t \geq 0$ it is sufficient to note that $\ell(0) = 0$ and that $\ell(t) = 0$ implies

$$\frac{\mathrm{d}}{\mathrm{d}t}\ell(t) \overset{(5.6)}{=} \frac{r_\ell}{H} > 0, \tag{A.1}$$

due to the strict positivity of the parameters. The positivities of h, m and $\tilde{\ell}$ are proved in an analog fashion. Since $\frac{f(0)}{m(0)} = f_0 \geq f_{\mathrm{Min}}$ and $\frac{f(t)}{m(t)} = f_{\mathrm{Min}}$ implies

$$\frac{\mathrm{d}}{\mathrm{d}t}\left(\frac{f(t)}{m(t)}\right) = \frac{\frac{\mathrm{d}}{\mathrm{d}t}f(t) - \frac{f(t)}{m(t)}\frac{\mathrm{d}}{\mathrm{d}t}m(t)}{m(t)} \overset{(5.6)}{\geq} \frac{\frac{r_m}{H}f_{\mathrm{In}} - f_{\mathrm{Min}}\frac{r_m}{H}}{m(t)} \geq 0, \tag{A.2}$$

it holds $\frac{f(t)}{m(t)} \geq f_{\mathrm{Min}} \; \forall t \geq 0$. This also implies the positivity of f. Given that $\frac{f(0)}{m(0)} = f_0 < f_{\mathrm{Max}}$ and that $\frac{f(t)}{m(t)} \to f_{\mathrm{Max}}$ implies

$$\frac{\mathrm{d}}{\mathrm{d}t}\left(\frac{f(t)}{m(t)}\right) = \frac{\frac{\mathrm{d}}{\mathrm{d}t}f(t) - \frac{f(t)}{m(t)}\frac{\mathrm{d}}{\mathrm{d}t}m(t)}{m(t)} \longrightarrow -\infty, \tag{A.3}$$

it follows $\frac{f(t)}{m(t)} \leq f_{\mathrm{Max}} \; \forall t \geq 0$. Hence, it is concluded that

$$\frac{f(t)}{m(t)} \in [f_{\mathrm{Min}}, f_{\mathrm{Max}}] \; \forall t \geq 0. \tag{A.4}$$

The positivity of b follows since $b(0) = 0$ and $b(t) = 0$ implies

$$\frac{\mathrm{d}}{\mathrm{d}t}b(t) \overset{(5.6)}{=} k_f \frac{\left(f(t) - f_{\mathrm{Min}}m\right)^2}{f_{\mathrm{Max}}m - f(t)} \overset{(A.4)}{\geq} 0 \tag{A.5}$$

which finishes the proof of (a). (It also follows that the time-dependent solution $(\ell(t), \tilde{\ell}(t), h(t), f(t), b(t), m(t)), t \geq 0$ of the initial value problem is unique and smooth because the smoothness of the right-hand side of the ODE (5.6) is now straightforward to show.)

Using (A.4)

$$\frac{\mathrm{d}}{\mathrm{d}t}m(t) \overset{(5.6),(A.4)}{\geq} -\underbrace{\mu_m \frac{\left(f_{\mathrm{Max}}\right)^{n_m}}{\left(\xi_m\right)^{n_m} + \left(f_{\mathrm{Max}}\right)^{n_m}}}_{=:z_{\mathrm{Max}}} m + \frac{r_m}{H} \tag{A.6}$$

holds, and by solving this ordinary differential inequality with associated initial condition $m(0) = m_0$ it follows

$$\begin{aligned} m(t) &\overset{(A.6)}{\geq} m_0 \exp\left(-z_{\mathrm{Max}} t\right) + \frac{r_m}{H z_{\mathrm{Max}}} \left(1 - \exp\left(-z_{\mathrm{Max}} t\right)\right) \\ &\geq \min\left(m_0, \frac{r_m}{H z_{\mathrm{Max}}}\right) \overset{(5.7), f_{\mathrm{Max}} > f_0}{=} \frac{r_m}{H z_{\mathrm{Max}}} \\ &= \frac{r_m}{H} \frac{(\xi_m)^{n_m} + (f_{\mathrm{Max}})^{n_m}}{\mu_m (f_{\mathrm{Max}})^{n_m}} \ \forall t \geq 0. \end{aligned} \tag{A.7}$$

In an analog manner, the upper bound for $m(t)$ is found, leading to

$$m(t) \in \Bigg[\underbrace{\frac{r_m}{H} \frac{(\xi_m)^{n_m} + (f_{\mathrm{Max}})^{n_m}}{\mu_m (f_{\mathrm{Max}})^{n_m}}}_{=: m_{\mathrm{Min}}}, \underbrace{\frac{r_m}{H} \frac{(\xi_m)^{n_m} + (f_{\mathrm{Min}})^{n_m}}{\mu_m (f_{\mathrm{Min}})^{n_m}}}_{=: m_{\mathrm{Max}}} \Bigg] \ \forall t \geq 0 \tag{A.8}$$

which finishes the proof of (b).

The boundedness of $\ell(t)$ is given by

$$\frac{\mathrm{d}}{\mathrm{d}t} \ell(t) \overset{(5.6),(A.8)}{\leq} - \left(q_{\ell,m} m_{\mathrm{Min}} + \frac{q_{\ell,e}}{H}\right) \ell(t) + \frac{r_\ell}{H} \tag{A.9}$$

since the solution of the ordinary differential inequality (with associated initial condition $\ell(0) = 0$) is bounded by

$$\begin{aligned} \ell(t) &\overset{(A.9)}{\leq} \frac{r_\ell}{H q_{\ell,m} m_{\mathrm{Min}} + q_{\ell,e}} \left(1 - \exp\left(-\left(q_{\ell,m} m_{\mathrm{Min}} + \frac{q_{\ell,e}}{H}\right) t\right)\right) \\ &\leq \underbrace{\frac{r_\ell}{H q_{\ell,m} m_{\mathrm{Min}} + q_{\ell,e}}}_{\ell_{\mathrm{Max}}} < \infty. \end{aligned} \tag{A.10}$$

In an analog manner, the boundedness of $h(t)$ is proved. The boundedness of $\tilde{\ell}(t)$ under the condition $\frac{r_\ell}{H} < \mu_{\tilde{\ell}} m_{\mathrm{Min}}$ is shown by a proof by contradiction. Hence, let $\tilde{\ell}(t)$ be unbounded, i.e., $\tilde{\ell}(t) \to \infty$ as $t \to \infty$ and $\frac{r_\ell}{H} < \mu_{\tilde{\ell}} m_{\mathrm{Min}}$. It follows

$$\begin{aligned} \frac{\mathrm{d}}{\mathrm{d}t} \tilde{\ell}(t) &\overset{(5.6),(A.10)}{\leq} \underbrace{\left(-\mu_{\tilde{\ell}} + q_{\ell,m} \ell_{\mathrm{Max}}\right)}_{<0, \text{ since } \frac{r_\ell}{H} < \mu_{\tilde{\ell}} m_{\mathrm{Min}}} m(t) + \frac{q_{\ell,e}}{H} \ell_{\mathrm{Max}} \\ &\overset{(A.8)}{\leq} -\mu_{\tilde{\ell}} m_{\mathrm{Min}} + q_{\ell,m} \ell_{\mathrm{Max}} m_{\mathrm{Min}} + \frac{q_{\ell,e}}{H} \ell_{\mathrm{Max}} = -\mu_{\tilde{\ell}} m_{\mathrm{Min}} + \frac{r_\ell}{H} < 0 \end{aligned} \tag{A.11}$$

which is in contradiction to the assumed unboundedness of $\tilde{\ell}(t)$. Hence, this finishes the proof of Proposition 1.

□

B Extended combined model and Proposition 2

The extended combined model introduced in Section 6.2.2 consists of the combined model from Section 5.1.2 enriched by the submodels $\boxed{5}$ and $\boxed{6}$ from Sections 6.1.1.2 and 6.1.1.3. Altogether, the extended combined model reads

$$
\begin{aligned}
\frac{\mathrm{d}}{\mathrm{d}t}\ell(t) =& -\mu_\ell \frac{\ell^{n_\ell}}{(\xi_\ell)^{n_\ell}+\ell^{n_\ell}} m - \left(q_{\ell,m}\ell m + \frac{q_{\ell,e}}{H}\ell\right)\cdot\frac{(k_h)^{n_h}}{(k_h)^{n_h}+h^{n_h}} + \frac{r_\ell(\ell,\|\boldsymbol{\tau}\|)}{H},\\
\frac{\mathrm{d}}{\mathrm{d}t}\tilde{\ell}(t) =& -\mu_{\tilde{\ell}} \frac{\tilde{\ell}^{n_{\tilde{\ell}}}}{(\xi_{\tilde{\ell}})^{n_{\tilde{\ell}}}+\tilde{\ell}^{n_{\tilde{\ell}}}} m + \left(q_{\ell,m}\ell m + \frac{q_{\ell,e}}{H}\ell\right)\cdot\frac{(k_h)^{n_h}}{(k_h)^{n_h}+h^{n_h}} + \frac{r_{\tilde{\ell}}(\tilde{\ell},\|\boldsymbol{\tau}\|)}{H},\\
\frac{\mathrm{d}}{\mathrm{d}t}h(t) =& -q_{h,m}hm - \frac{q_{h,e}}{H}h + \frac{r_h(h,\|\boldsymbol{\tau}\|)}{H},\\
\frac{\mathrm{d}}{\mathrm{d}t}f(t) =& +N_f\mu_\ell\frac{\ell^{n_\ell}}{(\xi_\ell)^{n_\ell}+\ell^{n_\ell}}m + N_f\mu_{\tilde{\ell}}\frac{\tilde{\ell}^{n_{\tilde{\ell}}}}{(\xi_{\tilde{\ell}})^{n_{\tilde{\ell}}}+\tilde{\ell}^{n_{\tilde{\ell}}}}m - k_f\frac{(f-f_{\mathrm{Min}}m)^2}{f_{\mathrm{Max}}m-f}\\
&+k_b b - \mu_f\frac{h^{n_f}}{(\xi_f)^{n_f}+h^{n_f}}(f-f_{\mathrm{Min}}m) + \frac{r_m\left(\tilde{\ell},\|\boldsymbol{\tau}\|\right)}{H}f_{\mathrm{In}},\\
\frac{\mathrm{d}}{\mathrm{d}t}b(t) =& +k_f\frac{(f-f_{\mathrm{Min}}m)^2}{f_{\mathrm{Max}}m-f} - k_b b,\\
\frac{\mathrm{d}}{\mathrm{d}t}m(t) =& -\mu_m\frac{f^{n_m}}{(\xi_m m)^{n_m}+f^{n_m}}m + \frac{r_m\left(\tilde{\ell},\|\boldsymbol{\tau}\|\right)}{H},
\end{aligned}
\tag{B.1}
$$

where

$$
\begin{aligned}
r_\ell\left(\ell,\|\boldsymbol{\tau}\|\right) &= P_\ell s_{\mathrm{P}}\left(\|\boldsymbol{\tau}\|\right)\left(\eta_\ell-\ell\right) + \left(1-\sigma_{\mathrm{F},\ell}\right)\left(\omega_\ell\eta_\ell+(1-\omega_\ell)\ell\right)J_{\mathrm{Vol}}(p,\|\boldsymbol{\tau}\|),\\
r_{\tilde{\ell}}(\tilde{\ell},\|\boldsymbol{\tau}\|) &= -P_{\tilde{\ell}}s_{\mathrm{P}}\left(\|\boldsymbol{\tau}\|\right)\tilde{\ell} + (1-\sigma_{\mathrm{F},\tilde{\ell}})(1-\omega_{\tilde{\ell}})\tilde{\ell}J_{\mathrm{Vol}}(p,\|\boldsymbol{\tau}\|),\\
r_h\left(h,\|\boldsymbol{\tau}\|\right) &= P_h s_{\mathrm{P}}\left(\|\boldsymbol{\tau}\|\right)\left(\eta_h-h\right) + \left(1-\sigma_{\mathrm{F},h}\right)\left(\omega_h\eta_h+(1-\omega_h)h\right)J_{\mathrm{Vol}}(p,\|\boldsymbol{\tau}\|),\\
r_m(\tilde{\ell},\|\boldsymbol{\tau}\|) &= P_m\left(1-\delta_m\frac{k_m}{k_m+\tilde{\ell}}\right)\frac{(\xi_\tau)^{\nu_\tau}}{(\xi_\tau)^{\nu_\tau}+\|\boldsymbol{\tau}\|^{\nu_\tau}},\\
J_{\mathrm{Vol}}(p,\|\boldsymbol{\tau}\|) &= L_p s_{\mathrm{L}}(\|\boldsymbol{\tau}\|)\left(\eta_p-p\right),\\
s_{\mathrm{P}}\left(\|\boldsymbol{\tau}\|\right) &= \frac{1}{\ln(2)}\ln\left(1+\zeta_\tau\frac{\gamma_\tau}{\|\boldsymbol{\tau}\|+\gamma_\tau}\right),\\
s_{\mathrm{L}}(\|\boldsymbol{\tau}\|) &= \gamma_p\ln\left(\mu_p\|\boldsymbol{\tau}\|+\xi_p\right).
\end{aligned}
\tag{B.2}
$$

Initial conditions similar to the combined model are employed

$$\begin{aligned} &\ell(0) = 0, \quad \tilde{\ell}(0) = \tilde{\ell}_0, \quad h(0) = 0, \quad f(0) = f_0 m_0, \\ &b(0) = b_0 m_0, \quad m(0) = m_0, \end{aligned} \tag{B.3}$$

where

$$\begin{aligned} m_0 &= \frac{r_m\left(\tilde{\ell}_0, \|\boldsymbol{\tau}\|\right)}{H} \frac{(\xi_m)^{n_m} + (f_0)^{n_m}}{\mu_m (f_0)^{n_m}}, \\ b_0 &= \frac{k_f}{k_b} \frac{(f_0 - f_{\mathrm{Min}})^2}{f_{\mathrm{Max}} - f_0}. \end{aligned} \tag{B.4}$$

Proposition 2. Let $\ell(t), \tilde{\ell}(t), h(t), f(t), b(t), m(t)$ $(t \geq 0)$ be the unique and smooth solution of the initial value problem defined by Equations (B.1), (B.2), (B.3) and (B.4) with strictly positive parameters fulfilling $(1 - \sigma_{\mathrm{F},i})(1 - \omega_i) J_{\mathrm{Vol}}(p, \|\boldsymbol{\tau}\|) \leq P_i s_{\mathrm{P}}(\|\boldsymbol{\tau}\|)$, $0 \leq \omega_i \leq 1$, $0 \leq \sigma_{\mathrm{F},i} \leq 1$ $(\forall i = \ell, \tilde{\ell}, h)$, $0 \leq p \leq \eta_p$, $f_{\mathrm{Min}} \leq f_{\mathrm{In}} < f_{\mathrm{Max}}$ and $f_{\mathrm{Min}} \leq f_0 < f_{\mathrm{Max}}$. Then the solution satisfies:

(A) $\ell(t), \tilde{\ell}(t), h(t), f(t), b(t), m(t) \geq 0$ for all $t \geq 0$.

(B) $m(t) \in \Bigg[\underbrace{\frac{P_m (1 - \delta_m)}{H} \frac{(\xi_\tau)^{\nu_\tau}}{(\xi_\tau)^{\nu_\tau} + \|\boldsymbol{\tau}\|^{\nu_\tau}} \frac{(\xi_m)^{n_m} + (f_{\mathrm{Max}})^{n_m}}{\mu_m (f_{\mathrm{Max}})^{n_m}}}_{= m'_{\mathrm{Min}}}, \underbrace{\frac{P_m}{H} \frac{(\xi_\tau)^{\nu_\tau}}{(\xi_\tau)^{\nu_\tau} + \|\boldsymbol{\tau}\|^{\nu_\tau}} \frac{(\xi_m)^{n_m} + (f_{\mathrm{Min}})^{n_m}}{\mu_m (f_{\mathrm{Min}})^{n_m}}}_{= m'_{\mathrm{Max}}} \Bigg]$ and

$\frac{f(t)}{m(t)} \in [f_{\mathrm{Min}}, f_{\mathrm{Max}}]$ for all $t \geq 0$.

(C) $\ell(t), \tilde{\ell}(t), h(t), f(t), m(t)$ are bounded.

Proof. The proof of Proposition 2 is similar to the proof of Proposition 1 given in Appendix A. First, it follows from $\eta_p \geq p$ that

$$J_{\mathrm{Vol}}(p, \|\boldsymbol{\tau}\|) \overset{(B.2)}{=} L_p s_{\mathrm{L}}(\|\boldsymbol{\tau}\|)(\eta_p - p) \geq 0. \tag{B.5}$$

To prove the positivity of ℓ, i.e., $\ell(t) \geq 0$ $\forall t \geq 0$ it is sufficient to note that $\ell(0) = 0$ and that $\ell(t) = 0$ implies

$$\frac{\mathrm{d}}{\mathrm{d}t}\ell(t) \overset{(B.1)}{=} \frac{P_\ell s_{\mathrm{P}}(\|\boldsymbol{\tau}\|)\eta_\ell + (1 - \sigma_{\mathrm{F},\ell})\omega_\ell \eta_\ell J_{\mathrm{Vol}}(p, \|\boldsymbol{\tau}\|)}{H} \overset{(B.5),1 \geq \sigma_{\mathrm{F},\ell}}{>} 0, \tag{B.6}$$

due to the strict positivity of the parameters. The positivities of h, m and $\tilde{\ell}$ are proved in an analog fashion. Since $\frac{f(0)}{m(0)} = f_0 \geq f_{\mathrm{Min}}$ and $\frac{f(t)}{m(t)} = f_{\mathrm{Min}}$ implies

$$\frac{\mathrm{d}}{\mathrm{d}t}\left(\frac{f(t)}{m(t)}\right) = \frac{\frac{\mathrm{d}}{\mathrm{d}t}f(t) - \frac{f(t)}{m(t)}\frac{\mathrm{d}}{\mathrm{d}t}m(t)}{m(t)} \overset{(B.1)}{\geq} \frac{\frac{r_m(\tilde{\ell}(t), \|\boldsymbol{\tau}\|)}{H} f_{\mathrm{In}} - f_{\mathrm{Min}} \frac{r_m(\tilde{\ell}(t), \|\boldsymbol{\tau}\|)}{H}}{m(t)} \geq 0, \tag{B.7}$$

it holds $\frac{f(t)}{m(t)} \geq f_{\mathrm{Min}}\ \forall t \geq 0$. This also implies the positivity of f. Given that $\frac{f(0)}{m(0)} = f_0 < f_{\mathrm{Max}}$ and that $\frac{f(t)}{m(t)} \to f_{\mathrm{Max}}$ implies

$$\frac{\mathrm{d}}{\mathrm{d}t}\left(\frac{f(t)}{m(t)}\right) = \frac{\frac{\mathrm{d}}{\mathrm{d}t}f(t) - \frac{f(t)}{m(t)}\frac{\mathrm{d}}{\mathrm{d}t}m(t)}{m(t)} \longrightarrow -\infty, \tag{B.8}$$

it follows $\frac{f(t)}{m(t)} \leq f_{\mathrm{Max}}\ \forall t \geq 0$. Hence, it is concluded that

$$\frac{f(t)}{m(t)} \in [f_{\mathrm{Min}}, f_{\mathrm{Max}}]\ \ \forall t \geq 0. \tag{B.9}$$

The positivity of b follows since $b(0) = 0$ and $b(t) = 0$ implies

$$\frac{\mathrm{d}}{\mathrm{d}t}b(t) \overset{\text{(B.1)}}{=} k_f \frac{\left(f(t) - f_{\mathrm{Min}}m\right)^2}{f_{\mathrm{Max}}m - f(t)} \overset{\text{(B.9)}}{\geq} 0 \tag{B.10}$$

which finishes the proof of (A). (It also follows that the time-dependent solution $(\ell(t), \tilde{\ell}(t), h(t), f(t), b(t), m(t)), t \geq 0$ of the initial value problem is unique and smooth because the smoothness of the right-hand side of the ODE (B.1) is now straightforward to show.)

Using (B.9)

$$\frac{\mathrm{d}}{\mathrm{d}t}m(t) \overset{\text{(B.1),(B.9)}}{\geq} -\underbrace{\mu_m \frac{\left(f_{\mathrm{Max}}\right)^{n_m}}{\left(\xi_m\right)^{n_m} + \left(f_{\mathrm{Max}}\right)^{n_m}}}_{=:z_{\mathrm{Max}}} m + \frac{r_m(\tilde{\ell}(t), \|\boldsymbol{\tau}\|)}{H} \overset{\text{(B.2)}}{\geq} -z_{\mathrm{Max}}m + \frac{r_m(0, \|\boldsymbol{\tau}\|)}{H} \tag{B.11}$$

holds, and by solving this ordinary differential inequality with associated initial condition $m(0) = m_0$ it follows

$$\begin{aligned} m(t) &\overset{\text{(B.11)}}{\geq} m_0 \exp\left(-z_{\mathrm{Max}}t\right) + \frac{r_m(0, \|\boldsymbol{\tau}\|)}{H z_{\mathrm{Max}}}\left(1 - \exp\left(-z_{\mathrm{Max}}t\right)\right) \\ &\geq \min\left(m_0, \frac{r_m(0, \|\boldsymbol{\tau}\|)}{H z_{\mathrm{Max}}}\right) \overset{\text{(B.4)},f_{\mathrm{Max}} > f_0}{=} \frac{r_m(0, \|\boldsymbol{\tau}\|)}{H z_{\mathrm{Max}}} \\ &= \frac{r_m(0, \|\boldsymbol{\tau}\|)}{H} \frac{\left(\xi_m\right)^{n_m} + \left(f_{\mathrm{Max}}\right)^{n_m}}{\mu_m \left(f_{\mathrm{Max}}\right)^{n_m}}\ \forall t \geq 0. \end{aligned} \tag{B.12}$$

In an analog manner, the upper bound for $m(t)$ is found, leading to

$$m(t) \in \Bigg[\underbrace{\frac{r_m(0, \|\boldsymbol{\tau}\|)}{H} \frac{\left(\xi_m\right)^{n_m} + \left(f_{\mathrm{Max}}\right)^{n_m}}{\mu_m \left(f_{\mathrm{Max}}\right)^{n_m}}}_{=:m'_{\mathrm{Min}}}, \underbrace{\frac{r_m(\infty, \|\boldsymbol{\tau}\|)}{H} \frac{\left(\xi_m\right)^{n_m} + \left(f_{\mathrm{Min}}\right)^{n_m}}{\mu_m \left(f_{\mathrm{Min}}\right)^{n_m}}}_{=:m'_{\mathrm{Max}}}\Bigg]\ \forall t \geq 0 \tag{B.13}$$

which finishes the proof of (B).

Due to $(1-\sigma_{\mathrm{F},\ell})(1-\omega_\ell)J_{\mathrm{Vol}}(p,\|\boldsymbol{\tau}\|) \leq P_\ell s_{\mathrm{P}}(\|\boldsymbol{\tau}\|)$, the boundedness of $\ell(t)$ is given by

$$\begin{aligned}
\frac{\mathrm{d}}{\mathrm{d}t}\ell(t) &\overset{(\mathrm{B.1}),(\mathrm{B.13})}{\leq} -\left(q_{\ell,m}m_{\mathrm{Min}} + \frac{q_{\ell,e}}{H}\right)\ell(t) + \frac{r_\ell\left(\ell,\|\boldsymbol{\tau}\|\right)}{H} \\
&\overset{(\mathrm{B.2})}{=} -\left(q_{\ell,m}m_{\mathrm{Min}} + \frac{q_{\ell,e}}{H}\right)\ell(t) + \left(P_\ell s_{\mathrm{P}}\left(\|\boldsymbol{\tau}\|\right) + (1-\sigma_{\mathrm{F},\ell})\omega_\ell J_{\mathrm{Vol}}(p,\|\boldsymbol{\tau}\|)\right)\frac{\eta_\ell}{H} \\
&\quad + \underbrace{\left(-P_\ell s_{\mathrm{P}}\left(\|\boldsymbol{\tau}\|\right) + (1-\sigma_{\mathrm{F},\ell})(1-\omega_\ell)J_{\mathrm{Vol}}(p,\|\boldsymbol{\tau}\|)\right)}_{\leq 0}\frac{\ell(t)}{H} \\
&\leq -\left(q_{\ell,m}m_{\mathrm{Min}} + \frac{q_{\ell,e}}{H}\right)\ell(t) + \left(P_\ell s_{\mathrm{P}}\left(\|\boldsymbol{\tau}\|\right) + (1-\sigma_{\mathrm{F},\ell})\omega_\ell J_{\mathrm{Vol}}(p,\|\boldsymbol{\tau}\|)\right)\frac{\eta_\ell}{H}
\end{aligned} \tag{B.14}$$

since the solution of the ordinary differential inequality (with associated initial condition $\ell(0)=0$) is bounded by

$$\begin{aligned}
\ell(t) &\overset{(\mathrm{B.14})}{\leq} \frac{\left(P_\ell s_{\mathrm{P}}\left(\|\boldsymbol{\tau}\|\right) + (1-\sigma_{\mathrm{F},\ell})\omega_\ell J_{\mathrm{Vol}}(p,\|\boldsymbol{\tau}\|)\right)\eta_\ell}{Hq_{\ell,m}m_{\mathrm{Min}} + q_{\ell,e}}\left(1 - \exp\left(-\left(q_{\ell,m}m_{\mathrm{Min}} + \frac{q_{\ell,e}}{H}\right)t\right)\right) \\
&\leq \frac{\left(P_\ell s_{\mathrm{P}}\left(\|\boldsymbol{\tau}\|\right) + (1-\sigma_{\mathrm{F},\ell})\omega_\ell J_{\mathrm{Vol}}(p,\|\boldsymbol{\tau}\|)\right)\eta_\ell}{Hq_{\ell,m}m_{\mathrm{Min}} + q_{\ell,e}} < \infty.
\end{aligned} \tag{B.15}$$

In an analog manner, the boundedness of $\tilde{\ell}(t)$ and $h(t)$ are proved which finishes the proof of Proposition 2.

□

Bibliography

[1] L. Ai and K. Vafai, A coupling model for macromolecule transport in a stenosed arterial wall, *International Journal of Heat and Mass Transfer* **49**, 1568–1591, 2006.

[2] R. Alon, P. D. Kassner, M. W. Carr, E. B. Finger, M. E. Hemler, and T. A. Springer, The integrin VLA-4 supports tethering and rolling in flow on VCAM-1, *The Journal of Cell Biology* **128**, 1243–1253, 1995.

[3] D. Ambrosi and F. Mollica, On the mechanics of a growing tumor, *International Journal of Engineering Science* **40**, 1297–1316, 2002.

[4] D. Arora, *Computational hemodynamics: Hemolysis and viscoelasticity*, PhD thesis, Citeseer, 2005.

[5] T. Asakura and T. Karino, Flow patterns and spatial distribution of atherosclerotic lesions in human coronary arteries, *Circulation Research* **66**, 1045–1066, 1990.

[6] L. Aslanidou, B. Trachet, P. Reymond, R. A. Fraga-Silva, P. Segers, and N. Stergiopulos, A 1D model of the arterial circulation in mice, *Alternatives to Animal Experimentation* **33**, 13, 2016.

[7] G. Assmann and J.-R. Nofer, Atheroprotective effects of high-density lipoproteins, *Annual Review of Medicine* **54**, 321–341, 2003.

[8] G. Astarita and G. Marrucci, *Principles of non-Newtonian fluid mechanics*, McGraw-Hill Companies, 1974.

[9] D. Balzani and T. Schmidt, Comparative analysis of damage functions for soft tissues: Properties at damage initialization, *Mathematics and Mechanics of Solids* **20**, 480–492, 2015.

[10] G. R. Barrenechea and F. Valentin, An unusual stabilized finite element method for a generalized Stokes problem, *Numerische Mathematik* **92**, 653–677, 2002.

[11] Y. Bazilevs, J. Gohean, T. Hughes, R. Moser, and Y. Zhang, Patient-specific isogeometric fluid–structure interaction analysis of thoracic aortic blood flow due to implantation of the Jarvik 2000 left ventricular assist device, *Computer Methods in Applied Mechanics and Engineering* **198**, 3534–3550, 2009.

[12] Y. Bazilevs, V. M. Calo, T. E. Tezduyar, and T. J. Hughes, YZβ discontinuity capturing for advection-dominated processes with application to arterial drug delivery, *International Journal for Numerical Methods in Fluids* **54**, 593–608, 2007.

[13] Y. Bazilevs, K. Takizawa, and T. E. Tezduyar, *Computational fluid-structure interaction: methods and applications*, John Wiley and Sons, 2013.

[14] J. Bear and Y. Bachmat, *Introduction to modeling of transport phenomena in porous media*, Volume 4, Springer Science and Business Media, 2012.

[15] F. B. Belgacem, The mortar finite element method with Lagrange multipliers, *Numerische Mathematik* **84**, 173–197, 1999.

[16] J. Berliner, M. Territo, A. Sevanian, S. Ramin, J. A. Kim, B. Bamshad, M. Esterson, and A. M. Fogelman, Minimally modified low density lipoprotein stimulates monocyte endothelial interactions, *Journal of Clinical Investigation* **85**, 1260, 1990.

[17] R. B. Bird, R. Armstrong, and O. Hassager, Dynamics of polymeric liquids. Vol. 1: Fluid mechanics, 1987.

[18] L. Boring, J. Gosling, M. Cleary, and I. F. Charo, Decreased lesion formation in CCR2-/- mice reveals a role for chemokines in the initiation of atherosclerosis, *Nature* **394**, 894–897, 1998.

[19] R. L. Bratzler, G. M. Chisolm, C. K. Colton, K. A. Smith, and R. S. Lees, The distribution of labeled low-density lipoproteins across the rabbit thoracic aorta in vivo, *Atherosclerosis* **28**, 289–307, 1977.

[20] F. Brezzi and M. Fortin, *Mixed and hybrid finite element methods*, Volume 15, Springer Science and Business Media, 2012.

[21] W. L. Briggs, V. E. Henson, and S. F. McCormick, *A multigrid tutorial*, SIAM, 2000.

[22] A. J. Brown, Z. Teng, P. C. Evans, J. H. Gillard, H. Samady, and M. R. Bennett, Role of biomechanical forces in the natural history of coronary atherosclerosis, *Nature Reviews Cardiology* **13**, 210 – 220, 2016.

[23] M. S. Brown and J. L. Goldstein, Lipoprotein metabolism in the macrophage: implications for cholesterol deposition in atherosclerosis, *Annual Review of Biochemistry* **52**, 223–261, 1983.

[24] M. S. Brown, J. L. Goldstein, M. Krieger, Y. Ho, and R. Anderson, Reversible accumulation of cholesteryl esters in macrophages incubated with acetylated lipoproteins, *The Journal of Cell Biology* **82**, 597–613, 1979.

[25] M. S. Brown, Y. Ho, and J. Goldstein, The cholesteryl ester cycle in macrophage foam cells. Continual hydrolysis and re-esterification of cytoplasmic cholesteryl esters, *Journal of Biological Chemistry* **255**, 9344–9352, 1980.

[26] N. Brownell and A. Rohatgi, Modulating cholesterol efflux capacity to improve cardiovascular disease, *Current Opinion in Lipidology* **27**, 398–407, 2016.

[27] M. A. Bulelzai and J. L. Dubbeldam, Long time evolution of atherosclerotic plaques, *Journal of Theoretical Biology* **297**, 1–10, 2012.

[28] J. C. Butcher, *Numerical methods for ordinary differential equations*, John Wiley and Sons, 3 Edition, 2016.

[29] V. Calvez, J. G. Houot, N. Meunier, A. Raoult, and G. Rusnakova, Mathematical and numerical modeling of early atherosclerotic lesions, *ESAIM: Proceedings and Surveys* **30**, 1 – 14, 2010.

[30] L. M. Cancel, A. Fitting, and J. M. Tarbell, In vitro study of LDL transport under pressurized (convective) conditions, *American Journal of Physiology-Heart and Circulatory Physiology* **293**, H126–H132, 2007.

[31] T. E. Carew, R. N. VAISHNAV, and D. J. PATEL, Compressibility of the arterial wall, *Circulation Research* **23**, 61–68, 1968.

[32] P. Causin, J.-F. Gerbeau, and F. Nobile, Added-mass effect in the design of partitioned algorithms for fluid–structure problems, *Computer Methods in Applied Mechanics and Engineering* **194**, 4506–4527, 2005.

[33] M. Cecelja and P. Chowienczyk, Role of arterial stiffness in cardiovascular disease, *JRSM Cardiovascular Disease* **1**, 1–10, 2012.

[34] A. D. Chalmers, A. Cohen, C. A. Bursill, and M. R. Myerscough, Bifurcation and dynamics in a mathematical model of early atherosclerosis, *Journal of Mathematical Biology* **71**, 1451–1480, 2015.

[35] A. D. Chalmers, C. A. Bursill, and M. R. Myerscough, Nonlinear dynamics of early atherosclerotic plaque formation may determine the efficacy of high density lipoproteins (hdl) in plaque regression, *PloS One* **12**, e0187674, 2017.

[36] Y. S. Chang, J. A. Yaccino, S. Lakshminarayanan, J. A. Frangos, and J. M. Tarbell, Shear-induced increase in hydraulic conductivity in endothelial cells is mediated by a nitric oxide–dependent mechanism, *Arteriosclerosis, Thrombosis, and Vascular Biology* **20**, 35–42, 2000.

[37] Y. S. Chatzizisis, A. U. Coskun, M. Jonas, E. R. Edelman, C. L. Feldman, and P. H. Stone, Role of endothelial shear stress in the natural history of coronary atherosclerosis and vascular remodeling: molecular, cellular, and vascular behavior, *Journal of the American College of Cardiology* **49**, 2379–2393, 2007.

[38] J. Chen and X.-Y. Lu, Numerical investigation of the non-Newtonian pulsatile blood flow in a bifurcation model with a non-planar branch, *Journal of Biomechanics* **39**, 818–832, 2006.

[39] N. Chen and W. H. Frishman, High-density lipoprotein infusion therapy and atherosclerosis: Current research and future directions, *Cardiology in Review* **24**, 298–302, 2016.

[40] C. Cheng, F. Helderman, D. Tempel, D. Segers, B. Hierck, R. Poelmann, A. van Tol, D. J. Duncker, D. Robbers-Visser, N. T. Ursem, et al., Large variations in absolute wall shear stress levels within one species and between species, *Atherosclerosis* **195**, 225–235, 2007.

[41] R. P. Chhabra and J. F. Richardson, *Non-Newtonian flow and applied rheology: engineering applications*, Butterworth-Heinemann, 2011.

[42] J.-J. Chiu, P.-L. Lee, C.-N. Chen, C.-I. Lee, S.-F. Chang, L.-J. Chen, S.-C. Lien, Y.-C. Ko, S. Usami, and S. Chien, Shear stress increases ICAM-1 and decreases VCAM-1 and E-selectin expressions induced by tumor necrosis factor-α in endothelial cells, *Arteriosclerosis, Thrombosis, and Vascular Biology* **24**, 73–79, 2004.

[43] Y. I. Cho and K. R. Kensey, Effects of the non-Newtonian viscosity of blood on flows in a diseased arterial vessel. Part 1: Steady flows, *Biorheology*, 241–62, 1991.

[44] J. Chung and G. Hulbert, A time integration algorithm for structural dynamics with improved numerical dissipation: the generalized-α method, *Journal of Applied Mechanics* **60**, 371–375, 1993.

[45] M. Cilla, E. Peña, and M. A. Martínez, Mathematical modelling of atheroma plaque formation and development in coronary arteries, *Journal of The Royal Society Interface* **11**, 20130866, 2014.

[46] C. Cobbold, J. Sherratt, and S. Maxwell, Lipoprotein oxidation and its significance for atherosclerosis: a mathematical approach, *Bulletin of Mathematical Biology* **64**, 65–95, 2002.

[47] R. Codina, Stabilized finite element approximation of transient incompressible flows using orthogonal subscales, *Computer Methods in Applied Mechanics and Engineering* **191**, 4295–4321, 2002.

[48] A. Cohen, M. R. Myerscough, and R. S. Thompson, Athero-protective effects of high density lipoproteins (HDL): An ODE model of the early stages of atherosclerosis, *Bulletin of mathematical biology* **76**, 1117–1142, 2014.

[49] L. Cominacini, U. Garbin, A. F. Pasini, A. Davoli, M. Campagnola, G. B. Contessi, A. M. Pastorino, and V. L. Cascio, Antioxidants inhibit the expression of intercellular cell adhesion molecule-1 and vascular cell adhesion molecule-1 induced by oxidized LDL on human umbilical vein endothelial cells, *Free Radical Biology and Medicine* **22**, 117–127, 1997.

[50] M. Coroneo, L. Yoshihara, and W. A. Wall, Biofilm growth: A multi-scale and coupled fluid-structure interaction and mass transport approach, *Biotechnology and Bioengineering* **111**, 1385–1395, 2014.

[51] O. Coussy, *Poromechanics*, John Wiley and Sons, 2004.

[52] P. Crosetto, P. Reymond, S. Deparis, D. Kontaxakis, N. Stergiopulos, and A. Quarteroni, Fluid–structure interaction simulation of aortic blood flow, *Computers and Fluids* **43**, 46–57, 2011.

[53] J. Crouse, J. Parks, H. Schey, and F. Kahl, Studies of low density lipoprotein molecular weight in human beings with coronary artery disease, *Journal of Lipid Research* **26**, 566–574, 1985.

[54] P. A. Curmi, L. Juan, and A. Tedgui, Effect of transmural pressure on low density lipoprotein and albumin transport and distribution across the intact arterial wall, *Circulation Research* **66**, 1692–1702, 1990.

[55] C. Cyron, R. Aydin, and J. Humphrey, A homogenized constrained mixture (and mechanical analog) model for growth and remodeling of soft tissue, *Biomechanics and Modeling in Mechanobiology* **15**, 1389–1403, 2016.

[56] M. J. Davies, P. D. Richardson, N. Woolf, D. R. Katz, and J. Mann, Risk of thrombosis in human atherosclerotic plaques: role of extracellular lipid, macrophage, and smooth muscle cell content, *Heart* **69**, 377–381, 1993.

[57] T. De Mulder, The role of bulk viscosity in stabilized finite element formulations for incompressible flow: A review, *Computer Methods in Applied Mechanics and Engineering* **163**, 1–10, 1998.

[58] E. de Souza Neto, D. Perić, M. Dutko, and D. Owen, Design of simple low order finite elements for large strain analysis of nearly incompressible solids, *International Journal of Solids and Structures* **33**, 3277–3296, 1996.

[59] D. De Wilde, B. Trachet, G. R. De Meyer, and P. Segers, Shear stress metrics and their relation to atherosclerosis: An in vivo follow-up study in atherosclerotic mice, *Annals of Biomedical Engineering*, 1–12, 2015.

[60] D. De Wilde, B. Trachet, N. Debusschere, F. Iannaccone, A. Swillens, J. Degroote, J. Vierendeels, G. R. De Meyer, and P. Segers, Assessment of shear stress related parameters in the carotid bifurcation using mouse-specific FSI simulations, *Journal of Biomechanics*, 2015.

[61] D. De Wilde, B. Trachet, C. Van der Donckt, B. Vandeghinste, B. Descamps, C. Vanhove, G. R. De Meyer, and P. Segers, Vulnerable plaque detection and quantification with gold particle–enhanced computed tomography in atherosclerotic mouse models, *Molecular Imaging* **14**, 7290–2015, 2015.

[62] D. De Wilde, B. Trachet, G. De Meyer, and P. Segers, The influence of anesthesia and fluid–structure interaction on simulated shear stress patterns in the carotid bifurcation of mice, *Journal of Biomechanics* **49**, 2741–2747, 2016.

[63] T. DeVries-Seimon, Y. Li, P. M. Yao, E. Stone, Y. Wang, R. J. Davis, R. Flavell, and I. Tabas, Cholesterol-induced macrophage apoptosis requires ER stress pathways and engagement of the type A scavenger receptor, *Journal of Cell Biology* **171**, 61–73, 2005.

[64] P. B. Dobrin and A. A. Rovick, Influence of vascular smooth muscle on contractile mechanics and elasticity of arteries, *American Journal of Physiology–Legacy Content* **217**, 1644–1651, 1969.

[65] S. Doll and K. Schweizerhof, On the development of volumetric strain energy functions, *Journal of Applied Mechanics* **67**, 17–21, 2000.

[66] S. Doll, K. Schweizerhof, R. Hauptmann, and C. Freischläger, On volumetric locking of low-order solid and solid-shell elements for finite elastoviscoplastic deformations and selective reduced integration, *Engineering Computations* **17**, 874–902, 2000.

[67] J. Donea and A. Huerta, *Finite element methods for flow problems*, John Wiley and Sons, 2003.

[68] A. C. Doran, N. Meller, and C. A. McNamara, The role of smooth muscle cells in the initiation and early progression of atherosclerosis, *Arteriosclerosis, Thrombosis, and Vascular Biology* **28**, 812–819, 2008.

[69] C. Eck, H. Garcke, and P. Knabner, *Mathematical Modelling*, Springer, 2008.

[70] E. El-Bassiouni, M. Helmy, S. El-Zoghby, E.-N. Kamel, and R. Hosny, Relationship between level of circulating modified LDL and the extent of coronary artery disease in type 2 diabetic patients, *British Journal of Biomedical Science* **64**, 109–116, 2007.

[71] F. El Halabi, D. González, A. Chico, and M. Doblaré, FE^2 multiscale in linear elasticity based on parametrized microscale models using proper generalized decomposition, *Computer Methods in Applied Mechanics and Engineering* **257**, 183–202, 2013.

[72] N. El Khatib, S. Génieys, B. Kazmierczak, and V. Volpert, Reaction–diffusion model of atherosclerosis development, *Journal of Mathematical Biology* **65**, 349–374, 2012.

[73] M. Epstein and G. A. Maugin, Thermomechanics of volumetric growth in uniform bodies, *International Journal of Plasticity* **16**, 951–978, 2000.

[74] P. Farah, A.-T. Vuong, W. Wall, and A. Popp, Volumetric coupling approaches for multiphysics simulations on non-matching meshes, *International Journal for Numerical Methods in Engineering* **108**, 1550–1576, 2016.

[75] D. P. Faxon, V. Fuster, P. Libby, J. A. Beckman, W. R. Hiatt, R. W. Thompson, J. N. Topper, B. H. Annex, J. H. Rundback, R. P. Fabunmi, et al., Atherosclerotic vascular disease conference writing group III: Pathophysiology, *Circulation* **109**, 2617–2625, 2004.

[76] A. Feintuch, P. Ruengsakulrach, A. Lin, J. Zhang, Y.-Q. Zhou, J. Bishop, L. Davidson, D. Courtman, F. S. Foster, D. A. Steinman, et al., Hemodynamics in the mouse aortic arch as assessed by MRI, ultrasound, and numerical modeling, *American Journal of Physiology-Heart and Circulatory Physiology* **292**, H884–H892, 2007.

[77] B. Feng, P. M. Yao, Y. Li, C. M. Devlin, D. Zhang, H. P. Harding, M. Sweeney, J. X. Rong, G. Kuriakose, E. A. Fisher, et al., The endoplasmic reticulum is the site of cholesterol-induced cytotoxicity in macrophages, *Nature Cell Biology* **5**, 781–792, 2003.

[78] J. Ferruzzi, M. Bersi, and J. Humphrey, Biomechanical phenotyping of central arteries in health and disease: advantages of and methods for murine models, *Annals of Biomedical Engineering* **41**, 1311–1330, 2013.

[79] F. Feyel, A multilevel finite element method (FE^2) to describe the response of highly non-linear structures using generalized continua, *Computer Methods in Applied Mechanics and Engineering* **192**, 3233–3244, 2003.

[80] A. Fick, On liquid diffusion, *Journal of Membrane Science* **100**, 33–38, 1995.

[81] C. A. Figueroa, S. Baek, C. A. Taylor, and J. D. Humphrey, A computational framework for fluid-solid-growth modeling in cardiovascular simulations, *Computer Methods in Applied Mechanics and Engineering* **198**, 3583–3602, 2009.

[82] N. Filipovic, M. Rosic, I. Tanaskovic, O. Parodi, and D. Fotiadis, Computer simulation and experimental analysis of LDL transport in the arteries, In *Engineering in Medicine and Biology Society, EMBC, 2011 Annual International Conference of the IEEE*, pages 195–198. IEEE, 2011.

[83] P.-W. Fok, Mathematical model of intimal thickening in atherosclerosis: vessel stenosis as a free boundary problem, *Journal of Theoretical Biology* **314**, 23–33, 2012.

[84] P.-W. Fok, Multi-layer mechanical model of Glagov remodeling in coronary arteries: Differences between in-vivo and ex-vivo measurements, *PloS One* **11**, e0159304, 2016.

[85] L. Formaggia, A. Quarteroni, and A. Veneziani, *Cardiovascular Mathematics: Modeling and simulation of the circulatory system*, Volume 1, Springer, 2010.

[86] C. Förster, *Robust methods for fluid-structure interaction with stabilised finite elements*, PhD thesis, Universität Stuttgart, 2007.

[87] C. Förster, W. A. Wall, and E. Ramm, Artificial added mass instabilities in sequential staggered coupling of nonlinear structures and incompressible viscous flows, *Computer Methods in Applied Mechanics and Engineering* **196**, 1278–1293, 2007.

[88] C. S. Fox, S. H. Golden, C. Anderson, G. A. Bray, L. E. Burke, I. H. De Boer, P. Deedwania, R. H. Eckel, A. G. Ershow, J. Fradkin, et al., Update on prevention of cardiovascular disease in adults with type 2 diabetes mellitus in light of recent evidence, *Circulation* **132**, 691–718, 2015.

[89] W. T. Friedewald, R. I. Levy, and D. S. Fredrickson, Estimation of the concentration of low-density lipoprotein cholesterol in plasma, without use of the preparative ultracentrifuge, *Clinical Chemistry* **18**, 499–502, 1972.

[90] A. Friedman and W. Hao, A mathematical model of atherosclerosis with reverse cholesterol transport and associated risk factors, *Bulletin of Mathematical Biology* **77**, 758–781, 2015.

[91] E. Frisdal, P. Lesnik, M. Olivier, P. Robillard, M. J. Chapman, T. Huby, M. Guerin, and W. Le Goff, Interleukin-6 protects human macrophages from cellular cholesterol accumulation and attenuates the proinflammatory response, *Journal of Biological Chemistry* **286**, 30926–30936, 2011.

[92] F. Fritzen and M. Hodapp, The finite element square reduced (FE^{2R}) method with GPU acceleration: towards three-dimensional two-scale simulations, *International Journal for Numerical Methods in Engineering* **107**, 853–881, 2016.

[93] J. Frostegard, A. Haegerstrand, M. Gidlund, and J. Nilsson, Biologically modified LDL increases the adhesive properties of endothelial cells, *Atherosclerosis* **90**, 119–126, 1991.

[94] K. Garikipati, E. Arruda, K. Grosh, H. Narayanan, and S. Calve, A continuum treatment of growth in biological tissue: the coupling of mass transport and mechanics, *Journal of the Mechanics and Physics of Solids* **52**, 1595–1625, 2004.

[95] M. W. Gee, U. Küttler, and W. A. Wall, Truly monolithic algebraic multigrid for fluid–structure interaction, *International Journal for Numerical Methods in Engineering* **85**, 987–1016, 2011.

[96] M. Gee, C. Förster, and W. Wall, A computational strategy for prestressing patient-specific biomechanical problems under finite deformation, *International Journal for Numerical Methods in Biomedical Engineering* **26**, 52–72, 2010.

[97] J.-F. Gerbeau and M. Vidrascu, A quasi-Newton algorithm based on a reduced model for fluid-structure interaction problems in blood flows, *ESAIM: Mathematical Modelling and Numerical Analysis* **37**, 631–647, 2003.

[98] G. S. Getz, Mouse model of unstable atherosclerotic plaque?, *Arteriosclerosis, Thrombosis, and Vascular Biology*, 2503–2505, 2000.

[99] G. S. Getz and C. A. Reardon, Animal models of atherosclerosis, *Arteriosclerosis, Thrombosis, and Vascular Biology* **32**, 1104–1115, 2012.

[100] F. Gijsen, E. Allanic, F. Van de Vosse, and J. Janssen, The influence of the non-Newtonian properties of blood on the flow in large arteries: unsteady flow in a 90° curved tube, *Journal of Biomechanics* **32**, 705–713, 1999.

[101] S. Glagov, E. Weisenberg, C. K. Zarins, R. Stankunavicius, and G. J. Kolettis, Compensatory enlargement of human atherosclerotic coronary arteries, *New England Journal of Medicine* **316**, 1371–1375, 1987.

[102] H. A. Golpon, V. A. Fadok, L. Taraseviciene-Stewart, R. Scerbavicius, C. Sauer, T. Welte, P. M. Henson, and N. F. Voelkel, Life after corpse engulfment: phagocytosis of apoptotic cells leads to VEGF secretion and cell growth, *The FASEB Journal* **18**, 1716–1718, 2004.

[103] S. Gordon and P. R. Taylor, Monocyte and macrophage heterogeneity, *Nature Reviews Immunology* **5**, 953–964, 2005.

[104] A. Goriely and M. B. Amar, On the definition and modeling of incremental, cumulative, and continuous growth laws in morphoelasticity, *Biomechanics and Modeling in Mechanobiology* **6**, 289–296, 2007.

[105] J. Gosling, S. Slaymaker, L. Gu, S. Tseng, C. H. Zlot, S. G. Young, B. J. Rollins, and I. F. Charo, MCP-1 deficiency reduces susceptibility to atherosclerosis in mice that overexpress human apolipoprotein B, *Journal of Clinical Investigation* **103**, 773, 1999.

[106] V. Gravemeier, A. Comerford, L. Yoshihara, M. Ismail, and W. A. Wall, A novel formulation for Neumann inflow boundary conditions in biomechanics, *International Journal for Numerical Methods in Biomedical Engineering* **28**, 560–573, 2012.

[107] D. Grobbee and M. Bots, Carotid artery intima-media thickness as an indicator of generalized atherosclerosis, *Journal of Internal Medicine* **236**, 567–573, 1994.

[108] D. G. Hackam and S. S. Anand, Emerging risk factors for atherosclerotic vascular disease: a critical review of the evidence, *Journal of the American Medical Association* **290**, 932–940, 2003.

[109] D. Hackett, G. Davies, and A. Maseri, Pre-existing coronary stenoses in patients with first myocardial infarction are not necessarily severe, *European Heart Journal* **9**, 1317–1323, 1988.

[110] G. K. Hansson and P. Libby, The immune response in atherosclerosis: a double-edged sword, *Nature Reviews Immunology* **6**, 508–519, 2006.

[111] W. Hao and A. Friedman, The LDL-HDL profile determines the risk of atherosclerosis: a mathematical model, *PloS One* **9**, e90497, 2014.

[112] D. Haskett, G. Johnson, A. Zhou, U. Utzinger, and J. V. Geest, Microstructural and biomechanical alterations of the human aorta as a function of age and location, *Biomechanics and Modeling in Mechanobiology* **9**, 725–736, 2010.

[113] M. Heil, T. Ziegelhoeffer, F. Pipp, S. Kostin, S. Martin, M. Clauss, and W. Schaper, Blood monocyte concentration is critical for enhancement of collateral artery growth, *American Journal of Physiology-Heart and Circulatory Physiology* **283**, H2411–H2419, 2002.

[114] M. Heil, A. L. Hazel, and J. Boyle, Solvers for large-displacement fluid–structure interaction problems: segregated versus monolithic approaches, *Computational Mechanics* **43**, 91–101, 2008.

[115] V. M. Heiland, C. Forsell, J. Roy, U. Hedin, and T. C. Gasser, Identification of carotid plaque tissue properties using an experimental–numerical approach, *Journal of the Mechanical Behavior of Biomedical Materials* **27**, 226–238, 2013.

[116] T. Henriksen, E. M. Mahoney, and D. Steinberg, Enhanced macrophage degradation of biologically modified low density lipoprotein, *Arteriosclerosis, Thrombosis, and Vascular Biology* **3**, 149–159, 1983.

[117] R. A. Herrmann, R. A. Malinauskas, and G. A. Truskey, Characterization of sites with elevated LDL permeability at intercostal, celiac, and iliac branches of the normal rabbit aorta, *Arteriosclerosis, Thrombosis, and Vascular Biology* **14**, 313–323, 1994.

[118] H. A. Himburg, D. M. Grzybowski, A. L. Hazel, J. A. LaMack, X.-M. Li, and M. H. Friedman, Spatial comparison between wall shear stress measures and porcine arterial endothelial permeability, *American Journal of Physiology-Heart and Circulatory Physiology* **286**, H1916–H1922, 2004.

[119] G. Himpel, E. Kuhl, A. Menzel, and P. Steinmann, Computational modelling of isotropic multiplicative growth, *Computer Modeling in Engineering Sciences* **8**, 119–134, 2005.

[120] A. H. Hoffman, Z. Teng, J. Zheng, Z. Wu, P. K. Woodard, K. L. Billiar, L. Wang, and D. Tang, Stiffness properties of adventitia, media, and full thickness human atherosclerotic carotid arteries in the axial and circumferential directions, *Journal of Biomechanical Engineering* **139**, 124501, 2017.

[121] Y. Hoi, Y.-Q. Zhou, X. Zhang, R. M. Henkelman, and D. A. Steinman, Correlation between local hemodynamics and lesion distribution in a novel aortic regurgitation murine model of atherosclerosis, *Annals of Biomedical Engineering* **39**, 1414–1422, 2011.

[122] G. A. Holzapfel, *Nonlinear solid mechanics*, John Wiley and Sons, 2000.

[123] G. A. Holzapfel, T. C. Gasser, and R. W. Ogden, A new constitutive framework for arterial wall mechanics and a comparative study of material models, *Journal of Elasticity and the Physical Science of Solids* **61**, 1–48, 2000.

[124] G. A. Holzapfel, G. Sommer, C. T. Gasser, and P. Regitnig, Determination of layer-specific mechanical properties of human coronary arteries with nonatherosclerotic intimal thickening and related constitutive modeling, *American Journal of Physiology-Heart and Circulatory Physiology* **289**, H2048–H2058, 2005.

[125] G. A. Holzapfel, J. J. Mulvihill, E. M. Cunnane, and M. T. Walsh, Computational approaches for analyzing the mechanics of atherosclerotic plaques: a review, *Journal of Biomechanics* **47**, 859–869, 2014.

[126] S. S. Hossain, S. F. Hossainy, Y. Bazilevs, V. M. Calo, and T. J. Hughes, Mathematical modeling of coupled drug and drug-encapsulated nanoparticle transport in patient-specific coronary artery walls, *Computational Mechanics* **49**, 213–242, 2012.

[127] T. K. Hsiai, S. K. Cho, P. K. Wong, M. Ing, A. Salazar, A. Sevanian, M. Navab, L. L. Demer, and C.-M. Ho, Monocyte recruitment to endothelial cells in response to oscillatory shear stress, *The FASEB Journal* **17**, 1648–1657, 2003.

[128] Z. Huang and J. Tarbell, Numerical simulation of mass transfer in porous media of blood vessel walls, *American Journal of Physiology - Heart and Circulatory Physiology* **273**, H464–H477, 1997.

[129] T. J. Hughes, *The finite element method: linear static and dynamic finite element analysis*, Courier Corporation, 2012.

[130] T. J. Hughes, L. P. Franca, and M. Balestra, A new finite element formulation for computational fluid dynamics: V. Circumventing the Babuška-Brezzi condition: a stable Petrov-Galerkin formulation of the Stokes problem accommodating equal-order interpolations, *Computer Methods in Applied Mechanics and Engineering* **59**, 85–99, 1986.

[131] J. Humphrey, *Cardiovascular solid mechanics: cells, tissues, and organs*, Springer, 2002.

[132] J. Humphrey and K. Rajagopal, A constrained mixture model for growth and remodeling of soft tissues, *Mathematical Models and Methods in Applied Sciences* **12**, 407–430, 2002.

[133] Y. Huo, X. Guo, and G. S. Kassab, The flow field along the entire length of mouse aorta and primary branches, *Annals of Biomedical Engineering* **36**, 685–699, 2008.

[134] Y. Huo, A. Hafezi-Moghadam, and K. Ley, Role of vascular cell adhesion molecule-1 and fibronectin connecting segment-1 in monocyte rolling and adhesion on early atherosclerotic lesions, *Circulation Research* **87**, 153–159, 2000.

[135] A. Ibragimov, C. McNeal, L. Ritter, and J. Walton, A mathematical model of atherogenesis as an inflammatory response, *Mathematical Medicine and Biology* **22**, 305–333, 2005.

[136] S. Inaba, G. S. Mintz, T. Shimizu, G. Weisz, R. Mehran, S. P. Marso, K. Xu, B. de Bruyne, P. W. Serruys, G. W. Stone, et al., Compensatory enlargement of the left main coronary artery: insights from the prospect study, *Coronary Artery Disease* **25**, 98–103, 2014.

[137] B. M. Irons and R. C. Tuck, A version of the aitken accelerator for computer iteration, *International Journal for Numerical Methods in Engineering* **1**, 275–277, 1969.

[138] M. Ismail, V. Gravemeier, A. Comerford, and W. Wall, A stable approach for coupling multidimensional cardiovascular and pulmonary networks based on a novel pressure-flow rate or pressure-only Neumann boundary condition formulation, *International Journal for Numerical Methods in Biomedical Engineering* **30**, 447–469, 2014.

[139] M. Ismail, W. A. Wall, and M. W. Gee, Adjoint-based inverse analysis of Windkessel parameters for patient-specific vascular models, *Journal of Computational Physics* **244**, 113–130, 2013.

[140] K. E. Jansen, C. H. Whiting, and G. M. Hulbert, A generalized-α method for integrating the filtered Navier–Stokes equations with a stabilized finite element method, *Computer Methods in Applied Mechanics and Engineering* **190**, 305–319, 2000.

[141] J.-R. Jeng, C.-H. Chang, S. Shih-Ming, and C. Hui-Chong, Oxidized low-density lipoprotein enhances monocyte-endothelial cell binding against shear-stress-induced detachment, *Biochimica et Biophysica Acta (BBA)-Molecular Cell Research* **1178**, 221–227, 1993.

[142] B. M. Johnston, P. R. Johnston, S. Corney, and D. Kilpatrick, Non-Newtonian blood flow in human right coronary arteries: steady state simulations, *Journal of Biomechanics* **37**, 709–720, 2004.

[143] G. Južnič and H. Klensch, Vergleichend-physiologische Untersuchungen über das Verhalten der Indices für Energieaufwand und Leistung des Herzens, *Pflüger's Archiv für die gesamte Physiologie des Menschen und der Tiere* **280**, 38–45, 1964.

[144] R. Karimi, T. Zhu, B. E. Bouma, and M. R. K. Mofrad, Estimation of nonlinear mechanical properties of vascular tissues via elastography, *Cardiovascular Engineering* **8**, 191–202, 2008.

[145] G. Karner and K. Perktold, Effect of endothelial injury and increased blood pressure on albumin accumulation in the arterial wall: a numerical study, *Journal of Biomechanics* **33**, 709–715, 2000.

[146] G. Karner, K. Perktold, and H. P. Zehentner, Computational modeling of macromolecule transport in the arterial wall, *Computer Methods in Biomechanics and Biomedical Engineering* **4**, 491–504, 2001.

[147] A. Katchalsky and P. F. Curran, *Nonequilibrium thermodynamics in biophysics*, Harvard University Press, 1967.

[148] O. Kedem and A. Katchalsky, Thermodynamic analysis of the permeability of biological membranes to non-electrolytes, *Biochimica et Biophysica Acta* **27**, 229–246, 1958.

[149] S. M. Klisch, T. J. Van Dyke, and A. Hoger, A theory of volumetric growth for compressible elastic biological materials, *Mathematics and Mechanics of Solids* **6**, 551–575, 2001.

[150] T. Klöppel, A. Popp, U. Küttler, and W. A. Wall, Fluid–structure interaction for non-conforming interfaces based on a dual mortar formulation, *Computer Methods in Applied Mechanics and Engineering* **200**, 3111–3126, 2011.

[151] A. Kontush and M. J. Chapman, Functionally defective high-density lipoprotein: a new therapeutic target at the crossroads of dyslipidemia, inflammation, and atherosclerosis, *Pharmacological Reviews* **58**, 342–374, 2006.

[152] N. Koshiba, J. Ando, X. Chen, and T. Hisada, Multiphysics simulation of blood flow and LDL transport in a porohyperelastic arterial wall model, *Journal of Biomechanical Engineering* **129**, 374–385, 2007.

[153] R. Krause and P. Zulian, A parallel approach to the variational transfer of discrete fields between arbitrarily distributed unstructured finite element meshes, *SIAM Journal on Scientific Computing* **38**, C307–C333, 2016.

[154] D. N. Ku, D. P. Giddens, C. K. Zarins, and S. Glagov, Pulsatile flow and atherosclerosis in the human carotid bifurcation. positive correlation between plaque location and low oscillating shear stress, *Arteriosclerosis, Thrombosis, and Vascular Biology* **5**, 293–302, 1985.

[155] E. Kuhl, R. Maas, G. Himpel, and A. Menzel, Computational modeling of arterial wall growth, *Biomechanics and Modeling in Mechanobiology* **6**, 321–331, 2007.

[156] V. V. Kunjathoor, M. Febbraio, E. A. Podrez, K. J. Moore, L. Andersson, S. Koehn, J. S. Rhee, R. Silverstein, H. F. Hoff, and M. W. Freeman, Scavenger receptors class AI/II and CD36 are the principal receptors responsible for the uptake of modified low density lipoprotein leading to lipid loading in macrophages, *Journal of Biological Chemistry* **277**, 49982–49988, 2002.

[157] U. Küttler, M. Gee, C. Förster, A. Comerford, and W. Wall, Coupling strategies for biomedical fluid–structure interaction problems, *International Journal for Numerical Methods in Biomedical Engineering* **26**, 305–321, 2010.

[158] U. Küttler, *Effiziente Lösungsverfahren für Fluid-Struktur-Interaktions-Probleme*, PhD thesis, Technische Universität, 2009.

[159] U. Küttler and W. A. Wall, Fixed-point fluid–structure interaction solvers with dynamic relaxation, *Computational Mechanics* **43**, 61–72, 2008.

[160] U. Küttler, C. Förster, and W. A. Wall, A solution for the incompressibility dilemma in partitioned fluid–structure interaction with pure Dirichlet fluid domains, *Computational Mechanics* **38**, 417–429, 2006.

[161] D. Kuzmin, A guide to numerical methods for transport equations, *University Erlangen-Nuremberg*, 2010.

[162] J. D. Lambert, *Numerical methods for ordinary differential systems: the initial value problem*, John Wiley and Sons, 1991.

[163] M. G. Larson and F. Bengzon, *The finite element method: Theory, implementation, and applications*, Volume 10, Springer, 2013.

[164] D. Lasseux, A. Ahmadi, and A. A. A. Arani, Two-phase inertial flow in homogeneous porous media: a theoretical derivation of a macroscopic model, *Transport in Porous Media* **75**, 371–400, 2008.

[165] D. S. Leake and S. M. Rankin, The oxidative modification of low-density lipoproteins by macrophages, *Biochemical Journal* **270**, 741–748, 1990.

[166] S.-W. Lee, L. Antiga, J. D. Spence, and D. A. Steinman, Geometry of the carotid bifurcation predicts its exposure to disturbed flow, *Stroke* **39**, 2341–2347, 2008.

[167] Y. T. Lee, H. Y. Lin, Y. W. F. Chan, K. H. C. Li, O. T. L. To, B. P. Yan, T. Liu, G. Li, W. T. Wong, W. Keung, et al., Mouse models of atherosclerosis: a historical perspective and recent advances, *Lipids in Health and Disease* **16**, 12, 2017.

[168] S. Lehoux and B. I. Lévy, Collateral artery growth, *Circulation Research;* **99**, 567–569, 2006.

[169] H. Lehr, C. Hübner, D. Nolte, B. Finckh, U. Beisiegel, A. Kohlschütter, and K. Messmer, Oxidatively modified human low-density lipoprotein stimulates leukocyte adherence to the microvascular endothelium in vivo, *Research in Experimental Medicine* **191**, 85–90, 1991.

[170] F. Leuschner, P. J. Rauch, T. Ueno, R. Gorbatov, B. Marinelli, W. W. Lee, P. Dutta, Y. Wei, C. Robbins, Y. Iwamoto, et al., Rapid monocyte kinetics in acute myocardial infarction are sustained by extramedullary monocytopoiesis, *Journal of Experimental Medicine* **209**, 123–137, 2012.

[171] K. Ley, C. Laudanna, M. I. Cybulsky, and S. Nourshargh, Getting to the site of inflammation: the leukocyte adhesion cascade updated, *Nature Reviews Immunology* **7**, 678–689, 2007.

[172] P. Libby, Molecular bases of the acute coronary syndromes, *Circulation* **91**, 2844–2850, 1995.

[173] P. Libby, Inflammation in atherosclerosis, *Nature* **420**, 868–874, 2002.

[174] P. Libby, P. M. Ridker, and G. K. Hansson, Progress and challenges in translating the biology of atherosclerosis, *Nature* **473**, 317, 2011.

[175] J. Lin, H. Li, M. Yang, J. Ren, Z. Huang, F. Han, J. Huang, J. Ma, D. Zhang, Z. Zhang, et al., A role of RIP3-mediated macrophage necrosis in atherosclerosis development, *Cell Reports* **3**, 200–210, 2013.

[176] M. Liu, H. Tang, J. K. Nicholson, and J. C. Lindon, Use of 1h nmr-determined diffusion coefficients to characterize lipoprotein fractions in human blood plasma, *Magnetic Resonance in Chemistry* **40**, S83–S88, 2002.

[177] X. Liu, Y. Fan, and X. Deng, Effect of spiral flow on the transport of oxygen in the aorta: a numerical study, *Annals of Biomedical Engineering* **38**, 917–926, 2010.

[178] X. Liu, Y. Fan, X. Deng, and F. Zhan, Effect of non-Newtonian and pulsatile blood flow on mass transport in the human aorta, *Journal of Biomechanics* **44**, 1123–1131, 2011.

[179] Y. Liu, C. Dang, M. Garcia, H. Gregersen, and G. S. Kassab, Surrounding tissues affect the passive mechanics of the vessel wall: theory and experiment, *American Journal of Physiology-Heart and Circulatory Physiology* **293**, H3290–H3300, 2007.

[180] J. Llodrá, V. Angeli, J. Liu, E. Trogan, E. A. Fisher, and G. J. Randolph, Emigration of monocyte-derived cells from atherosclerotic lesions characterizes regressive, but not progressive, plaques, *Proceedings of the National Academy of Sciences of the United States of America* **101**, 11779–11784, 2004.

[181] H. Lodish, D. Baltimore, A. Berk, S. L. Zipursky, P. Matsudaira, and J. Darnell, *Molecular cell biology*, Volume 3, Scientific American Books New York, 1995.

[182] H. M. Loree, B. J. Tobias, L. J. Gibson, R. D. Kamm, D. M. Small, and R. T. Lee, Mechanical properties of model atherosclerotic lesion lipid pools, *Arteriosclerosis, Thrombosis, and Vascular Biology* **14**, 230–234, 1994.

[183] M. Lougheed, C. M. Lum, W. Ling, H. Suzuki, T. Kodama, and U. Steinbrecher, High affinity saturable uptake of oxidized low density lipoprotein by macrophages from mice lacking the scavenger receptor class A type I/II, *Journal of Biological Chemistry* **272**, 12938–12944, 1997.

[184] A. J. Lusis, Atherosclerosis, *Nature* **407**, 233–241, 2000.

[185] E. Lutgens, D. Lievens, L. Beckers, E. Wijnands, O. Soehnlein, A. Zernecke, T. Seijkens, D. Engel, J. Cleutjens, A. M. Keller, et al., Deficient CD40-TRAF6 signaling in leukocytes prevents atherosclerosis by skewing the immune response toward an antiinflammatory profile, *The Journal of Experimental Medicine* **207**, 391–404, 2010.

[186] R. H. Mackey, L. Venkitachalam, and K. Sutton-Tyrrell, Calcifications, arterial stiffness and atherosclerosis, In *Atherosclerosis, Large Arteries and Cardiovascular Risk*, Volume 44, pages 234–244, Karger Publishers, 2007.

[187] M. Mackness, C. Abbott, S. Arrol, and P. Durrington, The role of high-density lipoprotein and lipid-soluble antioxidant vitamins in inhibiting low-density lipoprotein oxidation, *Biochemical Journal* **294**, 829–834, 1993.

[188] M. I. Mackness, S. Arrol, C. Abbott, and P. N. Durrington, Protection of low-density lipoprotein against oxidative modification by high-density lipoprotein associated paraoxonase, *Atherosclerosis* **104**, 129–135, 1993.

[189] K. Maiellaro and W. R. Taylor, The role of the adventitia in vascular inflammation, *Cardiovascular Research* **75**, 640–648, 2007.

[190] A. M. Malek, S. L. Alper, and S. Izumo, Hemodynamic shear stress and its role in atherosclerosis, *Journal of the American Medical Association* **282**, 2035–2042, 1999.

[191] H. Maoz, A. Polliack, V. Barak, S. Yatziv, S. Biran, H. Giloh, and A. J. Treves, Parameters affecting the in vitro maturation of human monocytes to macrophages, *Stem Cells* **4**, 167–185, 1986.

[192] M. Mayr, *A Monolithic Solver for Fluid-Structure Interaction with Adaptive Time Stepping and a Hybrid Preconditioner*, PhD thesis, Dissertation, München, Technische Universität München, 2016.

[193] M. Mayr, T. Klöppel, W. A. Wall, and M. W. Gee, A temporal consistent monolithic approach to fluid-structure interaction enabling single field predictors, *SIAM Journal on Scientific Computing* **37**, B30–B59, 2015.

[194] R. Melmed, P. Karanian, and R. Berlin, Control of cell volume in the J774 macrophage by microtubule disassembly and cyclic AMP, *The Journal of Cell Biology* **90**, 761–768, 1981.

[195] G. Meyer, A. Tedgui, et al., Effects of pressure-induced stretch and convection on low-density lipoprotein and albumin uptake in the rabbit aortic wall, *Circulation Research* **79**, 532–540, 1996.

[196] R. Milo, What is the total number of protein molecules per cell volume? A call to rethink some published values, *Bioessays* **35**, 1050–1055, 2013.

[197] P. Moireau, N. Xiao, M. Astorino, C. A. Figueroa, D. Chapelle, C. A. Taylor, and J.-F. Gerbeau, External tissue support and fluid–structure simulation in blood flows, *Biomechanics and Modeling in Mechanobiology* **11**, 1–18, 2012.

[198] K. J. Moore and I. Tabas, Macrophages in the pathogenesis of atherosclerosis, *Cell* **145**, 341–355, 2011.

[199] K. J. Moore, F. J. Sheedy, and E. A. Fisher, Macrophages in atherosclerosis: a dynamic balance, *Nature Reviews Immunology* **13**, 709–721, 2013.

[200] D. Morel, P. E. DiCorleto, and G. Chisolm, Endothelial and smooth muscle cells alter low density lipoprotein in vitro by free radical oxidation, *Arteriosclerosis, Thrombosis, and Vascular Biology* **4**, 357–364, 1984.

[201] D. M. Mosser and J. P. Edwards, Exploring the full spectrum of macrophage activation, *Nature Reviews Immunology* **8**, 958–969, 2008.

[202] D. Mozaffarian, E. J. Benjamin, A. S. Go, D. K. Arnett, M. J. Blaha, M. Cushman, S. R. Das, S. de Ferranti, J.-P. Després, H. J. Fullerton, et al., Heart disease and stroke statistics—2016 update, *Circulation* **133**, e38–e360, 2016.

[203] S. K. Nadkarni, B. E. Bouma, T. Helg, R. Chan, E. Halpern, A. Chau, M. S. Minsky, J. T. Motz, S. L. Houser, and G. J. Tearney, Characterization of atherosclerotic plaques by laser speckle imaging, *Circulation* **112**, 885–892, 2005.

[204] Y. Nagano, H. Arai, and T. Kita, High density lipoprotein loses its effect to stimulate efflux of cholesterol from foam cells after oxidative modification, *Proceedings of the National Academy of Sciences* **88**, 6457–6461, 1991.

[205] National Institutes of Health and National Heart, Lung and Blood Institute, ATP III guidelines at-a-glance quick desk reference, *NIH publication*, 2001.

[206] A. C. Newby and A. B. Zaltsman, Fibrous cap formation or destruction—the critical importance of vascular smooth muscle cell proliferation, migration and matrix formation, *Cardiovascular Research* **41**, 345–360, 1999.

[207] R. Ogden, Large deformation isotropic elasticity-on the correlation of theory and experiment for incompressible rubberlike solids, In *Proceedings of the Royal Society of London: Mathematical, Physical and Engineering Sciences*, Volume 326, pages 565–584. The Royal Society, 1972.

[208] R. Ogden, Nearly isochoric elastic deformations: application to rubberlike solids, *Journal of the Mechanics and Physics of Solids* **26**, 37–57, 1978.

[209] U. Olgac, V. Kurtcuoglu, and D. Poulikakos, Computational modeling of coupled blood-wall mass transport of LDL: effects of local wall shear stress, *American Journal of Physiology-Heart and Circulatory Physiology* **294**, H909–H919, 2008.

[210] U. Olgac, D. Poulikakos, S. C. Saur, H. Alkadhi, and V. Kurtcuoglu, Patient-specific three-dimensional simulation of LDL accumulation in a human left coronary artery in its healthy and atherosclerotic states, *American Journal of Physiology-Heart and Circulatory Physiology* **296**, H1969–H1982, 2009.

[211] M. S. Olufsen, C. S. Peskin, W. Y. Kim, E. M. Pedersen, A. Nadim, and J. Larsen, Numerical simulation and experimental validation of blood flow in arteries with structured-tree outflow conditions, *Annals of Biomedical Engineering* **28**, 1281–1299, 2000.

[212] A. Ougrinovskaia, *Mathematical Models of Atherosclerosis*, PhD thesis, University of Sydney, School of Mathematics and Statistics, 2011.

[213] A. Ougrinovskaia, R. S. Thompson, and M. R. Myerscough, An ODE model of early stages of atherosclerosis: mechanisms of the inflammatory response, *Bulletin of Mathematical Biology* **72**, 1534–61, 2010.

[214] C. Palombo and M. Kozakova, Arterial stiffness, atherosclerosis and cardiovascular risk: Pathophysiologic mechanisms and emerging clinical indications, *Vascular Pharmacology* **77**, 1–7, 2016.

[215] A. Parton, V. McGilligan, M. O'Kane, F. R. Baldrick, and S. Watterson, Computational modelling of atherosclerosis, *Briefings in Bioinformatics* **17**, 562–575, 2016.

[216] V. Peiffer, S. J. Sherwin, and P. D. Weinberg, Does low and oscillatory wall shear stress correlate spatially with early atherosclerosis? A systematic review, *Cardiovascular Research* **99**, 242–250, 2013.

[217] V. P.-A. Peiffer, *Study of the relation between blood flow and the age-dependent localisation of early atherosclerosis*, PhD thesis, Imperial College London, 2013.

[218] M. C. Phillips, K. L. Gillotte, M. P. Haynes, W. J. Johnson, S. Lund-Katz, and G. H. Rothblat, Mechanisms of high density lipoprotein-mediated efflux of cholesterol from cell plasma membranes, *Atherosclerosis* **137**, S13–S17, 1998.

[219] P. Poredos, Intima-media thickness: indicator of cardiovascular risk and measure of the extent of atherosclerosis, *Vascular Medicine* **9**, 46–54, 2004.

[220] S. Potteaux, E. L. Gautier, S. B. Hutchison, N. van Rooijen, D. J. Rader, M. J. Thomas, M. G. Sorci-Thomas, and G. J. Randolph, Suppressed monocyte recruitment drives macrophage removal from atherosclerotic plaques of Apoe–/–mice during disease regression, *The Journal of Clinical Investigation* **121**, 2025–2036, 2011.

[221] M. Prosi, P. Zunino, K. Perktold, and A. Quarteroni, Mathematical and numerical models for transfer of low-density lipoproteins through the arterial walls: a new methodology for the model set up with applications to the study of disturbed lumenal flow, *Journal of Biomechanics* **38**, 903–917, 2005.

[222] A. Quarteroni, M. Tuveri, and A. Veneziani, Computational vascular fluid dynamics: problems, models and methods, *Computing and Visualization in Science* **2**, 163–197, 2000.

[223] A.-R. A. Ragab and S. E. A. Bayoumi, *Engineering solid mechanics: fundamentals and applications*, CRC Press, 1998.

[224] T. Rajavashisth, A. Andalibi, M. Territo, J. Berliner, M. Navab, A. Fogelman, and A. Lusis, Induction of endothelial cell expression of granulocyte and macrophage colony-stimulating factors by modified low-density lipoproteins, *Nature* **344**, 254–257, 1990.

[225] I. Rajman, P. I. Eacho, P. Chowienczyk, and J. Ritter, LDL particle size: an important drug target?, *British Journal of Clinical Pharmacology* **48**, 125–133, 1999.

[226] G. Rappitsch and K. Perktold, Pulsatile albumin transport in large arteries: a numerical simulation study, *Journal of Biomechanical Engineering* **118**, 511–519, 1996.

[227] N. Resnick, H. Yahav, A. Shay-Salit, M. Shushy, S. Schubert, L. C. M. Zilberman, and E. Wofovitz, Fluid shear stress and the vascular endothelium: for better and for worse, *Progress in Biophysics and Molecular Biology* **81**, 177–199, 2003.

[228] C. S. Robbins, I. Hilgendorf, G. F. Weber, I. Theurl, Y. Iwamoto, J.-L. Figueiredo, R. Gorbatov, G. K. Sukhova, L. M. Gerhardt, D. Smyth, et al., Local proliferation dominates lesional macrophage accumulation in atherosclerosis, *Nature Medicine* **19**, 1166–1172, 2013.

[229] J. G. Robinson and S. S. Gidding, Curing atherosclerosis should be the next major cardiovascular prevention goal, *Journal of the American College of Cardiology* **63**, 2779–2785, 2014.

[230] S. Roccabianca, C. Figueroa, G. Tellides, and J. Humphrey, Quantification of regional differences in aortic stiffness in the aging human, *Journal of the Mechanical Behavior of Biomedical Materials* **29**, 618–634, 2014.

[231] E. K. Rodriguez, A. Hoger, and A. D. McCulloch, Stress-dependent finite growth in soft elastic tissues, *Journal of Biomechanics* **27**, 455–467, 1994.

[232] M. E. Rosenfeld, M. M. Averill, B. J. Bennett, and S. M. Schwartz, Progression and disruption of advanced atherosclerotic plaques in murine models, *Current Drug Targets* **9**, 210–216, 2008.

[233] R. Ross, Atherosclerosis—an inflammatory disease, *New England Journal of Medicine* **340**, 115–126, 1999.

[234] Y. Saad and M. H. Schultz, GMRES: A generalized minimal residual algorithm for solving nonsymmetric linear systems, *SIAM Journal on Scientific and Statistical Computing* **7**, 856–869, 1986.

[235] M. Sala and R. S. Tuminaro, A new Petrov–Galerkin smoothed aggregation preconditioner for nonsymmetric linear systems, *SIAM Journal on Scientific Computing* **31**, 143–166, 2008.

[236] C. Sansour, On the physical assumptions underlying the volumetric-isochoric split and the case of anisotropy, *European Journal of Mechanics-A/Solids* **27**, 28–39, 2008.

[237] D. M. Schrijvers, G. R. De Meyer, M. M. Kockx, A. G. Herman, and W. Martinet, Phagocytosis of apoptotic cells by macrophages is impaired in atherosclerosis, *Arteriosclerosis, Thrombosis, and Vascular Biology* **25**, 1256–1261, 2005.

[238] T. F. Sherman, On connecting large vessels to small. The meaning of Murray's law, *The Journal of General Physiology* **78**, 431–453, 1981.

[239] T. Shirai, M. Hilhorst, D. G. Harrison, J. J. Goronzy, and C. M. Weyand, Macrophages in vascular inflammation–from atherosclerosis to vasculitis, *Autoimmunity* **48**, 139–151, 2015.

[240] H. W. Sill, Y. S. Chang, J. R. Artman, J. Frangos, T. Hollis, and J. Tarbell, Shear stress increases hydraulic conductivity of cultured endothelial monolayers, *American Journal of Physiology-Heart and Circulatory Physiology* **268**, H535–H543, 1995.

[241] V. Singh, R. L. Tiwari, M. Dikshit, and M. K. Barthwal, Models to study atherosclerosis: a mechanistic insight, *Current Vascular Pharmacology* **7**, 75–109, 2009.

[242] R. Skalak, S. Zargaryan, R. K. Jain, P. A. Netti, and A. Hoger, Compatibility and the genesis of residual stress by volumetric growth, *Journal of Mathematical Biology* **34**, 889–914, 1996.

[243] N. Smith, A. Pullan, and P. J. Hunter, An anatomically based model of transient coronary blood flow in the heart, *SIAM Journal on Applied mathematics* **62**, 990–1018, 2002.

[244] H. Soran, J. D. Schofield, Y. Liu, and P. N. Durrington, How HDL protects LDL against atherogenic modification: paraoxonase 1 and other dramatis personae, *Current Opinion in Lipidology* **26**, 247–256, 2015.

[245] J. V. Soulis, O. P. Lampri, D. K. Fytanidis, and G. D. Giannoglou, Relative residence time and oscillatory shear index of non-Newtonian flow models in aorta, In *Biomedical Engineering, 2011 10th International Workshop on*, pages 1–4. IEEE, 2011.

[246] D. K. Stangeby and C. R. Ethier, Computational analysis of coupled blood-wall arterial LDL transport, *Journal of Biomechanical Engineering* **124**, 1–8, 2002.

[247] D. K. Stangeby and C. R. Ethier, Coupled computational analysis of arterial LDL transport – effects of hypertension, *Computer Methods in Biomechanics and Biomedical Engineering* **5**, 233–241, 2002.

[248] H. C. Stary, A. B. Chandler, S. Glagov, J. R. Guyton, W. Insull, M. E. Rosenfeld, S. A. Schaffer, C. J. Schwartz, W. D. Wagner, and R. W. Wissler, A definition of initial, fatty streak, and intermediate lesions of atherosclerosis. A report from the Committee on Vascular Lesions of the Council on Arteriosclerosis, American Heart Association, *Circulation* **89**, 2462–2478, 1994.

[249] H. C. Stary, A. B. Chandler, R. E. Dinsmore, V. Fuster, S. Glagov, W. Insull, M. E. Rosenfeld, C. J. Schwartz, W. D. Wagner, and R. W. Wissler, A definition of advanced types of atherosclerotic lesions and a histological classification of atherosclerosis, *Circulation* **92**, 1355–1374, 1995.

[250] D. Steingberg, Beyond cholesterol modification of low density lipoprotein that increase its atherogenecity, *New England Journal of Medicine* **320**, 915–924, 1989.

[251] S. Stender and D. Zilversmit, Transfer of plasma lipoprotein components and of plasma proteins into aortas of cholesterol-fed rabbits. Molecular size as a determinant of plasma lipoprotein influx, *Arteriosclerosis, Thrombosis, and Vascular Biology* **1**, 38–49, 1981.

[252] R. Stocker and J. F. Keaney, Role of oxidative modifications in atherosclerosis, *Physiological Reviews* **84**, 1381–1478, 2004.

[253] N. J. Stone, J. Robinson, A. H. Lichtenstein, C. N. B. Merz, C. B. Blum, R. H. Eckel, A. C. Goldberg, D. Gordon, D. Levy, D. M. Lloyd-Jones, et al., 2013 ACC/AHA guideline on the treatment of blood cholesterol to reduce atherosclerotic cardiovascular risk in adults, *Circulation* **129**, S1–S45, 2014.

[254] N. Sun, N. B. Wood, A. D. Hughes, S. A. Thom, and X. Y. Xu, Fluid-wall modelling of mass transfer in an axisymmetric stenosis: effects of shear-dependent transport properties, *Annals of Biomedical Engineering* **34**, 1119–1128, 2006.

[255] N. Sun, N. B. Wood, A. D. Hughes, S. A. M. Thom, and X. Y. Xu, Influence of pulsatile flow on LDL transport in the arterial wall, *Annals of Biomedical Engineering* **35**, 1782–90, 2007.

[256] N. Sun, N. B. Wood, A. D. Hughes, S. A. Thom, and X. Y. Xu, Effects of transmural pressure and wall shear stress on LDL accumulation in the arterial wall: a numerical study using a multilayered model, *American Journal of Physiology - Heart and Circulatory Physiology* **292**, H3148–H3157, 2007.

[257] J. Suo, D. E. Ferrara, D. Sorescu, R. E. Guldberg, W. R. Taylor, and D. P. Giddens, Hemodynamic shear stresses in mouse aortas implications for atherogenesis, *Arteriosclerosis, Thrombosis, and Vascular Biology* **27**, 346–351, 2007.

[258] I. Tabas, Consequences and therapeutic implications of macrophage apoptosis in atherosclerosis, *Arteriosclerosis, Thrombosis, and Vascular Biology* **25**, 2255–2264, 2005.

[259] I. Tabas, S. Marathe, G. A. Keesler, N. Beatini, and Y. Shiratori, Evidence that the initial up-regulation of phosphatidylcholine biosynthesis in free cholesterol-loaded macrophages is an adaptive response that prevents cholesterol-induced cellular necrosis proposed role of an eventual failure of this response in foam cell necrosis in advanced atherosclerosis, *Journal of Biological Chemistry* **271**, 22773–22781, 1996.

[260] K. Takahashi, M. Takeya, and N. Sakashita, Multifunctional roles of macrophages in the development and progression of atherosclerosis in humans and experimental animals, *Medical electron microscopy* **35**, 179–203, 2002.

[261] D. Tang, Z. Teng, G. Canton, C. Yang, M. Ferguson, X. Huang, J. Zheng, P. K. Woodard, and C. Yuan, Sites of rupture in human atherosclerotic carotid plaques are associated with high structural stresses, *Stroke* **40**, 3258–3263, 2009.

[262] A. Tedgui and M. Lever, Filtration through damaged and undamaged rabbit thoracic aorta, *American Journal of Physiology - Heart and Circulatory Physiology* **247**, H784–H791, 1984.

[263] T. Teerlink, P. G. Scheffer, S. J. Bakker, and R. J. Heine, Combined data from LDL composition and size measurement are compatible with a discoid particle shape, *Journal of Lipid Research* **45**, 954–966, 2004.

[264] S. R. Thomas and D. C. Mikulecky, Transcapillary solute exchange: A comparison of the kedem-katchalsky convection-diffusion equations with the rigorous nonlinear equations for this special case, *Microvascular Research* **15**, 207–220, 1978.

[265] M. P. Thon, H. Z. Ford, M. W. Gee, and M. R. Myerscough, A quantitative model of early atherosclerotic plaques parameterized using in vitro experiments, *Bulletin of Mathematical Biology* **80**, 175–214, 2018.

[266] M. P. Thon, A. Hemmler, A. Glinzer, M. Mayr, M. Wildgruber, A. Zernecke-Madsen, and M. W. Gee, A multiphysics approach for modeling early atherosclerosis, *Biomechanics and Modeling in Mechanobiology* **17**, 617–644, 2018.

[267] G. D. Tomaso, V. Díaz-Zuccarini, and C. Pichardo-Almarza, A multiscale model of atherosclerotic plaque formation at its early stage, *IEEE Transactions on Biomedical Engineering* **58**, 3460–3463, 2011.

[268] R. G. Tompkins, Quantitative analysis of blood vessel permeability of squirrel monkeys, *American Journal of Physiology - Heart and Circulatory Physiology* **260**, H1194–H1204, 1991.

[269] G. A. Truskey, W. L. Roberts, R. A. Herrmann, and R. A. Malinauskas, Measurement of endothelial permeability to 125I-low density lipoproteins in rabbit arteries by use of en face preparations, *Circulation Research* **71**, 883–897, 1992.

[270] P. Van, M. Brezina, J. Mandel, et al., Convergence of algebraic multigrid based on smoothed aggregation, *Numerische Mathematik* **88**, 559–579, 2001.

[271] N. M. van Popele, D. E. Grobbee, M. L. Bots, R. Asmar, J. Topouchian, R. S. Reneman, A. P. Hoeks, D. A. van der Kuip, A. Hofman, and J. C. Witteman, Association between arterial stiffness and atherosclerosis, *Stroke* **32**, 454–460, 2001.

[272] M. M. Véniant, S. Withycombe, and S. G. Young, Lipoprotein size and atherosclerosis susceptibility in Apoe-/- and Ldlr-/- mice, *Arteriosclerosis, Thrombosis, and Vascular Biology* **21**, 1567–1570, 2001.

[273] F. Verdugo and W. A. Wall, Unified computational framework for the efficient solution of n-field coupled problems with monolithic schemes, *Computer Methods in Applied Mechanics and Engineering* **310**, 335–366, 2016.

[274] R. Virmani, A. P. Burke, F. D. Kolodgie, and A. Farb, Vulnerable plaque: the pathology of unstable coronary lesions, *Journal of Interventional Cardiology* **15**, 439–446, 2002.

[275] A.-T. Vuong, *A Computational Approach to Coupled Poroelastic Media Problems*, PhD thesis, Technische Universität München, 2016.

[276] S. Wada, M. Koujiya, and T. Karino, Theoretical study of the effect of local flow disturbances on the concentration of low-density lipoproteins at the luminal surface of end-to-end anastomosed vessels, *Medical and Biological Engineering and Computing* **40**, 576–587, 2002.

[277] W. Wall and M. Gee, Baci: a parallel multiphysics finite element environment, *Institute for Computational Mechanics, Technische Universität München*, 2010.

[278] W. A. Wall, *Fluid-struktur-interaktion mit stabilisierten finiten elementen*, PhD thesis, Universität Stuttgart, 1999.

[279] W. Wang, Y. Lee, and C. H. Lee, Review: The physiological and computational approaches for atherosclerosis treatment, *International Journal of Cardiology* **167**, 1664–1676, 2013.

[280] J. J. Wentzel, Y. S. Chatzizisis, F. J. Gijsen, G. D. Giannoglou, C. L. Feldman, and P. H. Stone, Endothelial shear stress in the evolution of coronary atherosclerotic plaque and vascular remodelling: current understanding and remaining questions, *Cardiovascular Research* **96**, 234–243, 2012.

[281] N. Westerhof, J.-W. Lankhaar, and B. E. Westerhof, The arterial Windkessel, *Medical and Biological Engineering and Computing* **47**, 131–141, 2009.

[282] S. E. Whitesall, J. B. Hoff, A. P. Vollmer, and L. G. D'Alecy, Comparison of simultaneous measurement of mouse systolic arterial blood pressure by radiotelemetry and tail-cuff methods, *American Journal of Physiology-Heart and Circulatory Physiology* **286**, H2408–H2415, 2004.

[283] S. C. Whitman, A practical approach to using mice in atherosclerosis research, *The Clinical Biochemist Reviews* **25**, 81, 2004.

[284] F. Wiesmann, M. Szimtenings, A. Frydrychowicz, R. Illinger, A. Hunecke, E. Rommel, S. Neubauer, and A. Haase, High-resolution MRI with cardiac and respiratory gating allows for accurate in vivo atherosclerotic plaque visualization in the murine aortic arch, *Magnetic Resonance in Medicine* **50**, 69–74, 2003.

[285] T. Wiesner, *Flexible aggregation-based algebraic multigrid methods for contact and flow problems*, PhD thesis, Technische Universität München, 2015.

[286] K. J. Williams and I. Tabas, The response-to-retention hypothesis of early atherogenesis, *Arteriosclerosis, Thrombosis, and Vascular Biology* **15**, 551–561, 1995.

[287] J. L. Witztum and D. Steinberg, Role of oxidized low density lipoprotein in atherogenesis, *Journal of Clinical Investigation* **88**, 1785, 1991.

[288] B. I. Wohlmuth, A mortar finite element method using dual spaces for the Lagrange multiplier, *SIAM Journal on Numerical Analysis* **38**, 989–1012, 2000.

[289] World Healt Organisation (WHO). Global health estimates summary tables: Projections of mortality and causes of death, 2015 and 2030, 2013.

[290] World Healt Organisation (WHO). Cardiovascular diseases, fact sheet n^{o} 317, 2017.

[291] P. Wriggers, *Nonlinear finite element methods*, Springer, 2008.

[292] N. Xiao, J. Alastruey, and C. Alberto Figueroa, A systematic comparison between 1-D and 3-D hemodynamics in compliant arterial models, *International Journal for Numerical Methods in Biomedical Engineering* **30**, 204–31, 2014.

[293] C. Yang, D. Tang, C. Yuan, T. S. Hatsukami, J. Zheng, and P. K. Woodard, In vivo/ex vivo MRI-based 3D non-Newtonian FSI models for human atherosclerotic plaques compared with fluid/wall-only models, *Computer Modeling in Engineering Sciences* **19**, 233, 2007.

[294] N. Yang and K. Vafai, Modeling of low-density lipoprotein (LDL) transport in the artery – effects of hypertension, *International Journal of Heat and Mass Transfer* **49**, 850–867, 2006.

[295] Y. Yang, T. Richter, W. Jäger, and M. Neuss-Radu, An ALE approach to mechano-chemical processes in fluid–structure interactions, *International Journal for Numerical Methods in Fluids*, 2016.

[296] P. M. Yao and I. Tabas, Free cholesterol loading of macrophages induces apoptosis involving the fas pathway, *Journal of Biological Chemistry* **275**, 23807–23813, 2000.

[297] L. Yoshihara, M. Coroneo, A. Comerford, G. Bauer, T. Klöppel, and W. Wall, A combined fluid–structure interaction and multi–field scalar transport model for simulating mass transport in biomechanics, *International Journal for Numerical Methods in Engineering* **100**, 277–299, 2014.

[298] M. Zareh, G. Fradet, G. Naser, and H. Mohammadi, Are two-dimensional images sufficient to assess the atherosclerotic plaque vulnerability: a viscoelastic and anisotropic finite element model, *Cardiovascular System* **3**, 3, 2015.

[299] X. Zhu, J.-Y. Lee, J. M. Timmins, J. M. Brown, E. Boudyguina, A. Mulya, A. K. Gebre, M. C. Willingham, E. M. Hiltbold, N. Mishra, N. Maeda, and J. S. Parks, Increased cellular free cholesterol in macrophage-specific Abca1 knock-out mice enhances pro-inflammatory response of macrophages, *Journal of Biological Chemistry* **283**, 22930–22941, 2008.

[300] Z. Zi, Sensitivity analysis approaches applied to systems biology models, *IET Systems Biology* **5**, 336–346, 2011.

[301] O. C. Zienkiewicz and R. L. Taylor, *The Finite Element Method for Solid and Structural Mechanics*, Butterworth-Heinemann, 7 Edition, 2014.

[302] O. C. Zienkiewicz, R. L. Taylor, and J. Z. Zhu, *The Finite Element Method: Its Basis and Fundamentals*, McGraw-hill London, 7 Edition, 2013.

[303] O. C. Zienkiewicz, R. L. Taylor, and P. Nithiarasu, *The Finite Element Method for Fluid Dynamics*, Butterworth-Heinemann, 7 Edition, 2014.

[304] T. Zohdi, G. Holzapfel, and S. Berger, A phenomenological model for atherosclerotic plaque growth and rupture, *Journal of Theoretical Biology* **227**, 437–443, 2004.

[305] P. Zunino, *Mathematical and numerical modeling of mass transfer in the vascular system*, PhD thesis, Politecnico di Milano, 2002.